Structural Performance of Reinforced Fly Ash and Slag-based Geopolymer Concrete Beams Using Waste Glass-derived Sodium Silicate as an Alternative Activator

Prepared by

ANUOLUWAPO SOLA KOLADE

22838953

Submitted in accordance with the requirements for the degree of

MASTER OF ENGINEERING (M.Eng.)

in the subject

CIVIL AND ENVIRONMENTAL ENGINEERING AND BUILDING SCIENCE

at the

COLLEGE OF SCIENCE, ENGINEERING AND TECHNOLOGY (CSET)
UNIVERSITY OF SOUTH AFRICA

SUPERVISOR: Prof. Bolanle D. Ikotun
CO-SUPERVISOR: Dr. Damilola O. Oyejobi

May, 2026

DECLARATION

Name: Anuoluwapo Sola KOLADE

Student Number: 22838953

Degree: Master of Engineering (M.Eng.)

Dissertation Title: Structural Performance of Reinforced Fly Ash and Slag-based Geopolymer Concrete Beams Using Waste Glass-derived Sodium Silicate as an Alternative Activator

I declare that the above dissertation is my work and that all the sources that I have used or quoted have been indicated and acknowledged by means of complete references.

I further declare that I submitted the dissertation to originality checking software and that it falls within the accepted requirements for originality.

I further declare that I have not previously submitted this work, or part of it, for examination at UNISA for another qualification or at any other higher education institution.

SIGNATURE:  DATE: 15/05/2026

DEDICATION

I dedicate this work to the Almighty God, whose unfailing grace, wisdom and strength sustained me throughout this journey. Every step of this research has been guided by His providence, and without His light and endless mercies, this achievement would never have been possible. To Him be all the glory.

ACKNOWLEDGEMENTS

My profound appreciation goes to all the people God brought my way throughout this research.

First, my heartfelt thanks to my incredibly kind, patient and supportive supervisors — Professor Bolanle Ikotun and Dr. Damilola Oyejobi. Your outstanding mentorship, guidance and encouragement have been invaluable. I began this program with hope, and I am completing it with the skills and confidence needed to contribute meaningfully to the built environment as a researcher. Thank you for challenging me to grow and for pushing me beyond my limits. I am also grateful to the University of South Africa for granting me a scholarship and providing the resources and facilities that made this work possible.

To my darling wife (Olanike Kolade), thank you for the courage and sacrifice of staying in Nigeria while I pursued this degree. Your unwavering love and prayers have been my anchor and peace throughout this journey. My deepest gratitude also goes to my parents (Mr. and Mrs. Taye and Bose Kolade) and siblings (Taye, Kehinde and Bolade) for their constant check-ins, prayers and support, which often came at the exact moments I needed them most.

Special thanks to those who assisted with my experimental work; Ms. Palesa and the entire Civil Engineering lab team, Professor Motsa, Mr. Siya and Ms. Nosipho at iNanoWS (UNISA) for help with microstructural analysis, Mr. Tshepo and Sibusiso at the Mechanical Engineering lab for materials testing, Mr. Dombo and the Industrial Engineering lab team for materials processing, and Mr. Poopedi at the Mining Engineering lab for additional support with material processing.

I am also grateful to the industry partners who provided essential materials; CHRYSO for superplasticizers, Mr. Asser at Ash Resources (Lafarge) for fly ash, AfriSam for slag, and African Pegmatite for waste glass powder.

A heartfelt thank you to my senior colleagues and friends turned family, who stood with me through this process; Mr. Kilani, Mr. Aderinto, Mr. Aremu, Ms. Tosin, Mr. Paul, Mr. Gashaw, Dr. Rasheed, Dr. Madirisha, and Baba Akinwale. Your support and encouragement made a world of difference.

Above all, my greatest gratitude goes to God Almighty, who has been my help and sustainer. He guided me when I felt lost, provided clarity in moments of doubt, made a way where there seemed to be none and fulfilled His promises in my life through this program.

ABSTRACT

The pursuit of sustainable construction materials has advanced geopolymer concrete (GPC) as an alternative to Portland cement systems. However, most GPC systems rely on commercial sodium silicate (CSS), whose high cost, energy demand and environmental impacts limit its large-scale sustainable application. This study therefore investigated the structural performance and sustainability of reinforced fly ash–slag (FA–GGBFS) GPC beams using sodium silicate synthesized from waste glass (WGSS) as an alternative activator to CSS. Mix designs derived from oxide composition analysis of the constituent materials were proportioned to produce medium-strength structural GPC and enable comparison between CSS and WGSS activator systems. Mechanical characterization, reinforced beam testing under three-point loading and life cycle assessment (LCA) following ISO 14040 were conducted, with structural performance validated against Eurocode 2. The WGSS concrete mixes with FA:GGBFS ratios of 1:0, 7:1 and 3:1 achieved 28-day compressive strengths of 26.64, 40.17 and 45.74 MPa, respectively, while the control CSS concrete (FA:GGBFS = 1:0) reached 94.75 MPa. Among the WGSS formulations, the 7:1 mix demonstrated the most balanced structural, environmental and economic performance. Beams produced with this mix achieved a flexural moment capacity of 11.56 kNm, comparable to the 11.46 kNm recorded for the CSS control beam, while exhibiting greater mid-span deflection (7.2 mm vs 5.3 mm), indicating improved ductility despite the lower compressive strength. LCA further showed reductions in carbon emissions (~31%) and production cost (~10%) relative to the CSS system. These results demonstrate that WGSS-based GPC can achieve adequate structural capacity relative to design predictions while providing notable environmental and economic advantages for sustainable infrastructure applications.

Key Terms: Geopolymer concrete, fly ash, slag, sodium silicate, waste glass powder, structural performance, ductility, sustainability, carbon footprint, waste valorization.

ISIFINYEZO

Ukufuna izinto zokwakha ezisimeme kuholele ekuthuthukisweni kukakhonkolo we-geopolymer (GPC) njengendlela ehlukile esikhundleni sezinhlelo zikakhonkolo we-Portland cement. Nokho, iningi lezinhlelo ze-GPC zisebenzisa i-sodium silicate ethengiswayo (CSS), enezindleko eziphezulu, ukusetshenziswa kwamandla okukhulu kanye nemithelela emibi kwezemvelo, okunciphisa ukusetshenziswa kwayo okubanzi ngendlela esimeme. Ngakho-ke lolu cwaningo luhlole ukusebenza kwesakhiwo kanye nokusimama kwemishayo eqinisiwe ye-fly ash–slag (FA–GGBFS) GPC kusetshenziswa i-sodium silicate eyenziwe ngengilazi elahliwe (WGSS) njengendlela ehlukile esikhundleni se-CSS. Izinhlelo zokuxuba ezathuthukiswa ngokususelwa ekuhlaziyweni kokwakheka kwama-oxide ezintweni ezisetshenziswe zahlelwa ukuze kukhiqizwe ukhonkolo wesakhiwo onamandla aphakathi futhi kuvunyelwe ukuqhathaniswa phakathi kwezinhlelo ze-CSS ne-WGSS. Kwasetshenziswa ukuhlolwa kwezici zemishini, ukuhlolwa kwemishayo eqinisiwe ngaphansi komthwalo wamaphuzu amathathu (three-point loading) kanye nokuhlaziywa komjikelezo wempilo (LCA) ngokwe-ISO 14040, kanti ukusebenza kwesakhiwo kwaqinisekiswa kusetshenziswa i-Eurocode 2. Izixube ze-WGSS ezinesilinganiso se-FA:GGBFS esingu-1:0, 7:1 kanye no-3:1 zafinyelela amandla okucindezela angama-26.64, 40.17 kanye no-45.74 MPa ezinsukwini ezingama-28 ngokulandelana, kuyilapho ukhonkolo wokulawula we-CSS (FA:GGBFS = 1:0) wafinyelela ku-94.75 MPa. Phakathi kwezixube ze-WGSS, ingxube engu-7:1 yakhombisa ukusebenza okulinganiselayo kakhulu ngokwesakhiwo, kwezemvelo kanye nezomnotho. Imishayo eyakhiwe ngale ngxube yafinyelela umthamo wokugoba (flexural moment capacity) ongu-11.56 kNm, osondele kakhulu ku-11.46 kNm otholwe emishayweni yokulawula ye-CSS, kodwa yakhombisa ukuchezuka okukhulu maphakathi (7.2 mm uma kuqhathaniswa no-5.3 mm), okubonisa ukwanda kokaguquguquka (ductility) naphezu kwamandla okucindezela aphansi. Ukuhlaziywa kwe-LCA kwabonisa ukwehla kokukhishwa kwekhabhoni (~31%) kanye nezindleko zokukhiqiza (~10%) uma kuqhathaniswa nohlelo lwe-CSS. Le miphumela ikhombisa ukuthi ukhonkolo we-GPC osebenzisa i-WGSS ungakwazi ukufinyelela amandla esakhiwo anele uma kuqhathaniswa nezibikezelo zokuklama, ngesikhathi unikeza izinzuzo ezibalulekile kwezemvelo nezomnotho zokwakha ingqalasizinda esimeme.

Amagama Ayinhloko: Ukhonkolo we-geopolymer, i-fly ash, i-slag, i-sodium silicate, impushana yengilazi elahliwe, ukusebenza kwesakhiwo, ukuguquguquka (ductility), ukusimama, umkhondo wekhabhoni, ukwengeza inani lemfucuza.

TABLE OF CONTENTS

LIST OF FIGURES

LIST OF TABLES

LIST OF ABBREVIATIONS

Abbreviation	Definition
Al_2O_3	Alumina
AL/B	Alkaline solution-to-binder ratio
ANOVA	Analysis of variance
B	Mass of binder
CAC	CO_2 abatement cost
CaO	Calcium oxide
C–S–H	Calcium-silicate-hydrate
C–A–S–H	Calcium-aluminosilicate-hydrate
CO_2	Carbon dioxide
CSS	Commercial sodium silicate
EC2	Eurocode 2
EDS	Energy-dispersive X-ray spectroscopy
EE	Embodied energy
EI	Economic index
Fe_2O_3	Iron oxide
GGBFS	Ground granulated blast furnace slag
GHG	Greenhouse gas
GPC	Geopolymer concrete
GWP	Global warming potential
H_2O/Na_2O	Water-to-sodium oxide ratio
ICE	Inventory of carbon and energy
ITZ	Interfacial transition zone
LCA	Life cycle analysis
LCI	Life cycle inventory
LCIA	Life cycle impact assessment
LOI	Loss on ignition

NaOH	Sodium hydroxide
Na_2CO_3	Sodium carbonate
Na_2O/SiO_2	Sodium oxide-to-silica ratio
Na_2SiO_3	Sodium silicate
PC	Portland cement
PCC	Portland cement concrete
SDGs	Sustainable Development Goals
SEM	Scanning electron microscopy
SH	Mass of NaOH solution
SHconc.	NaOH concentration
SiO_2	Silica
SiO_2/Al_2O_3	Silica-to-alumina ratio
SiO_2/Na_2O	Silicate modulus
SP	Superplasticizer
SS	Mass of Na_2SiO_3 solution
SS/SH	Na_2SiO_3-to-NaOH ratio
Ti	Transportation impact
TiEE	Transport impact of EE
TiGWP	Transport impact of GWP
UTM	Universal testing machine
WGP	Waste glass powder
W/Gs	Water-to-geopolymer solids
W_{EX}	Extra water content in mortar mix
W_{SH}	Water content in NaOH solution
W_{SS}	Water content in Na_2SiO_3 solution
WGSS	Waste glass-derived sodium silicate
XRD	X-ray diffraction
XRF	X-ray fluorescence

CHAPTER 1

1 INTRODUCTION

1.1 Background

The global construction industry remains heavily reliant on Portland cement (PC) as the primary binder in concrete production (Parathi et al., 2021). Although concrete made with PC has facilitated remarkable infrastructural development over the past century, the manufacture of PC remains energy-intensive and environmentally detrimental, contributing significantly to global carbon dioxide (CO_2) emissions (Parathi et al., 2021; Wu et al., 2019). For instance, PC production accounts for 12 – 15% of global industrial energy use and 7 – 10% of global anthropogenic emissions (Bhutta et al., 2017; Delgado-Plana et al., 2024; Hossein et al., 2021; Mohamad et al., 2021; Wu et al., 2019). With the continued expansion of urbanization and industrialization, global demand for concrete is increasing, further intensifying environmental concerns. As a result, it has become a priority to search for sustainable and eco-efficient alternatives to conventional cement (Oyejobi et al., 2024; Radebe et al., 2025).

Geopolymer concrete (GPC) has emerged as a viable and sustainable alternative, with the potential to reduce CO_2 emissions by up to 80% compared to PC-based concrete (Chen et al., 2024; Kolade et al., 2025a; Turner and Collins, 2013). GPC utilizes alumino-silicate-rich industrial and agricultural by-products or wastes, such as fly ash, ground granulated blast furnace slag (GGBFS) and rice husk ash, which undergo alkali activation to form a hardened binder (Amran et al., 2020; Malkawi et al., 2018). Fly ash, rich in reactive aluminosilicates, contributes to long-term strength and workability, while GGBFS provides calcium content that enhances early strength gain and setting characteristics (Kolade et al., 2025a). The synergistic combination of both materials has been shown to produce balanced strength development and improved microstructural densification in GPC systems (Bellum et al., 2020; Kolade et al., 2026a). In addition to diverting industrial and agricultural waste from landfills, geopolymer technology supports circular economy initiatives and industrial symbiosis (Oyejobi et al., 2024). GPC is also known for its lower greenhouse gas emissions, enhanced chemical resistance, thermal stability and superior mechanical and durability performance, which collectively improve service life and reduce maintenance requirements (Eisa et al., 2022; El-Gamal and Selim, 2017; Kolade et al., 2025a; Parathi et al., 2021; Wadström et al., 2021).

A typical geopolymer system requires an alkaline activator, usually comprising sodium hydroxide (NaOH) and sodium silicate (Na_2SiO_3), to initiate the geopolymerization reaction

(Amran et al., 2020; Kolade et al., 2025a; Radebe et al., 2025). Despite its technical advantages, GPC faces economic and environmental challenges due to the dependence on commercial sodium silicate (CSS) and NaOH. Both activators are costly, energy-intensive to produce and emit significant CO_2 during manufacture, which limits the feasibility of large-scale application, especially in developing regions (Fernando et al., 2021; Kolade et al., 2025b; Martinez and Miller, 2005). CSS is typically manufactured through the high-temperature fusion of silica sand (SiO_2) with sodium carbonate (Na_2CO_3) in a furnace at temperatures of approximately 1200 – 1400 °C, producing molten sodium silicate glass that is subsequently dissolved in water to form liquid sodium silicate solutions. This process is highly energy-intensive because of the elevated temperatures required for silica melting and glass formation, resulting in substantial fossil-fuel consumption and associated greenhouse gas emissions (Kolade et al., 2025b; Rajan and Kathirvel, 2021; Umer et al., 2024). Furthermore, the use of sodium carbonate as a raw material contributes additional CO_2 emissions through thermal decomposition reactions occurring during fusion, pushing the total energy demand and emissions to about 5 MJ and 1.5 kgCO_2 per kg of CSS produced (Delgado-Plana et al., 2024; Rajan and Kathirvel, 2021). Also, the extraction and processing of high-purity silica sand involve environmentally disruptive mining and beneficiation activities (Umer et al., 2024). Consequently, the environmental footprint of CSS silicate remains considerable, creating a strong motivation to explore alternative activator sources derived from waste materials, such as waste glass, that can reduce energy demand and raw material extraction (Khasawneh, 2025; Kolade et al., 2025b).

Although several studies (Abdullah et al., 2024; Darmawan et al., 2019; Eisa et al., 2022; Kalaivani et al., 2020; Kumar et al., 2017) have investigated the behaviour of reinforced GPC elements produced with commercial activators, limited information exists on the structural response of GPC incorporating alternative or waste-derived activators. GPC beams, in particular, serve as fundamental test elements for assessing load capacity, stiffness, ductility, crack development and failure characteristics, which are parameters that define structural performance and support the safe design and standardization of GPC systems.

To address these challenges, researchers have explored alternative, low-cost sources of sodium silicate derived from various waste materials, including rice husk ash, waste glass powder (WGP), hazelnut shell ash, coal bottom ash, olive stone biomass ash and agricultural waste ashes (Delgado-Plana et al., 2024; Ghanim et al., 2025; Gok and Sengul, 2024; de Moraes Pinheiro et al., 2018; Omur et al., 2024; Tchakouté et al., 2016a; Umer et al., 2024). Two main synthesis approaches have been reported for producing sodium silicate from silica-rich wastes,

including hydrothermal dissolution and alkali thermal fusion (Alnahhal et al., 2021; Kolade et al., 2025a). Among these techniques, alkali thermal fusion has gained particular attention because it facilitates the breakdown of the amorphous silica network in glass at elevated temperatures (500 – 650 °C), producing highly soluble sodium silicate phases with improved reactivity and greater suitability for bulk-scale production (Alnahhal et al., 2021). Accordingly, WGP, which contains a high proportion of amorphous silica and is widely available worldwide, has shown considerable promise as a precursor for sodium silicate synthesis via alkali thermal fusion with NaOH, yielding activators suitable for geopolymer production (Kolade et al., 2025b; Siddika et al., 2021a; Vinai and Soutsos, 2019).

Most existing studies (Bianco et al., 2021; Delgado-Plana et al., 2024; Samarakoon et al., 2020, 2021; Vinai and Soutsos, 2019) have utilized WGP-derived sodium silicate in one-part (dry mix) geopolymer formulations, where solid activators are premixed with the binder and activated with water during mixing (Kolade et al., 2025b). Thus, there is limited research exploring its application in two-part (liquid activator) geopolymer systems, where the synthesized sodium silicate solution is combined with NaOH and mixed separately with the aluminosilicate binder during batching. Furthermore, most studies to date focus on mortar or paste-level investigations, with relatively few addressing the structural performance of reinforced GPC elements, especially those activated with synthesized or non-commercial alkalis (Cardenas-Pulido et al., 2020).

This study aims to bridge this gap by synthesizing sodium silicate from WGP via alkali thermal fusion and utilizing it in a two-part GPC system incorporating fly ash and GGBFS. The structural performance of reinforced concrete beams produced using this system is evaluated and compared against beams made with CSS. In particular, the study focuses on key structural indices, which include flexural and shear capacity, load–deflection response, cracking behaviour and failure modes, to provide insight into the applicability of waste-derived activators for structural-grade GPC. This comparative approach contributes to the limited body of knowledge on liquid-form synthesized activators in structural-grade GPC.

From an industrial standpoint, the ability to produce sodium silicate locally from abundant glass waste offers a cost-effective and environmentally sustainable pathway to GPC production. It reduces reliance on commercially manufactured activators and lowers the embodied energy and carbon footprint associated with sodium silicate production by up to 50%, making it especially attractive in regions where CSS is expensive or difficult to source

(Alnahhal et al., 2021; Kolade et al., 2025b; Passuello et al., 2017). Consequently, the findings from this study are expected to be valuable to both the scientific community and practitioners seeking scalable and sustainable solutions for infrastructure development. In this context, the outcomes of this study contribute to advancing sustainable geopolymer technology by demonstrating the feasibility of waste glass-derived sodium silicate (WGSS) for structural-grade two-part geopolymer concrete systems.

1.2 Problem Statement and Purpose of Study

1.2.1 Problem Statement

Despite the environmental advantages of GPC over PC-based systems, several challenges continue to hinder its large-scale adoption. The most significant of these is the reliance on CSS as part of the alkaline activator system. As established in Section 1.1, CSS is expensive and energy-intensive to produce, thereby reducing the total environmental benefits of GPC. In many developing regions, limited accessibility to CSS further complicates efforts to adopt geopolymer technology. If this dependence on commercial activators persists, the economic and environmental advantages of GPC may remain difficult to realize at scale, limiting its widespread implementation in sustainable construction.

Recent studies have explored the synthesis of sodium silicate from WGP via alkali thermal fusion with NaOH. While these efforts present a promising, low-cost and sustainable alternative, most applications have focused on one-part geopolymer systems, where solid activators are dry-blended with aluminosilicate precursors prior to the addition of water. Although this approach simplifies handling and transportation, several scientific and practical limitations have been reported, including difficulties in achieving uniform dispersion of solid activators within the binder matrix, slower dissolution of alkali components during mixing and variability in reaction kinetics. These factors may result in inconsistent geopolymerization and reduced mechanical performance. If this approach continues to dominate, it may restrict the broader adoption of synthesized activators in structural-grade applications, thereby slowing the transition toward more sustainable geopolymer technologies.

On the other hand, two-part geopolymer systems utilize pre-dissolved alkaline activators in liquid form, allowing better control of the activator modulus, improved homogeneity during mixing and more efficient dissolution of reactive species, which can enhance reaction kinetics and general binder performance. Furthermore, liquid activator systems are more consistent with

conventional concrete production practices, where liquid admixtures and solutions are routinely incorporated during batching. However, the performance and practicality of using synthesized sodium silicate in liquid form remain insufficiently explored.

Although extensive research has been conducted on the mechanical and microstructural properties of geopolymer pastes and mortars, there is limited information on the structural behaviour of reinforced GPC elements, especially those incorporating synthesized activators. In addition, the absence of a unified or standardized mix design methodology for GPC complicates the optimization and reproducibility of its mechanical and durability properties, leading to inconsistencies in reported results. These limitations represent a critical knowledge gap that reduces the confidence of engineers and practitioners in adopting GPC for structural applications. Without addressing these issues, the practical implementation of sustainable geopolymer systems using alternative activators may remain limited despite their demonstrated environmental advantages.

1.2.2 Purpose of Study

The purpose of this study is to explore a sustainable and cost-effective approach to producing GPC by synthesizing sodium silicate from WGP and evaluating its suitability as an alkaline activator in reinforced concrete applications. By doing so, the research aims to contribute to global efforts to decarbonize the construction sector, reduce dependency on energy-intensive commercial activators and promote the circular use of industrial waste materials. This aligns with the United Nations Sustainable Development Goals (SDGs) 9 (Industry, Innovation and Infrastructure) and 12 (Responsible Consumption and Production), which collectively emphasize the adoption of cleaner technologies and resource efficiency. The study also supports South Africa's National Development Plan (NDP) 2030 objectives of building resilient infrastructure, fostering sustainable industrial growth and transitioning toward a low-carbon, resource-efficient economy. The research is particularly relevant to contexts where CSS is either unaffordable or inaccessible and where local waste valorization could offer environmental and economic benefits.

1.3 Research Aim and Objectives

This research aimed at investigating the structural performance and sustainability of reinforced GPC beams incorporating varying proportions of fly ash and GGBFS, with particular emphasis

on evaluating the use of synthesized sodium silicate derived from WGP as an alternative alkaline activator. To achieve this aim, the study was designed to:

i. develop GPC mix designs using different ratios of fly ash and GGBFS.

ii. synthesize sodium silicate from WGP via alkali thermal fusion and evaluate its chemical properties and activation potential, including the influence of fusion temperature and duration on its phase structure, solubility and reactivity.

iii. assess and compare the structural performance of reinforced GPC beams produced with synthesised sodium silicate and CSS.

iv. evaluate the sustainability of GPC mixes activated with synthesized sodium silicate through life cycle impact assessment and life cycle cost analysis in comparison with mixes produced using CSS.

v. establish the significance and reliability of experimental results using statistical methods.

1.4 Research Questions

To guide the study, the following research questions were posed:

i. How do varying ratios and properties of fly ash and GGBFS influence the development and performance of GPC mixes?

ii. Can sodium silicate synthesized from WGP via alkali fusion serve as a viable alternative to CSS in GPC production? What are the effects of synthesis parameters on the chemical properties and activation potential of the synthesized sodium silicate?

iii. How does the structural behaviour of beams produced with synthesized sodium silicate compare to those made with CSS?

iv. What are the mechanical, environmental and economic implications of using synthesized sodium silicate in GPC production?

v. Are the observed differences in performance between synthesized and commercial sodium silicate-based GPC statistically significant?

1.5 Scope and Limitations

1.5.1 Scope of Study

This study focused on the development and structural evaluation of GPC produced using an alternative sodium silicate activator synthesized from WGP. The research began with the alkali-fusion synthesis of sodium silicate under different fusion temperatures and reaction times, followed by detailed characterization of the resulting products. Using both the synthesized activator and CSS for comparison, a range of mixes incorporating fly ash and GGBFS was designed and produced. The structural behaviour of these mixes was assessed through compressive testing of mass concrete cubes and flexural and shear testing of reinforced GPC beams to examine load capacity, deflection response and failure mechanisms. In addition to mechanical assessments, the study evaluated the sustainability implications of the different mix systems, considering environmental impact and material cost. Statistical methods were also applied throughout to analyze the experimental data and interpret the significance of variations observed across mixes and test conditions.

1.5.2 Limitations of Study

This study was conducted at laboratory scale and all synthesis, casting and testing activities were performed under controlled conditions. As such, the scalability of the synthesized sodium silicate and the behaviour of GPC at pilot or field scale were not assessed. The structural investigation also focused specifically on the flexural and shear performance of simply supported reinforced beams, as other structural elements, loading conditions and long-term durability aspects were beyond the scope of this research. In addition, the experimental programme covered a defined range of material proportions, fusion parameters and curing conditions, and therefore does not represent the full spectrum of possible mix or activation combinations. Sustainability assessments were also based on simplified estimates rather than full life-cycle modelling. Furthermore, certain advanced testing techniques and large-scale experiments could not be undertaken due to equipment and facility constraints. In particular, load–deflection behaviour could not be recorded during beam testing because the available flexural testing machine did not include displacement measurement instrumentation, and therefore beam stiffness, ductility and post-cracking deformation could not be directly evaluated.

1.6 Significance of Study

This study holds practical importance in promoting sustainable construction by exploring GPC as an alternative to PC, thereby contributing to global efforts to reduce the environmental footprint of PC-based materials. It also aligns with South Africa's pursuit of key Sustainable Development Goals (SDGs), especially SDG 9 (Industry, Innovation and Infrastructure) and SDG 12 (Responsible Consumption and Production). Specifically, the research supports Target 9.4, which emphasizes upgrading infrastructure through environmentally sound technologies, and Target 12.5, which promotes waste reduction and recycling. Hence, the study advances cleaner production and resource efficiency within the construction sector by valorizing WGP in producing alkaline activators for GPC.

From a scientific perspective, the research offers new insights into the use of WGSS in liquid form, which is an underexplored area compared to one-part systems. Hence, the study enhances the understanding of alkali-activated binder chemistry by examining how synthesis conditions affect the chemical and structural properties of the activator. Also, structural testing of reinforced GPC beams under flexural and shear loads further bridges the gap between material development and practical application.

From an industrial standpoint, the study proposes a sustainable and low-cost alternative to CSS by utilizing locally sourced WGP. This supports circular economy principles, reduces reliance on energy-intensive products and enhances material accessibility in low-resource settings. The inclusion of mechanical, environmental and economic assessments also provides a holistic framework for evaluating GPC's viability, providing practical guidance for engineers, researchers and policymakers aiming to reduce embodied carbon without sacrificing performance or cost-effectiveness.

1.7 Dissertation Structure

This dissertation is organized into eight chapters, each contributing to the systematic development and presentation of the research work. The structure is as follows:

Chapter 1: Introduction

This chapter presents the background, problem statement, purpose, significance, scope and limitations of the study. It also outlines the research questions and objectives guiding the investigation.

Chapter 2: Literature Review

This chapter reviews existing studies on geopolymer technology, sustainable binders, synthesis of alkali activators and structural performance of geopolymer concrete elements. It identifies research gaps and contextualizes the novelty and contributions of the current study.

Chapter 3: Materials and Methods

This chapter provides a detailed description of all materials used in the study as determined using standard laboratory techniques. It also outlines the experimental program, mix design procedures, sample preparation methods, testing methods, analytical techniques and statistical tools employed for data processing and interpretation.

Chapter 4: Trial Mix Results and Analysis

This chapter presents the preliminary development and testing of mortar mixes using different proportions of fly ash and GGBFS activated with commercial sodium silicate and NaOH. This helped identify the mixes with suitable workability and strength characteristics for further refinement and upscaling to concrete-level applications.

Chapter 5: Development and Evaluation of Alternative Sodium Silicate

This chapter describes the alkali-fusion synthesis of sodium silicate using WGP, with emphasis on the influence of fusion temperature and reaction time on phase composition, solubility and reactivity. The performance of mortars prepared using the synthesized sodium silicates is subsequently evaluated to determine its suitability as an alternative activator.

Chapter 6: Structural Performance of Reinforced Concrete Beams

This chapter presents experimental results on reinforced GPC beams under flexural and shear loading. It evaluates their load-bearing capacity, failure modes and deflection characteristics and compares beams produced with synthesized and commercial activators.

Chapter 7: Sustainability Evaluation of Concrete Mixes

This chapter assesses the mechanical, environmental and economic sustainability of the synthesized sodium silicate-based GPC relative to commercial alternatives. It also includes discussions on material efficiency and carbon footprint.

Chapter 8: Conclusions and Recommendations

The final chapter summarizes the key findings, highlights the contributions of the research and offers recommendations for future work and potential practical applications.

CHAPTER 2

2 LITERATURE REVIEW

2.1 Introduction

This chapter establishes the scientific and technical context for the study by reviewing developments in geopolymer technology, key materials, chemical processes and gaps in current knowledge. It begins with an overview of geopolymer chemistry and its evolution as a sustainable alternative to PC, followed by discussions on common precursors such as fly ash and GGBFS and on alkaline activators including both commercial and synthesized sodium silicate. The chapter further examines GPC mix design approaches, mechanical and durability properties and the structural behaviour of reinforced GPC beams under flexural and shear loadings. Sustainability considerations (environmental and economic) are also addressed to underscore GPC's relevance to green construction. As such, this review synthesizes current knowledge and identifies a key research gap: the application of liquid-phase WGSS in reinforced fly ash–GGBFS GPC beams. The insights gained form the basis for the experimental investigations in the chapters that follow.

2.2 Overview of Geopolymer Technology

2.2.1 Historical Development of Geopolymer Binders

The concept of geopolymers was introduced by Joseph Davidovits in the late 1970s as a class of inorganic binders formed by alkali-activating alumino-silicate materials under ambient or moderately elevated temperatures. He coined the term "geopolymer" to describe materials produced through this chemical process, characterized by a three-dimensional network of silicon and aluminum tetrahedra connected by oxygen bridges (Davidovits, 1991).

Davidovits controversially hypothesized that ancient construction technologies, such as those used in building the Egyptian pyramids and Roman structures, may have employed similar principles. While this theory remains debated, his pioneering research laid the foundation for modern studies on geopolymers, especially their potential as high-performance, fire-resistant and environmentally friendly alternatives to PC (Amran et al., 2020; Davidovits, 1991).

Over the last two decades, increasing concerns over climate change, carbon emissions and resource depletion have intensified interest in geopolymer technology. Researchers have explored various industrial by-products and natural alumino-silicate-rich materials, such as fly

ash, GGBFS, metakaolin, red mud and rice husk ash, as potential precursors in geopolymer binder formulations (El-Gamal and Selim, 2017; Kolade et al., 2025a; Parathi et al., 2021). These materials help reduce dependence on virgin raw materials and align with circular economy and waste valorization principles. A schematic overview of GPC composition, including common precursors and alkaline activators, is shown in Fig. 2.1.

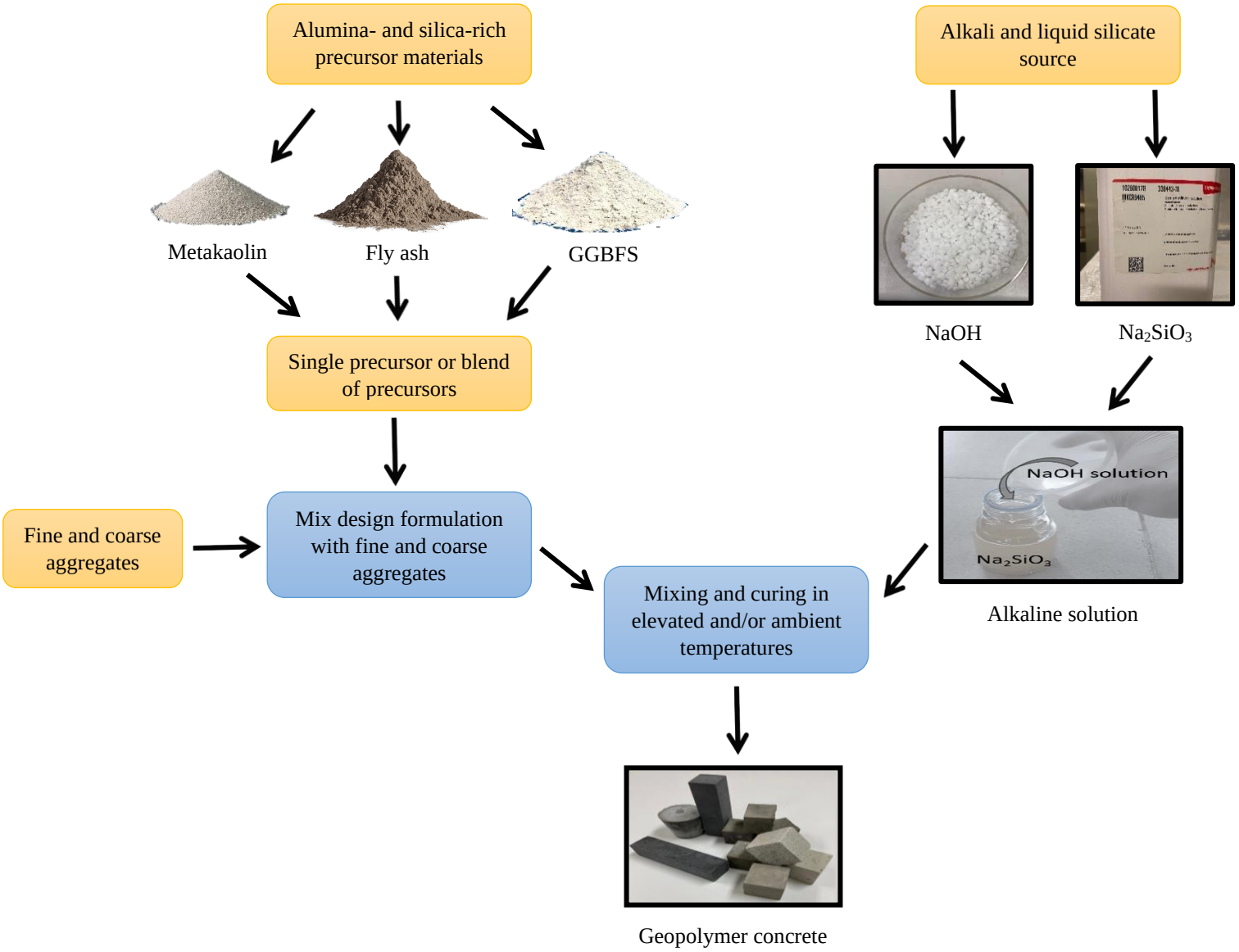

Fig. 2.1: Schematic representation of GPC constituents (Kolade et al., 2025a)

Beyond laboratory research, the real-world application of GPC has grown significantly. Australia has been at the forefront, implementing GPC in notable infrastructure projects such as the Brisbane West Wellcamp (BWW) Airport, the Global Change Institute (GCI) at the

University of Queensland and 55 MPa precast panels used in the Salmon Street bridge. Furthermore, GPC has been successfully adapted for 3D concrete printing, including initiatives at Nanyang Technological University (NTU), demonstrating its versatility and innovative potential. These developments (Fig. 2.2) underscore the growing acceptance of GPC in the construction sector as a practical and sustainable substitute for PC-based systems (Abbas et al., 2020; Glasby et al., 2015; Kolade et al., 2025a; Parathi et al., 2021; van Deventer et al., 2012; Wu et al., 2019).

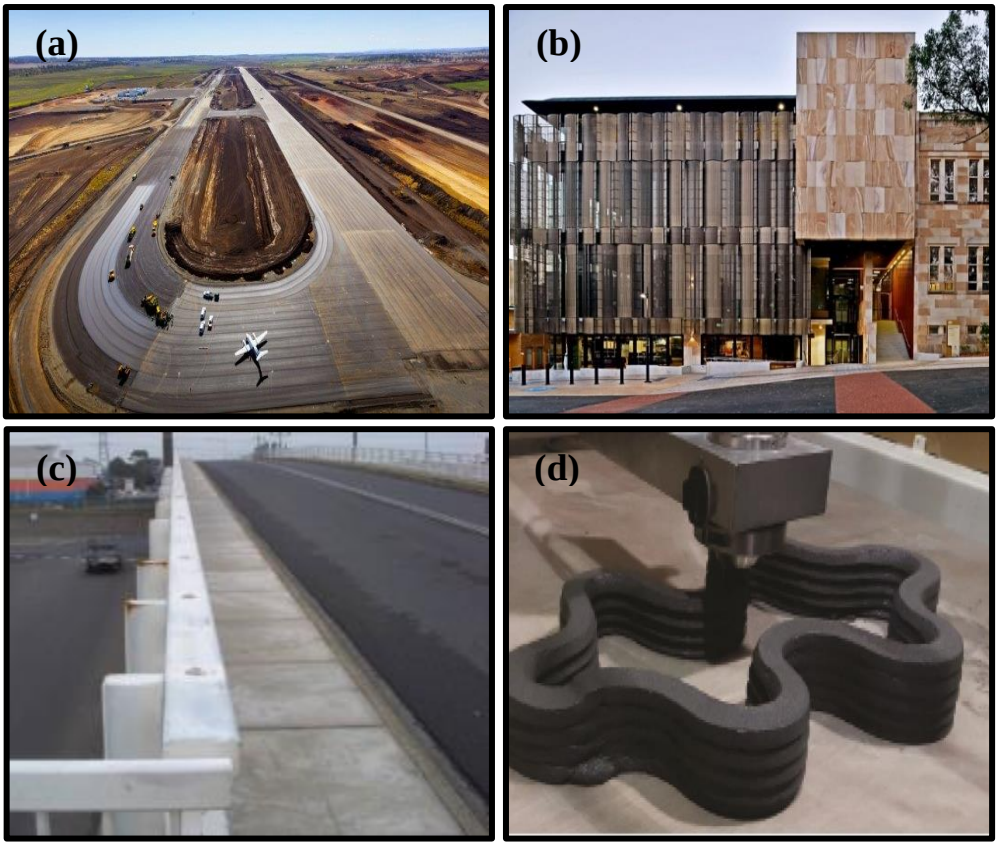

Fig. 2.2: Images of (**a**) BWW Airport (**b**) Queensland's GCI building (**c**) Salmon Street bridge's precast panels (**d**) NTU's 3D-printed GPC structure (Kolade et al., 2025a)

2.2.2 Comparison with Portland Cement Concrete (PCC)

GPC is a distinct class of cementitious material that differs fundamentally from PCC in terms of raw materials, chemical processes and performance characteristics. As shown in Fig. 2.3 and Table 2.1, GPC offers notable advantages, including lower embodied carbon, enhanced chemical resistance and superior long-term durability under harsh environmental conditions.

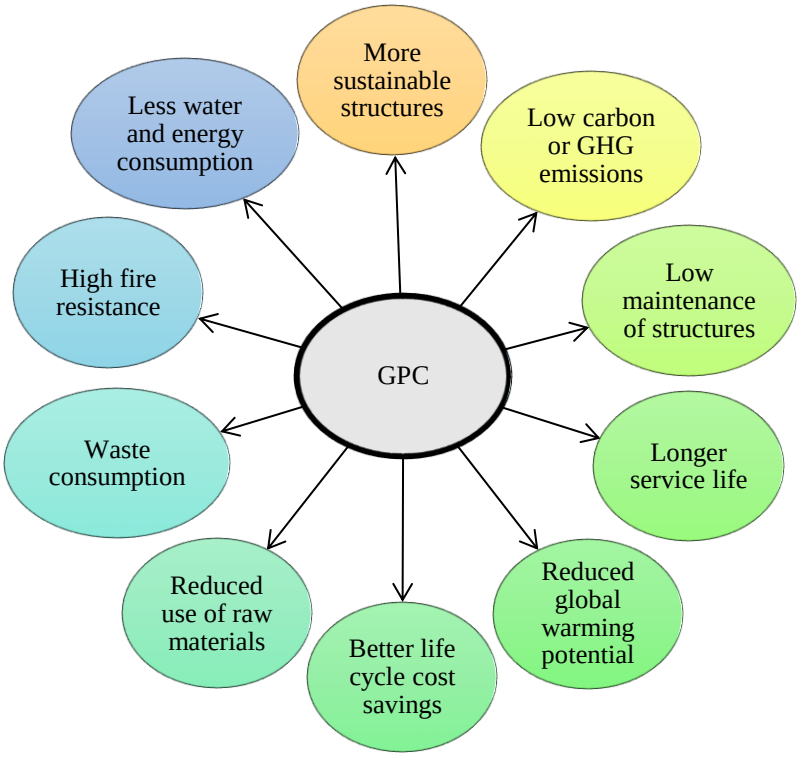

Fig. 2.3: Comparative advantages of GPC over PCC (Kolade et al., 2025a)

Table 2.1: Key differences between GPC and PCC (Kolade et al., 2025a)

Parameter	GPC	PCC
Environmental impact	Significantly reduced CO_2 emissions due to the use of industrial and agricultural by-products or wastes	High carbon footprint linked to the calcination of non-renewable limestone and clay
Compressive strength	Often equal to or greater than PCC, depending on precursor type and reactivity	Generally high and well-documented across standard mixes
Flexural strength	Can match PCC with optimized design, though may exhibit brittleness in some compositions	Consistently high due to well-understood reinforcement practices
Workability	May pose challenges without chemical admixtures; sensitive to mix proportions	Readily adjustable and compatible with various admixtures for desired consistency
Durability	Excellent resistance to chemical exposure and elevated temperatures	Prone to degradation from chlorides, sulphates and thermal variations

In terms of application, GPC has demonstrated versatility across various sectors of the built environment. In transport infrastructure, it has been used in roadways, bridge decks and precast elements, where its strength and durability extend service life (Almutairi et al., 2021; Ikotun et al., 2024a). In the precast industry, its rapid strength development under thermal curing improves production efficiency (Sumajouw et al., 2023). The building sector benefits from its use in beams, slabs and columns due to its low shrinkage, fire resistance and compatibility with green building standards like Leadership in Energy and Environmental Design (LEED) (Sumajouw et al., 2023). GPC also suits architectural and marine applications, such as facades, sculptures, seawalls and pipelines, due to its aesthetic adaptability, dense microstructure and resistance to freeze-thaw cycles and saltwater ingress (Almutairi et al., 2021; Sumajouw et al., 2023).

Despite these advantages, the broader adoption of GPC is still hindered by several challenges. One major issue is the variability in the properties of precursor materials, which can lead to inconsistency in performance. The mix design process is also more complex than for PCC, as geopolymer systems are highly sensitive to factors such as activator concentration, precursor composition, curing temperature and duration. Furthermore, the absence of standardized design codes and performance specifications for GPC impedes regulatory approval and widespread industry confidence. In addition, the handling of highly alkaline activators poses safety concerns during mixing and casting, requiring more stringent protocols than PC. These factors complicate large-scale implementation, though they do not diminish the material's potential as a sustainable alternative to PCC (De Weerdt, 2011; Ken et al., 2015; Kolade et al., 2026a; Wong, 2022).

2.2.3 General Chemistry of Geopolymerization

Geopolymerization refers to the chemical transformation of reactive aluminosilicate materials into a hardened, cement-like structure with a stable three-dimensional network. This transformation occurs through a series of polymerization reactions initiated by alkaline activating solutions, typically under IV–V fold coordination (Amran et al., 2020; Davidovits, 1991; 1994). The overall process can be summarized by Eq. (2.1).

$$2(Si_2O_5, Al_2O_2) + K_2(H_3SiO_4)_2 + Ca(H_3SiO_4)_2 \rightarrow (K_2O, CaO)(8SiO_2, 2Al_2O_3, nH_2O) \quad (2.1)$$

Geopolymerization generally progresses through several key stages: alkalination, silicate depolymerization, oligo-sialate gel formation, polycondensation, reticulation and solidification

(Amran et al., 2020; El-Gamal and Selim, 2017; Ikotun et al., 2024a; Kolade et al., 2025b). However, these can be broadly categorized into three overlapping core stages: dissolution, condensation and hydrolysis, as represented in Eq. (2.2) – (2.4).

Dissolution: Aluminosilicate (solid) + OH^- → $Al(OH)_4^-$ + $Si(OH)_4$ (2.2)

Condensation:

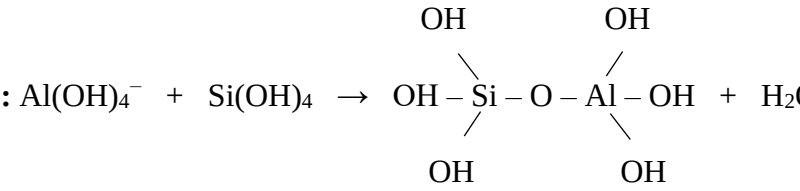

(2.3)

Hydrolysis:

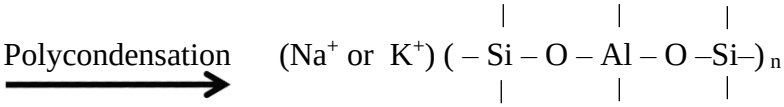

(2.4)

In the dissolution (leaching) stage, reactive silica (Si) and alumina (Al) species are leached from the solid precursor into the solution in the presence of a strong alkaline medium like NaOH or Na_2SiO_3. The condensation (oligomerization) stage involves the dissolved $(SiO_4)^{4-}$ and $(AlO_4)^{5-}$ species undergoing condensation reactions to form oligomeric sialate species. In the last hydrolysis stage (polycondensation), these oligomers reorganize into a cross-linked alumino-silicate network, forming a rigid and semi-crystalline three-dimensional polymer. The fundamental repeating unit of this network is the sialate monomer (–Si–O–Al–O–) (Davidovits, 1994; Duxson et al., 2007; Khale and Chaudhary, 2007; Komnitsas and Zaharaki, 2007; Singh et al., 2015; Singh and Singh, 2019). The general empirical formula of resulting geopolymer materials is given as $M_n\,[–(SiO_2)_z – AlO_2–]_n \cdot yH_2O$, where M is a monovalent alkaline cation (Na^+ or K^+), n is the degree of polymerization, z is the Si/Al ratio (typically between 1 and 3) and yH_2O represents the physically bound water (Davidovits, 1991; Davidovits, 1994; Khale and Chaudhary, 2007).

In addition, several factors significantly influence geopolymer properties, including the type and reactivity of the aluminosilicate precursor, Si/Al ratio, activator concentration and curing conditions (temperature, humidity and time) (Alaneme et al., 2023; De Weerdt, 2011; Duxson et al., 2007; Khale and Chaudhary, 2007). Also, in calcium-rich systems, such as those incorporating GGBFS, additional calcium-silicate-hydrate (C–S–H) gel phases may form, as shown in Eq. (2.5). These gels can improve early-age strength but may reduce chemical durability due to differing reaction mechanisms (Khale and Chaudhary, 2007). Hence, a comprehensive understanding of these chemical processes is essential for optimizing GPC

formulations, especially when utilizing non-commercial or waste-derived activators. Such knowledge enables tailored mix designs that balance mechanical performance and long-term durability, supporting the broader application of GPC in structural applications.

$$Ca^{2+} + Si(OH)_4 \rightarrow C–S–H + H_2O \quad (2.5)$$

2.3 Source Materials for GPC

GPC production relies heavily on aluminosilicate-rich source materials, typically industrial and agricultural by-products or wastes, which are activated by alkaline solutions to form a hardened binder matrix. Among these, fly ash and GGBFS are the most widely studied and used due to their availability, pozzolanic properties and environmental advantages. The chemical and physical characteristics of these precursors, such as particle size, glass content and oxide composition, play a vital role in the geopolymerization process and final performance of GPC (Abdel-Gawwad and Khalil, 2018; Emdadi et al., 2017; Hossain et al., 2018; Lee et al., 2021).

2.3.1 Fly ash

Fly ash is a fine, powdery material generated as a by-product of coal combustion in thermal power plants. It is classified into Class F and Class C, based on its chemical composition as defined by ASTM C618 (2022). Class F fly ash, derived from the combustion of bituminous or anthracite coal, is low in calcium (CaO < 18%) and rich in silica (SiO_2), alumina (Al_2O_3) and iron oxides (Fe_2O_3), as shown in Table 2.2. It is the most commonly used type in geopolymer research due to its high amorphous content and pozzolanic reactivity under alkaline conditions. On the other hand, Class C fly ash, produced from sub-bituminous coal, contains higher calcium content (CaO > 18%) and exhibits both pozzolanic and cementitious properties. Its elevated lime content can accelerate setting and strength development but may also interfere with long-term chemical stability (Jan et al., 2022; Kheimi et al., 2022; Kolade et al., 2025a, 2025b; Oyejobi et al., 2023; Parathi et al., 2021). The morphological descriptions and microstructural features of typical fly ash particles used in geopolymer systems are provided in Table 2.3, further illustrating the spherical shape, glassy surface texture and particle fineness that contribute to its reactivity

In addition, the reactivity of fly ash in geopolymer systems is primarily influenced by its glassy phase content, fineness and chemical composition. Amorphous phases dissolve readily in alkaline media, releasing reactive silica and alumina necessary for geopolymer gel formation. However, low-calcium Class F fly ash may require elevated temperature curing or blending

with other reactive materials to achieve desirable early strength (Kheimi et al., 2022; Kolade et al., 2025a; Parathi et al., 2021; Singh et al., 2015). Despite this limitation, Parathi et al. (2021) reported that fly ash-based GPC can attain compressive strengths of up to 80 MPa under optimized conditions.

Table 2.2: Key oxides composition of selected fly ash and GGBFS materials

Materials	Composition by weight (%)					Study
	SiO_2	Al_2O_3	Fe_2O_3	CaO	MgO	
Fly ash	58.23	25.08	4.56	2.87	1.21	Bellum et al. (2020)
Fly ash	59.87	23.96	3.70	5.06	0.48	Bhardwaj and Kumar (2019)
Fly ash	53.08	22.69	5.11	0.96	0.73	Debbarmaa et al. (2020)
Fly ash	28.52	12.34	29.32	17.91	1.78	Malkawi et al. (2018)
Fly ash	41.90	32.24	8.75	8.90	–	Oyejobi et al. (2023)
GGBFS	32.25	12.14	1.10	44.70	4.23	Bellum et al. (2020)
GGBFS	33.06	22.29	0.90	35.37	7.61	Bhardwaj and Kumar (2019)
GGBFS	34.11	15.36	0.83	35.99	6.58	Cheng et al. (2020)
GGBFS	36.00	13.80	0.30	42.60	5.80	Hu et al. (2019)
GGBFS	32.50	13.70	0.80	45.80	3.30	Sharmin et al. (2017)

Table 2.3: Morphology and microstructural features of fly ash and GGBFS

Materials	Particle shape	Surface texture	Internal structure	Microstructural implications	Study
Fly ash	Generally spherical	Smooth and glass-like	Predominantly amorphous	Improves flowability, lowers water requirement and enhances particle packing efficiency	Bellum et al. (2020); Kheimi et al. (2022); Singh et al. (2015)
GGBFS	Irregular – angular	Rough and uneven	Amorphous and glassy	Facilitates rapid alkaline dissolution and contributes to early geopolymer matrix formation	Kolade et al. (2025b); Podolsky et al. (2021)

2.3.2 GGBFS

GGBFS is a by-product of iron and steel production in blast furnaces, produced by rapidly quenching molten slag in water and then grinding it into a fine powder. It is a highly reactive, calcium-rich material composed mainly of CaO, SiO_2, Al_2O_3 and MgO (Kheimi et al., 2022; Parathi et al., 2021). In geopolymer systems, GGBFS contributes to accelerated setting times and enhanced early strength development, especially under ambient curing conditions, which is beneficial for improved constructability and faster turnaround in precast applications. GGBFS also improves workability and increases matrix density, which enhances durability and reduces porosity (Luhar and Luhar, 2022; Nadarajah et al., 2024; Parathi et al., 2021; Singh et al., 2024).

From a morphological perspective, GGBFS particles are typically angular with irregular, rough surfaces and an amorphous glassy internal structure. These characteristics promote rapid dissolution in alkaline media and facilitate early matrix formation, making GGBFS a highly effective precursor in blended geopolymer systems (Podolsky et al., 2021). However, the high CaO content, especially when exceeding 20%, may compromise long-term chemical stability, particularly under heat curing. Therefore, careful mix design is essential, considering not only calcium levels but also the presence of MgO and sulphates due to their potential effects on durability (Jan et al., 2022; Kolade et al., 2025b; Oyejobi et al., 2023).

2.3.3 Fly ash–GGBFS Blends in GPC

Blending fly ash and GGBFS in binary geopolymer formulations is a widely adopted strategy to leverage the complementary properties of both materials while significantly reducing carbon emissions compared to PC (Eisa et al., 2022). This synergy addresses the limitations of each precursor when used alone. For instance, GGBFS enhances the early strength and ambient curing capability of low-calcium fly ash, reducing reliance on elevated temperature curing (Bellum et al., 2020; Kolade et al., 2026a; Parathi et al., 2021). In addition, the co-formation of geopolymeric and C–S–H gels results in a denser, more refined microstructure, improving both mechanical performance and durability (Bellum et al., 2020; Kumar et al., 2017). Fly ash–GGBFS blends also show superior resistance to sulphate, chloride and acid attack due to their lower calcium hydroxide content and reduced permeability (Kolade et al., 2025a). Therefore, these blends offer a versatile and sustainable approach for producing GPC suitable for structural and infrastructure applications. However, the ratio of fly ash to GGBFS must be carefully optimized to balance strength, durability and cost. Studies have identified a 70:30 fly

ash-to-GGBFS ratio as optimal for achieving desirable performance outcomes (Kolade et al., 2025a; Parathi et al., 2021).

2.4 Alkaline Activators in Geopolymer Systems

2.4.1 Common Activators

Alkaline activators initiate the dissolution of reactive aluminosilicate precursors and drive the subsequent polymerization reactions that form the hardened geopolymer matrix. Accordingly, their type, concentration and composition greatly influence reaction kinetics and the final properties of GPC (De Weerdt, 2011; Duxson et al., 2007). The most commonly used activators are sodium hydroxide (NaOH) and sodium silicate (Na_2SiO_3), although increasing interest is being directed toward alternative activators derived from industrial and agricultural wastes.

NaOH functions primarily as a strong alkali (pH > 12), facilitating the dissolution of silica (Si) and alumina (Al) from the precursor materials. This step releases reactive species such as $(SiO_4)^{4-}$ and $(AlO_4)^{5-}$, which are essential for polymerization (Duxson et al., 2007; Khale and Chaudhary, 2007). On the other hand, Na_2SiO_3 (also known as waterglass) provides additional soluble silica that enhances the silica-to-alumina (Si/Al) ratio while improving viscosity, mixture homogeneity and gel formation. Its inclusion leads to improved mechanical strength, workability and setting characteristics compared to systems activated solely with NaOH (De Weerdt, 2011; Duxson et al., 2007; Khale and Chaudhary, 2007; Provis, 2014).

The combination of NaOH and Na_2SiO_3 is widely adopted in two-part geopolymer systems due to their synergistic effects in promoting rapid and efficient geopolymerization, especially under ambient or moderately elevated curing conditions (Parathi et al., 2021). To achieve optimal performance, both the concentration of the NaOH solution and the Na_2SiO_3-to-NaOH ratio must be carefully adjusted. NaOH solutions within the range of 8 – 16 molarity (M) promote the formation of a consistent polymeric matrix. However, overly concentrated solutions may generate excessive heat during mixing and increase the risk of efflorescence (De Weerdt, 2011). Conversely, using concentrations below 8 M can result in sluggish or incomplete dissolution, leading to poorly developed polymeric network structures (Alaneme et al., 2023; Fernandez-Jimenez and Palomo, 2005; Jan et al., 2022). Similarly, Na_2SiO_3-to-NaOH ratios greater than 1.5 generally encourage polycondensation and the development of a more refined microstructure. However, ratios below this threshold may limit structural integrity if insufficient silica is available for network formation (Alaneme et al., 2023; Jan et al., 2022).

2.4.2 Commercial Sodium Silicate (CSS)

CSS is typically composed of Na_2O, SiO_2 and H_2O and is conventionally produced through a high-temperature fusion process, where silica sand (SiO_2) reacts with caustic soda (Na_2CO_3) at temperatures exceeding 1,000 °C. While this method yields a highly effective alkaline activator, it is both energy-intensive and environmentally taxing, as it generates approximately 1.6 kg of CO_2-equivalent emissions per kilogram of product. CSS also accounts for approximately 30 – 50% of the embodied energy and 40 – 60% of the total carbon footprint associated with GPC, thereby partially offsetting the environmental benefits of replacing PC (Alsalman et al., 2021; Fernando et al., 2021; Kamseu et al., 2017; Kolade et al., 2025b; Martinez et al., 2025; Oyebisi et al., 2022; Turner and Collins, 2013; Vinai and Soutsos, 2019).

In addition to its environmental burden, CSS is relatively costly, often contributing 30 – 50% of the total material cost in GPC formulations (Fernando et al., 2021; Ghanim et al., 2025; McCloskey et al., 2024; Turner and Collins, 2013). This challenge is particularly acute in regions such as sub-Saharan Africa, where CSS is often imported, raising concerns about economic sustainability and supply chain reliability for large-scale or long-term infrastructure projects. Given these limitations, there is growing research interest in alternative, locally sourced and more sustainable activators. These alternatives aim to reduce both the environmental impact and the cost of geopolymer systems, thereby enhancing their viability for widespread adoption, especially in developing economies.

2.4.3 Sodium Hydroxide (NaOH)

NaOH is the second major alkaline activator used in geopolymer systems and plays a crucial role in initiating the dissolution of aluminosilicate precursors. Commercial NaOH, commonly known as caustic soda, is typically produced through electrolysis of sodium chloride (NaCl) in the chlor-alkali process, which is both energy-intensive and associated with significant carbon emissions (Turner and Collins, 2013). Despite its essential role in activating geopolymerization, the use of NaOH presents safety and sustainability challenges due to its corrosive nature, high alkalinity and the embodied energy associated with its manufacture (Guo et al., 2023). The concentration of NaOH solution strongly affects the rate of dissolution, gel formation and final strength of GPC, making its optimization critical for achieving desired structural performance (Alaneme et al., 2024; Kolade et al., 2025c). Accordingly, research continues to explore greener and less hazardous alkali sources to partially or fully replace conventional NaOH in geopolymer synthesis.

2.4.4 Alternative Activators from Waste Materials

In response to the environmental and economic challenges associated with CSS, considerable research has turned toward developing alkaline activators derived from industrial and agricultural wastes. Materials such as WGP, rice husk ash, hazelnut shell ash, coal bottom ash, sugarcane bagasse ash, nanosilica, olive stone biomass ash and agricultural waste ashes have shown strong potential in this regard, as they can even reduce the cost of CSS up to 70%. These waste products typically contain high levels of amorphous silica or potassium-based compounds, making them suitable for conversion into reactive silicate solutions under alkaline processing conditions (Delgado-Plana et al., 2024; Ghanim et al., 2025; Kolade et al., 2025a; de Moraes Pinheiro et al., 2018; Omur et al., 2024; Tchakouté et al., 2016a; Umer et al., 2024).

Among these alternatives, WGP has gained particular attention due to its abundance, high silica content (>70%), low crystalline structure and favourable chemical purity. Its fine particle size and high surface area further enhance its reactivity when treated in alkaline media, making it a highly efficient precursor for synthesizing sodium silicate. Despite the existence of glass recycling systems, a substantial volume of post-consumer waste glass still ends up in landfills, with disposal rates reported at approximately 15% in the United States and as high as 25% in both China and the European Union. This underutilization presents a unique opportunity for integrating waste glass into geopolymer binder systems, thereby promoting waste valorization and resource efficiency (Islam et al., 2017).

When WGP undergoes hydrothermal or thermochemical treatment with NaOH, it can be transformed into a reactive sodium silicate solution known as WGSS. This synthesized activator exhibits comparable chemical characteristics to CSS and has been successfully applied in geopolymer formulations with promising results (Alnahhal et al., 2021; Dadsetan et al., 2022; Kolade et al., 2025a, 2025b; Madirisha et al., 2024; Tchakouté et al., 2016b). Beyond reducing the demand for energy-intensive commercial silicates, the production of WGSS supports circular economy principles by converting post-consumer waste into a high-value construction input.

Experimental findings further reinforce the viability of WGSS as a substitute for CSS. For instance, fly ash–GGBFS geopolymer mortars produced with WGSS have achieved comparable compressive strengths with those produced using CSS, as reported by Vinai and Soutsos (2019). Delgado-Plana et al. (2024) also observed that mortars made from spent oil filtering earth and activated with WGSS achieved compressive and flexural strengths of 35.8

MPa and 12.7 MPa, respectively, outperforming the CSS-based reference mixes, which reached only 23.1 MPa and 10.2 MPa under similar ambient conditions. Similarly, Tchakouté et al. (2016b) reported that metakaolin-based geopolymer pastes activated with WGSS attained compressive strength of up to 39.7 MPa at 56 days. In terms of environmental performance, Dadsetan et al. (2022) estimated that using WGSS instead of CSS could reduce carbon emissions by more than 20%. Economic analysis by McCloskey et al. (2024) further demonstrated that WGSS could lower the material cost of geopolymer mortars by nearly 50%.

Although WGSS may present slight variations in silica modulus and viscosity compared to CSS, these differences can typically be managed through careful mix design and formulation. The combined environmental, economic and technical advantages of WGSS therefore make it a compelling alternative for sustainable geopolymer production, especially in contexts where cost constraints and resource availability are critical factors.

2.5 Mix Design Approaches for GPC

Developing an effective and globally standardized mix design methodology for GPC remains a major challenge due to the material's unique chemistry and reaction mechanisms, which differ significantly from those of PCC. Unlike PCC, where design is guided by empirical water-to-cement (w/c) ratios and established standards, GPC requires a more tailored approach that accounts for the specific reactivity of aluminosilicate precursors and the chemical composition of alkaline activators (Heshmati et al., 2025; Li et al., 2019a; Parathi et al., 2021).

Early mix design efforts often adapted conventional PCC practices by replacing cement with fly ash or GGBFS and applying a fixed alkaline activator dosage. However, these adaptations frequently produced inconsistent or suboptimal performance because geopolymerization is influenced by a wider range of interdependent variables, including precursor composition, activator chemistry, curing temperature and moisture content. To address this, researchers have proposed a range of alternative mix design methodologies, generally classified into three categories: empirical strength-based approaches, modified PCC-derived methods and performance-oriented frameworks with limited chemical depth (Hadi et al., 2019; Kolade et al., 2025c; Provis, 2018). Table 2.4 summarizes several representative mix design strategies, along with their strengths and limitations. These approaches highlight the diversity of methodologies currently in use and underscore the ongoing lack of consensus within the field.

Table 2.4: Overview of selected mix design methods for GPC

Study	Design parameters	Advantages	Drawbacks
Naghizadeh and Ekolu (2019)	Utilizes mix design charts informed by material properties; targets compressive strength and workability; thermal curing at 80 °C for 28 days	Delivers accurate strength predictions; goal-oriented methodology	Strong reliance on empirical charts and specific precursor characteristics; oversimplifies effects of aggregate and curing variations; limited to compressive strength outcomes
Ng and Foster (2013)	Focuses on binder characteristics, aggregate packing density and binder-to-aggregate ratio	Offers a systematic structure; highlights the importance of aggregates in minimizing binder use	High dependence on lab testing and discrete element modelling (DEM) simulations; narrowly focused on compressive strength; lacks full integration of chemical reactivity considerations
Patankar et al. (2015)	Applies a constant water-to-binder ratio (0.35), solution-to-fly ash ratio (0.35), Na_2SiO_3/NaOH ratio of 1.0, 13 M NaOH; cured at 60 °C for 24 hours	Straightforward and repeatable for specific lab conditions	Rigid framework not easily adapted to diverse materials or curing environments; prioritizes compressive strength and workability only
Alaneme et al. (2024)	Based on modified ACI 211 guidelines, accounting for aggregate gradation and	Adaptable framework bridging traditional PCC and GPC mix design methods	Leans on assumptions from PC design; may not reflect the nuances of GPC

	moisture levels; considers thermal and outdoor curing options		chemistry, especially water-to-solids ratio
Lloyd and Rangan (2010)	Suggests alkaline liquid-to-fly ash ratios (0.30 – 0.45); defines water-to-solids ratios; includes mixing time and thermal curing at 60 °C for 24 hours	Clear and performance-driven; emphasizes practical workability considerations	Assumes consistent fly ash properties; focused on heat-cured conditions; overlooks moisture variability in aggregates
Reddy et al. (2018)	Incorporates alkaline activator content to binder solids ratio (AAC/BS); inspired by traditional ACI water-cement design logic with graded aggregates	Adaptable for ambient curing; demonstrated compressive strength range of 32 – 66 MPa for AAC/BS ratios of 0.4 – 0.8	Simplifies geopolymer chemical mechanisms; limited consideration of precursor variability and long-term performance

In many investigations, optimization of mix proportions is first conducted at the mortar scale before being extended to concrete systems. Mortar formulations allow rapid evaluation of precursor reactivity, activator composition and curing conditions while minimizing material use and experimental variability (Kolade et al., 2025c; Ng and Foster, 2013). This staged approach facilitates early identification of promising mix ratios, which can then be refined and applied in concrete and structural-level studies. Accordingly, the present study follows this well-established progression, beginning with mortar trials as a foundation for subsequent concrete-scale optimization.

Despite considerable progress in identifying critical mix parameters, achieving standardization remains elusive. Wide variability in precursor composition, activator chemistry and curing regimes continues to hinder reproducibility and cross-study comparisons (Kolade et al., 2025c; Li et al., 2019a). Inconsistent material characterization and performance benchmarks further complicate the development of universally applicable design procedures. To enable broader adoption of GPC in structural applications, future mix design frameworks should integrate chemical and performance-based principles within a unified, adaptable system. Such methodologies must accommodate natural material variability while offering flexibility in adjusting key compositional ratios, such as Na_2SiO_3/NaOH, alkaline solution-to-binder (AL/B), water-to-geopolymer solids (W/Gs), SiO_2/Al_2O_3, Na_2O/SiO_2 and H_2O/Na_2O, to achieve targeted mechanical and durability outcomes. In line with this perspective, the present study proposes a tailored mix design framework that couples chemical composition control with empirical optimization to enhance structural and environmental performance.

2.6 Fresh, Hardened and Durability Properties of GPC

2.6.1 Fresh Properties

2.6.1.1 Setting Times

The setting characteristics of GPC are primarily governed by precursor chemistry, calcium content and activator formulation (Kolade et al., 2025a; Kuri et al., 2021; Samantasinghar and Singh, 2019). Studies commonly employ Vicat penetration or needle apparatus tests in line with ASTM C191 (2021) to determine setting behaviour. High-calcium binders, especially those rich in GGBFS or ground granulated ferronickel slag (GFNS), exhibit rapid setting, typically achieving initial set within 30 – 60 minutes and final set within 2 hours under ambient conditions. In contrast, low-calcium, fly ash-based systems generally require 8 – 24 hours to set when cured at room temperature due to slower aluminosilicate dissolution and

geopolymerization kinetics (Kolade et al., 2025b; Nadarajah et al., 2024; Samantasinghar and Singh, 2019; Temuujin et al., 2009).

In addition, Kuri et al. (2021) reported that replacing fly ash with up to 50% GFNS reduced setting times by approximately 35%, attributed to enhanced Ca–Si–Al gel formation. Similarly, Samantasinghar and Singh (2019) found that increasing NaOH molarity decreased initial and final setting times, though excessively high concentrations caused premature stiffening, limiting workable time. Thermal curing between 60 – 80 °C has also been shown to reduce setting times by up to 60% compared to ambient curing (Parathi et al., 2021). Thus, it can be deduced that the interaction between calcium content and activator chemistry is critical, as excess calcium promotes rapid strength gain but may compromise workability and finishing quality.

2.6.1.2 Soundness and Drying Shrinkage

Soundness and drying shrinkage are essential indicators of the volumetric stability and durability of GPC. Soundness is typically evaluated using the Le Chatelier expansion test, while drying shrinkage is measured under ASTM C596 (2023) conditions. Most studies report minimal expansion (<5%), confirming the absence of portlandite and the predominance of stable aluminosilicate gels (Kuri et al., 2021; Samantasinghar and Singh, 2019). This stability is further enhanced by the fine particle size and high reactivity of Class F fly ash and GGBFS, which promote dense microstructures and reduced capillary porosity (Kolade et al., 2025a). Kuri et al. (2021) also reported that GFNS replacement up to 50% had negligible influence on soundness, further validating the integrity of the geopolymer matrix.

Drying shrinkage in GPC generally ranges between 250 and 800 microstrain, depending on parameters such as the AL/B ratio, aggregate content and curing method (Castel et al., 2016; Meesala et al., 2020; Nadarajah et al., 2024; Zhao et al., 2017). Samantasinghar and Singh (2019) observed that shrinkage in fly ash–GGBFS blends is largely unaffected by NaOH concentration, indicating a resilient matrix structure. However, excessive GGBFS content (>60%) or residual free lime can lead to mild expansion, whereas high alkali concentrations tend to increase autogenous shrinkage due to rapid water loss. Early heat curing (60 – 80 °C for 24 hours) effectively mitigates long-term shrinkage by accelerating geopolymerization and refining pore structure (Castel et al., 2016; Mohamed et al., 2022). These findings suggest that GPC exhibits superior dimensional stability compared to PCC, provided that activator molarity and calcium content are carefully optimized to minimize microcracking.

2.6.1.3 Workability

Workability, commonly evaluated using flow table (ASTM C230 (2020)) or slump cone tests (ASTM C143 (2012)), reflects the rheological response of GPC mixes. Unlike PCC, GPC lacks continuous hydration reactions, making its flow behaviour highly sensitive to activator viscosity and concentration, silicate modulus (SiO_2/Na_2O), precursor fineness and the AL/B and W/Gs ratios (Alaneme et al., 2023; Criado et al., 2008; Ewa et al., 2023).

Reported flow diameters for fly ash–GGBFS blends typically range between 150 and 250 mm, with corresponding slump values of 40 – 225 mm, depending on mix composition (Bellum et al., 2020; Hu et al., 2019; Kolade et al., 2025b, 2025c; Reddy et al., 2018). Increasing GGBFS content from 0 to 50% generally decreases flow by 20 – 40%, attributed to faster reaction kinetics and the higher viscosity of sodium silicate solutions (Bellum et al., 2020; Hu et al., 2019; Nadarajah et al., 2024; Nguyen et al., 2020). Kuri et al. (2021) further noted improved flowability at Na_2SiO_3/NaOH ratios below 2.5, whereas higher ratios or NaOH concentrations ≥12 M markedly reduced workability, consistent with observations by Kolade et al. (2025a) and Luhar and Luhar (2022).

Moreover, Darmawan et al. (2019) found that Class C fly ash–based GPC exhibited high initial workability and stable setting times across varying activator concentrations, reflecting the moderating influence of intrinsic calcium on rheology. Hence, it can be concluded that fly ash–GGBFS blends offer a tunable balance, as higher calcium contents enhance early strength but reduce flowability, while low-calcium systems provide superior workability at the expense of slower setting.

2.6.2 Hardened Properties

2.6.2.1 Density

The density of GPC strongly influences its mechanical strength and long-term durability, as a denser microstructure generally corresponds to lower porosity and permeability (Amran et al., 2021). Reported hardened densities typically range between 2,200 and 2,500 kg/m^3, depending on precursor chemistry, aggregate packing and curing method (Bellum et al., 2020). Sharmin et al. (2017) observed that mixtures containing 65% GGBFS, 20% metakaolin and 15% rice husk ash achieved the highest dry density, primarily due to the high specific gravity and dense hydration products of GGBFS, whereas rice husk ash inclusion lowered density because of its high silica content and porous structure. Similarly, Hu et al. (2019) and Kolade et al. (2025b)

reported that GGBFS-based systems exhibited densities up to 5 – 8% higher than fly ash-based ones under comparable curing conditions, which reflect their enhanced polymerization and formation of denser C–S–H gels. Altogether, these findings emphasize that binder selection and proportioning critically determine microstructural compactness, which in turn affects strength, chemical resistance and thermal stability.

2.6.2.2 Compressive Strength

GPC can achieve compressive strengths comparable to or exceeding those of conventional PCC, depending on factors such as precursor composition, mix design, activator type and concentration and curing conditions (Alaneme et al., 2023; Nguyen et al., 2020). Blends rich in GGBFS consistently outperform fly ash-based systems due to their higher calcium content and accelerated reaction kinetics. Typically, ambient-cured fly ash-based mixes attain 20 – 50 MPa at 28 days, whereas thermally cured or GGBFS-blended systems can exceed 60 MPa, even under moderate curing temperatures. The presence of reactive calcium in GGBFS also promotes rapid strength gain, with over 70% of 28-day strength often achieved within the first three days of elevated-temperature curing (Bellum et al., 2020; Kolade et al., 2025b; Parathi et al., 2021; Samantasinghar and Singh, 2019).

Further improvements in mechanical performance have been observed with alternative calcium-rich precursors. Kuri et al. (2021) reported that replacing fly ash with 75% GFNS enhanced long-term strength by up to 35% after 56 days, attributed to slower but more complete geopolymerization and the formation of denser matrices. Also, several studies (Amran et al., 2021; Eisa et al., 2022; Samantasinghar and Singh, 2019) emphasize the vital role of optimizing the binder-to-activator ratio and alkaline activator composition, particularly the Na_2SiO_3-to-NaOH ratio and NaOH molarity, to maximize strength development. Despite these consistent trends, methodological differences across studies, especially in activator ratios, curing conditions and precursor fineness, limits direct comparison and model generalization. Consequently, while GPC can demonstrably equal or surpass PCC in compressive capacity, the absence of standardized mix design protocols continues to constrain the reliability and scalability of reported results.

2.6.2.3 Tensile and Flexural Strengths

Splitting tensile and flexural strengths indicate a material's resistance to tensile and bending stresses. In GPC, typical splitting tensile strengths range from 2 to 5 MPa, while flexural

strengths vary between 3 and 7 MPa, depending on mix composition, curing conditions and the inclusion of fibers or admixtures (Ahmed et al., 2021; Dinh et al., 2023; Liu et al., 2023; Quadflieg et al., 2020). Although the tensile-to-compressive strength ratio of GPC is generally comparable to that of PCC, typically 8 – 12%, incorporating 0.5 – 1.0% steel or polypropylene fibers can further enhance crack resistance and flexural capacity by 20 – 40% (Ahmed et al., 2021; Olivia and Nikraz, 2012; Parathi et al., 2021).

Eisa et al. (2022) further reported tensile strengths up to 4 MPa and flexural strengths up to 7 MPa for optimized fly ash–based GPC, though these values remained slightly below those of PCC due to differences in gel morphology (polymeric gels in GPC versus C–S–H in PCC). Performance, however, can be significantly improved with GGBFS incorporation, as its latent hydraulic activity promotes additional C–S–H formation, yielding a denser microstructure. For instance, Bellum et al. (2020) observed that increasing GGBFS content from 40% to 60% enhanced splitting tensile and flexural strengths by 17% and 23%, respectively. Likewise, optimizing activator formulation, particularly the Na_2SiO_3-to-NaOH ratio and silicate modulus, has been shown to further improve tensile and flexural performance in both fly ash and blended systems (Eisa et al., 2022; Kolade et al., 2025b).

2.6.3 Durability Performance

GPC generally exhibits superior durability compared to PCC, primarily due to its compact aluminosilicate gel network, low calcium content and reduced permeability. These microstructural features inhibit the ingress of aggressive ions, delay corrosion onset and mitigate degradation under chemical and thermal stresses (Amran et al., 2021; Parathi et al., 2021). However, durability outcomes vary widely depending on precursor composition, activator chemistry and curing conditions, which highlight the need for mix optimization based on exposure conditions.

Corrosion resistance is a key indicator of structural longevity. Tests such as accelerated corrosion (ASTM G109 (2021)) and chloride migration (NT BUILD 492 (1999)) have been applied to assess GPC's performance. Panneerselvam and Pazhani (2024) demonstrated that Class F fly ash–GGBFS-based beams exhibited superior corrosion resistance compared to PCC beams. Even after significant reinforcement corrosion, GPC beams retained higher residual load capacity and the onset of corrosion product formation was delayed by a factor of 3 – 5 relative to PCC. Similarly, Amorim Jr. et al. (2021) showed that metakaolin-based GPC achieved chloride diffusion coefficients 20 – 30% lower than those of PCC, confirming its

dense microstructure and low ionic mobility. These results actually suggest that the combination of low CaO and high Si/Al ratio promotes a chemically stable polymeric gel that effectively limits pore connectivity and chloride ingress.

GPC's acid resistance has also been extensively verified using immersion tests in H_2SO_4, HCl, acetic acid and $MgSO_4$ solutions, with common strength retention rates of 70 – 95% after 30 – 90 days that outperform PCC under identical conditions. For instance, Elyamany et al. (2018) and Bellum et al. (2020) found that fly ash–GGBFS blends outperformed PC mortars and concretes when exposed to 5% NaCl, Na_2SO_4, H_2SO_4 and $MgSO_4$ solutions, even when ambient cured. Furthermore, Meesala et al. (2020) observed that GPC retained 93% of compressive and 92% of tensile strength after 45 days in 10% H_2SO_4, with only 12 – 30% loss under $MgSO_4$ exposure. Davidovits (2015) reported about 7% mass loss after 30 days in 5% H_2SO_4 for metakaolin-based GPC, while Hardjito et al. (2004) recorded a 20% strength reduction after one year for Class F fly ash-based GPC in 5% H_2SO_4. Similarly, Chi (2012) found that GGBFS-based GPC lost 33% strength in acetic acid over one year, which was less than the 47% reduction in PCC under the same conditions. These results infer that the relatively lower degradation of GPC is attributed to its absence of $Ca(OH)_2$, which prevents deleterious calcium sulfate or calcium acetate formation. Nevertheless, mixes with excessive CaO or high GGBFS content can still exhibit localized leaching under prolonged acid attack, implying a trade-off between early strength and long-term chemical stability.

Thermal durability is another unique advantage of GPC, especially in high-temperature or fire-prone environments. Kong et al. (2007) reported that fly ash-based GPC gained up to 6% in compressive strength when exposed to 800 °C, attributed to stable microstructural densification and the absence of chemically bound water. Visual inspection revealed only surface discoloration without cracking, confirming the thermal compatibility between matrix and aggregates (Fig. 2.4). In contrast, metakaolin-based GPC exhibited a 34% strength loss at the same temperature, highlighting the importance of precursor type. This behaviour is consistent with the low thermal expansion of geopolymeric gels and their ability to redistribute internal stresses, unlike PCC, which undergoes microcracking and C–S–H decomposition above 400°C.

In terms of freeze–thaw conditions (ASTM C666 (1997)), GPC has consistently shown enhanced durability. Zhuang et al. (2016) reported that fly ash-based GPC exhibited 2.2 times greater resistance to freeze–thaw damage compared to PCC of equivalent compressive

strength. Similarly, Fu et al. (2011) found that GGBFS-based mixes withstood up to 300 cycles before showing a 5% strength reduction, far exceeding the 150-cycle limit typically observed in PCC. Zhang et al. (2021) further demonstrated that incorporating 10% crumb rubber as a fine aggregate replacement enhanced freeze–thaw durability by improving rigidity and reducing internal cracking, though higher rubber contents (>15%) slightly compromised compressive strength. Hence, these findings affirm that pore refinement, low permeability and improved elasticity of GPC collectively enhance its resistance to cyclic environmental degradation.

The above experimental evidences confirm that GPC offers superior chemical, thermal and cyclic durability relative to PCC. However, the degree of improvement depends strongly on precursor chemistry, as Class F fly ash systems excel in chemical resistance but show delayed strength gain, while GGBFS systems improve early strength and freeze–thaw resistance but are more prone to acid-induced mass loss. Moreover, the activator composition (especially the Na_2SiO_3/NaOH ratio) and curing conditions are pivotal in optimizing durability (Elyamany et al., 2018; Kolade et al., 2025b; Parathi et al., 2021).

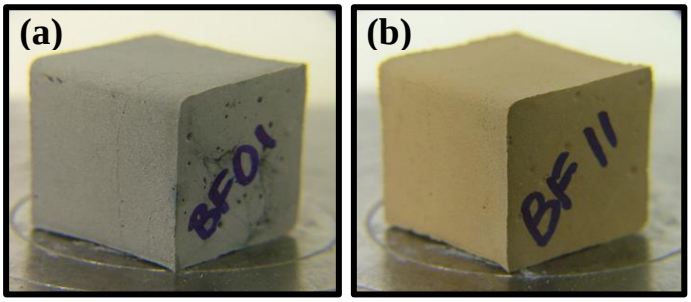

Fig. 2.4: Visual comparison of fly ash-based GPC specimens (**a**) before and (**b**) after high temperature exposure (Kong et al., 2007)

2.7 Structural Performance of Reinforced GPC Beams

The structural behaviour of reinforced GPC beams has attracted growing attention due to its implications for real-world applications. Despite the progress in understanding binder chemistry and durability, research into how these binders perform in full-scale structural members remains less developed compared to conventional PCC. The reviewed studies demonstrate that GPC beams can exhibit comparable flexural and shear behaviour to PCC beams, but are also influenced by unique factors such as precursor composition, alkali

concentration and curing condition. This section presents a critical synthesis of the flexural and shear performance of reinforced GPC beams, along with insights into their cracking patterns, deflection behaviour and failure modes. A consolidated overview of the selected studies is also presented in Table 2.5 towards the end of the section.

2.7.1 Flexural Performance of GPC Beams

Flexural performance remains a key benchmark for reinforced concrete beams. In GPC systems, it is influenced by factors such as precursor type, binder composition and activator alkalinity. For instance, Saeed and Al Amli (2023) reported that increasing the GGBFS content, alkali molarity and longitudinal steel ratio enhanced the first-crack, service and ultimate load capacities, achieving behaviour comparable to that of PCC beams. Kumar et al. (2017) also reported that incorporating up to 70% GGBFS with 30% metakaolin improved the compressive strength and bond performance of the GPC, which in turn contributed to higher ultimate load and moment capacity in reinforced beams, while maintaining a load–deflection response comparable to PCC beams.

Similarly, Hasan et al. (2023) reported that increasing the bottom reinforcement ratio in T-shaped GPC beams significantly enhanced both flexural strength and ductility, with ultimate strains exceeding 0.003. Likewise, Kalaivani et al. (2020) found that incorporating hydrated lime improved polymerization under ambient curing, leading to higher flexural performance. In contrast, fly ash–based GPC beams, particularly those using fly ash as the sole precursor, generally exhibited lower flexural strength and more brittle failure than PCC counterparts. Eisa et al. (2022) further confirmed this trend, noting that beams with low fly ash contents and reduced SS/SH ratios developed lower flexural capacity and pronounced cracking. This behaviour is primarily attributed to insufficient geopolymer gel formation and weak interfacial bonding between the paste and aggregate (Jayaprakash et al., 2025). Collectively, these findings highlight the strong dependence of flexural response on activator composition and justify the compositionally guided mix design framework adopted in this study.

2.7.2 Shear Performance of GPC Beams

Shear behaviour is another critical parameter in evaluating the structural reliability of GPC beams, owing to the inherently brittle nature of many geopolymer matrices. Experimental findings generally indicate that GPC beams can attain shear capacities comparable to those of conventional PCC beams (Darmawan et al., 2019). Saeed and Al Amli (2023) further

demonstrated that shear strength equations originally developed for PCC remain largely applicable to GPC, with both transverse and longitudinal reinforcement ratios exerting major influence on shear resistance. However, Darmawan et al. (2019) also highlighted the pronounced sensitivity of GPC to curing conditions, as seawater-cured beams exhibited higher crack load-to-failure ratios and improved shear strength relative to those cured at ambient temperature.

Mourougane et al. (2012) similarly reported that steam-cured, fly ash–based GPC beams achieved higher ultimate shear capacities than PCC beams of equivalent grade. Among the analytical models assessed, the ACI 318 (2019) predictions showed the closest alignment with experimental results, suggesting that existing PCC-based shear design equations can be effectively adapted for GPC when properly calibrated. Complementing this, Visintin et al. (2017) tested GPC beams without stirrups and found their shear-friction properties comparable to those of PCC. More recently, Abdullah et al. (2024) also confirmed that GPC beams reinforced with conventional steel bars can attain shear capacities similar to PCC beams. However, standard design equations tended to underestimate GPC performance at lower shear span-to-depth ratios. This discrepancy reflects the distinct cracking and interfacial bonding mechanisms of geopolymer matrices, which are not fully captured in PCC-based models. Altogether, these studies indicate that although GPC can achieve shear performance on par with PCC, its response remains highly dependent on precursor chemistry, activator composition, reinforcement configuration and curing conditions. Thus, existing design methodologies require careful calibration and possible refinement to reflect the unique material interactions governing geopolymer systems.

2.7.3 Crack Patterns, Load-Deflection Behaviour and Failure Modes

The failure mechanisms of reinforced GPC beams reflect the complex interaction between binder chemistry, reinforcement configuration and curing conditions. Experimental investigations conducted under standardized loading protocols, such as ASTM C78 (2009), generally show that adequately reinforced GPC beams fail in flexure, exhibiting load–deflection and crack propagation behaviours broadly comparable to those of PCC beams.

Kumar et al. (2017) tested 150 × 150 × 700 mm fly ash–GGBFS-based GPC beams reinforced with 8 mm, 10 mm and 12 mm steel bars, reporting a load–deflection response (maximum deflection close to 3.5 mm; Fig. 2.5) similar to that of PCC beams, though with slightly reduced ductility. Likewise, Eisa et al. (2022), using a 12M NaOH solution and Na_2SiO_3/NaOH ratios

ranging from 0.5 to 2.5 under ambient curing, observed more pronounced and wider flexural cracks in 100 × 150 × 800 mm fly ash–based GPC beams reinforced with 10 mm longitudinal bars. Their GPC beams exhibited a mid-span deflection of 3 mm at failure compared with 4 mm for PCC beams, indicating relatively brittle fracture and lower energy absorption capacity. Fig. 2.6 illustrates the more concentrated and sharper crack profiles observed in GPC beams under identical four-point bending conditions.

In terms of shear performance, Darmawan et al. (2019) reported that 100 × 150 × 1500 mm Class C fly ash–based GPC beams cured in seawater developed more distributed shear cracking and higher post-cracking load resistance than ambient-cured specimens (Fig. 2.7), with ultimate deflections reaching approximately 8 mm in both categories. Eisa et al. (2022) further observed that GPC beams reinforced with 12 mm bars failed primarily through concrete crushing in the compression zone at mid-span, accompanied by substantial bending similar to PCC beams. However, the ultimate elongation under shear loading was slightly lower in GPC beams (4.9 mm deflection and 0.0023 strain) than in PCC controls (4 mm deflection and 0.0031 strain), reaffirming their comparatively brittle post-yield behaviour. All in all, these findings highlight that although reinforced GPC beams can achieve structural responses broadly comparable to PCC, their ductility and failure modes remain highly sensitive to mix chemistry, activator concentration and curing environment, which are factors that must be carefully controlled in design and application.

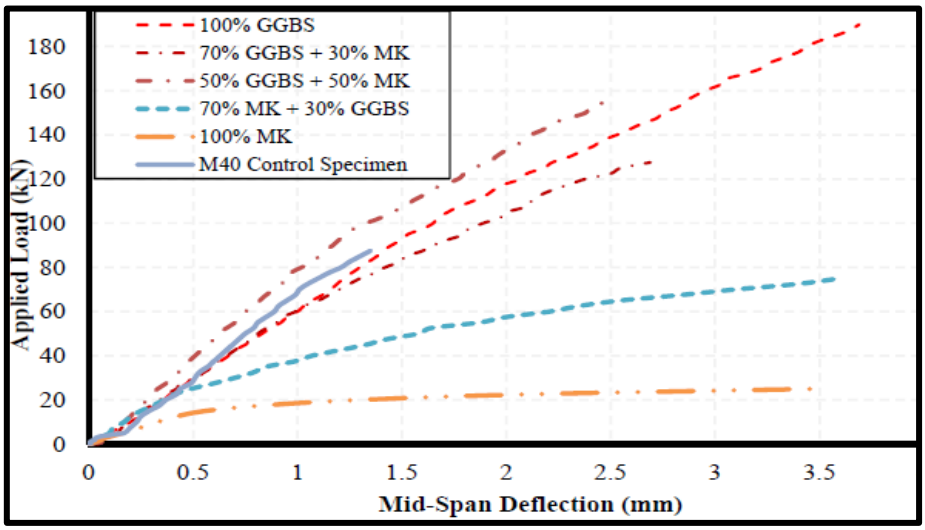

Fig. 2.5: Load–deflection behaviour of PCC and GPC beams containing GGBFS and fly ash (Kumar et al., 2017)

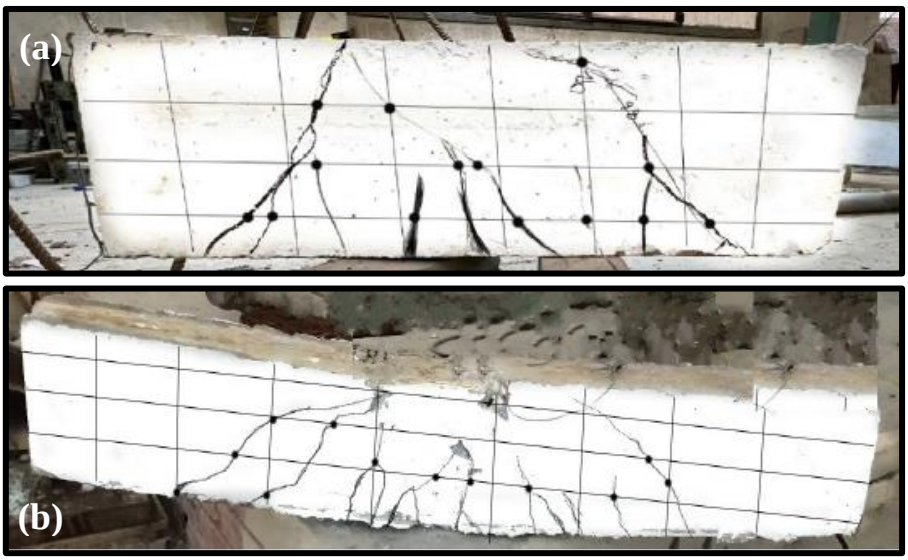

Fig. 2.6: Crack patterns under flexural loading (**a**) PCC beam (**b**) GPC beam (Eisa et al., 2022)

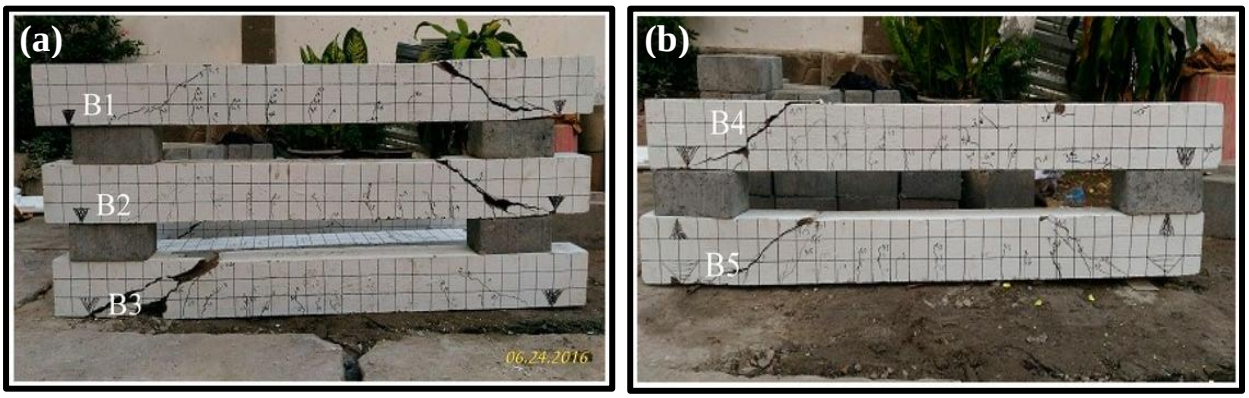

Fig. 2.7: Shear crack propagation in GPC beams cured (**a**) at room temperature and (**b**) in seawater (Darmawan et al., 2019)

Table 2.5: Summary of structural behaviour of selected reinforced GPC beams

Study	Precursor type	Key focus	Structural observation
Eisa et al. (2022)	Class F fly ash	Effect of alkaline ratio on flexural strength	GPC beams showed lower flexural capacity and brittle behaviour compared to PCC. Mid-span deflection was 3 mm for GPC vs 4 mm for PCC, with wider crack widths and lower energy absorption.
Kumar et al. (2017)	GGBFS and metakaolin	Influence of precursor ratio on flexure	70% GGBFS and 30% MK mix yielded optimal compressive strength and bond performance, achieving a load–deflection response up to 3.5 mm comparable to PCC but with slightly lower ductility.
Hasan et al. (2023)	Class F fly ash	Impact of rebar type and reinforcement ratio	Higher bottom steel ratio improved both strength and ductility. GPC beams exceeded PCC in ultimate strain ($\varepsilon > 0.003$).
Kalaivani et al. (2020)	Fly ash, GGBFS and lime	Influence of lime and NaOH molarity	Lime-enhanced heat generation led to better polymerization and increased flexural performance under ambient curing conditions.
Saeed and Al Amli (2023)	Class F fly ash	Effect of reinforcement ratios on shear	Shear strength aligned with PCC codes. Comparable bond and deflection behaviour observed. Transverse and longitudinal reinforcement ratios were key to shear resistance.

Study	Precursor type	Key focus	Structural observation
Darmawan et al. (2019)	Class C fly ash	Curing method and NaOH concentration	Seawater-cured beams had better crack resistance and higher shear strength than ambient-cured beams. Ultimate deflection reached approximately 8 mm, confirming improved post-cracking load transfer.
Mourougane et al. (2012)	Fly ash and GGBFS	Influence of curing condition and stirrup spacing on shear	Steam-cured beams exhibited higher ultimate shear capacity than PCC of similar grade. Beams with 150–230 mm stirrup spacing failed in shear, with ACI 318 predictions showing closest agreement to experimental values (mean = 1.04).
Visintin et al. (2017)	Class F fly ash	Validation of shear models without stirrups	GPC beams without stirrups displayed shear-friction behaviour within PCC ranges. The mechanics-based segmental model accurately predicted shear strength, supporting its applicability to GPC design.
Abdullah et al. (2024)	Class F fly ash	Shear capacity evaluation using conventional reinforcement	GPC beams with standard steel reinforcement achieved similar shear capacity to PCC. However, PCC-based equations underestimated performance at low shear span-to-depth ratios due to differing crack propagation and bond mechanisms.

2.8 Sustainability Considerations in Geopolymer Research

2.8.1 Environmental Benefits, Economic Evaluations and Life Cycle Perspectives

The primary environmental advantage of GPC lies in its significantly lower carbon footprint compared to PCC. Conventional PC production emits nearly 900 kg of CO_2 per tonne, primarily due to limestone calcination and energy-intensive clinkerization processes (Bhutta et al., 2017). In contrast, GPC, especially those based on fly ash and GGBFS, can reduce embodied CO_2 emissions by 40 – 80%, depending on mix composition and curing conditions (Alsalman et al., 2021; Martinez et al., 2025; Turner and Collins, 2013). For instance, fly ash/GGBFS blends typically emit only 200 – 300 kg CO_2 per tonne, offering a substantial emissions advantage (Cong et al., 2024).

Beyond emissions, GPC also demonstrates significant energy savings. Whereas PC production consumes around 3.2 GJ of thermal energy per tonne (Mohamad et al., 2021), GPC manufacturing can require 30 – 60% less energy due to the absence of high-temperature clinker formation (Olsson et al., 2024). These savings are particularly evident in ambient-cured systems or those employing synthesized activators, which further minimize thermal input.

Although the upfront material costs of GPC, especially those using CSS, may surpass those of PC systems, LCAs frequently reveal long-term economic benefits when performance and environmental impacts are considered. Studies by Oyebisi et al. (2022) and Cong et al. (2024) show that incorporating factors such as carbon pricing, reduced maintenance from enhanced durability and avoided landfill costs can result in 15 – 30% life cycle cost savings over conventional concrete. Furthermore, using alternative alkaline activators derived from local waste, such as WGP and biomass ash, can reduce production costs by 10 – 50%, improving GPC's affordability, especially in resource-constrained regions (Dadsetan et al., 2022; Kolade et al., 2025b; McCloskey et al., 2024; Umer et al., 2024).

GPC's economic viability is also shaped by regional factors including energy mix, transport logistics and the local availability of precursors. LCA sensitivity analysis confirm that cost and environmental benefits are maximized in regions with renewable energy access, abundant industrial by-products and robust supply chains (Abdulkareem et al., 2021; Bianco et al., 2021; Umer et al., 2024). In addition, policy instruments such as carbon taxation and green building incentives further enhance GPC's competitiveness by internalizing external environmental costs. Real-world applications reinforce these insights. Several infrastructure projects across Asia and Australia have successfully deployed GPC in structural and non-structural elements,

reporting tangible reductions in emissions and lifecycle costs (Kolade et al., 2025a). These outcomes underscore GPC's dual potential to meet environmental targets and economic expectations, particularly when supported by sound policies and supply chain optimization.

2.8.2 Role of Local Waste Materials and Circular Economy Promotion

The integration of locally sourced industrial waste materials into geopolymer production supports industrial symbiosis, which is a collaborative model where the by-products or wastes of one industry serve as raw materials for another, thereby enhancing resource efficiency (Kolade et al., 2025a; Wadstrom et al., 2021). Abundant waste streams such as fly ash, GGBFS and WGP are often landfilled despite being rich in reactive aluminosilicates and silica, making them ideal for both precursor and activator synthesis in geopolymer systems. Thus, geopolymer technology aligns strongly with circular economy principles by utilizing these materials, enabling the diversion of vast quantities of industrial and post-consumer waste from landfills and reintegrating them into the construction value chain (Nodehi and Taghvaee, 2022; Oyejobi et al., 2024).

In particular, WGP presents substantial untapped potential. Of the 100 million tonnes of post-consumer glass waste generated globally each year, an estimated 60 – 65% remains unused or landfilled. Repurposing this waste in alkaline activator synthesis offers a dual benefit of reducing environmental burden while replacing carbon-intensive and costly CSS. Similarly, global estimates indicate the annual generation of approximately 900 million tonnes of fly ash and 350 million tonnes of GGBFS, much of which remains underutilized (Nodehi and Taghvaee, 2022).

Beyond environmental benefits, leveraging local waste resources also strengthens regional supply chains, minimizes transportation-related emissions and enhances material security, especially critical in low- and middle-income countries where reliance on imported cementitious materials poses economic and logistical challenges (Nodehi and Taghvaee, 2022; Oyejobi et al., 2024; Parathi et al., 2021). Hence, the use of locally available waste-derived materials in GPC offers a multi-dimensional sustainability pathway, addressing environmental, economic and supply chain resilience objectives simultaneously.

2.9 Statistical Methods for Assessing Significance and Reliability in GPC Research

The application of statistical methods in geopolymer binder studies incorporating alternative or waste-derived activators remains relatively limited despite their essential role in validating

experimental findings and enhancing the reliability of scientific conclusions. Most published investigations (Dadsetan et al., 2022; Delgado-Plana et al., 2024; Ghanim et al., 2025; Rajan and Kathirvel, 2021; Tchakouté et al., 2016b; Vinai and Soutsos, 2019) focus on reporting fresh and mechanical properties such as workability, compressive strength and flexural strength, typically presenting mean values and standard deviations derived from a small number of specimens. Although such descriptive statistics provide a basic indication of experimental variability, they often do not establish whether the observed differences between mix compositions, curing conditions or activator systems are statistically significant (Ge et al., 2026). Consequently, interpretations of material behaviour or performance improvements are frequently based on direct numerical comparisons rather than rigorous statistical inference.

A number of studies (Ahmed et al., 2022; Cui et al., 2020; Kishore et al., 2022; Wang et al., 2025) have attempted to address this limitation in geopolymer systems activated with commercial activators by incorporating formal statistical analysis into experimental investigations. Techniques such as t-tests, analysis of variance (ANOVA) and regression modelling have been used to evaluate the influence of key mix parameters, including precursor composition, activator concentration and curing conditions, on the mechanical and durability properties of GPC. In addition, response surface methodology (RSM) and factorial experimental designs have been applied in some cases to optimize geopolymer mix formulations and quantify the interaction effects among multiple variables (Ge et al., 2026; Rani and Shudha, 2024). These approaches provide a more robust basis for interpreting experimental data, enabling researchers to distinguish genuine material trends from variations arising from experimental uncertainty.

Despite these developments, the application of statistical analysis across GPC studies remains inconsistent and often limited in scope. Statistical assessments are often confined to basic hypothesis testing, while complementary indicators such as effect sizes, confidence intervals and power analysis are less commonly reported, despite their importance in interpreting the practical significance and reliability of observed differences (Ge et al., 2026). Moreover, studies involving alternative or waste-derived activators frequently report promising mechanical performance without systematically evaluating whether such improvements are statistically robust. This limitation introduces uncertainty in the interpretation of reported results and makes it difficult to compare findings across different material systems or experimental conditions.

The integration of comprehensive statistical analysis is therefore essential for strengthening the credibility, reproducibility and interpretability of GPC research. By quantifying the statistical significance and magnitude of observed differences, statistical tools allow researchers to identify meaningful trends, evaluate the reliability of experimental observations and provide stronger evidence for the practical advantages of emerging geopolymer systems (Matsimbe et al., 2024; Terrones-Saeta et al., 2023). In the context of developing alternative activators, such analysis are important for establishing confidence in the performance of non-commercial materials. Accordingly, this study incorporates a systematic statistical framework to evaluate the reliability of experimental results obtained from geopolymer systems activated with CSS and WGSS. Independent sample t-tests, one-way ANOVA and effect-size indices are employed to assess the statistical significance and practical magnitude of differences observed in mechanical and structural performance. Thus, the study provides a more rigorous and transparent comparison between CSS and WGSS-activated systems by integrating statistical analysis with experimental characterization, thereby contributing to a clearer understanding of the potential of waste-derived activators in structural-grade GPC applications.

2.10 Summary, Research Gaps and Justification

This chapter reviewed the current state of knowledge on GPC, examining its constituent materials, mix design methodologies, fresh and hardened properties, durability performance, structural behaviour, sustainability potential and the statistical methods used to assess the significance and reliability of experimental results. A recurring theme in the literature is the distinctive chemistry of GPC, which differentiates it from conventional PCC and necessitates a more chemistry-informed approach to its design, optimization and application.

Despite notable advances, particularly in understanding the roles of alkaline activators and aluminosilicate precursors, several important research gaps remain. The continued reliance on CSS, despite its high cost, substantial carbon footprint and limited availability in developing regions, highlights the need for more sustainable and accessible alternatives. Although liquid-phase WGSS has demonstrated promising results at the binder and paste scales, its application in full structural elements, such as reinforced beams, remains largely unexplored. In addition, many existing studies focus on isolated performance indicators, typically compressive strength or workability, with limited consideration of integrated assessments that simultaneously address mechanical performance, environmental impact and economic feasibility. The application of rigorous statistical analysis to evaluate the significance and reliability of

experimental findings is also relatively limited in GPC research, especially in studies involving alternative activator systems. These limitations create uncertainties regarding the robustness, scalability and long-term viability of GPC systems utilizing non-commercial activators such as WGSS.

To consolidate these observations, Table 2.6 summarizes the key research gaps identified in the literature and outlines how the present study addresses them. In particular, the study investigates mix design standardization, evaluates the sustainability of alternative activators, examines the structural behaviour of reinforced GPC beams and applies statistical methods to establish the reliability of the experimental results. Through this integrated approach, the study aims to contribute toward the standardization and broader adoption of GPC, particularly in sustainability-driven and resource-constrained construction contexts.

Table 2.6: Summary of key research gaps and study contributions

Research gap identified	Supporting literature	This study's contribution
Lack of standardization in mix design methodologies	Alaneme et al. (2024) Li et al. (2019a)	Proposes and validates a composition and performance-driven mix design incorporating key design ratios (W/Gs, SiO_2/Al_2O_3, Na_2O/SiO_2 and H_2O/Na_2O)
Heavy reliance on CSS despite environmental and cost concerns	Provis (2018); McCloskey et al. (2024); Vinai and Soutsos (2019)	Develops a liquid-phase WGSS to replace CSS
Limited application of waste-derived activators in full structural elements, such as beams	Tchakouté et al. (2016b); Dadsetan et al. (2022); McCloskey et al. (2024)	Evaluates the structural performance of reinforced GPC beams using WGSS
Minimal life cycle or circular economy and cost analysis of GPC systems incorporating waste-based activators	Vinai and Soutsos (2019); Martinez et al. (2025)	Incorporates mechanical, environmental and cost comparisons between WGSS and CSS activators to further promote sustainability
Limited use of statistical analysis to evaluate the significance and reliability of experimental results in GPC studies	Ge et al. (2026)	Applies statistical techniques to assess the significance and reliability of differences observed between CSS and WGSS-activated systems

CHAPTER 3

3 MATERIALS AND METHODOLOGY

3.1 Research Design Overview

This study adopted a laboratory-based experimental and analytical research design to develop, characterize and evaluate geopolymer mortars and concretes activated with synthesized WGSS and CSS. All geopolymer mixes were produced using a two-part activation system, in which the alkaline activator was prepared as a liquid solution comprising NaOH and sodium silicate (either CSS or WGSS) prior to mixing with the aluminosilicate binder materials. The research followed a phased methodological framework, beginning with raw material sourcing, processing and physicochemical characterization. Preliminary binder optimization was undertaken using mortar formulations activated with CSS to establish baseline performance and identify suitable binder compositions.

It is important to note that although mortar specimens were employed for initial optimization and mechanical characterization, classification of binder strength adheres to SANS 50197-1 (2000) cement strength classes. In alignment with standard convention, binder strength notation is therefore adopted when referencing strength class requirements, while mortar performance remains the basis of experimental evaluation.

Following binder optimization, WGSS was synthesized via alkali-fusion, characterized and incorporated into mortar and concrete systems. Mechanical, microstructural, structural performance and durability-related assessments were subsequently conducted, followed by statistical analysis to enable direct comparison between WGSS and CSS-based mixes, alongside a life-cycle assessment (LCA) to evaluate environmental performance. The research workflow is illustrated in Fig. 3.1, comprising the following five interconnected phases:

i. raw material characterization

ii. mix design development and binder optimization via mortar trials

iii. WGSS synthesis and characterization

iv. mechanical and structural testing

v. statistical analysis and LCA.

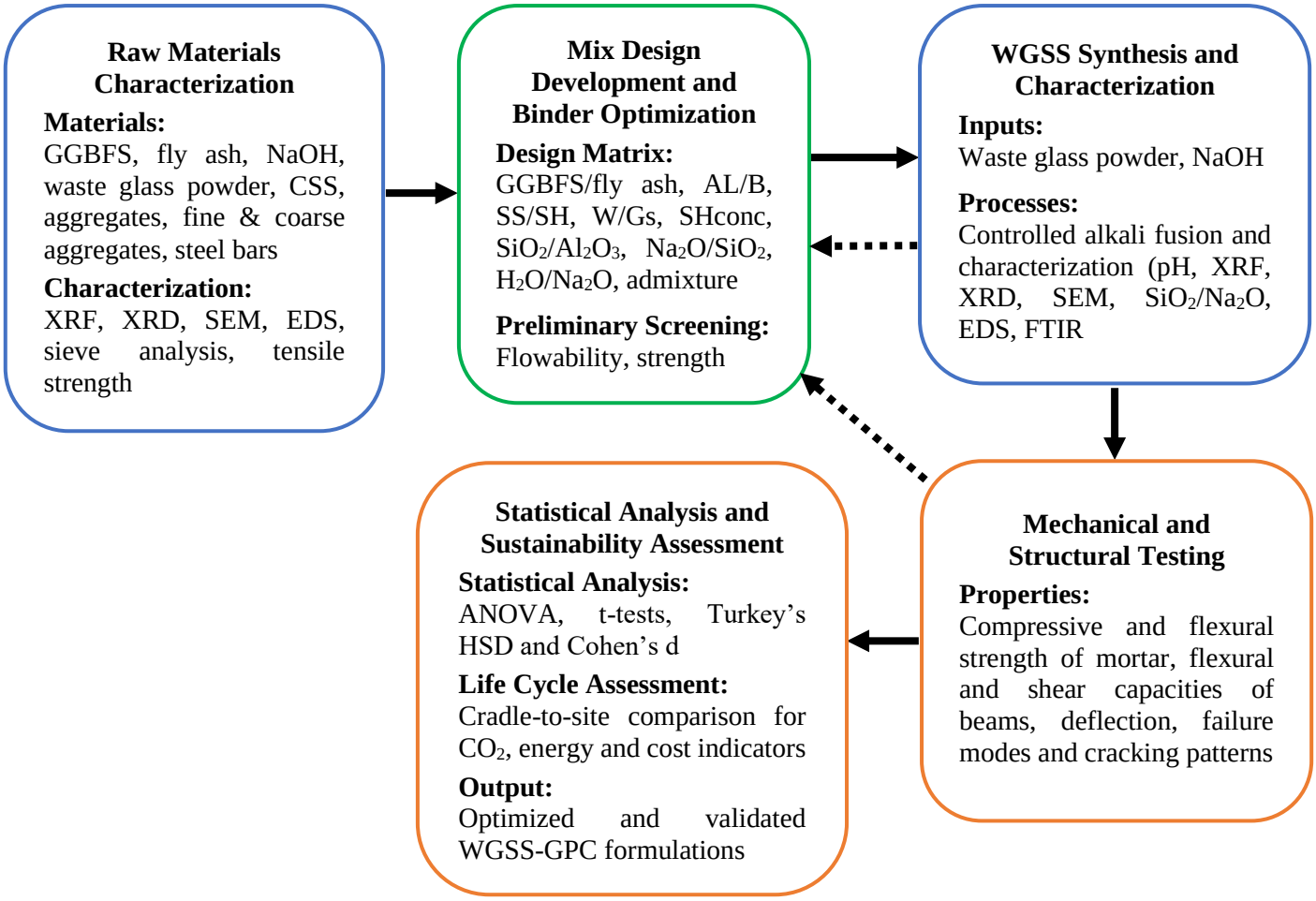

Fig. 3.1: Schematic representation of the five-phase research methodology

3.2 Materials and Processing

This section describes the source, preparation and processing of all materials used in this study. Fig. 3.2 presents the materials, including fly ash, GGBFS, WGP, NaOH pellets, CSS, fine and coarse aggregates, water and a polycarboxylate-based superplasticizer (SP), which were all locally sourced in South Africa to support the sustainability objectives of the research and to reflect regionally available production conditions.

The fly ash was sourced from the Lethabo Power Station via Ash Resources (Lafarge) and used as the primary aluminosilicate precursor in its as-received condition. GGBFS, obtained from AfriSam (South Africa) (Pty) Ltd, was incorporated to enhance early-age strength and reaction kinetics due to its calcium-rich composition. WGP, sourced from African Pegmatite (Pty) Ltd, was used as a silica-rich feedstock for the synthesis of WGSS. To improve reactivity and ensure uniformity, the WGP was sieved through a 150 µm mesh prior to use. Analytical-grade NaOH pellets (≥ 97% purity), supplied by Minema Chemicals, were used as both a primary activator

and in the synthesis of WGSS. CSS, sourced from Sigma-Aldrich, served as a control activator for performance benchmarking.

An SP, supplied by CHRYSO and conforming to SANS 50934-2 (2011), was used to enhance workability. A dosage of 5% by weight of binder was adopted based on preliminary trials. Potable water from the University of South Africa (UNISA) supply was used for alkaline solution preparation as well as for mortar and concrete mixing. CEN standard sand was used for mortar preparation, while crusher sand served as the fine aggregate in concrete mixes. Crushed granite with a nominal maximum size of 19 mm was used as the coarse aggregate. Deformed reinforcing steel bars of 8 mm and 10 mm diameters were used for beam reinforcement.

Fig. 3.2: Representative images of (**a**) fly ash (**b**) GGBFS (**c**) NaOH pellets (**d**) WGP (**e**) SP (**f**) CSS (**g**) Standard sand (**h**) Crusher sand (**i**) Coarse aggregates (**j**) Reinforcing steel bars

3.3 Characterization Methods

Comprehensive characterisation of the materials was conducted to determine their chemical, physical, mechanical, morphological and spectroscopic properties and to confirm their suitability for GPC production. All tests were performed in accordance with established standards to ensure accuracy, reliability and reproducibility.

3.3.1 Particle Size Distribution

The sieve analysis technique was used to determine the particle size distribution and fineness of CEN standard sand, crusher sand and coarse aggregates in accordance with SANS 3001-AG1 (2012), while laser diffraction was used for fly ash and GGBFS. These measurements were used to assess packing density and potential reactivity of the materials. The sieve analysis was conducted in the concrete laboratory of UNISA's Civil Engineering department, while the laser diffraction was conducted at the concrete laboratory of the department of Civil Engineering, University of Witwatersrand.

3.3.2 Chemical composition (XRF)

Major oxide compositions (SiO_2, Al_2O_3, CaO, Fe_2O_3, Na_2O, K_2O, MgO and others) of fly ash, GGBFS, WGP and synthesized activator were determined using a PANalytical Axios mAX X-ray fluorescence spectrometer operated at 4 kW with a Rh anode X-ray tube, following established procedures reported in previous geopolymer and cementitious materials studies (Ibrahim et al., 2022; Tchakouté et al., 2016b). Samples were oven-dried at 105°C for 24 hours, ground to pass through a 75 µm sieve and fused into glass beads using lithium tetraborate flux prior to analysis. Calibration was performed using certified reference materials to ensure analytical accuracy. The analysis was conducted in the Chemistry/Chemical Engineering department of UNISA.

3.3.3 Phase Identification (XRD)

X-ray diffraction was performed using a Bruker D8 Advance diffractometer equipped with Cu Kα radiation ($\lambda = 1.5406$ Å), operating at 40 kV and 40 mA, in accordance with widely adopted procedures for amorphous and crystalline phase analysis in alkali-activated materials (Tchakouté et al., 2016b; Vinai and Soutsos, 2019). Powdered samples (< 75 µm) of WGP and the synthesized activators were scanned over a 2θ range of 5° – 90° with a step size of 0.01° and a scanning rate of 1°/min. The crystalline phases were identified using Bruker EVA

software with the ICDD PDF-4+ database, while the amorphous content was estimated from baseline hump intensity. The analysis was conducted in the Physics department, UNISA.

3.3.4 Morphology and microstructure (SEM)

The surface texture and morphology of the fly ash, GGBFS and synthesized activators were examined using a JEOL JSM-IT300 scanning electron microscope at iNanoWS (UNISA), following standard sample preparation and imaging procedures reported in the literature (Kanagaraj et al., 2022; Oyejobi et al., 2023). Powdered samples were mounted on carbon tape and sputter-coated with a thin layer of gold (~10 nm) to prevent charging. Images were captured at an accelerating voltage of 15 kV under high-vacuum mode at magnifications ranging from 500× to 10000×.

3.3.5 Elemental Analysis (EDS)

Energy-dispersive X-ray spectroscopy (EDS) attached to the SEM (Oxford Instruments X-Max 20 mm^2 detector) at iNanoWS (UNISA) was used to identify elemental constituents of fly ash, GGBFS and synthesized activators, following established analytical approaches (Delgado-Plana et al., 2024; Oyejobi et al., 2023). Spectra were collected at a working distance of 10 mm and analyzed using INCA software. The results were used to qualitatively validate XRF findings and confirm the uniform distribution of key elements such as Si, Al, Na and Ca.

3.3.6 Spectroscopic Characterization (FTIR)

To verify the dissolution of waste glass and confirm silicate network formation in the alternative activators, Fourier Transform Infrared Spectroscopy (FTIR) was conducted at iNanoWS (UNISA) using a Bruker Alpha II spectrometer equipped with an ATR (attenuated total reflectance) module, following standard procedures commonly adopted in geopolymer research (Delgado-Plana et al., 2024; Vinai and Soutsos, 2019). First, the alternative activator samples were air-dried at 60°C to obtain a gel residue for analysis. Afterwards, spectra were collected in the 4000 – 600 cm^{-1} range at a resolution of 4 cm^{-1}, averaging 32 scans per sample. The resulting spectral features were used to validate the successful conversion of waste glass into soluble silicate oligomers.

3.3.7 Alkalinity Verification (pH Measurement)

The pH of the alternative activators was measured using a calibrated Mettler Toledo digital pH meter at iNanoWS (UNISA) to ensure consistent alkalinity and dissolution efficiency of the waste glass feedstock. Measurements were taken at 23 ± 2°C following instrument calibration with standard buffer solutions (pH 7 and 12).

3.3.8 Tensile Strength of Reinforcement Steel Bars

The tensile properties of deformed reinforcing steel bars (8 mm and 10 mm diameter) were determined using an Instron 8801 servo-hydraulic universal testing machine (UTM) located in the Department of Mechanical Engineering at UNISA, as presented in Fig. B8 (Appendix B). The Instron 8801 is a high-precision testing system capable of applying controlled monotonic loading under displacement or strain control, making it suitable for accurate characterisation of metallic materials. Tensile testing was conducted in accordance with SANS 6892-1 (2010), with reference to SANS 920 (2011) requirements for reinforcing steel. The specimens were tested under uniaxial tension at ambient laboratory conditions. Each bar was securely gripped using appropriate wedge grips to prevent slippage during loading and the load was applied at a controlled rate until failure. The parameters measured included yield strength, ultimate tensile strength, Young's modulus, elongation at fracture and yield ratio. These properties were used to evaluate the mechanical performance and compliance of the reinforcement bars with relevant standards.

3.4 Materials Characterization Results

3.4.1 Fly Ash

XRF analysis revealed a combined SiO_2, Al_2O_3 and Fe_2O_3 content of 91.17%, exceeding the 70% minimum required by ASTM C618 (2022) for Class F pozzolans. The CaO content was relatively low at 3.63% (< 18%), while the loss on ignition (LOI) was 0.80% (< 5%), indicating minimal unburnt carbon. Particle size analysis revealed a fine material with a median particle diameter (D_{50}) of approximately 4.13 µm, which is beneficial for enhancing reactivity and packing density. The fly ash's detailed oxides composition and physical properties are presented in Table 3.1. EDS results further confirmed silicon (Si), aluminium (Al) and oxygen (O) as the dominant elements in Fig. 3.3a. SEM images also revealed smooth, spherical and vitreous particles of varying sizes, a morphology that enhances workability, particle packing,

reduces porosity and contributes to improved geopolymer strength (Bellum et al., 2020; Kolade et al., 2025b).

Table 3.1: Oxides composition and physical properties of fly ash, GGBFS and WGP

Oxides composition (% wt.)	Fly ash	GGBFS	WGP	CSS
SiO_2	53.83	34.69	70.08	26.5
Al_2O_3	33.18	17.37	2.16	–
Fe_2O_3	4.16	0.72	1.13	–
CaO	3.63	35.08	10.50	–
TiO_2	1.51	0.78	0.27	–
MgO	0.93	7.71	1.06	–
K_2O	0.68	1.01	0.23	–
P_2O_5	0.44	0.01	0.23	–
Na_2O	0.11	0.26	12.41	10.6
SO_3	0.08	1.13	0.38	–
MnO	–	1.24	–	–
Mn_2O_3	1.45	–	–	–
Mn_3O_4	–	–	0.32	–
Cr_2O_3	–	–	0.77	–
H_2O	–	–		62.9
LOI	0.80	–	0.86	–
Physical properties	**Fly ash**	**GGBFS**	**WGP**	**CSS**
Density (g/cm^3)	2.36	2.92	1.40	1.35
D_{10} (μm)	0.24	0.22	–	–
D_{50} (μm)	4.13	38.46	–	–
D_{90} (μm)	41.51	59.40	75.00	–
Colour	Pale grey	White	Pale grey	Colourless

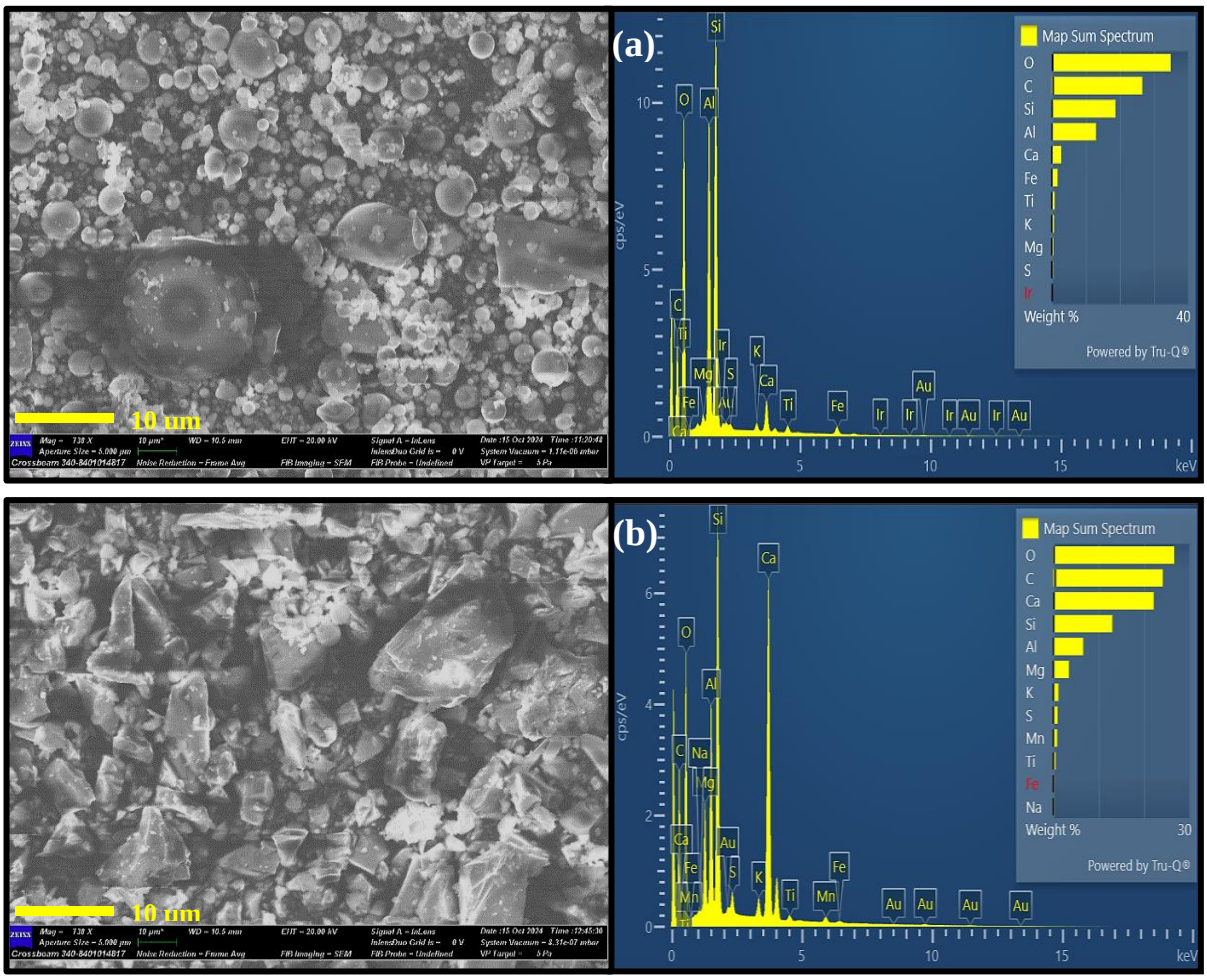

Fig. 3.3: SEM and EDS analysis of (**a**) fly ash and (**b**) GGBFS, illustrating their surface morphology and elemental composition

3.4.2 GGBFS

XRF results presented in Table 3.1 confirmed that GGBFS is rich in CaO, SiO_2 and Al_2O_3, with a (CaO + MgO)/SiO_2 ratio of 1.26, satisfying the requirement of BS EN 15167-1 (2006) for hydraulic slags that the ratio must exceed 1.0. The high calcium content is beneficial for accelerating geopolymerization and enhancing early-age strength. According to Table 3.1, particle size distribution indicated D_{10}, D_{50} and D_{90} values of 0.22 µm, 38.46 µm and 59.40 µm, respectively, indicating a comparatively coarser material than the fly ash. The EDS spectrum presented in Fig. 3.3b identified Ca, Si and O as the dominant elements, while SEM observations revealed a predominantly amorphous, angular morphology with rough particle surfaces. This texture contributes to improved mechanical interlocking, enhanced reaction kinetics and the formation of additional binding phases, thereby increasing strength and durability (Bellum et al., 2020; Kolade et al., 2025b).

3.4.3 WGP

XRF analysis indicated a high SiO_2 content exceeding 70%, along with notable amounts of Na_2O and CaO and a minor presence of Al_2O_3. The non-crystalline, amorphous structure of the material was verified via XRD. As shown in Fig. 3.4, the XRD pattern displays a broad hump between $2\theta = 10° – 40°$, which is characteristic of amorphous glass. It also shows a medium-intensity peak near $2\theta = 26.63°$, corresponding to crystalline quartz (SiO_2). These results are consistent with observations by Ikotun et al. (2024b). Furthermore, the broad hump within 15° – 35° reflects the amorphous nature typical of supplementary cementitious materials, where lower peak intensities are indicative of higher disorder and consequently, better pozzolanic activity (Raveendran and Vasugi, 2024). Based on its high amorphous content (94.81%) and elevated SiO_2 concentration, the WGP was deemed suitable for producing WGSS.

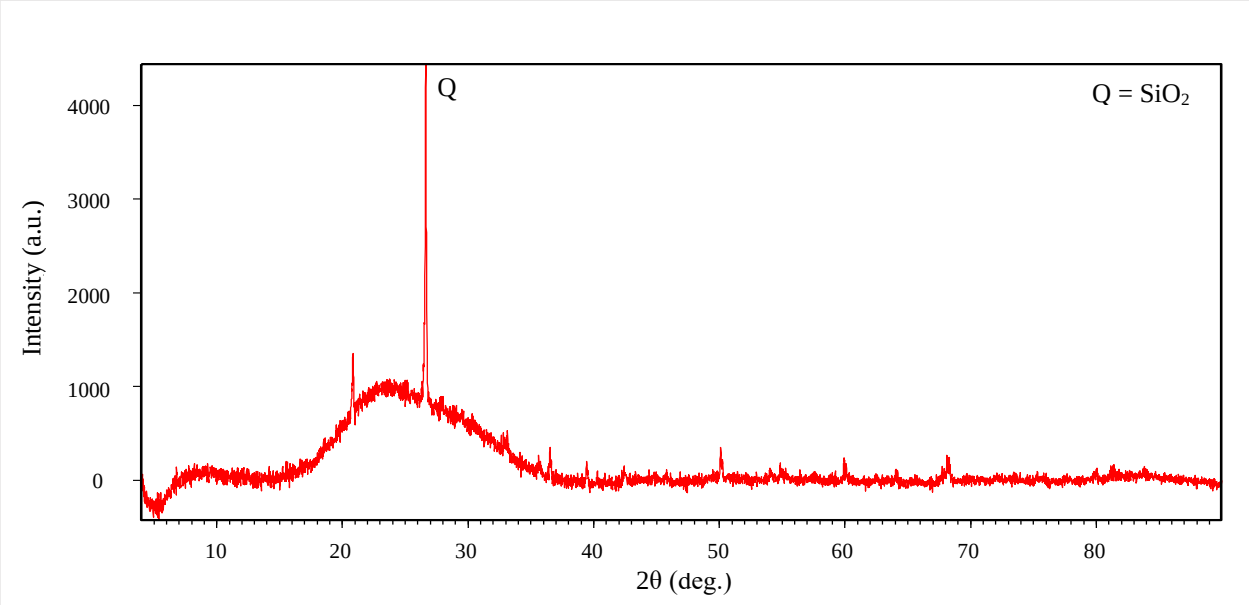

Fig. 3.4: XRD pattern of WGP showing a broad amorphous hump

3.4.4 CSS

The CSS exhibited a typical silica modulus (SiO_2/Na_2O) of 2.5, with its composition presented in Table 3.1. It exhibited a density of 1.39 g/mL at 25 °C and a pH of 12.5. As such, its high alkalinity and silica content contribute to its effectiveness as an alkaline activator

3.4.5 Fine Aggregates

The particle size distribution of the CEN standard and crusher sands are shown in Fig. 3.5 and Table A1 and A2, respectively. The CEN standard sand conformed to EN 196-1 (2016) and exhibited a fineness modulus (FM) of 2.57. This FM reflects a moderate level of coarseness, which contributes to improved workability and cohesion in mortar mixes while helping to limit excessive water demand (Kolade et al., 2025b). Also, the crusher sand exhibited a FM of approximately 3.0, indicating a relatively coarser grading compared to standard sand. As shown in Table A2, 95.6% of the material passed the 5 mm sieve, which falls within the specified range of 92 – 100%. Similarly, 15.56% of the material passed the 150 µm sieve, comfortably within the required range of 5 – 25% for that fraction. These results confirmed that the crusher sand satisfies the SANS 1083 (2013) grading limits, indicating a well-graded fine aggregate suitable for concrete applications. In addition to favorable grading characteristics, the crusher sand exhibited a specific gravity of 2.65 and a water absorption of 0.5%. These physical properties, together with the compliant particle size distribution, supported its effective use in the geopolymer mix, ensuring adequate workability and packing density without excessive water demand.

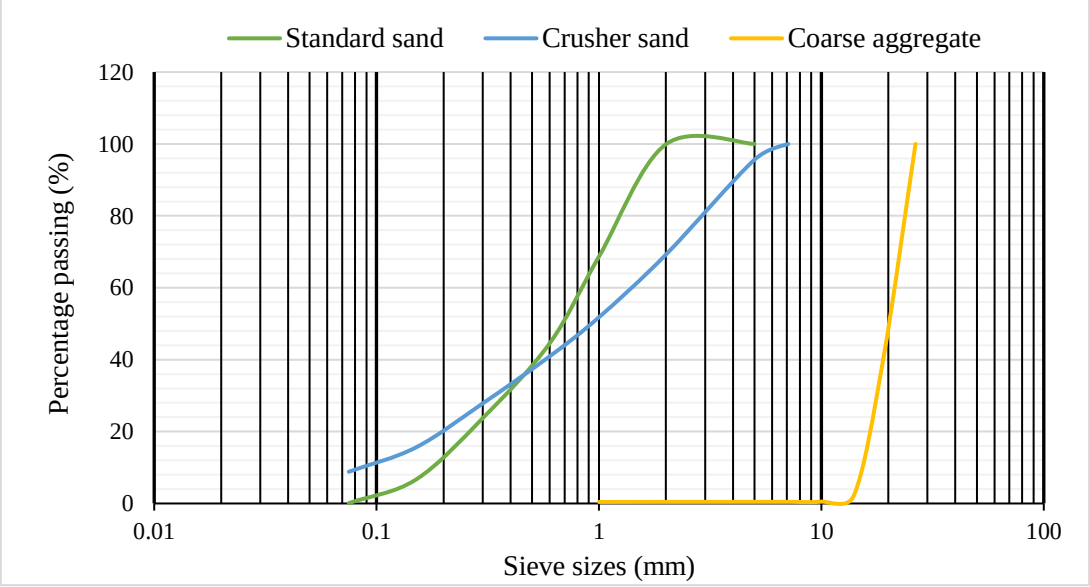

Fig. 3.5: Particle size distribution curves for fine and coarse aggregates

3.4.6 Coarse Aggregates

The particle size distribution is presented in Table A3, with the cumulative grading curve shown in Fig. 3.5. According to Table A3, only 40.38% of the sample passes the 19 mm sieve (59.62% is retained), which is well below the SANS 1083 (2013) target range of 85 – 100% passing at this size. Likewise, only 2.23% passed the 14 mm sieve compared with the required 15 – 55%, indicating a pronounced gap-graded distribution dominated by coarse particles. Such gradation reduces packing efficiency and interparticle contact, increases void content and can adversely affect fresh-state properties (workability and cohesion) and hardened properties unless corrected (for example by blending with finer material or adjusting aggregate grading).

Despite this, the crusher sand used as fine aggregate contained a slightly higher proportion of fines (Section 3.4.5), which likely helped offset the coarse aggregate gap by improving particle packing and reducing voids in the matrix. The coarse aggregate also exhibited favourable physical and mechanical properties, including a specific gravity of 2.65, compacted bulk density of 1500 kg/m^3, water absorption of 0.5%, aggregate crushing value of 21.7%, elongation index of 12.6%, flakiness index of 26.23% and fineness modulus of 6.55. The angular shape and rough surface texture of the granite further contributed to strong mechanical interlock and improved bond with the geopolymer binder.

3.4.7 Reinforcing Steel Bars

The tensile properties of the deformed reinforcing steel bars are summarized in Table 3.2. The 8 mm bars exhibited higher yield strength but lower ductility (~518 MPa and 10.5% elongation at failure) compared to the 10 mm bars (~402 MPa and 12.3%). Based on SANS 920 (2011) classification, the 8 mm bars satisfy the requirements for high-yield reinforcement (Grade 500), while the 10 mm bars fall below the minimum characteristic yield strength of 450 MPa required for high-yield steel and are therefore more consistent with lower-grade reinforcement (approximately Grade 400). Despite this variation, both bar sizes satisfied the SANS 920 (2011) requirement that the ultimate tensile strength must be at least 15% greater than the yield strength. In addition, both bars exceeded the minimum elongation requirement of 10%, confirming adequate ductility. (10.5% and 12.3%, respectively). The observed cup-and-cone fracture pattern presented in Fig. 3.6 further confirms ductile behaviour. Thus, the reinforcement exhibited sufficient mechanical performance for use in the GPC beams, with the 8 mm bars providing higher strength capacity and the 10 mm bars contributing improved ductility.

Table 3.2: Tensile properties of 8 mm and 10 mm reinforcing bars

Parameter	Unit	8 mm rebar (avg.)	10 mm rebar (avg.)
Yield strength (fy)	MPa	518.28	401.63
Ultimate tensile strength (fu)	MPa	669.64	545.33
Young's modulus (E)	GPa	193.12	161.18
Elongation at fracture (Ɛu)	%	10.46	12.28
Yield ratio (fy/fu)	–	0.774	0.736
Failure mode	–	Cup-and-cone	Cup-and-cone

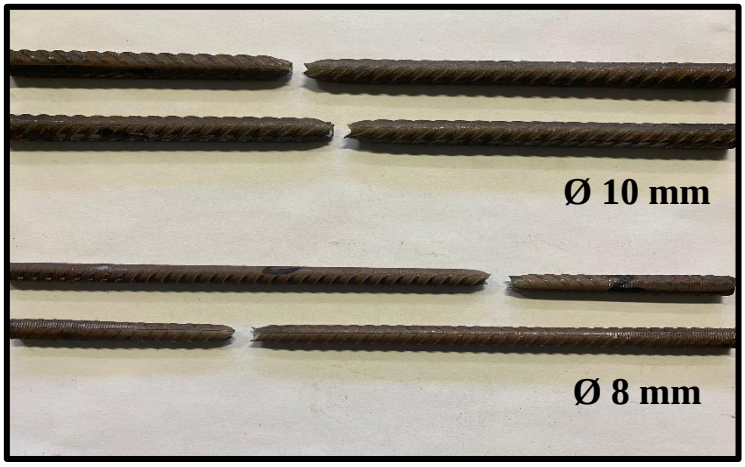

Fig. 3.6: Typical cup-and-cone failure observed in reinforcing bars after tensile testing

3.5 Mix Design Development and Optimization

3.5.1 Positioning This Study Within Existing Mix Design Frameworks

Developing a robust and adaptable mix design methodology is essential for ensuring the performance, consistency and scalability of geopolymer systems. Unlike Portland cement materials, geopolymers are governed by complex interactions between aluminosilicate precursors and alkaline activators, with the type, composition and concentration of constituents directly influencing fresh and hardened properties (Kolade et al., 2025a, 2025c). As highlighted in Section 2.5, previous GPC mix design approaches, such as those presented by Alaneme et al. (2024), Lloyd and Rangan (2010), Patankar et al. (2015) and Reddy et al. (2018), have contributed significantly to understanding proportioning strategies. However, these methods often rely on empirical strength-based procedures or modified PCC-derived approaches and

rarely incorporate detailed chemical composition analysis, reactivity profiling or adaptable proportioning mechanisms suitable for diverse precursors and sustainability targets.

The present study addresses these gaps by developing a composition and performance-driven mix design framework tailored to the use of commercial and alternative activators. The framework integrates stoichiometric molar ratios with empirical performance metrics to ensure chemical coherence while optimizing mechanical and durability properties. Key variables, such as AL/B, SiO_2/Al_2O_3, SiO_2/Na_2O, H_2O/Na_2O, W/G_s and the fly ash/GGBFS ratio, were systematically varied to achieve balanced fresh and hardened properties suitable for structural-grade GPC.

To operationalize this approach, seven mortar mixes were initially developed to examine how compositional variations influence compressive strength, flexural strength, workability and water absorption. Based on these preliminary results, the formulations were narrowed to four optimized mixes and subsequently upscaled to concrete level for structural testing. Comparative studies were carried out by preparing control mixes with CSS and test mixes with the alternative activators, enabling direct assessment of the alternative activators as being sustainable within an optimized design framework.

3.5.2 Framework for Mix Design Development

The mix design framework adopted in this study builds on established principles while introducing a more structured, quantitative approach to geopolymer proportioning. Foundational methodologies by Davidovits (1991), Hardjito and Rangan (2005) and Wallah and Rangan (2006) emphasized the role of aluminosilicate reactivity, oxide balance and activator characteristics in governing geopolymer performance. Later works, including Sathonsaowaphak et al. (2009), Lloyd and Rangan (2010) and Naghizadeh and Ekolu (2019), further highlighted the importance of ratios such as AL/B, SS/SH, SiO_2/Al_2O_3, H_2O/Na_2O, Na_2O/SiO_2 and W/G_s in mix optimization.

While these frameworks established important conceptual guidelines, many presented the parameters descriptively or empirically, with limited procedures for calculating them or integrating them into a sequential design process. The present study advances previous approaches by developing a twelve-step, equation-based methodology that translates established ratios into a quantifiable, replicable and logically ordered design pathway. The framework progresses from raw material characterization to compositional balancing, molar

ratio control and iterative performance optimization, ensuring coherence between chemical design and engineering requirements. As such, this structured formulation consolidates existing knowledge while providing a practical implementation route, especially for systems incorporating alternative activators. It also offers transparency, repeatability and adaptability that are key attributes required for advancing geopolymer mix design beyond empirical adjustments and toward a chemistry-grounded engineering methodology.

Seven geopolymer mortar mixes were developed based on the twelve-step, equation-based methodology, with varying fly ash-to-GGBFS ratios of 1:0, 7:1, 3:1, 1:1, 1:3, 1:7 and 0:1. These ratios were selected to systematically investigate the influence of calcium content on geopolymer performance by spanning the full compositional range from low-calcium (fly ash-dominated) to high-calcium (GGBFS-dominated) systems, which is known to significantly influence reaction mechanisms and strength development. The inclusion of intermediate ratios also enabled identification of optimal binder synergy and performance thresholds. The detailed mix design procedure for the 7:1 fly ash-to-GGBFS ratio is presented below.

Step 1: Analysis of oxide Composition

The total oxide compositions of the fly ash and GGBFS employed in this study are already presented in Table 3.1. Although these compositions do not distinguish between the reactive (amorphous) and non-reactive (crystalline) fractions, potentially affecting the accuracy of calculated ratios such as SiO_2/Al_2O_3 and Na_2O/SiO_2, it remains a practical preliminary approach for compositional evaluation. Importantly, the mix design strategy adopted includes performance-based validation, allowing iterative refinement in response to actual material behaviour. This ensures that the framework remains flexible, reliable and suitable for a broad range of precursor materials. In addition, the alkaline activator system comprised a 12 M NaOH solution with a density of 1.38 g/mL and a CSS solution containing 10.6% Na_2O, 26.5% SiO_2 and 62.9% H_2O. Both activators were blended at an SS/SH ratio of 1.5.

Step 2: Definition of Binder-to-Sand Ratio

A binder-to-sand ratio of 1:3, in line with the SANS 6255 (2006) specification, was adopted, along with an AL/B ratio of 0.5. Based on these proportions, the mix comprised 450 g of binder and 1350 g of sand.

Step 3: Design of Binder Composition

As earlier established, the binder blend consisted of fly ash and GGBFS in a 7:1 ratio, initially corresponding to 393.75 g and 56.25 g, respectively. However, since the densities of these materials differ from the reference cement density of 3.14 g/cm^3 specified in SANS 6255 (2006), adjustments were required to maintain volume consistency. After accounting for these density variations, the corrected binder quantities were 296 g for fly ash and 53 g for GGBFS.

Step 4: Calculation of Alkaline Solution Composition

Using predetermined mass of binder (B), AL/B and SS/SH ratios, the required quantities of alkaline components were calculated with Eq. (3.1) – (3.3).

$$\text{Mass of alkaline solution} = \frac{\text{AL}}{\text{B}} \times \text{B} \tag{3.1}$$

$$\text{Mass of NaOH solution (SH)} = \frac{\text{mass of alkaline solution}}{\frac{\text{SS}}{\text{SH}} + 1} \tag{3.2}$$

$$\text{Mass of } Na_2SiO_3 \text{ solution (SS)} = \frac{\left(\frac{\text{SS}}{\text{SH}}\right) \times \text{mass of alkaline solution}}{\frac{\text{SS}}{\text{SH}} + 1} \tag{3.3}$$

Accordingly,

Mass of alkaline solution = 0.5 × 450 g = 225 g

$$\text{NaOH solution mass (SH)} = \frac{225\text{ g}}{1.5 + 1} = 90\text{ g}$$

$$\text{Sodium silicate solution mass (SS)} = \frac{1.5 \text{ x } 225\text{ g}}{1.5 + 1} = 135\text{ g}$$

Step 5: Preparation of Sodium Hydroxide Solution

Eq. (3.4) – (3.5) was applied to make NaOH solution with a target concentration SHconc.:

$$\text{NaOH solid mass} = \text{SH}_{\text{conc.}} \times \frac{\text{SH}}{\text{density of solution}} \times \text{NaOH molar mass (40 g/mol)} \tag{3.4}$$

$$\text{Water in NaOH solution } (W_{SH}) = \text{SH} - \text{NaOH solid mass} \tag{3.5}$$

Accordingly,

$$\text{NaOH solid mass} = \frac{12\text{ mol/L} \times 90\text{ g}}{1.38\text{ g/mL} \times 1000} \times 40\text{ g/mol} = 31.3\text{ g}$$

Water in NaOH solution (W_{SH}) = 90 g – 31.3 g = 58.7 g

Step 6: Determination of Total Water Content

Water content in the mix comes from NaOH (W_{SH}) and Na_2SiO_3 (W_{SS}) solutions and any extra water (W_{EX}) added. Suppose y% of the Na_2SiO_3 solution is water, then Eq. (3.6) – (3.7) was applied as follows:

$$\text{Water in } W_{SS} = \frac{y}{100} \times SS \tag{3.6}$$

$$\text{Total water } (W) = W_{SS} + W_{SH} + W_{EX} \tag{3.7}$$

Noting that 62.9% of the CSS solution is water, thus:

$$\text{Water in CSS solution } (W_{SS}) = \frac{0.629}{100} \times 135 \text{ g} = 84.92 \text{ g}$$

Total water in the mix (W) = $W_{SS} + W_{SH} + W_{EX}$ = 84.92 g + 58.7 g + 0 = 143.61 g

Step 7: Evaluation of SiO_2/Al_2O_3 ratio

This molar ratio governs the structural and durability performance of the aluminosilicate matrix. Eq. (3.8) – (3.13) was used to assess and tailor it.

$$SiO_2 \text{ moles in precursor} = \frac{\text{fraction of } SiO_2 \text{ in precursor}}{\text{molar mass of } SiO_2} \times \text{mass of precursor} \tag{3.8}$$

$$SiO_2 \text{ moles in } Na_2SiO_3 = \frac{\text{fraction of } SiO_2 \text{ in } Na_2SiO_3}{\text{molar mass of } SiO_2} \times \text{mass of } Na_2SiO_3 \tag{3.9}$$

$$\text{Total } SiO_2 = SiO_2 \text{ in precursor} + SiO_2 \text{ in } Na_2SiO_3 \tag{3.10}$$

$$Al_2O_3 \text{ moles in precursor} = \frac{\text{fraction of } Al_2O_3 \text{ in precursor}}{\text{molar mass of } SiO_2} \times \text{mass of precursor} \tag{3.11}$$

$$\text{Total } Al_2O_3 = Al_2O_3 \text{ in precursor} \tag{3.12}$$

$$SiO_2/Al_2O_3 = \frac{\text{Total } SiO_2}{\text{Total } Al_2O_3} \tag{3.13}$$

Accordingly,

$$SiO_2 \text{ moles in fly ash} = \frac{0.875 \times 0.5383}{60.08 \text{ g/mol}} \times 296 \text{ g} = 2.321 \text{ mol}$$

$$SiO_2 \text{ moles in GGBFS} = \frac{0.125 \times 0.3469}{60.08 \text{ g/mol}} \times 53 = 0.038 \text{ mol}$$

SiO_2 moles in Na_2SiO_3 = $\frac{0.265}{60.08\ \text{g/mol}} \times 135\ \text{g} = 0.595\ \text{mol}$

Total SiO_2 = 2.321 mol + 0.038 mol + 0.595 mol = 2.954 mol

Al_2O_3 moles in fly ash = $\frac{0.875 \times 0.3318}{101.96\ \text{g/mol}} \times 296\ \text{g} = 0.843\ \text{mol}$

Al_2O_3 moles in GGBFS = $\frac{0.125 \times 0.1737}{101.96\ \text{g/mol}} \times 53\ \text{g} = 0.011\ \text{mol}$

Total Al_2O_3 = 0.843 mol + 0.011 mol = 0.854 mol

SiO_2/Al_2O_3 = $\frac{2.954\ \text{mol}}{0.854\ \text{mol}} = 3.46$

Step 8: Calculation of W/Gs Ratio

This ratio affects workability, reaction kinetics and final properties and was computed via Eq. (3.14).

$$W/Gs = \frac{\text{Total water in the mix}}{\text{Mass of geopolymer solids}} \quad (3.14)$$

Accordingly,

Geopolymer solids (Gs) = binder + NaOH solids + (SS – W_{SS})

= (296 + 53) + 31.3 + (135 – 84.92) = 430.38 g

Water-to-geopolymer solids ratio (W/Gs) = $\frac{143.61\ \text{g}}{430.38\ \text{g}} = 0.33$

Step 9: Step 9: Verification of Na_2O/SiO_2 ratio

This ratio influences geopolymer reaction rate, microstructure and durability and was estimated using Eq. (3.15) – (3.20).

$$Na_2O \text{ moles in precursor} = \frac{\text{fraction of } Na_2O \text{ in fly ash}}{\text{molar mass of } Na_2O} \times \text{mass of precursor} \quad (3.15)$$

$$Na_2O \text{ moles in } Na_2SiO_3 = \frac{\text{fraction of } Na_2O \text{ in } Na_2SiO_3}{\text{molar mass of } Na_2O} \times \text{mass of } Na_2SiO_3 \text{ solution} \quad (3.16)$$

$$\text{Equivalent } Na_2O \text{ moles in NaOH solids} = \frac{\text{mass of NaOH solids}}{2 \times \text{molar mass of NaOH}} \quad (3.17)$$

Total Na_2O = Na_2O in precursor + Na_2O in Na_2SiO_3 + Equivalent Na_2O in NaOH solids (3.18)

Total SiO_2 = SiO_2 in precursor + SiO_2 in Na_2SiO_3 (3.19)

$$Na_2O/SiO_2 = \frac{\text{Total } Na_2O}{\text{Total } SiO_2} \quad (3.20)$$

Accordingly,

$$Na_2O \text{ moles in fly ash} = \frac{0.875 \times 0.0011}{61.98 \text{ g/mol}} \times 296 \text{ g} = 0.005 \text{ mol}$$

$$Na_2O \text{ moles in GGBFS} = \frac{0.125 \times 0.0026}{61.98 \text{ g/mol}} \times 53 \text{ g} = 0.0003 \text{ mol}$$

$$Na_2O \text{ moles in } Na_2SiO_3 = \frac{0.106}{61.98 \text{ g/mol}} \times 135 \text{ g} = 0.231 \text{ mol}$$

$$\text{Equivalent } Na_2O \text{ moles in NaOH solids} = \frac{31.3 \text{ g}}{2 \times 40 \text{ g/mol}} = 0.391 \text{ mol}$$

Total Na_2O = 0.005 mol + 0.0003 mol + 0.231 mol + 0.391 mol = 0.627 mol

Total SiO_2 = 2.454 mol

$$Na_2O/SiO_2 = \frac{0.627 \text{ mol}}{2.954 \text{ mol}} = 0.21$$

Step 10: Assessment of H_2O/Na_2O ratio

Closely linked with W/Gs, this ratio informs key behaviours such as setting time, strength and shrinkage. This ratio was determined using Eq. (3.21) – (3.27).

$$H_2O \text{ moles in } Na_2SiO_3 = \frac{\text{fraction of } H_2O \text{ in } Na_2SiO_3}{\text{molar mass of } H_2O} \times Na_2SiO_3 \text{ solution} \quad (3.21)$$

$$\text{Equivalent } H_2O \text{ moles in NaOH solids} = \frac{\text{mass of NaOH solids}}{2 \times \text{molar mass of NaOH}} \quad (3.22)$$

$$H_2O \text{ moles in NaOH solution} = \frac{\text{mass of water in NaOH solution}}{\text{molar mass of } H_2O} \quad (3.23)$$

$$H_2O \text{ moles in extra water} = \frac{\text{mass of extra}}{\text{molar mass of } H_2O} \quad (3.24)$$

Total H_2O = H_2O in Na_2SiO_3 + Equivalent H_2O in NaOH solids + H_2O in NaOH solution + H_2O in extra water (W_{EX}) (3.25)

Total Na_2O = Na_2O in precursor + Na_2O in Na_2SiO_3 + Equivalent Na_2O in NaOH (3.26)

$$H_2O/Na_2O = \frac{\text{Total } H_2O}{\text{Total } Na_2O} \quad (3.27)$$

Accordingly,

$$H_2O \text{ moles in } Na_2SiO_3 = \frac{0.629}{18.02 \text{ g/mol}} \times 135 \text{ g} = 4.712 \text{ mol}$$

$$\text{Equivalent } H_2O \text{ moles in NaOH solids} = \frac{31.3 \text{ g}}{2 \times 40 \text{ g/mol}} = 0.391 \text{ mol}$$

$$H_2O \text{ moles in NaOH solution} = \frac{58.7 \text{ g}}{18.02 \text{ g/mol}} = 3.257 \text{ mol}$$

Total H_2O = 4.712 mol + 0.391 mol + 3.257 mol = 8.361 mol

Total Na_2O = 0.627 mol

$$H_2O/Na_2O = \frac{8.361 \text{ mol}}{0.627 \text{ mol}} = 13.33$$

Step 11: Mixing, Casting and Curing

The mix constituents, including fly ash, GGBFS, activator and fine aggregates, were proportioned and mixed thoroughly to achieve a homogeneous blend. The fresh geopolymer mortar was then cast into moulds and cured under controlled thermal and ambient conditions. Detailed procedures for batching, mixing and curing are provided in Section 3.6.

Step 12: Performance Evaluation and Optimization

After curing, the mortar specimens were tested for mechanical and durability properties. Where performance targets were not achieved, key mix design parameters and chemical ratios were adjusted within recommended ranges for geopolymer systems, as reported in the literature (Alaneme et al., 2024, Jan et al., 2022; Kolade et al.,2025a) and summarized ed in Table 3.3. The optimization procedure involved:

i. Refinement of precursor blend proportions and/or NaOH concentration to enhance reactivity
ii. Adjustment of the W/Gs ratio to improve workability without compromising strength
iii. Fine-tuning of the AL/B ratio to balance reactivity and flowability

iv. Modification of the SS/SH ration to enhance strength development and microstructure

v. Iterative repetition of the process, with systematic documentation to identify an optimal and validated mix design

Table 3.3: Suggested ranges of key geopolymer mix design parameters (Alaneme et al., 2024; Jan et al., 2022; Kolade et al., 2025a)

Parameter	Recommended range	Role
AL/B	0.3 – 0.5	Controls workability and promotes adequate geopolymerization
SHconc.	8 – 16 M	Determines the alkalinity of the activator and influences precursor dissolution
SS/SH	0.4 – 2.5	Affects silicate structure, setting time and gel formation
W/Gs	0.2 – 0.3	Balances fresh workability with hardened strength and durability
SiO_2/Al_2O_3	2.5 – 4.5	Influences the degree of polymerization and mechanical performance
H_2O/Na_2O	12 – 17.5	Governs setting time, workability and long-term stability
Na_2O/SiO_2	0.12 – 0.28	Reflects system alkalinity and affects shrinkage, durability and gel structure

To further illustrate the structured sequence of the mix design process, a flowchart is presented in Fig. 3.7. The process is organised into three phases: Steps 1 – 6 define input parameters, Steps 7 – 10 serve as validation checks for key chemical ratios, and Steps 11 – 12 address practical implementation and performance evaluation. The flowchart also indicates feedback loops, highlighting which steps should be revisited when critical parameters deviate from their target ranges according to Table 3.3, thereby enabling an efficient and iterative optimization process.

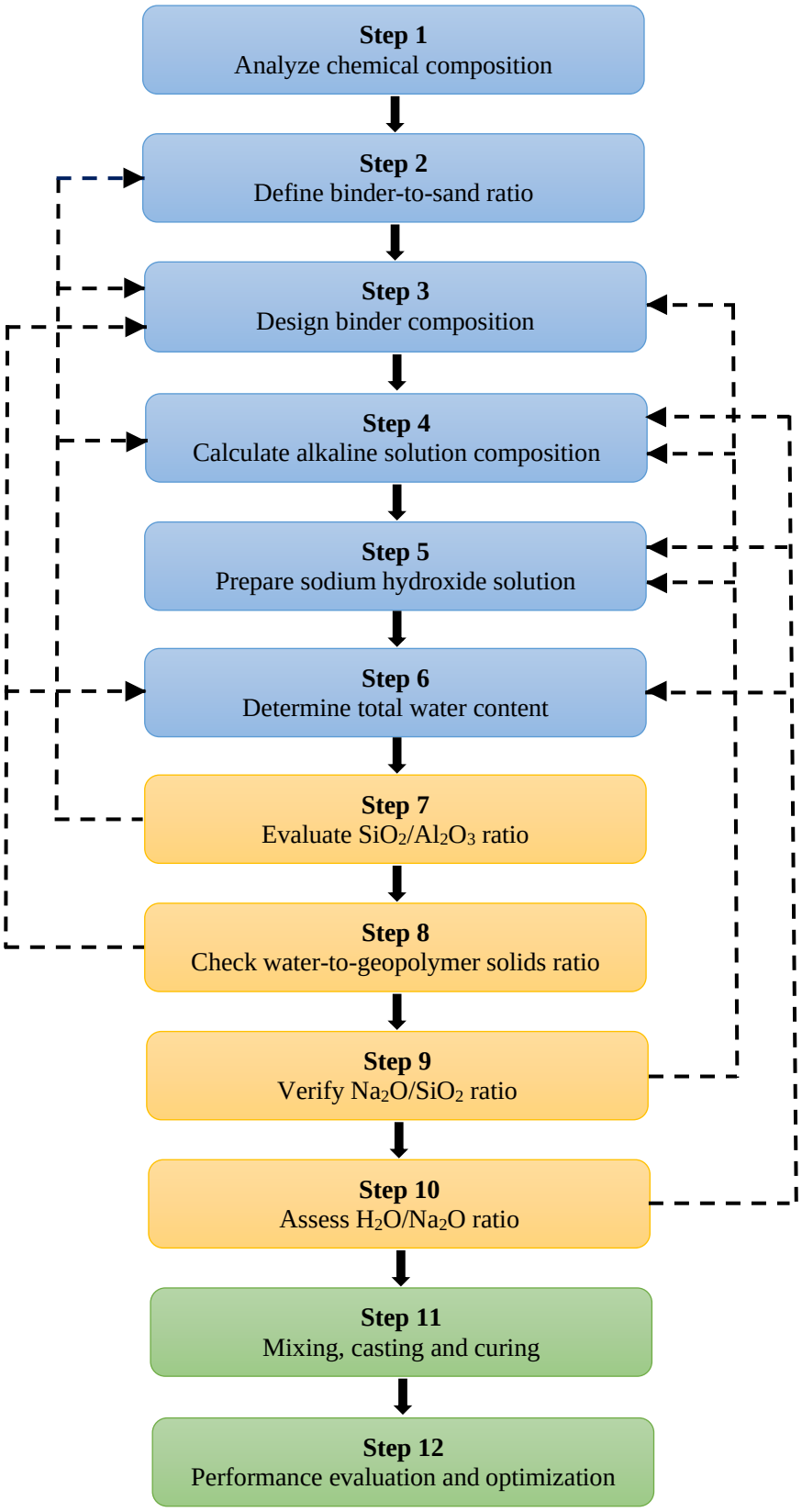

Fig. 3.7: Schematic representation of the geopolymer mix design process

3.6 Specimen Preparation

3.6.1 Mortar Specimens

Prior to specimen preparation, the alkaline activators (NaOH and CSS or WGSS) were prepared 24 hours ahead, following the two-part geopolymer formulation described in Section 3.1, to ensure complete dissolution, adequate cooling and chemical stability for consistent geopolymerization. On the casting day, the geopolymer mortar mixes were prepared and cast in accordance with SANS 5861-1 (2006). Initially, the precursors were blended for 30 seconds using a mechanical mixer at a low speed of 60 rpm. The alkaline solution was then added and mixing continued for an additional 60 seconds. Sand was gradually introduced into the mixture, followed by another minute of mixing. The mixer was paused for 30 seconds to scrape down the sides of the bowl, after which mixing resumed at a high speed of 120 rpm for one final minute.

The fresh mortar was poured into prism (40 × 40 × 160 mm) and cubic (40 × 40 × 40 mm) moulds, with three specimens cast per batch for each specimen type. All specimens were compacted using an automated vibrating table and left to set for 24 hours at ambient temperature. After demoulding, they were thermally cured in an oven at 80°C for 24 hours, followed by ambient curing at 23 ± 2°C for 3, 7 and 28 days prior to testing. Thermal curing at elevated temperature was adopted based on findings by Yılmaz et al. (2024) and Singh et al. (2022), which indicate that curing geopolymers between 50 – 90°C enhances early strength development by accelerating the geopolymerization process and promoting effective setting of the binder.

3.6.2 Concrete Specimens

The GPC mixes were also prepared and cast in accordance with SANS 5861-1 (2006). In this process, constituent materials, including the binder (fly ash and GGBFS), fine aggregates and coarse aggregates, were placed simultaneously into the mixing bowl of a mechanical mixer. The materials were first blended for 30 seconds, after which the alkaline activators were added and mixing continued at a low speed of 60 rpm for an additional 60 seconds. The mixer was then paused for 30 seconds to allow for scraping down the sides of the bowl, followed by a final 90 seconds of mixing.

The fresh concrete was cast into 100 × 100 × 100 mm cube moulds for compressive strength testing and 150 × 150 × 700 mm beam moulds for structural performance evaluation. All

specimens were compacted using an automated vibrating table and left to set for 24 hours at ambient temperature. After demoulding, the specimens were thermally cured in an oven at 80°C for 24 hours, then subjected to ambient curing at 23 ± 2°C for 7 and 28 days before testing.

3.7 Experimental Program

The experimental program comprised a series of tests aimed at evaluating the fresh, hardened and structural properties of the geopolymer mortar and concrete mixes. To clearly distinguish the different phases of the experimental program, specific mix designations were used at each stage of the study. In the preliminary mortar mix design investigation, mixes were labeled M1 – M7. During the evaluation of the synthesized WGSS, two selected formulations were denoted as Mix 1 and Mix 2. In the subsequent activator comparison stage, mortars were identified as Mix 1 – Mix 4, with the suffixes "C" and "GP" representing CSS-activated and WGSS-activated systems, respectively. Finally, the GPC mixes used for the mechanical and reinforced beam tests were designated M1 – M4. This notation system was adopted to distinguish clearly between the different experimental stages and material systems investigated. In addition, all tests were conducted in accordance with relevant South African National Standards (SANS) and international ASTM procedures to ensure methodological consistency and result reliability, as summarized in Table 3.4.

3.7.1 Fresh Property Tests

3.7.1.1 Consistency and setting times (paste)

The consistency and setting characteristics of the geopolymer paste were evaluated following the procedures outlined in SANS 50196-3 (2006). To determine consistency, the paste was tested with a Vicat apparatus and the quantity of alkali activator required to obtain a penetration depth of 6 ± 2 mm was established. The setting time was then assessed using pastes prepared at 0.85 of the identified consistency value. An automatic Vicat device recorded the penetration resistance at predetermined intervals, allowing the initial and final setting times to be established.

3.7.1.2 Flowability (mortar)

The flowability of the mortar was assessed using a flow table test following ASTM C1437 (2015). Fresh mortar was placed into the standard mould, which was then lifted vertically

before applying 15 drops of the flow table at the prescribed rate. The final spread diameter of the mortar was measured to provide an indication of its workability and ease of placement.

3.7.1.3 Workability (concrete)

Concrete workability was evaluated using the slump cone procedure described in SANS 5862-1 (2006). The cone was filled in three layers, with each layer compacted 25 times to ensure uniform consolidation. After lifting the mould vertically, the slump (the reduction in height of the concrete) was measured. This value was used to quantify plasticity and flow behaviours.

3.7.2 Hardened Property Tests

3.7.2.1 Density (mortar and concrete)

Density measurements were carried out in accordance with SANS 6251 (2006). At the designated curing ages, mortar and concrete specimens were weighed and their volumes were determined. Density was then calculated to assess the degree of compaction and the mass per unit volume of each mix.

3.7.2.2 Water absorption (mortar)

Water absorption testing followed the procedure specified in SANS 1058 (2012). Oven-dried mortar samples at 100 ± 5°C for 24 hours were immersed in water for 24 hours, after which the saturated surface-dry mass was recorded. The percentage increase in mass was used to estimate accessible porosity and the material's vulnerability to moisture ingress.

3.7.2.3 Compressive strength (mortar and concrete)

The compressive strength of mortar was determined using 40 × 40 × 40 mm cubes in accordance with SANS 50196-1 (2006). These cubes were subjected to uniaxial loading until failure and strength was computed from the maximum load. Concrete compressive strength testing was also performed on 100 × 100 × 100 mm cubes according to SANS 5863 (2006). Cubes were loaded monotonically to failure and the peak load was also used to calculate compressive resistance.

3.7.2.4 Flexural strength (mortar and concrete)

Flexural strength for mortar was measured using the 3-point bending method described in SANS 50196-1 (2006). Prisms (40 × 40 × 160 mm) were placed on two supports and loaded at

mid-span until rupture and the peak load was used to compute flexural strength. Concrete flexural strength was evaluated using 150 × 150 × 700 mm beams in accordance with SANS 5864 (2006), also tested under a 3-point bending configuration. Beams were loaded to failure and the bending stress at fracture was calculated.

3.7.2.5 Shear strength (concrete)

Shear strength was determined using the same 150 × 150 × 700 mm beam specimens tested under SANS 5864 (2006). The beams were loaded until diagonal cracking or shear failure occurred and the corresponding failure load was used to estimate their shear capacity.

Table 3.4: Summary of experimental tests and relevant standards

Test category	Test description	Applicable standard	Specimen type
Fresh properties	Consistency and setting times	SANS 50196-3 (2006)	Paste
	Flowability	ASTM C1437 (2015)	Fresh mortar
	Slump test (workability)	SANS 5862-1 (2006)	Fresh concrete
Hardened properties	Density (mortar and concrete)	SANS 6251 (2006)	All specimens
	Compressive strength	SANS 50196-1 (2006); SANS 5863 (2006)	Mortar prisms; concrete cubes
	Flexural strength	SANS 50196-1 (2006); SANS 5864 (2006)	Mortar prisms; reinforced concrete beams
	Shear strength	SANS 50196-1 (2006); SANS 5864 (2006)	Reinforced concrete beams
	Water absorption	SANS 1058 (2012)	Mortar prisms
Structural performance	Load–deflection response, flexural and shear capacities, cracking, failure modes	Custom setup (3-point bending)	Reinforced concrete beams
Reinforcement steel	Tensile strength	SANS 6892-1 (2010); SANS 920 (2011)	8 mm and 10 mm steel bars

3.7.3 Structural Performance Tests

The structural behaviour of the reinforced GPC beams was evaluated under a three-point bending configuration to simulate combined flexural and shear loading. Testing was carried out using a 300 kN capacity flexural testing machine, where monotonic loading was applied at mid-span at a constant rate of 0.03 MPa/s until failure (Fig. 3.8). This setup enabled a comprehensive assessment of both the mechanical response and the failure characteristics of beams produced with CSS and WGSS activators. During testing, several structural performance indicators were monitored, including the first-crack load, ultimate load capacity and mid-span deflection at failure. Crack initiation and propagation patterns were also recorded throughout the loading process to provide additional insight into the ductility and structural integrity of the beams. Afterwards, the final failure mode was documented to distinguish between flexural, shear or combined mechanisms. Collectively, these measurements enabled a robust comparison of the structural performance of the different geopolymer beam systems.

Fig. 3.8: Experimental setup for beam testing

For this evaluation, beams produced from WGSS-based mixes reaching a target 28-day compressive strength of 40 MPa were compared with a control CSS mix. In total, 24 beams (150 × 150 × 700 mm) were cast for the three mixes investigated, with each mix tested at two ages (7 and 28 days). At each testing age, two structural behaviours (flexure and shear) were examined and two identical specimens were prepared for each test type to ensure repeatability. This provided four beams per mix per testing day (2 flexural + 2 shear). Consequently, each testing age involved 12 beams across the three mixes, giving a total of 24 beams.

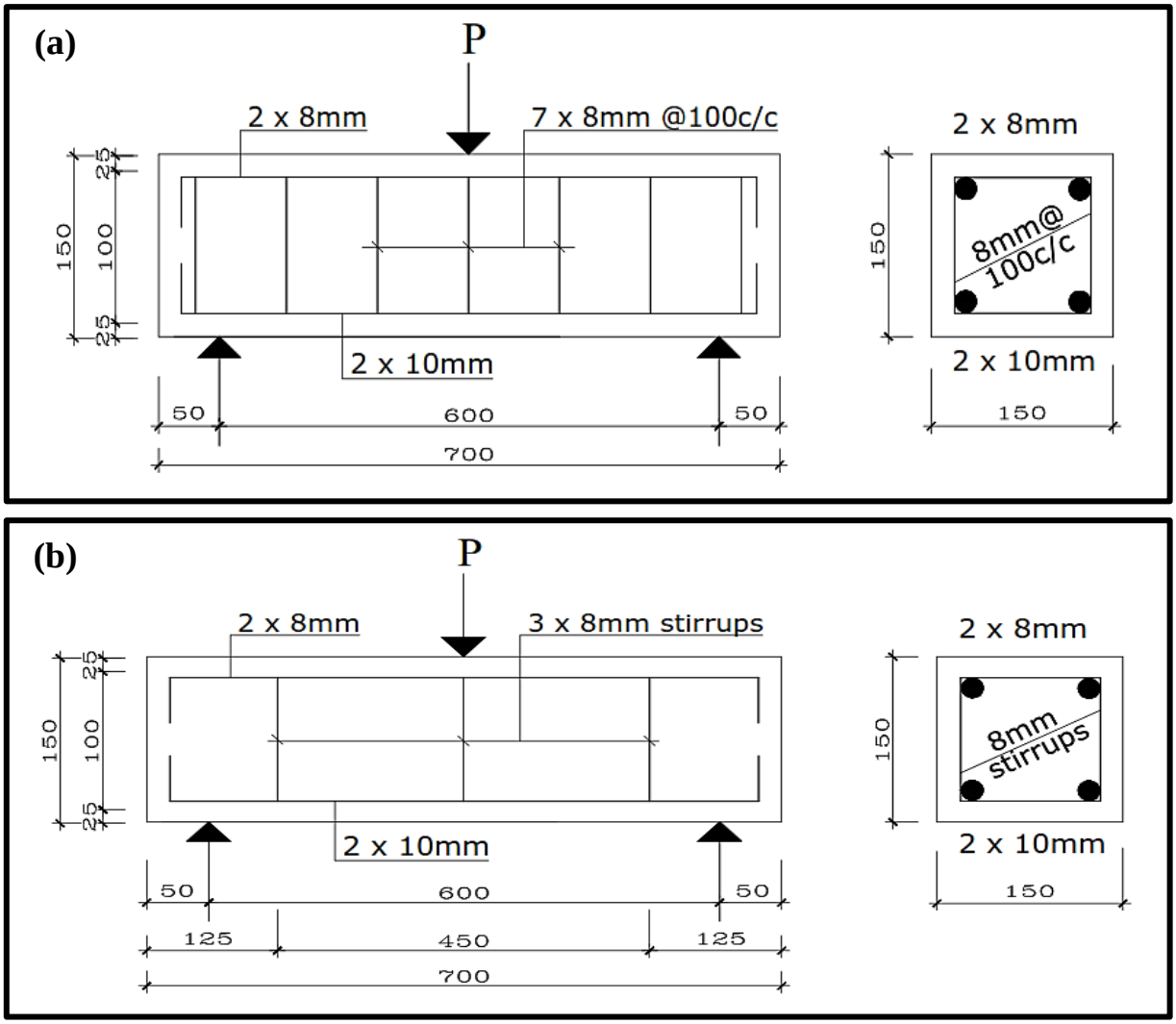

Fig. 3.9: Reinforcement arrangement and beam designs for (**a**) flexural failure (**b**) shear failure

The reinforcement configurations adopted to promote flexural and shear failure are illustrated in Fig. 3.9. For the flexural-failure specimens shown in Fig. 3.9a, the beams were reinforced with two 10 mm diameter bottom bars and two 8 mm diameter top bars, together with 8 mm diameter stirrups placed at 100 mm centres throughout the span. This configuration ensured

sufficient shear capacity so that failure would be dominated by flexure. For the shear-failure specimens, the same longitudinal reinforcement was used. However, the transverse reinforcement was intentionally reduced by providing only three 8 mm diameter stirrups positioned at specific locations along the span, as shown in Fig. 3.9b. This discontinuous and sparse arrangement of shear links was designed to lower the shear resistance of the beam and thereby promote shear-dominated failure. The distinction between Fig. 3.9a and Fig. 3.9b is therefore primarily in the amount and distribution of the stirrups, which is uniform and closely spaced in the flexural specimens but minimal and strategically placed in the shear specimens. This set-up ensures clear differentiation in structural behaviour and supports the intended failure modes.

In addition, all reinforcement consisted of deformed steel bars, with their tensile and yield strengths provided in Table 3.2 (Chapter 3). The reinforcement layouts were selected in accordance with conventional reinforced concrete design principles for under-reinforced sections, following Eurocode 2 (EN 1992-1-1, 2004), to ensure ductile flexural failure rather than brittle compression failure under bending. Based on the beam geometry, the concrete strengths (~40 MPa for the WGSS mixes M3 and M4 and ~90 MPa for the CSS control mix M1) and the yield strength of the 10 mm tension bars (~400 MPa), the corresponding under-reinforced ranges of reinforcement ratio (ρ) determined using Eurocode 2 (Eqs. (3.28) – (3.30)) are 0.23 – 4.11% for the WGSS mixes and 0.39 – 9.14% for the CSS control mix. The beams in this study provided a reinforcement ratio of $\rho = 0.87\%$, calculated from the tension steel area (157.1 mm^2), a beam width of 150 mm and an effective depth of 120 mm (150 mm overall depth minus a 25 mm cover and half the 10mm bar diameter). This value lies comfortably within the under-reinforced limits for both mixes, confirming that flexural behaviour would govern as intended. This was further confirmed by the computed yield strain (ε_y) of the tension reinforcement (0.002), obtained using Eq. (3.31), which is lower than the typical ultimate concrete strain (ε_{cu}) of 0.0035 and 0.0026 for normal and high-strength concretes, respectively, specified in Eurocode 2 (EC2). This indicates that the sections were ductile (tension-controlled), as the reinforcement would yield before the concrete reached its crushing strain. Furthermore, the percentage of longitudinal reinforcement provided (0.70%) relative to the gross concrete cross-section (150 mm × 150 mm) satisfies the requirements of SANS 10100-1 (2000), which prescribes a minimum of 0.13% and a maximum of 4% for beams of this size, thereby confirming compliance with both EC2 and SANS 10100-1 design provisions.

$$\text{Reinforcement ratio } (\rho) = \frac{A_s}{bd^2} \tag{3.28}$$

$$\rho_{max} = 0.53 \frac{f_{cd}}{f_{sd}} \text{ (using x/d max = 0.53 for steel grade 400 MPa)} \tag{3.29}$$

$$\rho_{min} = 0.26 \frac{f_{ctm}}{f_{yk}} \tag{3.30}$$

$$\text{Steel yield strain } (\varepsilon_y) = \frac{f_{yk}}{E_s} \tag{3.31}$$

Where: ρ = reinforcement ratio, A_S = tensile steel area; b = beam width; d = effective depth; x = neutral axis depth; $f_{cd} = f_{ck}/\gamma_c$; $f_{sd} = f_{yk}/\gamma_s$; $f_{ctm} = 0.3(f_{ck}^{2/3})$; f_{yk} = steel yield strength; f_{ck} = concrete strength; γ_c = concrete material factor (1.5); γ_s = steel material factor (1.15); E_s = steel young's modulus (200,000 MPa).

During testing, the beams were supported over an effective span of 600 mm, leaving a clear space of 50 mm at each end. A point load was then applied at the middle of the beams which is 300 mm from each support. Applied loads were recorded in kN using the testing machine, while mid-span deflection was measured using a digital dial gauge with a least count of 0.1 mm. The deflection readings were taken at the point of ultimate load (failure) and the corresponding mid-span deflection values were recorded for each beam. As such, the reported deflection values represent peak deformation at failure instead of a continuous load–deflection response. Crack initiation and propagation were also closely monitored using magnification and directed lighting until failure. Thus, the evaluation focused on load-carrying capacity, deflection behaviour, crack development and the resulting failure modes. In addition, it is important to note that strain measurements were not recorded because a UTM equipped with strain-measuring instrumentation like linear variable differential transformers (LVDTs) or strain gauges was not available for the structural performance tests.

3.8 Data Analysis and Statistical Evaluation

Descriptive and inferential statistical methods were employed in this study to derive meaningful insights from the experimental results and to evaluate the significance of observed trends. This multi-level approach enabled exploratory data summarization and rigorous hypothesis testing to ensure reliable interpretation of performance differences across the various GPC mixes based on statistically significant evidence. All statistical analyses were

performed using IBM SPSS Statistics to ensure robustness in hypothesis testing and data interpretation, while graphical representations, trend analyses and regression plots were generated using OriginPro to facilitate high-quality data visualization and enhanced interpretation of results. The specific statistical methods applied are briefly described in the subsequent sub-sections.

3.8.1 Descriptive Statistics

Basic statistical measures, including mean, standard deviation (SD), minimum and maximum, were computed for each performance parameter. These provided a quantitative summary of the data distribution, variation and central tendencies for both mortar and concrete samples across different mix formulations.

3.8.2 Inferential Statistics

To test the statistical significance of differences between mix groups and to evaluate the impact of specific variables, the following inferential tools were applied in accordance with established analytical procedures as outlined by Diener (2010) and Field (2024).

3.8.2.1 Independent samples T-tests

This was conducted to compare mean differences between mixes activated with CSS and those activated with synthesized WGSS. The resulting p-value (p) indicates the probability that the observed difference occurred by chance under the null hypothesis. Therefore, a significance threshold of $p < 0.05$ was adopted. To complement statistical significance and assess the practical relevance of differences, effect size was determined using Cohen's d. Accordingly, the t-statistic and effect size (d) were calculated using Eqs. (3.32) and (3.33).

$$t = \frac{\ddot{X}_1 - \ddot{X}_2}{\sqrt{\frac{{S_1}^2}{n_1} + \frac{{S_2}^2}{n_2}}} \tag{3.32}$$

Where: $\ddot{X}_1$ = group mean of CSS mixes, $\ddot{X}_2$ = group mean of synthesized WGSS mixes, ${S_1}^2$ = variance of CSS mixes, ${S_2}^2$ = variance of synthesized WGSS mixes, n_1, n_2 = number of samples in each group (both equal to 4)

$$d = \frac{\ddot{X}_1 - \ddot{X}_2}{s_p} \tag{3.33}$$

where: $S_p = \sqrt{\frac{(n_1 - 1)\, S_1^{\,2} + (n_2 - 1)\, S_2^{\,2}}{n_1 + n_2 - 2}}$

The pooled standard deviation (S_p) provides a weighted estimate of variability across both groups.

3.8.2.2 ANOVA

This was applied to assess the influence of mix composition on workability and mechanical outcomes across more than two groups. One-way ANOVA helped determine whether observed differences were likely due to the variable of interest rather than random variation. Accordingly, the total sum of squares (SS_{total}), sum of squares between groups ($SS_{between}$), sum of squares within groups (SS_{within}), mean square for treatment (MST), mean square for error (MSE), F-statistic and effect size (eta-squared = η^2) were calculated using Eqs. (3.34) – (3.40).

$$SS_{total} = \sum (X_{ij} - \ddot{X})^2 \tag{3.34}$$

$$SS_{between} = \sum n_i(\ddot{X}_i - \ddot{X})^2 \tag{3.35}$$

$$SS_{within} = \sum (X_{ij} - \ddot{X}_i)^2 \tag{3.36}$$

$$MST = \frac{SS_{between}}{df_{between}} \tag{3.37}$$

$$MSE = \frac{SS_{within}}{df_{within}} \tag{3.38}$$

$$F = \frac{MST}{MSE} \tag{3.39}$$

$$\eta^2 = \frac{SS_{between}}{SS_{total}} \tag{3.40}$$

Where: n_i = number of observations in group i, X_{ij} = the j-th observation within group i, $\ddot{X}_i$ = mean of group i, $\ddot{X}$ = mean of all observations, df = degrees of freedom; $SS_{total} = SS_{between} + SS_{within}$; η^2 close to 1 = strong effect with most variation due to treatment; η^2 close to 0 = weak effect with most variation due to random/error

3.8.2.3 Tukey's Honest Significant Difference (HSD) post-hoc test:

This was conducted post-ANOVA via Eq. (3.41) when significant differences were found, this test identified which specific group pairs differed significantly. This was critical in identifying the optimal mix configurations from a performance standpoint.

$$\text{Tukey's HSD} = q \cdot \sqrt{\frac{MS_{within}}{n}} \tag{3.41}$$

where: q = studentized range statistic; MS_{within} = mean square within groups; n = sample size per group (or harmonic mean if unequal)

3.9 Sustainability and Economic Assessment

To evaluate the environmental and economic sustainability of the GPC produced with WGSS as a substitute for CSS, an MS Excel-based life cycle inventory (LCI) tool was employed. The assessment was guided by the principles outlined in ISO 14040 (2006), encompassing four main phases, including goal and scope definition, inventory analysis, impact assessment and result interpretation. The system boundary adopted was cradle-to-site, covering raw material extraction, processing, alternative activator synthesis and transportation of all materials to the point of concrete production at the UNISA Science Campus, Florida, Johannesburg. The functional unit was also defined as 1 cubic meter (1 m^3) of fresh GPC, allowing consistent performance and impact comparisons across all mix designs (Oyebisi et al., 2022). Input parameters included the quantities and types of raw materials used, energy required for WGSS synthesis and curing and transportation distances. Output data consisted of CO_2 emissions and resource consumption metrics, which were subsequently used for calculating environmental impacts and sustainability indicators.

To provide a holistic view of GPC sustainability, the study computed several environmental and economic metrics. Transportation impact was assessed to quantify the emissions and energy associated with transporting raw materials to the production site. The global warming potential of each mix was calculated to determine the total greenhouse gas emissions expressed in CO_2 equivalents over the lifecycle of the material. The mixes were further evaluated in terms of embodied energy, representing the cumulative energy required to produce, process and deliver all material constituents. A sustainability index was then derived as a normalized metric integrating compressive strength, global warming potential and embodied energy, allowing each mix to be ranked from a sustainability perspective. Economic performance was as well

assessed using an economic index, which compared material input costs relative to mechanical performance outputs. In addition, the CO_2 abatement cost was calculated to reflect the economic cost of reducing one kilogram of CO_2 emissions when substituting CSS with WGSS as the activator. Together, these indicators enabled the identification of trade-offs between structural performance, environmental footprint and economic viability, facilitating a balanced and evidence-based material selection strategy for sustainable construction applications. This multi-criteria assessment complements the mechanical testing results and reinforces the study's overarching aim of advancing the practical, scalable adoption of WGSS in GPC production in resource-constrained contexts.

CHAPTER 4

4 TRIAL MIX RESULTS AND ANALYSIS

Preliminary mix formulation for geopolymer mortars activated with NaOH and CSS was carried out using the composition and performance-driven framework presented in Section 3.5.2. Accordingly, the key mix design parameters for the seven trial formulations discussed in the section were computed and are summarized in Table 4.1. A comparative evaluation against recommended ranges reported in the literature is also provided in Table 4.2. From Table 4.2, it can be deduced that the close agreement between the calculated parameters and established benchmark values indicates that the mixes were well-designed and chemically coherent. This alignment suggests that the selected proportions are practically viable and capable of achieving the intended mechanical and durability performance, a conclusion further supported by the subsequent fresh and hardened property results obtained for the mortar mixes.

Table 4.1: Computed mix design parameters for geopolymer mortars

Mix ID	Sand (g)	FA:GGBFS ratio	Fly ash (g)	GGBFS (g)	SP (g)	SiO_2/Al_2O_3	Na_2O/SiO_2	H_2O/Na_2O	W/Gs
M1	1350	1 : 0	338	0	–	3.29	0.17	13.31	0.34
M2	1350	7 : 1	296	53	–	3.46	0.21	13.33	0.33
M3	1350	3 : 1	254	105	–	3.69	0.26	13.34	0.33
M4	1350	1 : 1	169	209	–	4.32	0.32	13.31	0.31
M5	1350	1 : 3	84	314	22.5	4.56	0.30	13.22	0.30
M6	1350	1 : 7	42	367	22.5	4.43	0.25	13.15	0.29
M7	1350	0 : 1	0	418	22.5	4.23	0.21	13.07	0.29

Table 4.2: Comparison of designed mix parameters with recommended ranges from literature (Alaneme et al., 2024; Jan et al., 2022; Kolade et al., 2025a)

Parameter	Designed mixes	Range	Remarks
AL/B	0.5	0.3 – 0.5	Lies at the upper bound of the typical range, promoting high reactivity but may require careful control of workability, particularly in low-water systems.
SHconc.	12 M	8 – 16 M	Falls within optimal limits, ensuring sufficient dissolution of aluminosilicates and effective activation.
SS/SH	1.5	0.4 – 2.5	Well within the conventional range, supporting balanced silicate availability for geopolymer gel formation.
W/Gs	0.29 – 0.34	0.2 – 0.3	Slightly exceeds the typical limit in some mixes, but remains close enough to preserve performance and workability without significant compromise.
SiO_2/Al_2O_3	3.29 – 4.56	2.5 – 4.5	Mostly within recommended bounds, enhancing mechanical strength and chemical stability.
H_2O/Na_2O	13.07 – 13.34	12 – 17.5	Comfortably within optimal range, supporting stable reaction kinetics and reducing likelihood of alkali leaching or efflorescence.
Na_2O/SiO_2	0.17 – 0.32	0.12 – 0.28	Slightly exceed the upper limit, potentially accelerating reaction but warranting monitoring for rapid setting or shrinkage.

4.1 Computed Mix Design Parameters

The trial mixes exhibited clear and systematic compositional variations driven primarily by changes in the fly ash–to–GGBFS ratio. As summarized in Table 4.1, the SiO_2/Al_2O_3 ratio increased progressively from M1 (3.29) to M5 (4.56), reflecting the increasing substitution of aluminosilicate-rich fly ash with silica and calcium-rich GGBFS. Beyond M5, a slight reduction was observed in M6 and M7, likely due to the diminishing contribution of reactive silica relative to calcium at very high GGBFS contents. This behaviour is consistent with the known chemical disparity between the two precursors. Furthermore, a relatively low W/Gs ratio (0.29 – 0.34) was consistently maintained across all mixes to restrict activator dilution and promote higher early-age geopolymerization, an approach aligned with the

recommendations of Albidah et al. (2021). The controlled W/Gs ratio also ensured that variations in fresh and hardened behaviour could be more directly attributed to precursor composition rather than water content.

The Na_2O/SiO_2 ratios across the mixes also generally remained within the optimal range reported in the literature for stable geopolymerization (Alaneme et al., 2024). Notably, the ratio increased from M1 (0.17) to M4 (0.32), after which it decreased toward M7 (0.21). This shift reflects the dual influence of precursor chemistry and activator distribution, as initial increases enhance the alkalinity required for dissolution, but excessively high GGBFS content reduces the relative amount of silica available, thereby lowering the ratio despite constant activator mass (Kolade et al., 2025a; 2025c). In addition, the H_2O/Na_2O ratio remained tightly controlled, varying only slightly from 13.31 in M1 to 13.07 in M7. Although the numerical range is narrow, such small variations can still influence ion mobility, reaction kinetics and gel formation (Luan et al., 2021). The gradual reduction with increasing GGBFS content suggests a reduced water availability per unit of alkali, which may have implications for the development of reaction products in calcium-rich systems.

It is also important to note that the introduction of superplasticizer (SP) in M5 – M7 represents a compositional change driven not by the framework's calculated ratios but by the practical need to offset the workability challenges presented by high-GGBFS mixes. Although the SP helped improve flow, its presence has implications for subsequent microstructural development and was therefore considered carefully in the interpretation of hardened results. Altogether, the mix design parameters reveal coherent trends that provide an important foundation for explaining the subsequent fresh and hardened behaviour of the geopolymer mortars. These parameter variations capture the evolving chemical environment of the system and enable a clear link between precursor composition and performance outcomes.

4.2 Fresh Properties of Mortars

As presented in Table 4.3, flowability reduced progressively with increasing GGBFS content, which can be attributed to the typically higher angularity and finer surface texture of GGBFS particles compared to fly ash. Although specific surface area and particle morphology were not directly measured in this study, previous investigations (Hu et al., 2019; Mo et al., 2017) have reported that GGBFS generally exhibits a rougher, more irregular shape and a higher specific surface area in the range of 400 – 600 m^2/kg. These characteristics increase interparticle friction and water demand, thereby reducing workability in geopolymer mixes. In parallel, the

relatively low W/Gs ratio across all mixes limited the amount of free water available for particle lubrication during mixing, thereby intensifying the workability challenges observed in the high-GGBFS formulations. Likewise, although the Na_2O/SiO_2 ratios remained within recommended limits to ensure stable geopolymerization, they offered little compensatory benefit in mitigating the reduction in flow associated with increasing GGBFS content. To counter these combined chemical and physical effects, a SP dosage of 5% (relative to a 450 g cement reference) was introduced in M5 – M7. The SP improved workability by dispersing densely packed particles, although this adjustment later contributed to modest strength reductions due to steric hindrance of reactive sites (Anudeep et al., 2024). The transition from mixes without SP to those with SP highlights how flow behaviour is not only affected by precursor chemistry but also by strategic modification of key mix-design parameters.

The influence of precursor composition was similarly reflected in density and water absorption trends. Density increased from 2117 kg/m^3 (M1) to 2220 kg/m^3 (M7), which corresponds to the increasing replacement of lower-specific-gravity fly ash with denser GGBFS (Hu et al., 2019). This trend is also consistent with the observed reduction in H_2O/Na_2O ratios (13.31 in M1 to 13.07 in M7), which supported lower porosity and enhanced matrix compaction. Consequently, water absorption values for all mixes remained below the SANS 1058 (2012) upper limit of 6.5%, with GGBFS-rich blends displaying the lowest absorption that is attributable to denser microstructural packing and reduced pore continuity. It can, therefore, be inferred from the fresh property results that the rheology of geopolymer mortars is governed by an interconnected influence of precursor chemistry, computed mix composition parameters and rheological modifiers.

Table 4.3: Summary of average properties and standard deviation of mortar mixes

Mix ID	Density (kg/m^3)	Flow (%)	Water absorption (%)
M1	2117 ± 2.71	145 ± 0.47	4.6 ± 0.07
M2	2159 ± 3.01	140 ± 1.00	5.2 ± 0.14
M3	2182 ± 2.45	120 ± 0.47	5.3 ± 0.10
M4	2214 ± 2.78	90 ± 0.50	5.4 ± 0.03
M5	2138 ± 4.29	90 ± 1.00	4.5 ± 0.20
M6	2153 ± 2.15	80 ± 0.47	4.8 ± 0.06
M7	2220 ± 3.08	70 ± 0.50	4.9 ± 0.14

4.3 Hardened Properties of Mortars

The hardened performance results presented in Fig. 4.1 further demonstrate the interconnected effects of precursor composition and mix design parameters on the mechanical behaviour of the geopolymer mortars. As expected, both compressive and flexural strengths increased with curing age across all mixes, reflecting normal progression of geopolymerization. However, the magnitude of strength development varied markedly with changes in the fly ash–to–GGBFS ratio and accompanying shifts in chemical parameters such as SiO_2/Al_2O_3 and Na_2O/SiO_2.

The highest strengths were obtained for M1 (the fly ash-only mix) that achieved 68.25 MPa compressive strength and 9.63 MPa flexural strength at 28 days. This superior performance is attributable to its balanced SiO_2/Al_2O_3 ratio (3.29), moderate Na_2O/SiO_2 ratio (0.17) and stable H_2O/Na_2O value (13.31), which collectively promote extensive polymeric network formation. These conditions are known to favour the development of polymeric type gels and a continuous three-dimensional aluminosilicate matrix, which are characteristic of high-strength fly ash-based geopolymers (Hu et al., 2019). Conversely, mixes with high GGBFS contents (M5 – M7) exhibited lower compressive and flexural strengths despite possessing higher densities. While GGBFS contained significant amounts of SiO_2 (34.69%) and Al_2O_3 (17.37%), which can contribute to aluminosilicate gel formation, its high CaO content (35.08%) altered the dominant reaction pathway. The presence of calcium promotes the formation of C–A–S–H-type gels, which coexist with or partially replace the geopolymeric network. Although the silica and alumina in GGBFS can participate in secondary gel formation and contribute to matrix densification, their role is often overshadowed by calcium-driven reactions that favour rapid precipitation of less polymerized phases. As a result, the microstructure tends to become more heterogeneous, characterized by a combination of C–A–S–H and discontinuous aluminosilicate gels, which disrupts the continuity of the three-dimensional network. This limits the effective contribution of SiO_2 and Al_2O_3 from GGBFS to long-range structural integrity, thereby reducing general mechanical performance despite increased density (Nadarajah et al., 2024).

Additional insight is gained from examining the Na_2O/SiO_2 and H_2O/Na_2O ratios in Table 4.1. Although Na_2O/SiO_2 values remained within ranges typically associated with stable geopolymerization (Alaneme et al., 2024), a downward shift from 0.32 in M4 to 0.21 in M7 indicates a decreasing relative alkalinity as GGBFS content rises. This reduction could hinder dissolution kinetics, contributing to the lower reaction extent and diminished strength observed in high-GGBFS mixes. Similarly, the slight reduction in H_2O/Na_2O ratio from 13.31 (M1) to 13.07 (M7) may appear small but suggests progressively reduced water availability per alkali

content, which can impede ion mobility and slow gel formation (Kolade et al., 2025c). Together, these changes further explain the mechanical decline in calcium-rich mixes.

Although the incorporation of superplasticizer in M5 – M7 was intended solely to improve flowability, its potential inhibitory effects on geopolymer reaction sites likely compounded the influence of high calcium content. This combination may have contributed to the particularly modest strength values observed for these mixes compared with their fly ash-dominant counterparts. That said, the hardened property results emphasize that while GGBFS enhances density and reduces porosity, excessive calcium disrupts the formation of a robust aluminosilicate network. Therefore, an optimal balance between fly ash and GGBFS, supported by well-proportioned activator chemistry, is essential for achieving high-performance structural-grade geopolymers.

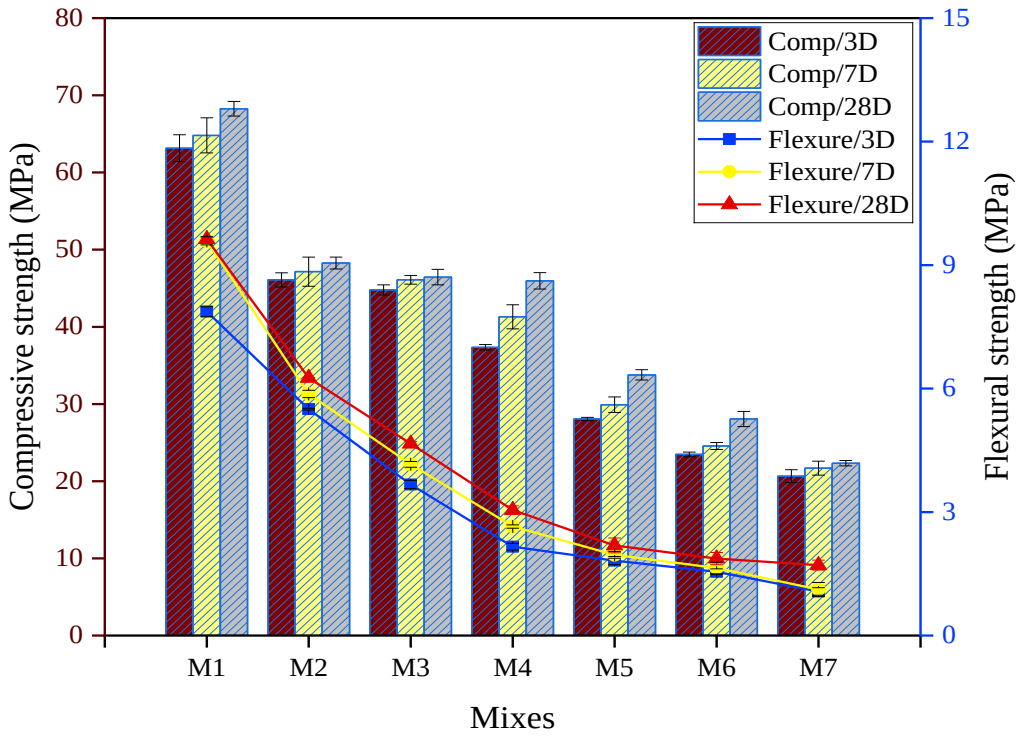

Fig. 4.1: Compressive and flexural strengths for the various mortar formulations

4.4 Performance-based Mix Selection

Based on a comprehensive evaluation of the seven trial mixes, three formulations (M1, M2 and M3) were selected for further development and upscaling to concrete-level applications. The selection was based on a balanced assessment of workability (flow), mechanical strength

(compressive and flexural) and water absorption, with additional consideration given to material efficiency.

M1 was chosen as the benchmark mix due to its superior mechanical performance, achieving the highest compressive and flexural strengths, alongside moderate flowability and a favourable SiO_2/Al_2O_3 ratio. This outcome indicates that the fly ash-only system provided the most effective balance of chemical composition and mechanical behaviour among all the mixes, highlighting the advantage of a low-calcium system with balanced alkalinity in promoting a continuous and durable geopolymeric network. Building on this benchmark performance, the remaining mixes were evaluated relative to M1. M2 demonstrated lower strength and workability but was retained for its balance between performance and material economy. M3 offered acceptable performance despite lower precursor reactivity and reduced flowability, representing a viable lower-bound formulation. Although M4 exhibited comparable compressive strength to M3, its significantly lower flowability was a limiting factor, as it could present practical challenges during concrete mixing and placement. It was therefore excluded from further development.

In general, the findings suggest that for achieving high-strength geopolymer systems, mixes should be designed with predominantly fly ash-based precursors while maintaining controlled Na_2O/SiO_2 and H_2O/Na_2O ratios within optimal ranges. The incorporation of GGBFS should be limited or carefully optimized to avoid excessive calcium content that may compromise structural integrity.

It is also important to note that the selection process prioritized performance, robustness and scalability, with particular attention to mix adaptability when using synthesized activators such as WGSS. Accordingly, the final three mixes (M1, M2 and M3) served as the foundation for all subsequent mortar and concrete trials, structural performance evaluations and sustainability assessments presented in the following chapters. For upscaling to concrete-level applications, fine and coarse aggregates were introduced while maintaining the same binder compositions and molar ratios. This iterative optimization strategy provides a replicable framework for geopolymer development, especially for systems incorporating both conventional and alternative alkaline activators.

CHAPTER 5

5 DEVELOPMENT AND EVALUATION OF ALTERNATIVE SODIUM SILICATE

This chapter presents the synthesis, characterization and performance evaluation of an alternative sodium silicate (WGSS) from waste glass powder (WGP) using the alkali fusion method. The process provides a sustainable route for converting post-consumer glass waste into a geopolymer activator, aligning with circular economy principles. Emphasis is placed on optimizing fusion temperature and reaction time to tailor the phase structure, solubility and chemical reactivity of the resulting silicate.

5.1 Alkali Fusion Procedure for WGSS Synthesis

The alkali fusion procedure was adapted from the method described by Vinai and Soutsos (2019), with modifications in fusion temperature and duration. A weight ratio of 2:1 (NaOH to WGP) was adopted for the synthesis process, as shown in Eq. (5.1), to ensure sufficient alkali availability for the disruption and reformation of silicate bonds. Based on this ratio and assuming 100% purity of NaOH and a silica content of 70.08% in WGP, producing 1 kg of WGSS required 655 g of NaOH and 345 g of WGP.

$$2NaOH\,(s) + SiO_2\,(s) \xrightarrow{500 - 650°C} Na_2SiO_3\,(s) + H_2O\,(g) \qquad (5.1)$$

The synthesis procedure is illustrated in Fig. 5.1. It involved thoroughly dry-mixing NaOH pellets and WGP using aluminium foil as the mixing medium, followed by thermal activation under varying conditions. Prior to fusion, the muffle furnace was pre-heated to the target temperature, after which the mixed materials were introduced into the furnace. Fusion was conducted in a laboratory muffle furnace at the following temperature–time combinations: 500°C for 3 hours, 550°C for 2 hours, 550°C for 3 hours, 600°C for 2 hours, 600°C for 3 hours and 650°C for 2 hours. At the end of each fusion cycle, the resulting materials were removed immediately from the furnace and allowed to cool to ambient temperature in a covered container. Following cooling, the fused WGSS was ground using a laboratory-scale ball mill (steel rod media) for 1 hour per batch to obtain a fine powder suitable for subsequent characterization and use in experimental formulations. For the preparation of the liquid WGSS, the WGSS fine powder was dissolved in water to match the composition of the reference CSS solution (37.1% solids and 62.9% H_2O). The mixture was stirred until a homogeneous solution was obtained without filtering prior to use as an activator.

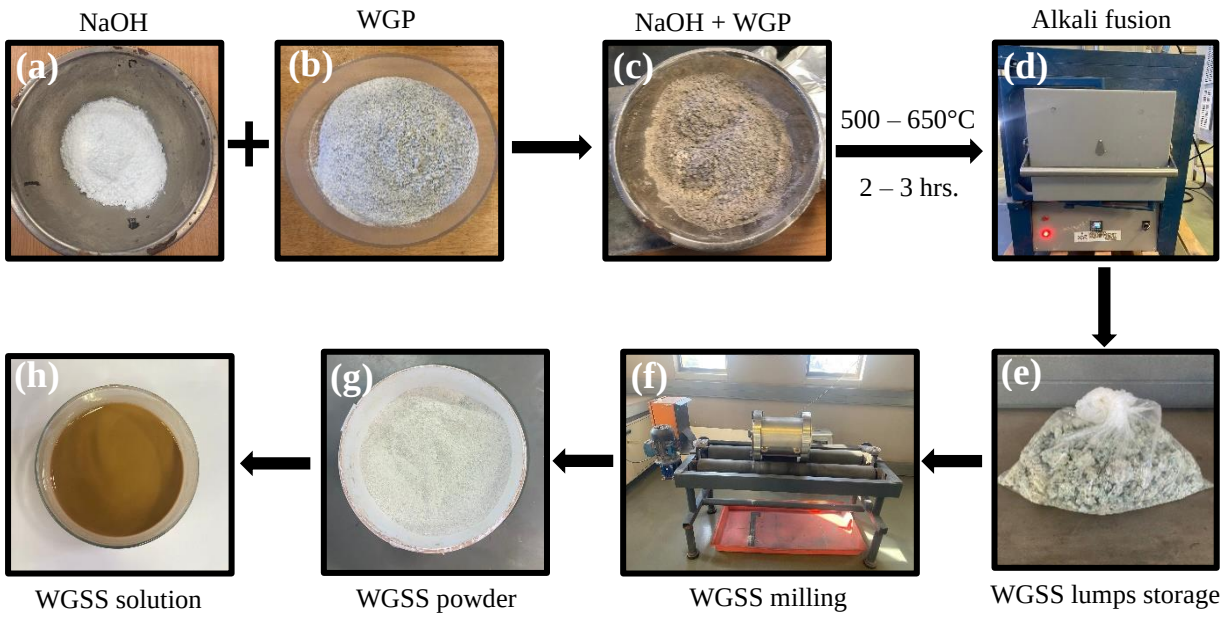

Fig. 5.1: Schematic workflow for the synthesis of WGSS solution: (**a**) 655 g of NaOH (**b**) 345 g of WGP (**c**) dry mixing (**d**) thermal fusion (**e**) cooling and storage (**f**) milling (**g**) WGSS fine powder (**h**) WGSS dissolution in water (unfiltered)

5.2 Effect of Fusion Temperature and Duration

The synthesized WGSS samples were initially characterized for phase composition, morphology, elemental and oxide contents, functional groups and alkalinity using XRD, SEM, EDS, XRF, FTIR and pH measurements. Their suitability as alkaline activators was assessed through 7 and 28-day compressive and flexural strength testing. For the mechanical evaluation, four mortar mixes were produced with a fixed binder-to-aggregate ratio of 1:3, AL/B ratio of 0.5 and an SS/SH ratio of 1.5, as detailed in Table 5.1. The results from these assessments elucidate the influence of fusion parameters on WGSS reactivity and binder performance, offering a scalable approach for transforming locally available waste glass into sustainable construction materials.

Table 5.1: Mortar mix proportions for three test specimens

Mix ID	FA:GGBFS	GGBFS (g)	FA (g)	Sand (g)	AL/B ratio	NaOH conc. (M)	SS/SH ratio	NaOH soln. (g)	WGSS or CSS soln. (g)
Mix 1	7:1	53	296	1350	0.5	12	1.5	90	135
Mix 2	3:1	105	254	1350	0.5	12	1.5	90	135

5.2.1 WGSS Characterization

5.2.1.1 XRD Analysis

XRD analysis of the synthesized WGSS powder samples was performed over a 2θ range of 5 – 90° and the resulting diffractograms are presented in Fig. 5.2. The spectra exhibited a relatively smooth baseline interrupted by distinct sharp peaks, which indicate the coexistence of amorphous and crystalline phases. This hybrid pattern is similar to the XRD patterns reported by Antunes et al. (2024) for CSS and other alternative sodium silicates, as shown in Fig. 5.3, confirming that the synthesized WGSS exhibits a comparable phase assemblage to standard activators.

The most prominent crystalline phase in the WGSS was identified as Na_2SiO_3, whose diffraction peak intensity within the 18 – 35° range increased progressively with higher fusion temperatures. Additional crystalline phases identified included sodium carbonate (Na_2CO_3), appearing between 29 – 42° and likely originating from atmospheric carbonation during cooling; calcium hydroxide sodium hydrate ($Na_4Ca(OH)_6$) within 31 – 42°, attributed to CaO residues in the glass precursor; and partially reacted SiO_2 observed in the 22 – 39° region, suggesting residual amorphous or semi-crystalline silica. At the highest fusion temperatures, more thermodynamically stable phases, such as sodium orthosilicate (Na_4SiO_4) and sodium pyrosilicate ($Na_6Si_2O_7$), were also detected. However, unlike the CSS reported in the literature, whose diffraction pattern is dominated by a single Na_2SiO_3 phase according to Fig. 5.3, the WGSS exhibited additional peaks corresponding to secondary crystalline phases and compositional impurities inherited from the glass precursor, which reflect its more heterogeneous composition.

It is important to note that the observed secondary phases may adversely affect the reactivity and dissolution behaviour of the synthesized WGSS by reducing the availability of soluble silicate species. For instance, increased crystallinity and the presence of stable silicate phases (such as Na_4SiO_4 and $Na_6Si_2O_7$) can limit dissolution kinetics, while carbonate formation may alter alkalinity. To enhance the quality and performance of WGSS, approaches such as pre-treatment (washing or chemical cleaning) of the glass precursor to reduce impurities, optimization of fusion temperature to limit excessive crystallization and controlled cooling conditions to minimize atmospheric carbonation could be adopted (Kolade et al., 2026b; McCloskey et al., 2024). These measures would promote a higher proportion of reactive amorphous phases and improve the efficiency of the synthesized activator.

In addition, the amorphous fraction of the WGSS was quantified according to the approach of Tiainen et al. (2002), where peak deconvolution was performed to distinguish broad amorphous humps from discrete crystalline peaks. The crystalline-to-total area ratio was used to estimate relative crystallinity. This analysis revealed a reduction in amorphous content from 84.78% for samples fused at 500°C for 3h to 72.88% for those produced at 650°C for 2h, confirming that higher fusion temperatures encourage the reduction of available reactive amorphous sodium silicate. This reduction in amorphous content also has important implications for geopolymerization, as amorphous phases are generally more soluble and reactive in alkaline environments. Thus, a decrease in amorphous content limits the release of silicate species necessary for gel formation, which can negatively impact the mechanical performance of the resulting geopolymer (Kolade et al., 2026b). Consequently, controlling fusion conditions to preserve a higher amorphous fraction is vital for optimizing the reactivity and effectiveness of WGSS as an activator.

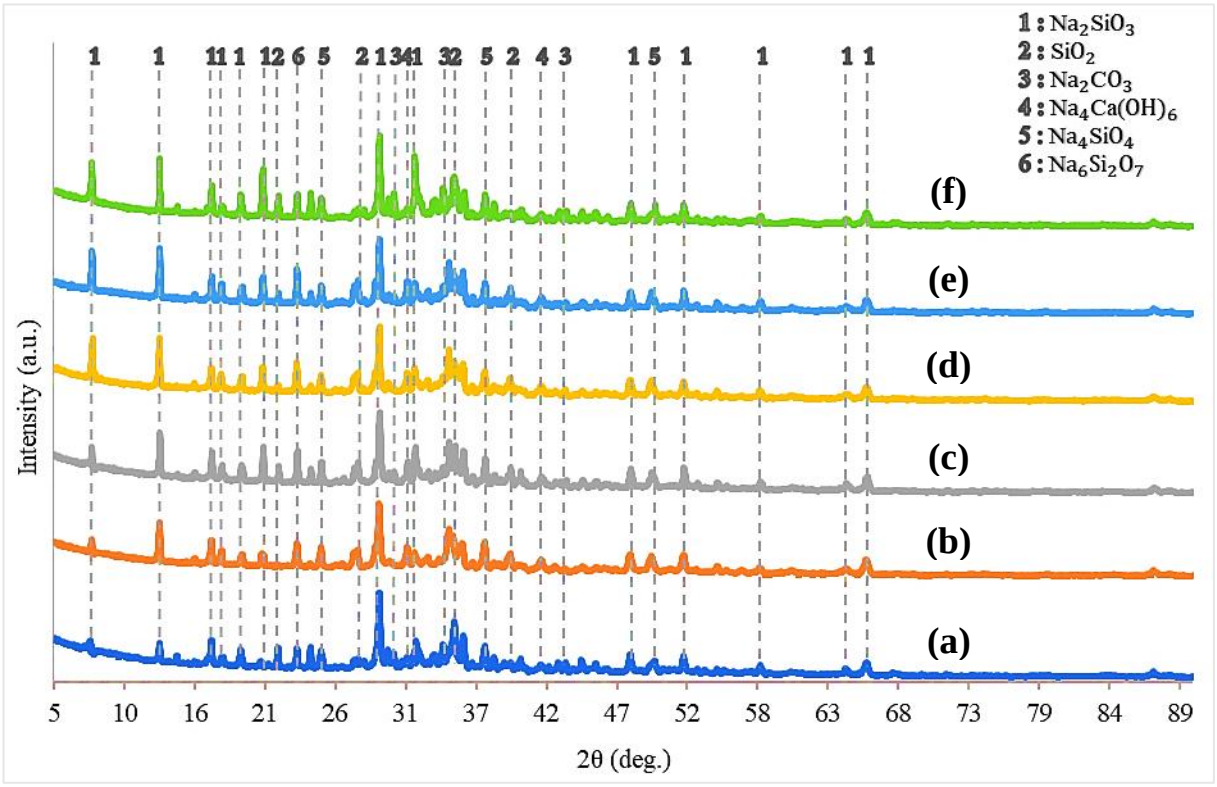

Fig. 5.2: XRD spectra of WGSS synthesized at (**a**) 500°C, 3h (**b**) 550°C, 2h (**c**) 550°C, 3h (**d**) 600°C, 2h (**e**) 600°C, 3h (**f**) 650°C, 2h

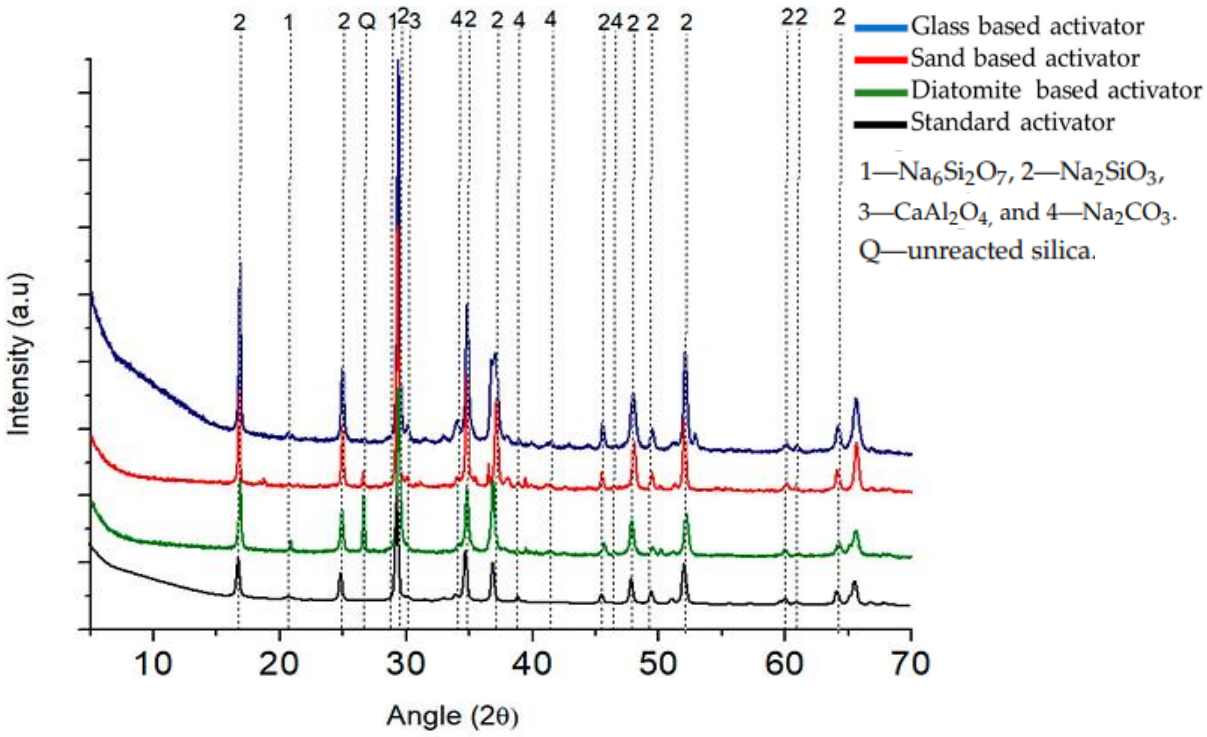

Fig. 5.3: Comparative XRD spectra of CSS (standard activator) and other alternative sodium silicates (Antunes et al., 2024)

5.2.1.2 SEM Analysis

SEM observations of the WGSS powder samples (Fig. 5.4a–f) reveal a distinct progression in surface texture as fusion temperature increases. At lower fusion temperatures, the particles exhibit relatively smooth surfaces, while higher temperatures lead to more pronounced features such as interstitial gaps and crater-like depressions. These morphological changes align with findings by Li et al. (2019b), suggesting partial volatilization during fusion followed by uneven cooling, which produces irregular surface patterns.

Furthermore, a marked transformation is evident in specimens fused at 600°C for 3h and 650°C for 2h, where the microstructure develops a foamed, expanded appearance accompanied by fibrous silicate strands (Fig. 5.4g). This feature is likely linked to excessive crystallization, phase segregation and gas release, all of which can diminish solubility and reactivity. The presence of inclusions, where smaller particles are embedded within larger ones (Fig. 5.4h), points to residual unreacted SiO_2 from WGP, potentially influencing uniformity and dissolution rates. Also, the roughened particle surfaces observed in Fig. 5.4i suggest increased porosity, a trait that can compromise mechanical strength (Kolade et al., 2026b). These microstructural trends are in agreement with the XRD results, highlighting the significant role of fusion

conditions in controlling phase composition, porosity and textural characteristics, factors that ultimately determine the suitability of WGSS as an alkaline activator.

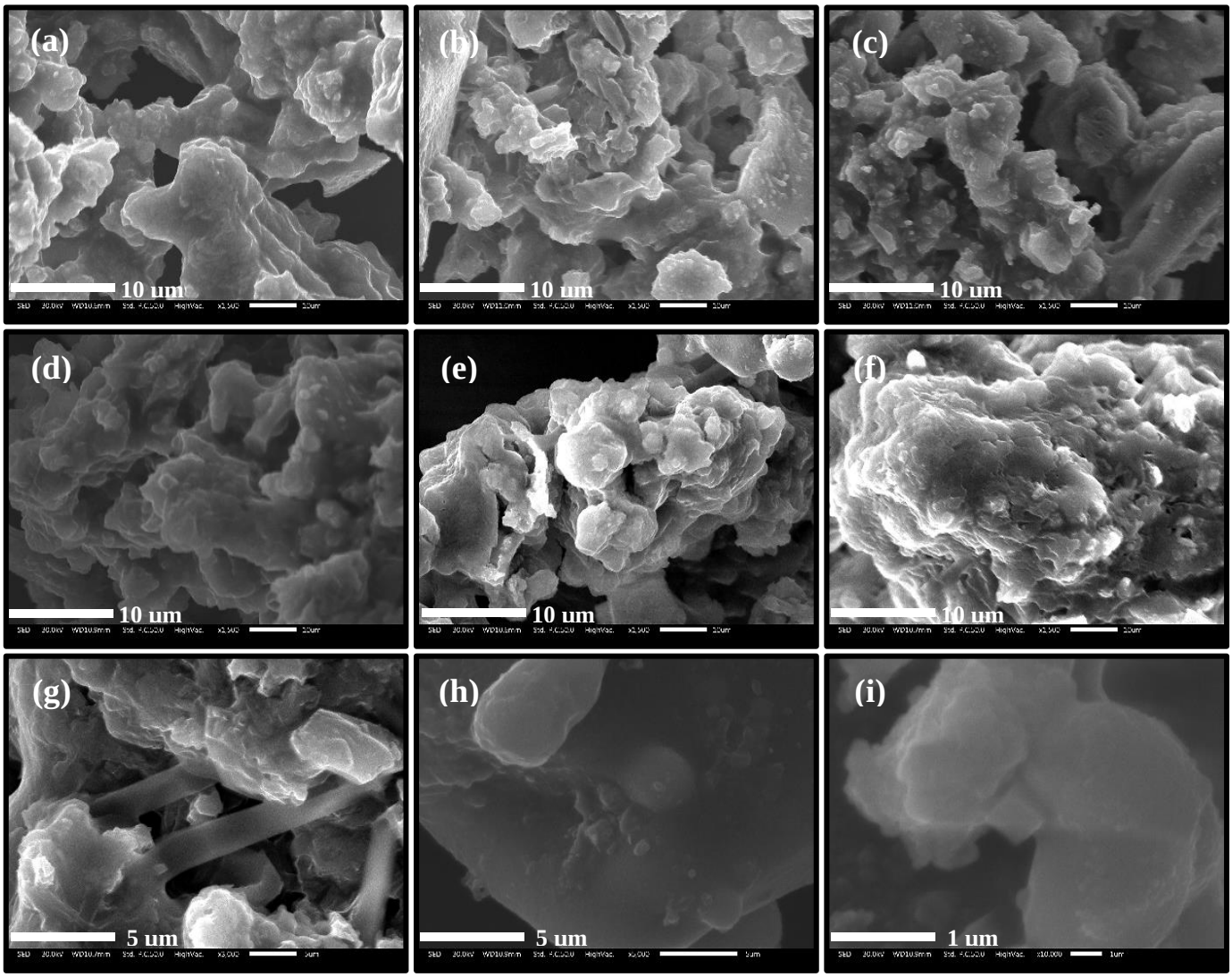

Fig. 5.4: SEM micrographs of WGSS samples fused at (**a**) 500°C, 3h (**b**) 550°C, 2h (**c**) 550°C, 3h (**d**) 600°C, 2h (**e**) 600°C, 3h (**f**) 650°C, 2h. Panels (**g–i**) are presented at higher magnification to highlight specific morphological features, including (**g**) fibrous gel-like structures (**h**) a particle encapsulated within another (**i**) surface roughening and dissolution pits on reacted particles

5.2.1.3 EDS Analysis

The EDS spectra presented in Fig. 5.5a–f confirm the presence of Na, Si, O, Ca and C as the primary elemental constituents across all WGSS samples. The quantitative elemental

compositions are summarized in Table 5.2. At lower fusion temperatures (500°C), the samples showed the highest Na (34.6 wt.%) and Si (14.4 wt.%) contents, indicating dominance of sodium-rich silicate phases. At mid-range fusion conditions (550°C), Na and Si decreased sharply while carbon increased significantly (up to 30 wt.%), suggesting Na_2CO_3 formation, consistent with XRD results. With further increases in temperature (600°C), Na and Si levels increased again and carbon content reduced, indicating decomposition of carbonate phases and enhanced silicate formation. Oxygen proportion also increased at this stage, reflecting improved structural ordering. However, the sample at 650°C showed a new increase in carbon (19.2 wt.%), suggesting partial re-carbonation during cooling or surface carbonation effects, while calcium remained relatively stable across all samples, attributable to unreacted Ca-bearing residues from WGP (Kolade et al., 2026b). Thus, the compositional evolution observed in the EDS results corroborates the phase changes identified by XRD, highlighting temperature-dependent transitions among sodium silicate, carbonate and silica-rich structures.

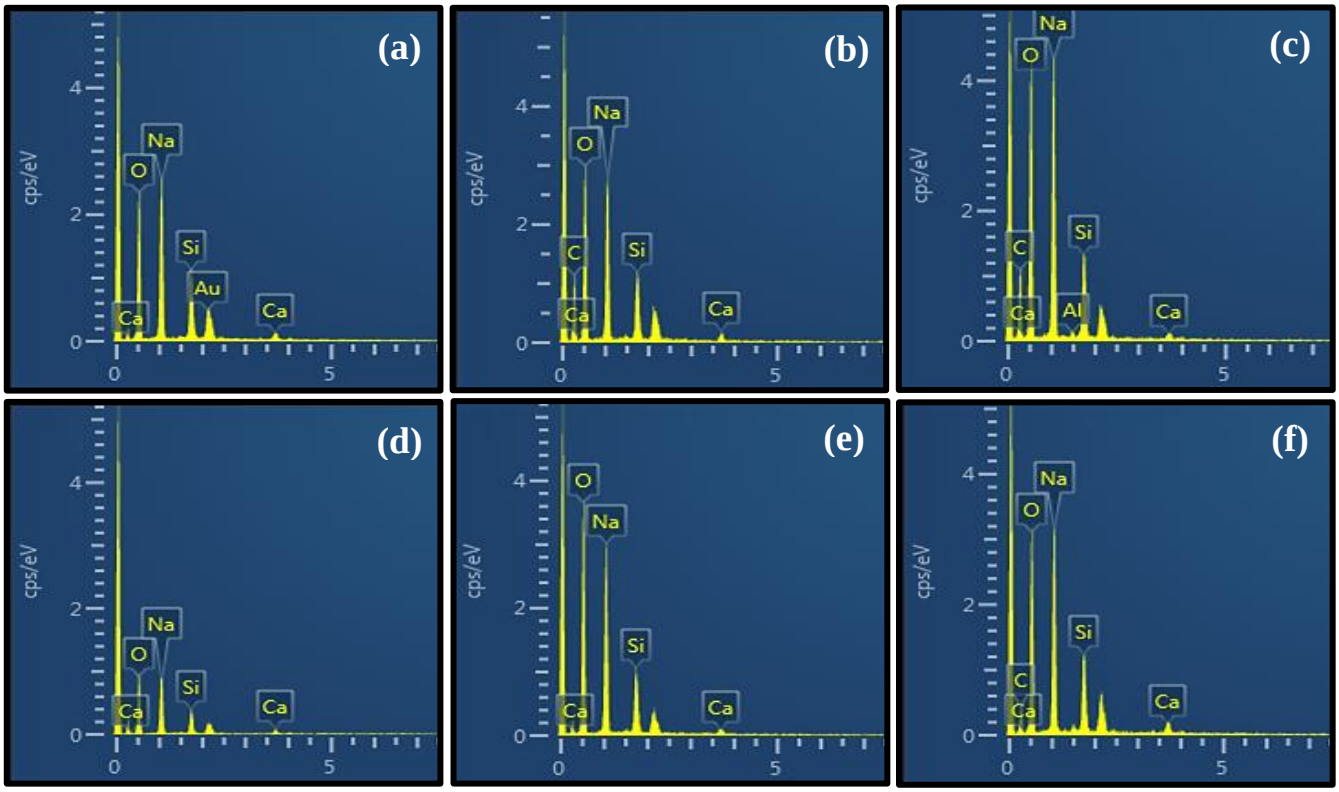

Fig. 5.5: EDS spectra of WGSS samples fused at (**a**) 500°C, 3h (**b**) 550°C, 2h (**c**) 550°C, 3h (**d**) 600°C, 2h (**e**) 600°C, 3h (**f**) 650°C, 2h

Table 5.2: Elemental composition of WGSS samples determined by EDS (wt.%)

Fusion condition	Na (%)	Si (%)	O (%)	Ca (%)	C (%)
500°C, 3h	34.6	14.4	48.0	3.0	–
550°C, 2h	18.2	6.7	42.8	1.8	30.5
550°C, 3h	21.7	6.0	44.8	1.0	26.1
600°C, 2h	32.6	12.7	50.5	4.2	–
600°C, 3h	33.0	10.7	54.4	1.8	–
650°C, 2h	24.1	8.5	45.6	2.6	19.2

Note: *"–" indicates trace/undetected carbon below quantification limit*

5.2.1.4 pH Analysis

To evaluate the alkalinity and potential activating capability of the produced WGSS, pH testing was carried out for each fusion condition. The WGSS powders were diluted in water to replicate the composition of the CSS solution (37.1% solids and 62.9% H_2O), after which the suspensions were allowed to stabilize before measurement. The pH readings for the WGSS solutions are presented in Table 5.3, which shows a gradual pH reduction as both fusion temperature and time increased. The slight reduction in alkalinity at higher fusion conditions is attributed to lower silicate solubility, arising from greater crystallinity and enhanced silicate network polymerization. These microstructural changes limit the release of hydroxide ions (OH^-) and other soluble alkaline species, thereby producing marginally lower pH values (Gao et al., 2014; Kolade et al., 2026b; Vinai and Soutsos, 2019). For comparison, the CSS solution recorded a pH of 12.5. The fact that all WGSS formulations maintained pH values above 13 suggests a more strongly alkaline environment, which is favourable for geopolymerization and could promote faster early-age reaction rates and improved strength gain (Gao et al., 2014; Kolade at al., 2026).

Table 5.3: pH measurements of WGSS synthesized under varying fusion conditions

Fusion condition	pH of WGSS solution
500°C, 3h	13.42
550°C, 2h	13.31
550°C, 3h	13.30
600°C, 2h	13.27
600°C, 3h	13.26
650°C, 2h	13.25

5.2.1.5 XRF Analysis

XRF characterization was conducted on the WGSS produced at 500°C for 3h, which was identified as the optimal fusion condition based on overall performance evaluation. It should be noted that the selection of this sample was primarily guided by its observed mechanical performance and workability behaviour, while the XRF analysis was subsequently carried out to provide chemical insight into the composition of the selected material. The oxide composition (Table 5.4) revealed a dominance of silica (50.08 wt.%) and sodium oxide (48.11 wt.%), the two primary constituents of sodium silicate–based activators. This composition yields a SiO_2/Na_2O marginally above 1, aligning with the optimum range reported by Delgado-Plana et al. (2024) for promoting geopolymerization efficiency.

Trace levels of other oxides, including alumina, lime and magnesia, were also detected, which can aid in early gel network formation and densification of the binder matrix. The very low LOI reflects minimal volatile matter, indicating both high chemical purity and a complete fusion reaction (Kolade et al., 2026b). Although XRF analysis was limited to this sample due to experimental constraints, the obtained chemical composition is consistent with the reactivity trends inferred from the alkalinity, strength and workability behaviour discussed in Sections 5.2.1.4 and 5.2.2. The substantial sodium content is likely a key factor in the strong alkaline environment and efficient dissolution of precursor materials observed.

Table 5.4: Oxide composition (wt.%) of the optimally synthesized WGSS at 500°C for 3h

Oxide	SiO_2	Na_2O	Fe_2O_3	Al_2O_3	CaO	TiO_2	MgO	K_2O	MnO	P_2O_5	SO_3	LOI
Content (wt.%)	50.08	48.11	0.07	0.97	0.46	0.05	0.13	0.06	0.04	0.02	0.01	0.06

5.2.1.6 FTIR Analysis

The FTIR spectrum of the WGSS synthesized at 500°C for 3h (Fig. 5.6) closely aligns with observations reported by Delgado-Plana et al. (2024) and Vinai and Soutsos (2019). It displays vibrational features typical of silicate-based networks, confirming successful conversion of waste glass into reactive soluble silicate species. The strong, broad band between 1100 – 800 cm^{-1} corresponds to asymmetric Si–O–T stretching (T = Na^+, forming Si–O–Na), indicative of the partial depolymerization of the original Si–O–Si framework of waste glass and the formation of silicate oligomers. The greater intensity toward 800 cm^{-1} relative to 1100 cm^{-1} suggests a low SiO_2/Na_2O modulus, consistent with XRF results. Broadening in this region

also signifies the presence of mixed $Q^2 – Q^4$ units, characteristic of partially condensed sodium silicates, which are favourable for rapid dissolution and precursor activation in geopolymer systems (Dadsetan et al., 2022; Delgado-Plana et al., 2024; Patrick et al., 2024; Vinai and Soutsos, 2019).

In addition, the incorporation of Na into the Si–O–Si network produces non-bridging oxygens, leading to splitting of the Si–O–Na band into secondary peaks at 1034 cm^{-1}, 966 cm^{-1} and 876 cm^{-1}. These peaks correspond with XRD confirmation of crystalline sodium silicate formation, exhibiting 84.78% crystallinity. The presence of non-bridging oxygens enhances chemical reactivity and promotes disruption of glassy silicate chains, beneficial for alkali activation (Delgado-Plana et al., 2024; Vinai and Soutsos, 2019).

A broad hump between 2500 – 3300 cm^{-1} and a small peak at 1444 cm^{-1} indicate minor carbonation (Na_2CO_3 formation) due to atmospheric CO_2 interaction, consistent with XRD and EDS data. Meanwhile, the sharper peak at 3576 cm^{-1} corresponds to O–H stretching in unreacted NaOH (Delgado-Plana et al., 2024; Vinai and Soutsos, 2019). Collectively, these FTIR features confirm effective depolymerization of waste glass and formation of reactive sodium silicate phases, validating the suitability of WGSS as an alternative alkaline activator for geopolymer binder production.

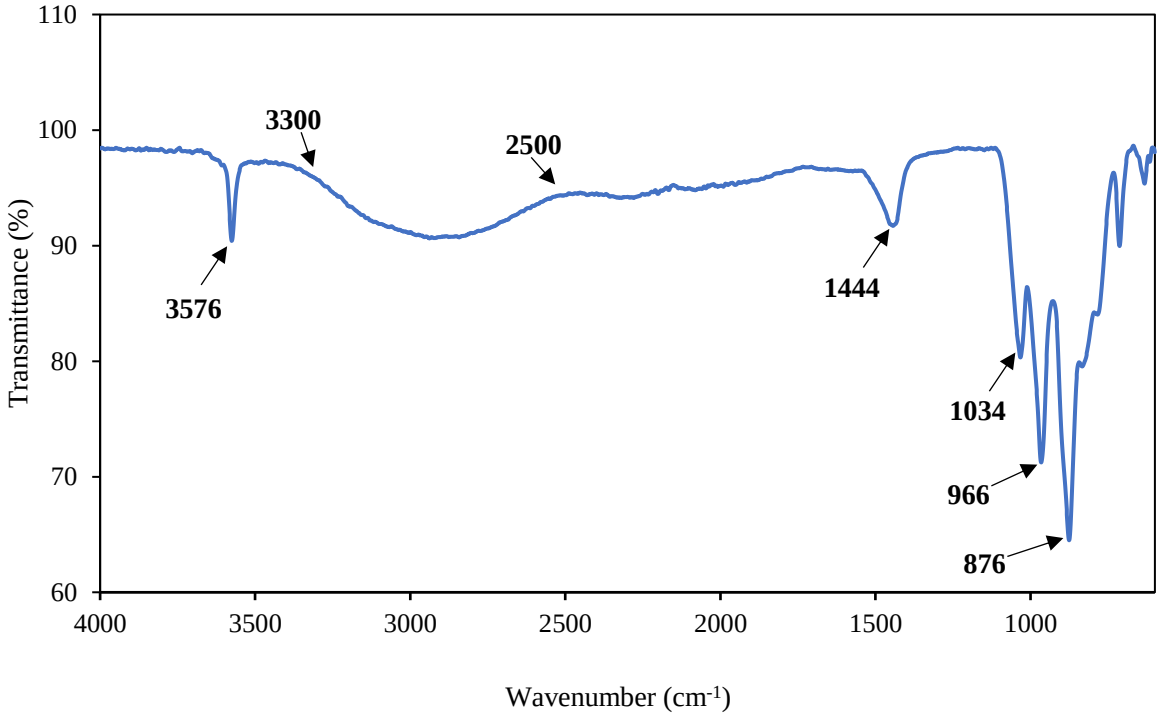

Fig. 5.6: FTIR spectrum of WGSS synthesized at 500°C for 3h

5.2.2 Performance Evaluation of Mortars Prepared with Synthesized WGSS

5.2.2.1 Workability

Table 5.5 presents the measured flow values for all mortar formulations. In general, workability improved as the fusion temperature increased, reaching maximum values at 600°C (2 hours). Particularly, flow increased from 90% at 500°C (3 hours) to 140% at 600°C (2 hours) for Mix 1 (FA:GGBFS = 7:1) and from 75% to 130% for Mix 2 (FA:GGBFS = 3:1), representing improvements of approximately 56% and 73%, respectively. Beyond this temperature–time combination, flowability showed a slight decrease before stabilizing. These values were comparable to those of the CSS reference mix, which exhibited flow values of 140% and 120% for Mixes 1 and 2, indicating that the optimized WGSS condition achieved similar workability performance. In addition, the enhanced flow observed at higher fusion conditions can be attributed to reduced early-stage reactivity associated with increased crystallinity. Under such conditions, the formation of less soluble silicate phases slows dissolution, postpones gelation and thereby prolongs the mix's fluid state during placement (Vinai and Soutsos, 2019). These results are consistent with pH and XRD data, which revealed reduced solubility and alkalinity at elevated fusion temperatures.

In contrast, mortars incorporating WGSS produced at 500 – 550°C demonstrated lower flow values, a behaviour attributed to their higher amorphous content and rapid dissolution rate, which accelerated gelation and increased viscosity (Kolade et al., 2025b, 2026). As such, the findings highlight the trade-off between reactivity and workability when developing WGSS-based activators: while higher reactivity can enhance strength development, it may also hinder casting and compaction. Therefore, selecting fusion parameters should aim to optimize both mechanical performance and fresh-state handling.

Table 5.5: Workability (flow %) of mortars prepared with WGSS and CSS activators

Activator type and fusion condition	Flow – Mix 1 (%)	Flow – Mix 2 (%)
WGSS, 500°C, 3h	90 ± 0.63	75 ± 0.20
WGSS, 550°C, 2h	100 ± 0.82	80 ± 0.47
WGSS, 550°C, 3h	110 ± 0.77	105 ± 0.50
WGSS, 600°C, 2h	140 ± 1.29	130 ± 0.65
WGSS, 600°C, 3h	120 ± 0.82	110 ± 0.50
WGSS, 650°C, 2h	120 ± 0.96	110 ± 0.47
CSS (reference mix)	140 ± 0.96	120 ± 0.77

5.2.2.2 Compressive Strength

Fig. 5.7 presents the compressive strength results of the geopolymer mortars, revealing a strong influence of the fusion condition used in producing the WGSS activator. Peak values of 35.32 MPa for Mix 1 (FA:GGBFS = 7:1) and 33.07 MPa for Mix 2 (FA:GGBFS = 3:1) were recorded when the activator was fused at 500°C for 3 hours, suggesting that this condition provided the best balance of solubility and chemical reactivity. Increasing the fusion temperature or extending the heating period led to a gradual reduction in strength, with the lowest performance observed at 650°C for 2 hours. This reduction corresponds with XRD observations showing a higher proportion of crystalline phases and reduced amorphous content in WGSS at elevated fusion conditions. As such, their predominance can restrict geopolymerization and suppress strength gain because crystalline silicate phases dissolve more slowly and release fewer reactive species (Gao et al., 2014; Kolade et al., 2026b; Torres-Carrasco and Puertas, 2017).

Across all synthesis conditions, Mix 1 consistently exhibited higher strength than Mix 2, with 28-day strength increases of 6.8%, 5.8%, 15.2%, 18.8%, 34.7% and 36.3% for WGSS synthesized at 500°C for 3 hours, 550°C for 2 hours, 550°C for 3 hours, 600°C for 2 hours, 600°C for 3 hours and 650°C for 2 hours, respectively. This advantage is linked to its lower GGBFS content, which favours the formation of geopolymeric gel networks rather than C–A–S–H gels (Kolade et al., 2025b). In contrast, the higher GGBFS proportion in Mix 2 promotes C–A–S–H formation, yielding a denser but more brittle matrix that may compromise long-term strength relative to the more durable and flexible geopolymeric gel (Luhar and Luhar, 2022; Tchakouté et al., 2016b). Similar effects of elevated calcium content and competing gel phases on compressive strength have been noted in prior studies (Kolade et al., 2025b; Mohamed et al., 2023).

When compared to the CSS-activated control mortars, which recorded compressive strengths of 47.15 MPa for Mix 1 and 46.09 MPa for Mix 2, the WGSS mixes exhibited lower compressive strengths ranging from 23 – 35 MPa for Mix 1 and 17 – 33 MPa for Mix 2 across the investigated fusion conditions. These values correspond to reductions of approximately 25 – 50% for Mix 1 and 28 – 60% for Mix 2, respectively. Although these reductions are notable, the best-performing WGSS mix still achieved compressive strengths exceeding 30 MPa, which fall within the range typically considered adequate for structural-grade geopolymer binders. This difference is likely due to residual undissolved glass particles and the lower activator modulus ($SiO_2/Na_2O \approx 1$) in the WGSS solutions, both of which can limit the formation of

strong –Si–O–Si– bonds that underpin high strength in geopolymeric binders (Gao et al., 2014; Kolade et al., 2026b; Torres-Carrasco and Puertas, 2017).

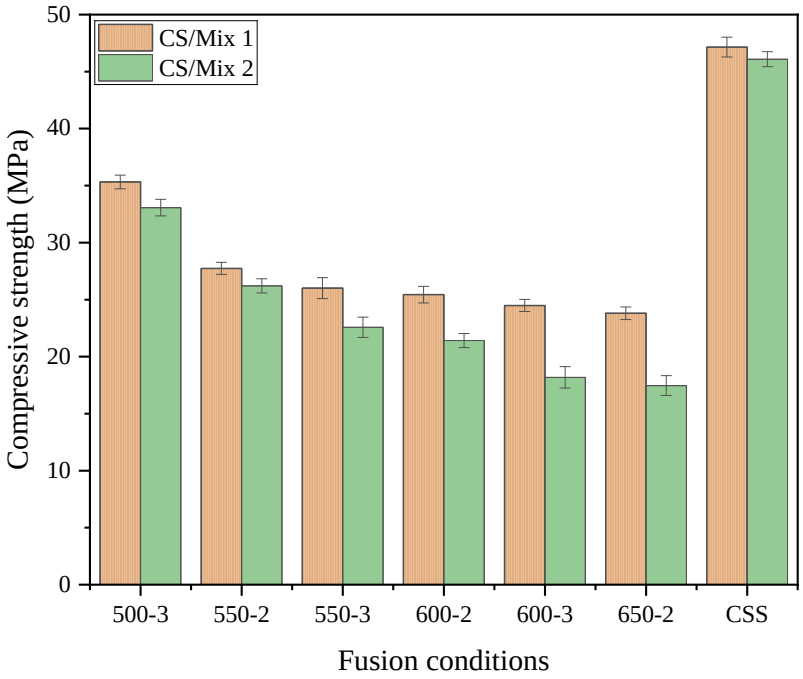

Fig. 5.7: Mortar compressive strength performance at 28 days

Note: Fusion conditions are expressed as "temperature-time" (500-3 = 500°C for 3h)

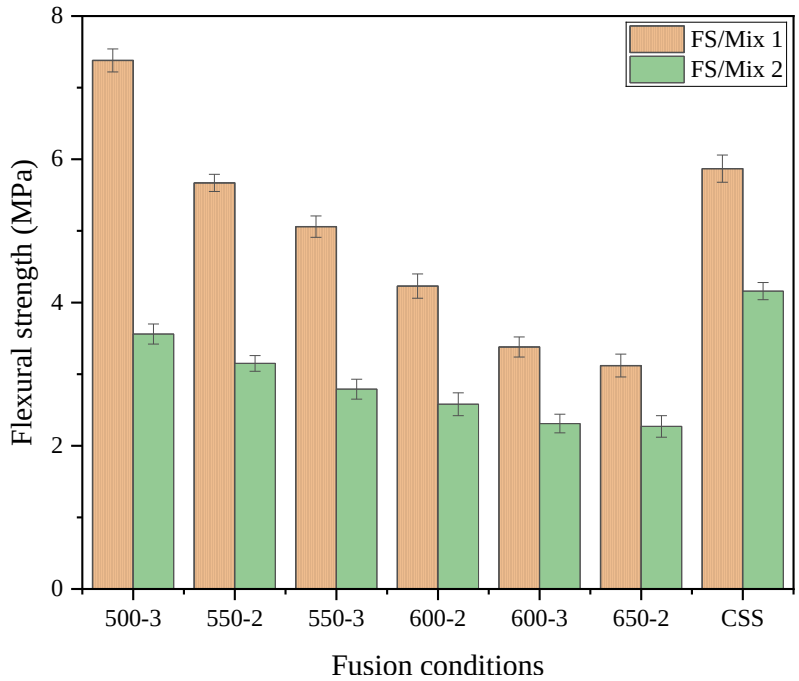

Fig. 5.8: Mortar flexural strength performance at 28 days

5.2.2.3 Flexural Strength

The flexural strength results presented in Fig. 5.8 largely mirrored those observed for compressive strength, showing a progressive reduction as fusion temperature and duration increased. However, mortars activated with WGSS, especially those derived under lower fusion conditions, achieved flexural strengths comparable to and in some cases exceeding those of the CSS-based controls. The highest values were recorded for WGSS synthesized at 500°C for 3 hours, reaching 7.38 MPa in Mix 1 (FA:GGBFS = 7:1) and 3.56 MPa in Mix 2 (FA:GGBFS = 3:1). These results highlight the beneficial role of amorphous-rich WGSS produced under moderate fusion parameters in improving matrix cohesion and resisting crack propagation (Kolade et al., 2025b, 2026). Notably, the peak strength in Mix 1 closely matches the 7.3 MPa value reported by Gok and Sengul (2024), further underscoring the potential of glass-derived activators to deliver excellent flexural performance.

Several mechanisms may account for this behaviour. Residual unreacted WGP particles can act as micro-fillers, reducing porosity and bridging microcracks, while also serving as nucleation sites for geopolymeric gel formation, thus improving the interfacial transition zone (ITZ) between binder and aggregates (Delgado-Plana et al., 2024; Ikotun et al., 2025; Siddika et al., 2021b). The high elastic modulus of glass may also enhance tensile and flexural load resistance by improving energy absorption and crack-bridging capacity (Kolade et al., 2026b; Siddika et al., 2021b). Furthermore, microstructural evidence from SEM studies suggests that glass-based particles contribute to refining the matrix and minimizing weak zones, which in turn improves stress transfer across the ITZ (Siddika et al., 2021b; Torres-Carrasco and Puertas, 2017).

From a compatibility perspective, the observed flexural performance also reflects the effective interaction between WGSS and GGBFS within the geopolymer system. The calcium-rich nature of GGBFS promotes the formation of C–A–S–H type gels alongside geopolymeric gels derived from the aluminosilicate precursors, resulting in a hybrid binding system with improved cohesion and toughness. The presence of WGSS, especially in its more amorphous and reactive form, enhances the dissolution of both fly ash and slag, thereby facilitating gel formation and improving the bonding characteristics within the matrix. This synergistic interaction is especially evident in Mix 1, where the balanced incorporation of GGBFS contributes to improved flexural resistance without excessive brittleness.

When compared to CSS controls, WGSS mortars at the optimal fusion condition demonstrated superior flexural strength. This indicates the suitability of WGSS as a sustainable, low-carbon alkaline activator and its ability to enhance ductility and toughness in geopolymer composites. Likewise, the results confirm the feasibility of combining WGSS with GGBFS in geopolymer mixes, especially when fusion conditions are optimized to preserve amorphous content and reactivity. That said, the consistent outperformance of Mix 1 relative to Mix 2 supports the view that a higher GGBFS content leads to a denser but more brittle matrix, which is more prone to crack initiation and propagation under flexural loading (Luhar and Luhar, 2022).

5.2.3 Optimized WGSS for Use as Activator

Based on comprehensive characterization and mechanical performance results, the WGSS synthesized at 500°C for 3 hours was identified as the optimal activator formulation. This product exhibited excellent water solubility, a pH value comparable to CSS, a sufficiently high amorphous content to promote geopolymerization and flexural strengths that matched or exceeded those of CSS-activated mixes. Consequently, this optimized WGSS sample was selected for subsequent mortar and concrete production, as presented in the following sub-sections, to further assess its viability as a sustainable alternative to CSS.

5.3 Comparative Performance of CSS and Optimized WGSS in Mortar Applications

This section presents a direct comparison between geopolymer mortars activated with CSS and those produced using the optimized WGSS. The evaluation focused on fresh and hardened properties, including consistency, setting time, workability, density, compressive strength, flexural strength and water absorption. Both sets of mortars were designed using the same precursor and activator proportions to ensure that performance differences could be attributed primarily to the type of sodium silicate solution used. The mix compositions used for the comparative study are summarized in Table 5.6. The CSS-activated mortars are designated as Mix 1-C, Mix 2-C, Mix 3-C and Mix 4-C, while the WGSS-activated mortars are designated as Mix 1-GP, Mix 2-GP, Mix 3-GP and Mix 4-GP. It should be noted, however, that the experimental design was structured to enable a controlled comparison between CSS and WGSS and not to conduct a full factorial evaluation of all influencing variables.

Table 5.6: Mix proportions for CSS and WGSS-activated geopolymer mortars

Mix ID	Sand (g)	FA:GGBFS ratio	FA (g)	GGBFS (g)	SS/SH mass ratio	NaOH conc. (M)	AL/B ratio	NaOH soln. (g)	CSS soln. (g)	WGSS soln. (g)
Mix 1-C	1350	1 : 0	338	0	1.5	12	0.50	90	135	–
Mix 1-GP	1350	1 : 0	338	0	1.5	12	0.50	90	–	135
Mix 2-C	1350	7 : 1	296	53	1.5	12	0.50	90	135	–
Mix 2-GP	1350	7 : 1	296	53	1.5	12	0.50	90	–	135
Mix 3-C	1350	3 : 1	254	105	1.5	12	0.50	90	135	–
Mix 3-GP	1350	3 : 1	254	105	1.5	12	0.50	90	–	135
Mix 4-C	1350	1 : 1	169	209	1.5	12	0.50	90	135	–
Mix 4-GP	1350	1 : 1	169	209	1.5	12	0.50	90	–	135

5.3.1 Fresh Properties of CSS and Optimized WGSS Mortars

5.3.1.1 Consistency and Setting Time

As presented in Table 5.7, the WGSS mixes (Mix 1-GP to Mix 4-GP) consistently demanded a greater proportion of alkaline activator to achieve the target penetration depth. The measured consistency values (29.5 – 42.1%) are in line with the general ranges reported for fly ash–GGBFS geopolymer pastes, typically between 26% and 39% (Samantasinghar and Singh, 2019; Rao and Rao, 2015). The increasing activator requirement with rising GGBFS content in both CSS and WGSS systems can be attributed to the angular and irregular morphology of GGBFS particles. Such surface characteristics increase internal friction, thereby requiring a higher alkali dosage to attain normal consistency. In comparison, fly ash particles, which are largely spherical and smooth, create less resistance and allow easier penetration of the Vicat plunger at lower activator levels. This trend corresponds with the findings of Rao and Rao (2015) but contrasts with the observations reported by Samantasinghar and Singh (2019). Furthermore, the incomplete dissolution of waste glass in the WGSS may have further elevated the water demand, thus reducing the workability of these pastes.

Table 5.7: Consistency parameters for CSS and WGSS-based geopolymer pastes

Mix ID	Binder System	Fly ash (g)	GGBFS (g)	Activator dosage (%)	Activator mass (g)	Penetration (mm)
Mix 1-C	CSS	338	0	29.5	99.71	6
Mix 2-C	CSS	296	53	30.6	106.79	7
Mix 3-C	CSS	254	105	32.3	115.96	6
Mix 4-C	CSS	169	209	33.4	126.25	5
Mix 1-GP	WGSS	338	0	38.4	129.79	5
Mix 2-GP	WGSS	296	53	39.8	138.90	6
Mix 3-GP	WGSS	254	105	40.8	146.47	4
Mix 4-GP	WGSS	169	209	42.1	159.14	4

In addition, a marked difference in setting behaviour was observed between the CSS and WGSS systems (Fig. 5.9). The WGSS pastes exhibited significantly shorter setting times, with IST values ranging from 20 to 127 minutes and FST between 149 and 381 minutes. By comparison, CSS mixes showed much slower kinetics, with IST ranging from 205 to 913 minutes and FST extending from 238 up to 1073 minutes. The accelerated setting of the WGSS system is primarily linked to its higher alkalinity and greater ionic activity, which hastens the geopolymerization process. The additional silica released from WGP also contributed to faster gel formation. Notably, the CSS mix containing only fly ash (Mix 1-C) showed very long setting times (about 15 h for IST and 18 h for FST), highlighting the inherently slow reactivity of fly ash under ambient curing, consistent with Samantasinghar and Singh (2019). The incorporation of GGBFS counteracted this sluggish reaction by forming secondary products during geopolymerization, which helped shorten the setting duration (Kolade et al., 2025; Lei et al., 2023; Rao and Rao, 2015; Singh et al., 2020). Interestingly, CSS pastes generally displayed a narrower gap between IST and FST compared with WGSS mixes, suggesting a more uniform transition from the plastic state to a hardened structure. This behaviour points to improved structural stability and potentially better strength development during hardening.

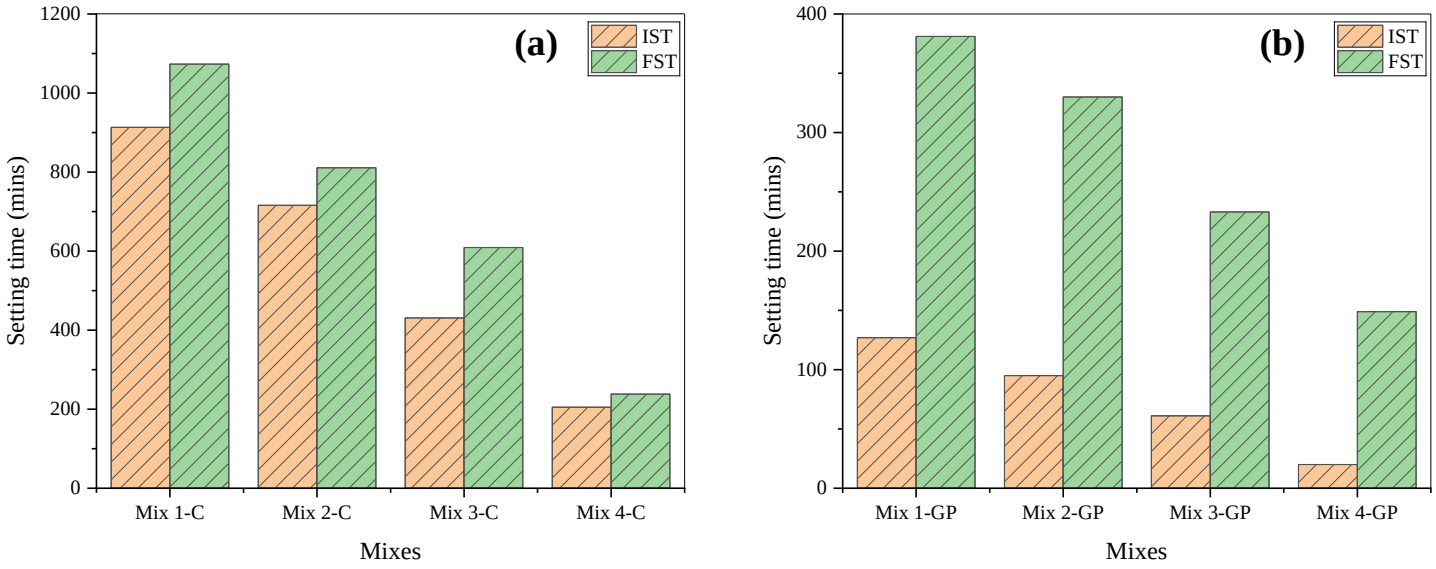

Fig. 5.9: IST and FST for geopolymer pastes based on (**a**) CSS and (**b**) WGSS systems

5.3.1.2 Workability of CSS and Optimized WGSS Mortars

The flow measurements presented in Fig. 5.10 indicate higher workability for CSS mortars, ranging from 145% in Mix 1-C to 90% in Mix 4-C. By comparison, WGSS mortars exhibited lower flow values, from 75% (Mix 1-GP) down to 50% (Mix 4-GP). On average, the CSS group recorded 123.75 ± 24.96%, which was almost double that of the WGSS group at 63.75 ± 11.09%. A t-test confirmed this difference to be statistically significant ($t(6) = 4.394$, $p = 0.005$), with a large effect size (Cohen's $d = 3.107$), pointing to a strong practical distinction between the two systems. This contrast is largely due to the chemistry of the activators. WGSS, with its lower SiO_2/Na_2O ratio, contains shorter silicate chains that speed up gel formation and shorten workable mixing time (Criado et al., 2008). Its higher density, reflecting greater concentrations of dissolved solids and oligomers, also influenced rheology and hindered water dispersion (Ghanim et al., 2025). As illustrated in Fig. 5.10, increasing solution density correspond to decreased mortar flow. In addition, minor phases such as $Na_4Ca(OH)_6$ present in WGSS may have accelerated early reactions, further reducing flowability (Dadsetan et al., 2022; Ghanim et al., 2025).

Mix proportions also played a role. Mortars with higher fly ash content exhibited better flow, owing to the smooth, spherical morphology of fly ash particles, which enhances particle packing and lubrication (Hu et al., 2019). In contrast, GGBFS, with its angular grains, larger surface area and high calcium content, increased water demand and promoted faster setting, both of which reduced workability. Also, the higher powder density of GGBFS relative to fly

ash likely contributed to reduced flow by increasing paste viscosity and limiting particle mobility (Sunarsih et al., 2024). These combined effects explain the progressive decline in flowability observed from Mix 1 through Mix 4 in both mortar series.

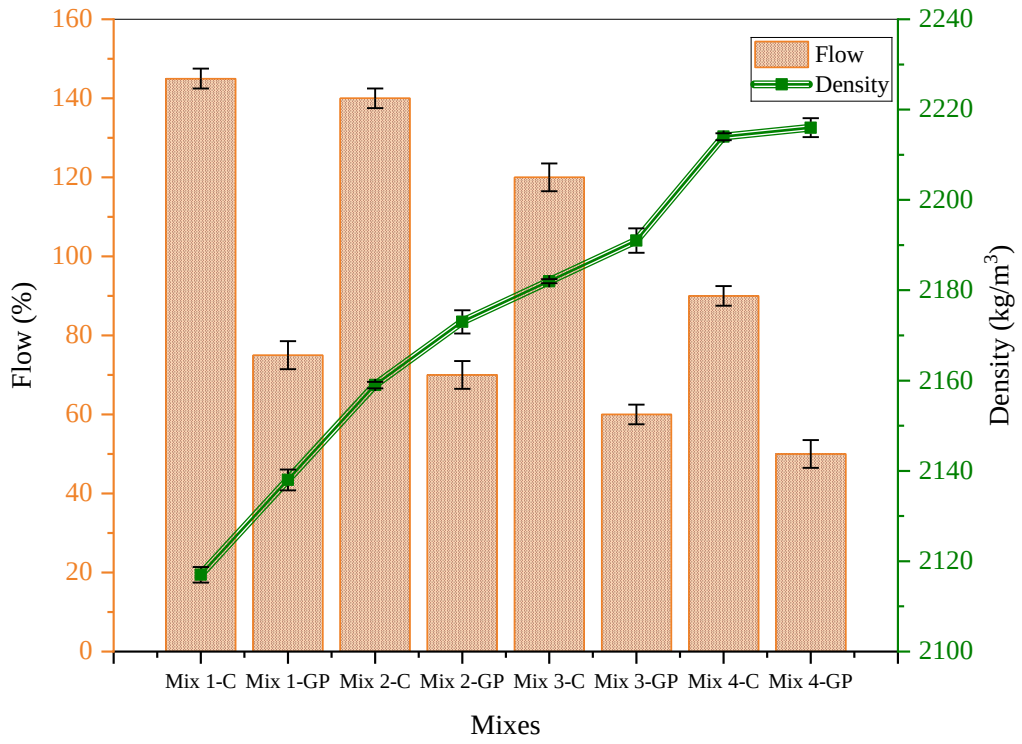

Fig. 5.10: Correlation between density and flowability of geopolymer mortars

5.3.2 Physical Properties

5.3.2.1 Density of CSS and Optimized WGSS Mortars

CSS mortars recorded densities between 2117 and 2214 kg/m^3, whereas WGSS mortars ranged from 2138 to 2216 kg/m^4, as depicted in Fig. 5.10. The progressive density increment across both series reflects the increasing GGBFS replacement, since GGBFS's angular particle morphology and higher specific gravity enhance packing efficiency and generate denser matrices than fly ash–rich mixes (Hu et al. 2019). In addition, the elevated calcium content in GGBFS promotes the early formation of C–S–H gels, which are denser than aluminosilicate geopolymer gels (Luhar and Luhar 2022; Nadarajah et al., 2024; Singh et al., 2024). This effect is most evident in Mix 4-C and Mix 4-GP, both of which produced the highest densities in their respective groups.

WGSS mortars also consistently achieved slightly higher densities than their CSS counterparts. This outcome may be attributed to the higher Na_2O/SiO_2 ratio of the WGSS (approximately

0.96) compared to the CSS with 0.40, which supplied greater alkali availability for precursor dissolution and enhanced polycondensation reactions, thereby forming a denser geopolymer matrix with reduced internal porosity (Delgado-Plana et al., 2024). Furthermore, the higher intrinsic density of WGSS (1.41 g/mL) relative to CSS enhanced solid packing and reduced pore volume, aligning with reported ranges of 1.17 – 1.57 g/mL for synthesized silicates (Ghanim et al., 2025; Kamseu et al., 2017). Also, some studies indicate that the greater silica availability and reduced viscosity of WGSS can improve gel formation and fill voids more efficiently, thereby reducing porosity and increasing density (Ghanim et al., 2025; Torres-Carrasco and Puertas, 2017). These internal refinements provide a rational explanation for the superior density observed in WGSS-based mortars.

5.3.2.2 Water Absorption of CSS and Optimized WGSS Mortars

As shown in Fig. 5.11, all CSS and WGSS mortars satisfied the SANS 1058 (2012) requirement of < 6.5% water absorption. However, their absorption values were higher than the 2.1% reported by Gok and Sengul (2020). The highest absorption of 5.4% for CSS and 5.9% for WGSS occurred in the mixes containing a 1:1 fly ash-to-GGBFS ratio. This trend is attributed to the influence of GGBFS, as its calcium-rich reaction products can modify the pore structure and increase capillary porosity during geopolymerization (Mohamed et al., 2023). The SEM images in Fig. 3.3 further support this behaviour, as fly ash particles are predominantly spherical, promoting close packing and reduced voids, whereas GGBFS particles are angular and irregular, contributing to higher inter-particle voids. Although visible porosity was not prominent in the micrographs, literature indicates that GGBFS also possesses greater internal micro-porosity and reactivity, which increases bound water and promotes capillary pore development (Ahmad et al., 2022). These combined factors explain the higher water absorption in mixes with increased GGBFS content.

Furthermore, WGSS mortars consistently showed slightly higher absorption compared with CSS. This can be linked to their lower SiO_2/Na_2O ratio and higher alkalinity, which accelerate reaction kinetics but also promote uneven gel formation and moisture loss, leaving behind additional microvoids (El-Naggar and El-Dessouky, 2017; Oyejobi et al., 2023). Comparable findings were reported by Kamseu et al. (2017). Furthermore, partially dissolved WGP residues in WGSS improved packing under flexural loads but did not completely integrate into the binder matrix, thereby contributing to microporosity (Ikotun et al., 2024b).

Contrary to studies by Delgado-Plana et al. (2024) and Hu et al. (2019), which associated higher density with lower absorption, the present results reveal that WGSS mortars, though denser, retained greater microporosity, which increased water uptake. While these differences are unlikely to compromise short-term performance, the higher pore volume in WGSS mortars may have long-term durability implications, such as increased susceptibility to freeze–thaw damage, alkali–silica reaction or alkali–carbonate reaction (Amran et al., 2021).

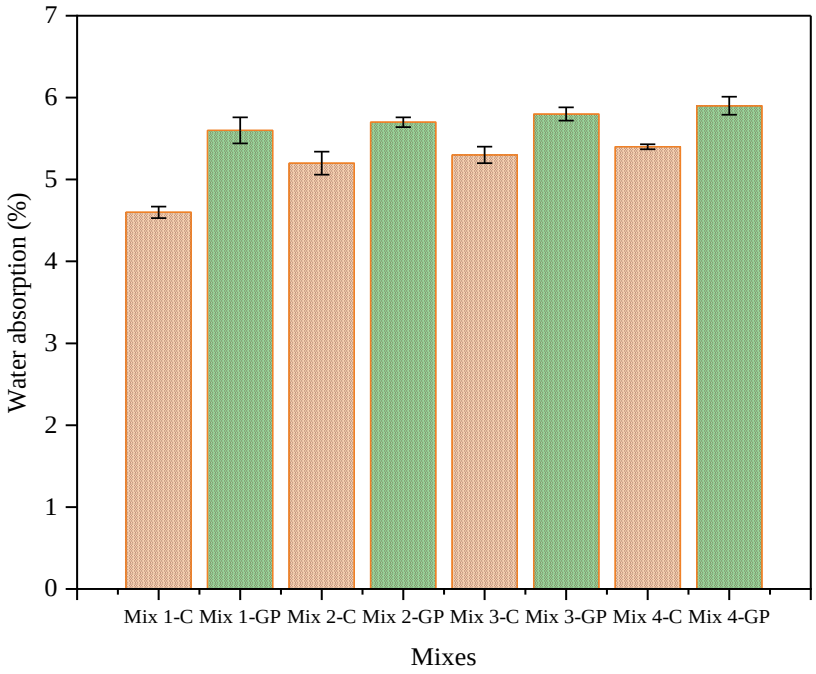

Fig. 5.11: Water absorption of geopolymer mortar mixes

5.3.3 Mechanical Properties

5.3.3.1 Compressive Strength of CSS and Optimized WGSS Mortars

Across all mix proportions and curing periods, CSS-based mortars consistently exhibited higher compressive strengths than WGSS-based mortars, as illustrated in Fig. 5.12. At 28 days, CSS mortars ranged from 45 – 68 MPa, while WGSS mortars ranged from 25 – 46 MPa, indicating a consistent strength advantage for CSS activation across all mix compositions. This pattern has also been observed by Gok and Sengul (2020) in WGP-activated GGBFS-based mortars compared to CSS-based mortars. When considered collectively, the CSS group achieved an average strength of 52.23 ± 10.73 MPa, compared to 37.76 ± 8.93 MPa for WGSS mortars, as determined by an independent samples t-test ($t(6) = 2.074$, $p = 0.083$). While this difference does not meet the generally accepted statistical significance threshold of $p < 0.05$, the effect size (Cohen's $d = 1.464$) suggests a practically meaningful difference. From an

engineering perspective, this represents a strength reduction of approximately 14 MPa (27%), indicating that although WGSS mortars remain structurally viable, CSS activation produces a stronger binder matrix across the investigated mix range.

The elevated strength of the CSS mortars, especially in the fly ash-rich Mix 1-C, can be attributed to an optimal SiO_2/Al_2O_3 ratio that encouraged the formation of a dense, silica-rich polymer network (Mohamed et al., 2023). As the GGBFS fraction increased, the development of calcium-rich C–S–H gels, although beneficial for early-age strength, appeared to interfere with the continuity of the geopolymer matrix, resulting in slightly lower long-term compressive performance (Oyejobi et al., 2023). Comparable trends have been noted in other fly ash-GGBFS systems (Mohamed et al., 2023). On the other hand, Mix 2-GP (FA:GGBFS = 7:1) achieved the highest compressive strength among the WGSS mixes at 28 days (45.31 MPa), exceeding the strength of Mix 1-GP (43.44 MPa). This improvement is attributed to the moderate addition of GGBFS, which introduced calcium that promoted the formation of additional C–A–S–H type gels alongside the geopolymeric network. The coexistence of these gel phases can densify the matrix and enhance load transfer, leading to higher compressive strength compared to the purely fly ash-based system.

Furthermore, the reduced performance of WGSS mortars compared to CSS mortars is linked to several interrelated microstructural factors. The lower modulus and partial dissolution of WGSS left residual particles that acted as weak points within the matrix, limiting the formation of a continuous polymer network (Oyejobi et al., 2023). Research also shows that higher silicate-to-alkali ratios favour –Si–O–Si– bond formation over –Si–O–Al– linkages, conferring enhanced mechanical strength (Luhar and Luhar, 2022; Siddika et al., 2021b). By contrast, CSS solutions provide finer, more reactive silica species, promoting faster and more complete polycondensation reactions that improve matrix compactness (Torres-Carrasco and Puertas, 2017). To achieve similar performance with WGSS, several optimization approaches can be considered, including refining the synthesis conditions to maximize amorphous phase formation and solubility. Also, improving the dissolution process through enhanced mixing, controlled temperature dissolution, or extended aging time can promote the release of reactive silicate species. Further modification of the silicate modulus, for instance through partial adjustment with supplementary silica sources or blending with small proportions of CSS, may also help to improve reactivity and gel formation. Pre-treatment of the waste glass to reduce impurities and finer grinding to increase surface area can further enhance dissolution kinetics and overall activator performance (Kolade et al., 2026b; McCloskey et al., 2024).

Porosity also contributes to the lower strength of WGSS mortars. WGP-derived silicates can generate additional micropores due to incomplete void filling during gel formation (Samarakoon et al., 2021; Torres-Carrasco and Puertas, 2017), which diminishes load-bearing efficiency. Furthermore, the ITZ between paste and sand may be less well-developed in WGSS mortars, creating potential weak points for crack initiation under compression (Siddika et al., 2021b). Supporting evidence from FTIR studies indicates that WGSS matrices typically exhibit weaker Si–O–Si and Si–O–Al vibration bands, reflecting a lower degree of polymerization and reduced network cross-linking (Ghanim et al., 2025; Vinai and Soutsos, 2019).

In addition, the influence of curing time is evident in the progressive strength development observed from 3 to 28 days. The initial heat curing of all the mixes actually accelerated early geopolymerization and promoted rapid formation of initial gel structures. Subsequent curing under ambient conditions allowed continued dissolution of aluminosilicate species and gradual densification of the matrix, resulting in consistent strength gains between 7 and 28 days. For instance, Mix 2-GP increased from 33.35 MPa at 3 days to 45.31 MPa at 28 days, representing a strength gain of approximately 36%. Such behaviour highlights the importance of combined heat and ambient curing in promoting both early reaction kinetics and long-term microstructural development in geopolymer systems.

Taken together, these factors explain the observed differences in compressive strength between CSS and WGSS-based geopolymer mortars. Furthermore, the SEM analysis of concrete mixes later discussed in Section 6.5 corroborates the observed trends in matrix densification, gel morphology and residual unreacted particles, reflecting the mechanical behaviour reported here. These findings highlight the superior compactness achieved with CSS activation and the enhanced densification of WGSS systems with moderate GGBFS addition.

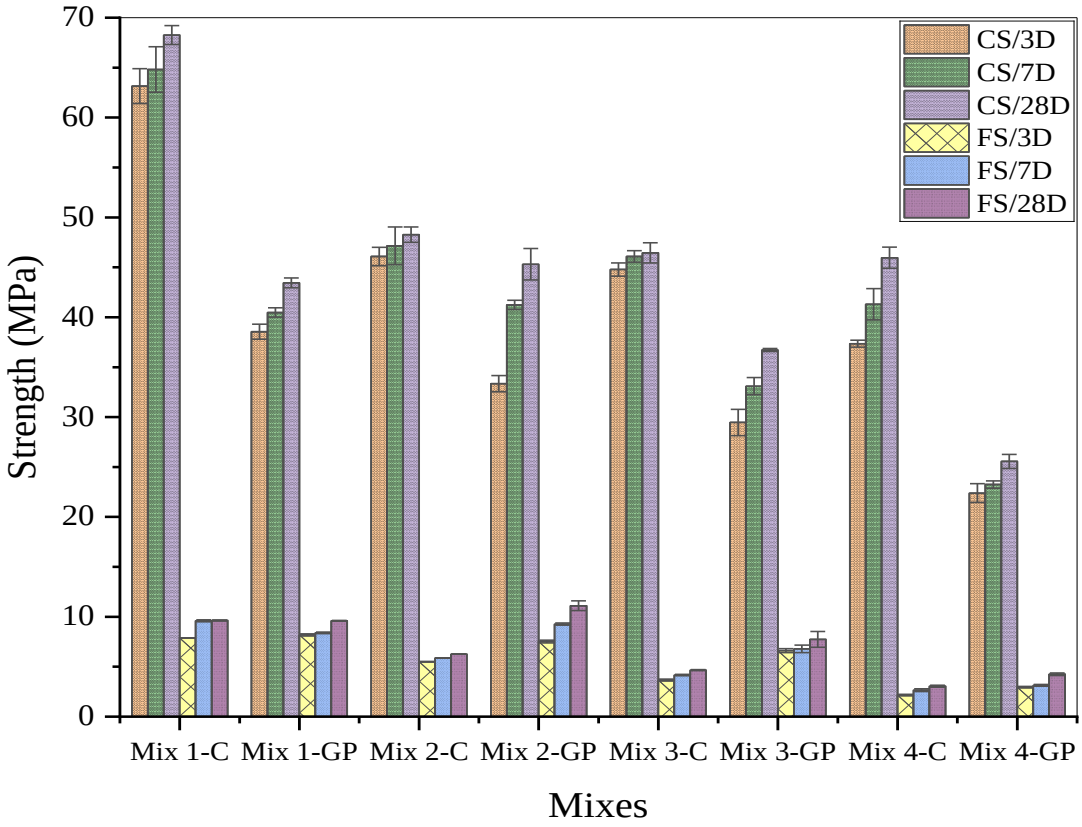

Fig. 5.12: Flexural (FS) and compressive (CS) strength values for geopolymer mortar mixes

5.3.3.2 Flexural Strength of CSS and Optimized WGSS Mortars

Flexural strength of CSS-based mortars decreased as the GGBFS content increased, going from 9.63 MPa in Mix 1-C to 3.05 MPa in Mix 4-C at 28 days, as presented in Fig. 5.12. These results reflect the strong silica-rich networks promoted by CSS in fly ash-dominant mixes, which enhanced bending resistance in Mix 1-C. However, higher proportions of GGBFS led to increased formation of calcium-rich C–A–S–H phases, producing stiffer, more brittle matrices with diminished flexural ductility. Similar findings have been reported by Luhar and Luhar (2022), who observed that geopolymer-based networks generally outperform C–A–S–H systems in flexural behaviour.

In comparison, WGSS-based mortars generally exhibited superior flexural strength at 28 days, ranging from 4 – 12 MPa and indicating that the WGSS system produced higher flexural capacity in three of the four mix compositions. The greatest gains were observed in Mix 2-GP, Mix 3-GP and Mix 4-GP, which achieved flexural strengths of 11.11 MPa, 7.73 MPa and 4.25 MPa, corresponding to increases of 77.5%, 65.9% and 39.3% over their CSS counterparts. It is worth noting that the flexural strength of Mix 3-GP is similar to the 7.3 MPa reported by Gok and Sengul (2020), supporting the effectiveness of glass-based activators in producing

strong mechanical performance. When considered collectively, the WGSS mixes had an average of 8.17 ± 2.96 MPa, exceeding the 5.90 ± 2.81 MPa measured for CSS mortars. Although this difference was not statistically significant ($t(6) = -1.113$, $p = 0.308$), the effect size (Cohen's $d = -0.787$) suggests a potentially meaningful improvement. From an engineering perspective, the average increase of approximately 2.3 MPa corresponds to a ~39% improvement in flexural strength, indicating that WGSS activation may enhance bending resistance despite its lower compressive strength.

The enhanced performance of WGSS mortars is primarily attributed to the optimized SiO_2/Na_2O ratio, which accelerates geopolymerization and strengthens bonding at the paste–aggregate interface. Partially dissolved WGP particles act as rigid inclusions, reinforcing the matrix through a filler effect, serving as nucleation sites for geopolymer gel and improving the ITZ (Delgado-Plana et al., 2024; Ikotun et al., 2025; Siddika et al., 2021b). These particles help arrest microcracks by bridging the particle–gel interface, dissipating fracture energy and delaying crack coalescence, thereby improving toughness and load-bearing capacity (Siddika et al., 2021b). In addition, the intrinsically higher modulus of elasticity (E-value) of glass contributes to the increased stiffness of WGSS mortars. The rigid glass particles reduce local deformation under flexural stress, enhance load transfer across the ITZ and further improve the total bending resistance of the system. SEM observations of similar systems also indicate that these glass inclusions densify the pore structure, reduce stress concentrations and reinforce the matrix, complementing the mechanical advantages provided by chemical and microstructural factors (Siddika et al., 2021b; Torres-Carrasco and Puertas, 2017).

5.3.4 Summary of Comparative Performance of CSS and WGSS Mortars and Binder Strength Classification

This comparative study between CSS and WGSS-based geopolymer mortars demonstrated the feasibility of replacing CSS with a waste-derived activator without compromising essential performance requirements. WGSS-based mortars showed distinct advantages in certain areas, particularly flexural performance, where the optimized formulation (Mix 2-GP) achieved 15.4% higher strength than the best CSS mix.

The independent samples t-test (Table 5.8) further reinforced these trends. Flowability was significantly lower in WGSS mortars compared to CSS, reflecting the influence of residual glass phases and higher solution viscosity. Although CSS mortars recorded a higher mean compressive strength, the difference was not statistically significant and the WGSS mortars

still met structural performance thresholds. This suggests that further refinement of the synthesis process and mix proportions could further narrow or even eliminate this gap. Notably, WGSS mortars also achieved a higher mean flexural strength, indicating improved matrix cohesion and bond characteristics, though this difference was also not statistically significant. Also, WGSS mortars exhibited marginally higher water absorption, which is likely due to micro-voids and residual insoluble phases. However, this property remained within acceptable practical limits for construction use.

Table 5.8: Summary of independent samples t-test results for CSS and WGSS mortars

Property	Group	Mean ± SD	t-value	df	p-value	Cohen's d
Flowability (mm)	CSS	123.75 ± 24.96				
	WGSS	63.75 ± 11.09	4.394	6	0.005	3.107
Compressive strength (MPa)	CSS	52.23 ± 10.73				
	WGSS	37.76 ± 8.93	2.074	6	0.083	1.464
Flexural strength (MPa)	CSS	5.90 ± 2.81				
	WGSS	8.17 ± 2.96	-1.113	6	0.308	-0.787

From a binder-classification standpoint, SANS 50197-1 (2000) specifies 32.5, 42.5 and 52.5 MPa as the standard 28-day strength classes for common cements. Because the classification is primarily intended for PC systems, the comparison presented is used only as a performance benchmark rather than a formal classification of the geopolymer binders. Using these benchmarks, the 28-day compressive strengths of the WGSS-activated mixes (Fig. 5.12) were used to assign indicative strength-class equivalence, as summarized in Table 5.9. Mix 1-GP and Mix 2-GP meet the 42.5-class 28-day strength threshold, while Mix 3-GP corresponds to the 32.5-class levels. Mix 4-GP falls below the 32.5 threshold and therefore does not satisfy the minimum standard class. However, it should be noted that formal classification according to SANS 50197-1 (2000) also requires verification of early-age strength (typically at 2 days for N and R subclasses). Since the present study evaluated strength development from 3 days onward, the classifications reported here are intended only as indicative comparisons based on 28-day compressive strength instead of full compliance with the cement standard. Nevertheless, these findings demonstrate that appropriately formulated WGSS systems can deliver binder-equivalent performance comparable to commercial PC, with Mix 1-GP and Mix 2-GP in particular exhibiting high-grade strength potential. As such, the results validate WGSS

as a viable and sustainable alternative to CSS, with opportunities for further optimization in lower-performing formulations.

Table 5.9: 28-day compressive strength and indicative strength-class equivalence based on SANS 50197-1 (2000) for WGSS-activated geopolymer binders

Mix ID	FA:GGBFS ratio	SS/SH ratio	NaOH conc. (M)	AL/B ratio	28-day strength (MPa)	Indicative 28-day strength class	Classification remarks
Mix 1-GP	1:0	1.5	12	0.5	43.44	42.5 Class	Meets 28-day threshold for Class 42.5
Mix 2-GP	7:1	1.5	12	0.5	45.31	42.5 Class	Meets 28-day threshold for Class 42.5
Mix 3-GP	3:1	1.5	12	0.5	36.72	32.5 Class	Meets 28-day threshold for Class 32.5
Mix 4-GP	1:1	1.5	12	0.5	25.56	Below 32.5 Class	Below minimum 28-day strength requirement

CHAPTER 6

6 STRUCTURAL PERFORMANCE OF REINFORCED CONCRETE BEAMS

This chapter evaluates the performance of GPC mixes prepared with both CSS and WGSS. Four mix formulations were designed with varying fly ash-to-GGBFS ratios, as summarized in Table 6.1, in order to examine the combined effects of activator type and binder composition. The formulations were guided by preliminary experimental trials and insights from prior studies (Alsalman et al., 2021; Oyebisi et al., 2022), with the aim of achieving a target compressive strength of approximately 40 MPa at 28 days. However, to enable a controlled assessment of the influence of activator type, identical mix proportions and chemical parameters were maintained across both CSS and WGSS-based systems. As a result, some mixes, especially the CSS-based formulation, exceeded the target strength. Consequently, the results presented in this chapter are interpreted based on fixed mix compositions, with the CSS system serving as a compositional reference and not a strength-matched benchmark.

The chapter is structured to first present the fresh and hardened properties of the developed mixes, focusing on slump and compressive strength results, which serve as the basis for selecting suitable mixtures for structural applications. Thereafter, the selected GPC mixes were used to cast reinforced concrete beams, which were subjected to flexural and shear testing under a three-point bending configuration. The first crack, yield (computed) and ultimate loads, maximum deflection at failure, flexural and shear capacities, crack patterns and failure modes were examined to provide insights into the ductility, stiffness and structural integrity of beams incorporating GPC with different activators. As such, this comprehensive evaluation links material-level performance (workability and strength) with structural-level behaviour, thereby contributing to a more holistic understanding of the potential of WGSS-activated GPC as a viable alternative for reinforced concrete structures.

Table 6.1: Proportions of GPC mixes per kg/m^3

Mix ID	FA:GGBFS ratio	Fly ash	GGBFS	Fine agg.	Coarse agg.	NaOH soln.	WGSS soln.	CSS soln.	Water	SP
M1	1:0	533.3	–	800	1066.6	106.7	–	160	–	–
M2	1:0	533.3	–	800	1066.6	106.7	160	–	53.3	16
M3	7:1	452.3	81	800	1066.6	106.7	160	–	53.3	16
M4	3:1	377.3	156	800	1066.6	106.7	160	–	53.3	16

6.1 Workability of GPC Mixes

The slump results for the GPC mixes are shown in Fig. 6.1, indicating a systematic reduction in workability with higher GGBFS incorporation and the transition from CSS to WGSS. All mixes exhibited a true slump, with no shear or collapse behaviour, confirming stable deformation characteristics. Although the WGSS mixes contained additional water and superplasticizer compared to the control, their slump values were substantially lower. In terms of cohesiveness, the CSS mix was more plastic and cohesive with minimal segregation, whereas the WGSS mixes became progressively stiffer and less cohesive as GGBFS content increased. No bleeding or excessive segregation was observed in any mix, but WGSS systems showed a noticeably harsher texture.

In addition, the target workability range of 50 – 100 mm commonly reported for laboratory-prepared fly ash/GGBFS-based GPCs (Waqas et al., 2021) was met by all mixes except WGSS M4 (30 mm). The CSS mix (100 mm) and WGSS mixes M2 (60 mm) and M3 (50 mm) fell within the desired range, although workability decreased when switching from CSS to WGSS despite the high admixture dosage. This reduction can be attributed to two key factors. First, lowering the activator modulus from 2.5 (CSS) to approximately 1.0 (WGSS) produced a denser system with modified rheology, including shorter silicate chain formation and reduced fluidity (Criado et al., 2008; Ghanim et al., 2025). Second, increasing the GGBFS content raised binder fineness and calcium availability, accelerating reaction kinetics and increasing water demand, which led to faster stiffening and lower slump. Similar reductions in workability with higher GGBFS incorporation have been reported elsewhere (Hu et al., 2019).

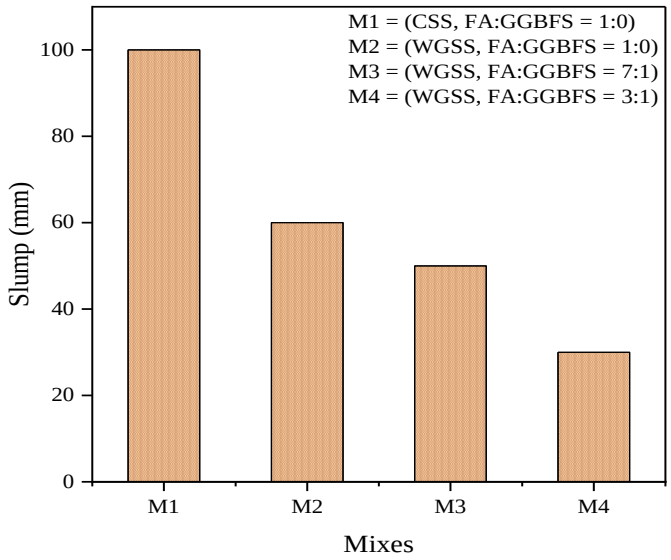

Fig. 6.1: Slump behaviour of GPC mixes as influenced by GGBFS content and type of activator

6.2 Hardened Density of GPC mixes

The average wet (bulk) densities of the GPC mixes at 28 days are presented in fig. 6.2. A consistent trend of increasing density is observed with higher GGBFS incorporation, while WGSS-activated mixes generally showed slightly lower or comparable densities to the CSS-based control (M1). The relatively low density of M2 (2190 kg/m^3) is attributed to its fly ash-only binder system, which forms a less compact matrix due to limited calcium availability. In contrast, the progressive inclusion of GGBFS in M3 and M4 supplied sufficient calcium for the co-formation of C–A–S–H alongside geopolymer gel (as confirmed in Section 6.5), improving matrix densification and resulting in the highest density in M4 (2298 kg/m^3).

Aggregate grading also played a role in the density behaviour. The predominance of the 19 mm coarse fraction, which is approximately 60% of the total aggregate, created a gap-graded profile with minimal material passing the 14 mm and 10 mm sieves (Table A3). This reduced packing efficiency and increased inter-particle voids that contributed to slightly lower bulk densities. Nonetheless, adequate compaction and the higher GGBFS content in some mixes mitigated this effect by enhancing gel formation and improving particle packing.

Although the CSS-activated control (M1) exhibited a marginally higher density than the WGSS-activated M2 (~30 kg/m^3 difference), this small variation indicates that WGSS activation does not significantly affect hardened density. Instead, the density increase from M2 to M4 demonstrates that binder chemistry, especially calcium content, has a stronger influence than activator type. According to EN 206 (2013), concretes with densities between 2000 – 2600 kg/m^3 are classified as normal-weight concrete. All mixes in this study (2190 – 2298 kg/m^3) fall within this range, confirming their suitability for structural applications. Thus, these results reinforce the potential of WGSS as a sustainable activator capable of producing density values consistent with standard structural-grade fly ash/GGBFS-based GPCs reported by Hu et al. (2019).

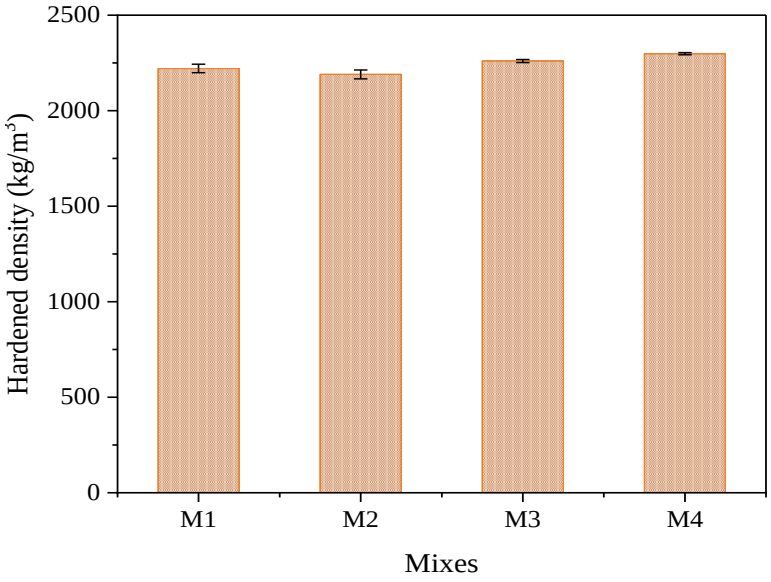

Fig. 6.2: Hardened density of the GPC mixes at 28 days

6.3 Compressive Strength of GPC Mixes

The 28-day compressive strength results are shown in Fig. 6.3, with all mixes except M2 achieving the target 40 MPa. A one-way ANOVA was conducted to examine the effect of mix formulation on compressive strength and the results presented in Table 6.2 indicate a highly significant difference among groups ($F(3,8) = 862.95$, $p < 0.001$). For $\alpha = 0.05$ and df(3,8), the corresponding F-critical value is 4.07, confirming that the calculated F far exceeds the rejection threshold. The effect-size indices presented in Table 6.3 further show that nearly all observed variability is attributable to mix composition ($\eta^2 = 0.997$). Because the ANOVA was significant, Tukey's HSD post-hoc analysis was performed to identify specific pairwise differences, as shown in Table 6.4. The results show that the CSS-activated control (M1) was significantly stronger than all WGSS-activated mixes ($p < 0.001$), while within the WGSS group, M2 was significantly weaker than M3 and M4 ($p < 0.001$). Although M3 and M4 were also significantly different at the 0.05 level ($p = 0.019$), the magnitude of the difference was relatively small, suggesting that increases in GGBFS beyond the M3 level yield diminishing returns in strength development. These observations are consistent with those reported by Hu et al. (2019), who observed that the benefit of GGBFS incorporation eventually stabilizes as the reactive calcium contribution approaches saturation. From an engineering design perspective, such a modest strength difference between M3 and M4 would be unlikely to produce a substantial change in structural member design, since beam capacity is typically governed by reinforcement rather than concrete compressive strength and both mixes would generally fall within the same practical strength class for design purposes.

Furthermore, the reduced performance of WGSS mixes can be linked to their lower activator modulus compared with CSS (~1.0 vs. 2.5), which likely shortened silicate chains, reduced dissolution efficiency and hindered geopolymer gel formation. Residual solids in WGSS may also have slowed reaction kinetics (Luhar and Luhar, 2022; Siddika et al., 2021b). For M2, the absence of adequate calcium limited the co-formation of C–S–H, resulting in the lowest strength. In contrast, the incorporation of GGBFS in M3 and M4 supplied reactive calcium, promoted hybrid gel formation, densified the binder matrix and improved strength. That said, the observed strength range of M2 – M4 is consistent with literature reports (26 – 52 MPa) for similar fly ash-GGBFS blends using CSS activators (Hu et al., 2019).

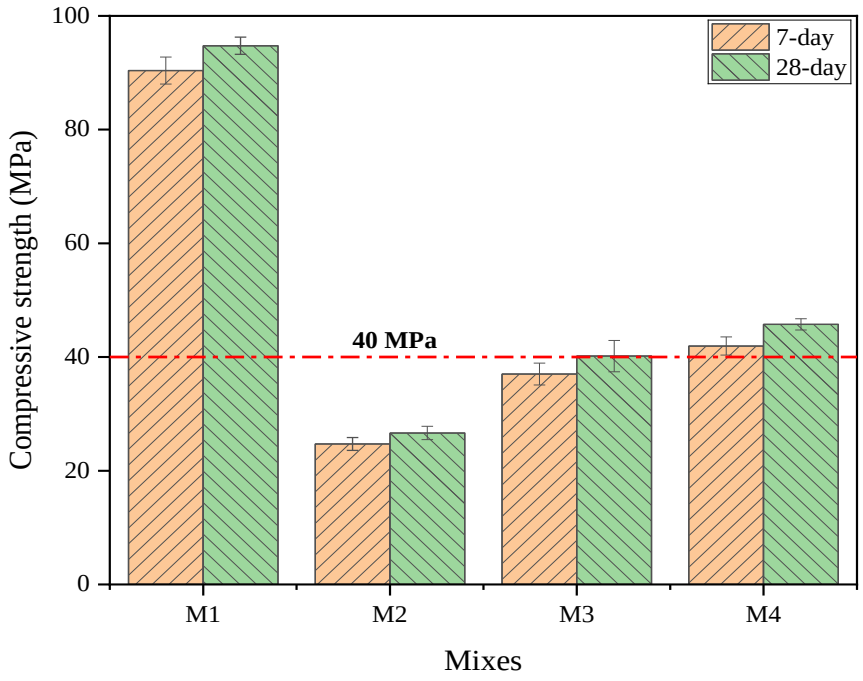

Fig. 6.3: Mean compressive strength of GPC mixes at 7 and 28 days

Table 6.2: One-way ANOVA for compressive strength

Source of variation	Sum of Squares	df	Mean Square	F	Sig.
Between groups	7949.240	3	2649.747	862.948	< 0.001
Within groups	24.565	8	3.071	–	–
Total	7973.805	11	–	–	–

Table 6.3: Effect size estimates for ANOVA

Effect size measure	Point estimate	95% confidence interval	
		Lower	Upper
Eta-squared (η^2)	0.997	0.983	0.998
Epsilon-squared	0.996	0.977	0.997
Omega-squared Fixed-effect	0.995	0.975	0.997
Omega-squared Random-effect	0.986	0.928	0.991

Table 6.4: ANOVA Tukey HSD multiple comparison results for strength

(I) Mix	(J) Mix	Mean difference (I-J)	Std. error	Sig.	95% confidence interval	
					Lower bound	Upper bound
1	2	68.11000*	1.43075	< 0.001	63.5282	72.6918
	3	54.58000*	1.43075	< 0.001	49.9982	59.1618
	4	49.01333*	1.43075	< 0.001	44.4316	53.5951
2	1	-68.11000*	1.43075	< 0.001	-72.6918	-63.5282
	3	-13.53000*	1.43075	< 0.001	-18.1118	-8.9482
	4	-19.09667*	1.43075	< 0.001	-23.6784	-14.5149
3	1	-54.58000*	1.43075	< 0.001	-59.1618	-49.9982
	2	13.53000*	1.43075	< 0.001	8.9482	18.1118
	4	-5.56667*	1.43075	0.019	-10.1484	-0.9849
4	1	-49.01333*	1.43075	< 0.001	-53.5951	-44.4316
	2	19.09667*	1.43075	< 0.001	14.5149	23.6784
	3	5.56667*	1.43075	0.019	0.9849	10.1484

*Mean differences marked with * are significant at $\alpha = 0.05$.*

To consolidate the results presented in this section and provide a clear basis for the subsequent discussion on structural performance, a summary Table 6.5 is included. The table compiles the key characteristics and performance indicators of all GPC mixes, including mix ID, binder composition, activator type and modulus, workability (slump), hardened density and 28-day compressive strength. This integrated overview facilitates direct comparison between mixes and supports the interpretation of trends discussed throughout this chapter.

Table 6.5: Summary of mix proportions and key performance properties of GPC mixes

Mix ID	FA:GGBFS Ratio	Activator type	Activator modulus	Slump (mm)	Density (kg/m^3)	28-day Compressive Strength (MPa)
M1	1:0	CSS	2.50	100	2221 ± 22.34	94.75 ± 1.52
M2	1:0	WGSS	~1.0	60	2190 ± 23.52	26.64 ± 1.18
M3	7:1	WGSS	~1.0	50	2260 ± 8.19	40.17 ± 2.76
M4	3:1	WGSS	~1.0	30	2298 ± 5.51	45.74 ± 0.99

6.4 Structural Performance of GPC Mixes

6.4.1 Load-carrying Capacity of GPC Beams

The load-carrying capacity of the beams was evaluated through their first-crack and ultimate load responses in both flexure and shear. The experimental results presented in Table 6.6 show clear distinctions between the control and WGSS mixes in terms of cracking load, ultimate load capacity and the progression of structural performance from 7 to 28 days. The curing age was restricted to 28 days because heat-cured GPC typically develops strength rapidly, achieving structurally reliable performance at much earlier ages than conventional PCC. This early high-strength behaviour indicates that curing periods may be shortened in practice, allowing construction activities to be accelerated without compromising load-carrying capacity.

Table 6.6: Beam test results at 7 and 28 days

Mix ID	Curing days	Comp. strength (MPa)	Flexure				Shear			
			First crack (kN)	Ultimate load (kN)	Mid-span deflection (mm)	Mass (kg)	First crack (kN)	Ultimate load (kN)	Mid-span deflection (mm)	Mass (kg)
M1	7 days	90.39	52.11	74.40	5.1	37.77	53.00	82.00	5.2	37.96
	28 days	94.75	54.30	76.40	5.3	38.70	55.10	84.60	5.2	37.00
M3	7 days	37.01	30.35	67.04	5.4	36.55	27.91	59.51	4.2	35.99
	28 days	40.17	34.96	77.09	7.2	36.56	28.61	62.70	3.9	35.76
M4	7 days	41.94	21.57	59.58	4.1	36.98	20.46	55.27	4.0	36.57
	28 days	45.64	24.83	67.38	4.9	37.20	20.88	62.73	4.3	36.53

6.4.1.1 First Crack Load, Flexural Moments and Shear Capacities

The first crack responses presented in Table 6.6 show a clear distinction between the CSS and WGSS beams at both curing ages. In flexure, the control mix consistently exhibited the highest first crack loads, reaching 52.11 kN at 7 days and 54.30 kN at 28 days. In contrast, M3 attained 30.35 kN and 34.96 kN, while M4 achieved 21.57 kN and 24.83 kN over the same period. A similar pattern was observed in shear, with the CSS beams recording 53.00 kN and 55.10 kN compared with 27.91 kN and 28.61 kN for M3 and 20.46 kN and 20.88 kN for M4. These trends reflect the stronger early-age tensile behaviour of the CSS mix, which benefits from a denser matrix and a more developed binder structure relative to the WGSS systems.

To express these crack initiation loads in structural terms, the experimental flexural first crack moments ($M_{exp,cr}$) and shear ($V_{exp,cr}$) capacities were calculated using the standard mid-span point-load relations according to Eqs. (6.1) and (6.2). Also, the theoretical cracking moments ($M_{EC2,cr}$) and shear capacities ($V_{EC2,cr}$) without shear reinforcements were computed according to EC2 provisions using Eqs. (6.3) and (6.4).

$$\text{First crack moment capacity } (M_{exp,cr}) = \frac{P_{cr}L}{4} \tag{6.1}$$

$$\text{First crack shear capacity } (V_{exp,cr}) = \frac{P_{vcr}}{2} \tag{6.2}$$

Where: P_{cr} = experimental first crack flexural load, P_{vcr} = experimental first crack shear load and L = beam clear span (600 mm, Fig. 3.9).

$$\text{EC2 cracking moment } (M_{EC2,cr}) = f_{ctm}\frac{I_g}{y} \tag{6.3}$$

Where: $I_g = bh^3/12$; y = half of beam depth (h/2); $f_{ctm} = 0.3(f_{ck}^{2/3})$ for $f_{ck} \leq 50$ MPa or 2.12 ln $(1 + (f_{cm}/10))$ for $f_{ck} > 50$ MPa; $f_{cm} = f_{ck} + 8$; f_{ck} = concrete strength.

$$\text{EC2 shear capacity } (V_{EC2,cr}) = (C_{Rd,c}k\,(100\rho_l f_{ck})^{1/3} + k_1\sigma_{cp})\,bd \tag{6.4}$$

Where: $C_{Rd,c} = 0.18/\gamma_c$; $k = 1 + \sqrt{200/d} \leq 2.0$ ("d" in mm); $\rho_l = A_{sl}/bd$; d = effective depth

$k_1 = 0.15$; σ_{cp} = axial stress (zero here); A_{sl} = area of tensile reinforcement; γ_c = concrete material factor.

Tables 6.7 and 6.8 present the computed experimental cracking capacities of the GPC beams. Despite the lower early-age capacities of the WGSS beams, they still exhibited notable

improvements between 7 and 28 days. Both M3 and M4 recorded approximately 15% increases in flexural cracking load and moment capacity, compared with only a 4% increase in the CSS beams, indicating continued geopolymerization and matrix densification associated with the fine WGP particles, which promote secondary gel formation and strengthen interfacial bonding (Delgado-Plana et al., 2024; Siddika et al., 2021b). The shear capacities showed smaller age-related increases, consistent with the greater sensitivity of diagonal tension cracking to early-age matrix quality. At 28 days, the flexural first crack load of M3 approached the 30 – 37 kN range reported by Eisa et al. (2022) and Kalaivani et al. (2020) for CSS-activated fly ash/GGBFS beams, whereas M4 remained below this benchmark. This lower performance of M4 can be attributed to its higher GGBFS content, which promoted the formation of C–A–S–H-type gels at the expense of a well-developed geopolymer gel network, thereby weakening interparticle bonding and facilitating earlier crack propagation under flexural loading. Nevertheless, the shear cracking loads of both WGSS mixes were lower than the 36 – 40 kN typically reported in those studies.

It is also important to note that while the lower early-age resistance of WGSS beams may influence short-term serviceability, their more distributed and gradually propagating cracking pattern (Section 6.4.3) suggests reduced brittleness and potentially improved long-term crack stability. Thus, the combined load and capacity results show that WGSS mixes have weaker early tensile and shear resistance relative to CSS but develop meaningful later-age improvements that enhance their crack initiation behaviour.

Table 6.7: First crack flexural moment capacity — experimental vs. EC2 design

Mix ID	Curing Days	Comp. strength (MPa)	First crack (P_{cr}, kN)	$M_{exp,cr}$ (kNm)	$M_{EC2,cr}$ (kNm)	$M_{exp,cr}/M_{EC2,cr}$
M1	7 days	90.39	52.11	7.82	2.84	2.75
	28 days	94.75	54.30	8.15	2.89	2.82
M3	7 days	37.01	30.35	4.55	1.87	2.43
	28 days	40.17	34.96	5.24	1.98	2.64
M4	7 days	41.94	21.57	3.24	2.04	1.59
	28 days	45.64	24.83	3.72	2.16	1.72

Table 6.8: First crack shear capacity — experimental vs. EC2 design

Mix ID	Curing Days	Comp. strength (MPa)	First crack (P_{vcr}, kN)	$V_{exp,cr}$ (kN)	$V_{EC2,cr}$ (kN)	$V_{exp,cr}/V_{EC2,cr}$
M1	7 days	90.39	53.00	26.50	18.53	1.43
	28 days	94.75	55.10	27.55	18.82	1.46
M3	7 days	37.01	27.91	13.96	13.76	1.01
	28 days	40.17	28.61	14.31	14.14	1.01
M4	7 days	41.94	20.46	10.23	14.34	0.71
	28 days	45.64	20.88	10.44	14.75	0.71

In addition, the measured flexural cracking moments of all beams exceeded the theoretical estimates. For the CSS beams (M1), the experimental flexural cracking moments were approximately 2.7 – 2.8 times the EC2 predictions, while the WGSS beams (M3 and M4) exceeded EC2 values by 2.4 – 2.6 and 1.6 – 1.7, respectively. This consistent upward deviation demonstrates that EC2 provides a conservative lower-bound estimate of flexural cracking, especially for high-strength concretes whose tensile strength develops more rapidly than assumed in the code's generic formulations. A similar trend is also observed for shear-cracking performance, although with greater mix-dependent variability. The CSS beams again outperformed EC2 estimates, achieving first-crack shear capacities 43 – 46% higher than predicted. The M3 beams showed near-perfect agreement, with experimental-to-EC2 ratios of approximately 1.00, indicating that EC2 reliably predicted shear cracking for mixes with moderate strength and more conventional tensile behaviour. Conversely, the M4 beams recorded shear capacities about 29% lower than EC2 values, likely due to a less mature microstructure or reduced aggregate interlock, both critical to shear transfer. That said, the results show that while EC2 predictions are generally conservative, their accuracy varies with binder type and strength class. Notably, these findings contrast with Ozkilic et al. (2025) and Ozturk and Arslan (2023), who reported EC2 overestimating first-crack behaviour in GPC beams made with conventional alkaline activators and designed for flexural and shear failures.

6.4.1.2 Ultimate Load Capacity, Flexural Moments and Shear Capacities

The ultimate load results (Fig. 6.4) established that the control CSS beams achieved 28-day flexural and shear capacities of 76.40 kN and 84.60 kN, respectively. The higher shear capacity

observed for M1 relative to its flexural capacity can be attributed mainly to the very high compressive strength of the CSS concrete (>90 MPa), which increased the concrete contribution to shear resistance. On the other hand, the flexural capacity of a singly reinforced beam is primarily governed by the tensile reinforcement and therefore does not increase proportionally with concrete compressive strength. Furthermore, M3 achieved 77.09 kN in flexure and 62.70 kN in shear, while M4 recorded 67.38 kN in flexure and 62.73 kN in shear. Notably, M3 slightly exceeded the control in flexural capacity (77.09 kN vs. 76.40 kN), despite its much lower compressive strength. This indicates that flexural performance of the WGSS beams remained comparable to the control despite substantially lower compressive strength.

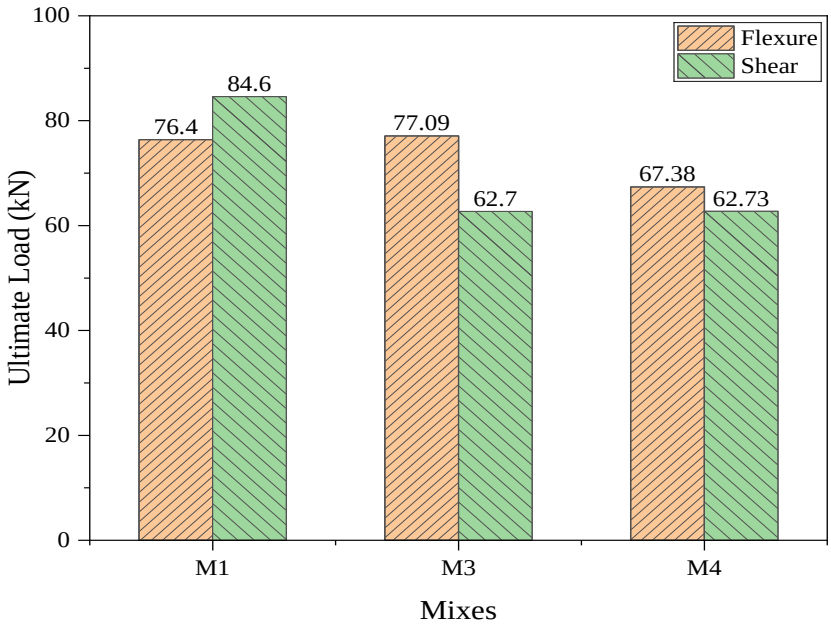

Fig. 6.4: 28-day ultimate load in flexure and shear of GPC beams

To interpret these behaviours in design-relevant terms, the recorded ultimate loads were converted using Eq. (6.5) – (6.8) to bending moments (M_{exp}) and shear capacities (V_{exp}) and compared with the EC2 design resistance (M_{Rd}, V_{Rd}), as shown in Tables 6.9 and 6.10.

Design moment resistance (factored) for rectangular singly reinforced section (M_{Rd}):

$$M_{Rd} = A_s \times f_{sd} \times z \qquad (6.5)$$

Where: A_S = tensile steel area; lever arm (z) = d – 0.4x;

$$\text{design compressive block depth (x)} = \frac{A_s \times f_{sd}}{0.85 \times f_{cd} \times b}$$

b = beam width; $f_{cd} = f_{ck}/\gamma_c$; $f_{sd} = f_{yk}/\gamma_s$; f_{yk} = steel yield strength; f_{ck} = concrete strength;

γ_c = concrete material factor; γ_s = steel material factor.

$$\text{Total shear resistance } (V_{Rd}) = V_{Rd,c} + V_{Rd,s} \quad (6.6)$$

$$V_{Rd,c} = (C_{Rd,c} k (100\rho_l f_{ck})^{1/3} + k_1 \sigma_{cp}) bd \quad (6.7)$$

$$V_{Rd,s} = \frac{A_{sw} \times f_{sd} \times Z}{s} \quad (6.8)$$

Where: $C_{Rd,c} = 0.18/\gamma_c$; $k = 1 + \sqrt{200/d} \leq 2.0$ ("d" in mm); $\rho_l = A_{sl}/bd$; $k_1 = 0.15$;

σ_{cp} = axial stress (zero here); A_{sw} = area of shear reinforcement; z = lever arm

s = stirrup spacing; $f_{sd} = f_{yk}/\gamma_s$; A_{sl} = area of tensile reinforcement.

Table 6.9: Ultimate flexural moment capacity — experimental vs. EC2 design

Mix ID	Curing days	Comp. strength (f_{ck}, MPa)	Ultimate load (P_u, kN)	M_{exp} (kNm)	M_{Rd} (kNm, EC2)	M_{exp}/M_{Rd}
M1	7 days	90.39	74.40	11.16	6.40	1.74
	28 days	94.75	76.40	11.46	6.41	1.79
M3	7 days	37.01	67.04	10.06	6.18	1.63
	28 days	40.17	77.09	11.56	6.21	1.86
M4	7 days	41.94	59.58	8.94	6.23	1.43
	28 days	45.64	67.38	10.11	6.25	1.61

Table 6.10: Ultimate shear capacity — experimental vs. EC2 design

Mix ID	Curing days	Comp. strength (f_{ck}, MPa)	Ultimate load (P_{vu}, kN)	V_{exp} (kN)	$V_{Rd,c}$ (kN)	$V_{Rd,s}$ (kN)	V_{Rd} (kN)	V_{exp}/V_{Rd}
M1	7 days	90.39	82.00	41.00	18.53	18.22	36.75	1.12
	28 days	94.75	84.60	42.30	18.82	18.24	37.06	1.14
M3	7 days	37.01	59.51	29.76	13.76	17.58	31.34	0.95
	28 days	40.17	62.70	31.35	14.14	17.66	31.80	0.99
M4	7 days	41.94	55.27	27.64	14.34	17.70	32.04	0.86
	28 days	45.64	62.73	31.37	14.75	17.78	32.53	0.96

Under flexure, all mixes demonstrated significant reserve capacity beyond the EC2 design predictions, with M_{exp}/M_{Rd} ratios ranging from 1.43 to 1.86. The 28-day M3 beam exhibited the highest value (1.86), indicating that its experimental moment capacity exceeded the EC2 design moment by 86%. This enhanced behaviour can be attributed to several factors, including the calibration of EC2 formulas for normal cement concrete, the inherent conservative nature of EC2 stress-block formulations, the use of partial safety factors and strain-hardening effects of the reinforcement that are not captured by the simplified design model. The performance of M3 is particularly noteworthy, as it achieves a higher moment capacity than CSS control despite possessing less than half of its compressive strength. This behaviour demonstrates the efficiency of WGSS binders in translating compressive strength into flexural performance, which can be attributed to the microstructural role of WGP particles in refining the ITZ, enhancing particle packing and improving stress transfer pathways (Delgado-Plana et al., 2024; Siddika et al., 2021b). The 7 – 28-day increases further highlight this effect, as M3 and M4 recorded +15% and +13% improvements in ultimate load compared with only +3% for the control, confirming the sustained geopolymerization and densification characteristic of WGSS systems.

The shear capacity results also reveal a different trend. While the control CSS beams achieved V_{exp}/V_{Rd} values above unity (1.12 – 1.14), indicating a comfortable margin above EC2 design resistance, the WGSS mixes approached unity more gradually. M3 increased from 0.95 at 7 days to 0.99 at 28 days and M4 from 0.86 to 0.96. These results indicate that WGSS beams develop adequate shear resistance but with a smaller reserve than in flexure, reflecting the greater dependency of shear on aggregate interlock and diagonal tension behaviour, which are mechanisms that improve with age but respond less strongly to the microstructural benefits imparted by WGP. Nevertheless, the near-unity values at 28 days confirm that WGSS mixes attain reliable shear performance and are structurally competitive.

From a broader design perspective, these findings challenge the conventional assumption that compressive strength alone governs structural capacity. WGSS GPCs, especially M3, demonstrate a favourable balance of tensile efficiency and toughness, making them attractive for flexure-dominated components such as beams and slabs. Their strong performance is further supported by comparisons with literature, as the 28-day flexural capacities of WGSS beams fall above the 44 – 62 kN range reported for CSS-activated fly ash/GGBFS beams and their shear capacities exceed the 42 – 53 kN ranges commonly documented in earlier studies (Eisa et al., 2022; Kalaivani et al., 2020; Ozkilic et al., 2025). When combined with the

environmental advantages of waste-glass activation, the mechanical results strengthen the case for WGSS binders as viable and structurally efficient alternatives to conventional CSS systems.

6.4.1.3 Theoretical Yield Load Prediction Using EC2

Theoretical yield loads of the beams were calculated analytically because they could not be obtained experimentally due to the limitation of the testing setup. As such, the yield moment (M_y) and corresponding yield load (P_y) for a simply supported beam under a central point load were estimated using sectional equilibrium at steel yield based on an EC2-style rectangular stress block. The governing equation (Eq. (6.5)) was rearranged to obtain expressions for the yield moment (Eq. (6.9)) and yield load (Eq. (6.10)). The calculated yield loads (P_y = 46 – 49 kN) were then compared with the experimentally measured first-crack (P_{cr} = 21 – 55 kN) and ultimate (P_u = 59 – 77 kN) flexural loads, as summarized in Table 6.11.

$$\text{Yield moment } (M_y) = A_s \times f_y \times z \tag{6.9}$$

$$\text{Yield load } (P_y) = \frac{4\,M_y}{L} \tag{6.10}$$

Where: A_S = tensile steel area; lever arm (z) = d – 0.4x; $x = \dfrac{A_s \times f_y}{0.85 \times f_{cd} \times b}$

$f_{cd} = \alpha_{cc} f_{ck}/\gamma_c$; α_{cc} = 0.85; b = beam width; $f_y = f_{yk}$; f_{yk} = ~400 MPa;

γ_s = steel material factor (1.15); L = beam clear span (600mm).

Table 6.11: Computed yield moments and loads using the EC2-equilibrium approach

Mix ID	Curing days	Comp. strength (f_{ck}, MPa)	M_y (kNm)	P_y (kN)	P_{cr} (kN)	P_u (kN)
M1	7 days	90.39	7.30	48.65	52.11	74.40
	28 days	94.75	7.31	48.73	54.30	76.40
M3	7 days	37.01	6.99	46.64	30.35	67.04
	28 days	40.17	7.00	46.64	34.96	77.09
M4	7 days	41.94	7.02	46.79	21.57	59.58
	28 days	45.64	7.06	47.07	24.83	67.38

For mixes M3 and M4, the experimental first-crack loads were lower than the theoretical yield loads ($P_{cr} < P_y$: M3 = 34.96 kN < 46.64 kN and M4 = 24.83 kN < 47.07 kN at 28 days), which aligns with expected behaviour in reinforced concrete where flexural cracking initiates prior to reinforcement yielding. Similarly, for both mixes the experimental ultimate loads exceeded the theoretical yield loads ($P_u > P_y$: M3 = 77.09 kN > 46.64 kN and M4 = 67.38 kN > 47.07 kN), indicating that the tensile steel likely yielded during loading before the beams reached failure. This interpretation is consistent with strain-compatibility principles, since the steel yield strain ($\varepsilon_y \approx 0.002$) represents the curvature at which yielding initiates in the reinforcement. Also, the fact that $P_u \gg P_y$ in M3 and M4 suggests that the tensile steel strains exceeded ε_y, allowing the beams to enter a post-yield phase with increasing deformation capacity prior to ultimate failure.

In contrast, for mix M1 the theoretical yield load (~48 kN) was lower than the experimentally observed first-crack loads (52 – 54 kN), creating an apparent anomaly. This behaviour is attributed to the very high compressive strength of M1 (>90 MPa), which enhanced section stiffness and tensile resistance, thereby delaying visible cracking relative to EC2 predictions. Because EC2 flexural equations are calibrated for normal-strength concretes, they tend to underestimate the flexural capacity of high-strength or low-crack-width GPCs. This limitation becomes more pronounced at higher strengths where the shape and depth of the stress block deviate significantly from the rectangular assumptions of EC2, especially above C50/60 (Iskhakov and Ribakov, 2019). In such stiff, high-strength matrices, the neutral axis shifts upward and curvature at first crack may remain below the steel yield strain, meaning cracking can occur at load levels that exceed the code-predicted P_y without any contradiction to strain theory.

In addition, the experimental ultimate loads were substantially greater than the theoretical yield loads ($P_u > P_y$) across all mixes, confirming that steel yielding likely occurred prior to failure and that additional moment capacity was developed through mechanisms such as strain hardening in the reinforcement, aggregate interlock and enhanced concrete compression redistribution. These post-yield contributions are activated only after the steel surpasses ε_y, which further supports the conclusion that the beams, particularly for M3 and M4, experienced significant tensile-steel yielding during the loading history.

6.4.2 Mid-span Deflection at Failure

The mid-span deflection values at failure provide insight into ductility and deformation capacity. In flexure, the control beams failed at constant deflections of approximately 5 mm at

both 7 and 28 days, indicating a stiff and relatively brittle response. By contrast, M3 showed an increase from 5.4 mm to 7.2 mm and M4 from 4.1 mm to 4.9 mm over the same curing interval, suggesting that WGSS beams can sustain greater deformation prior to failure, which is a desirable attribute for structural resilience. This trend is consistent with strain-compatibility expectations, since the steel yield strain corresponds to the onset of yielding in the tensile reinforcement. Thus, beams that exhibit larger deflection at ultimate are those that undergo greater curvature and rotation before the steel reaches or exceeds its yield strain. The higher mid-span deflections observed in M3 therefore indicate that the beam progressed further into the post-yield regime compared with the control, confirming enhanced ductility and a more favourable tension-controlled failure mode. This enhanced ductility implies better energy absorption and load redistribution capacity, making WGSS concretes more suited for applications where toughness and post-cracking deformation are critical, such as seismic-resistant structures or elements subjected to cyclic or impact loading.

In shear, however, the trends were less pronounced, as M3 recorded a decrease in deflection from 4.2 mm to 3.9 mm, while M4 remained constant at approximately 4 mm and the control at 5 mm. These results indicate that the ductility advantages of WGSS binders are more evident in flexural behaviour than in shear. It is also important to note that at 28 days the WGSS beams exhibited deflections that surpassed the 3 mm reported by Eisa et al. (2022) and were consistent with the 6 – 8 mm range observed by Kalaivani et al. (2020) for fly ash/GGBFS beams activated with CSS.

In addition, predicted midspan deflections were obtained using the nonlinear moment–curvature method in accordance with EC2 Clauses 3.1.2 – 3.2, with curvature integration for deflection evaluation as outlined in Annex B. The procedure involved deriving the moment–curvature relationship for each beam section by integrating the concrete and steel stresses based on their nonlinear constitutive models. The corresponding curvature distribution along the span was then numerically integrated to estimate the midspan deflection. This method captures key nonlinear phenomena such as post-cracking behaviour, tension stiffening and stiffness degradation to provide a more realistic representation of reinforced concrete response than linear elastic serviceability approaches (Bhatt et al., 2014).

Table 6.12 presents the comparison between experimental and predicted deflections under flexure and shear. The predicted values are consistently higher than the measured ones, with the discrepancy most pronounced for the high-strength mix M1. This behaviour can be

attributed to the more brittle nature of high-strength concrete, which, despite its higher compressive strength, exhibits lower ultimate strain and reduced curvature capacity after cracking. Consequently, the nonlinear moment–curvature analysis predicts larger curvatures and hence larger deflections for M1. Conversely, the lower-strength mixes (M3 and M4) display more ductile post-cracking behaviour, resulting in smaller predicted deflections and better agreement with experimental observations. As such, the results highlight the sensitivity of nonlinear deflection prediction to material properties, especially concrete strength and ductility.

Table 6.12: Experimental vs. predicted midspan deflection using EC2

Mix ID	Curing days	Compressive strength (MPa)	Flexure		Shear	
			Experimental deflection (mm)	Predicted deflection (mm)	Experimental deflection (mm)	Predicted deflection (mm)
M1	7 days	90.39	5.1	15.1	5.2	18.2
	28 days	94.75	5.3	16.1	5.2	19.3
M3	7 days	37.01	5.4	9.5	4.2	5.0
	28 days	40.17	7.2	13.7	3.9	7.1
M4	7 days	41.94	4.1	5.1	4.0	4.5
	28 days	45.64	4.9	9.9	4.3	4.7

6.4.3 Crack Propagation and Failure Modes

The crack development and failure behaviour of the beams showed clear differences that can be attributed to variations in matrix composition, reinforcement arrangement and activator type. In the control beams (CSS-activated), the ultimate shear capacity exceeded the flexural capacity, consistent with the tendency of high-strength matrices to exhibit flexure-controlled response due to their high compressive resistance and low tensile ductility (Cai et al., 2024; Hasan and Saeed, 2023). Flexural cracks initiated at mid-span where tensile stress is maximum (Fig. 6.5a), appearing few in number but wide (up to 3 mm). This behaviour is expected in beams where reinforcement ratio is relatively low compared with the high matrix strength, causing reinforcement to yield before the concrete reaches its compressive limit (Kumar et al., 2017; Pam et al., 2001). As yielding occurred, crack widths increased rapidly, leading to brittle

flexural failure with minimal strain redistribution. Reinforcement placement also influenced crack spacing, as the single-layer longitudinal steel resulted in wider spacing and fewer cracks, consistent with established crack-control principles in reinforced concrete (Gilbert, 2018; Lofgren, 2007). In shear, diagonal cracks formed around the centrally placed stirrup and terminated before reaching the next stirrups (Fig. 6.6a). This pattern reflects the role of shear links in arresting crack growth by providing confinement and restraining crack propagation. However, because of the dense and brittle nature of the CSS matrix, diagonal cracks propagated steeply toward the load points, producing sudden shear failure that is a response consistent with observations in high-strength concrete beams lacking adequate post-cracking ductility (Abdullah et al., 2024; Ismail, 2016).

Conversely, beams activated with WGSS (M3 and M4) exhibited flexural capacities that exceeded their shear capacities, consistent with their lower compressive strength (Eisa et al., 2022). Flexural cracks developed earlier (Fig. 6.5b,c) but were more numerous, narrower and more evenly distributed along the span. The increased crack multiplicity reflects the lower stiffness and higher strain capacity of WGSS-based binders, which permit more uniform stress distribution and delayed localization of damage (Xie et al., 2017). Compared with allowable crack width limits in standards such as EC2 (0.3 mm for non-detrimental exposure conditions), the observed crack widths of up to 5 mm exceed serviceability limits significantly, confirming that the cracks correspond to ultimate rather than service load behaviour. In addition, higher crack density and increased propagation loads reflected ongoing matrix development, improved tensile resistance and enhanced geopolymerization between 7 and 28 days, which aligns with age-dependent strengthening patterns observed in alkali-activated systems (Hassan et al., 2022). In shear, diagonal cracks in the WGSS beams developed gradually near the supports and progressed stepwise toward the load points (Fig. 6.6b,c), with the central stirrup acting as a local restraint that delayed the widening of diagonal cracks in its vicinity (Ismail, 2016; Panneerselvam and Pazhani, 2024). However, the generally wide spacing of the stirrups meant that most of the shear span remained unrestrained, so the improved ductility observed in WGSS beams is better attributed to the fracture behaviour of the binder rather than to confinement effects. The gradual coalescence and branching of cracks, along with distributed microcracking characteristic of geopolymer systems, contributed to a delayed shear failure compared with the abrupt diagonal cracking observed in the CSS beams.

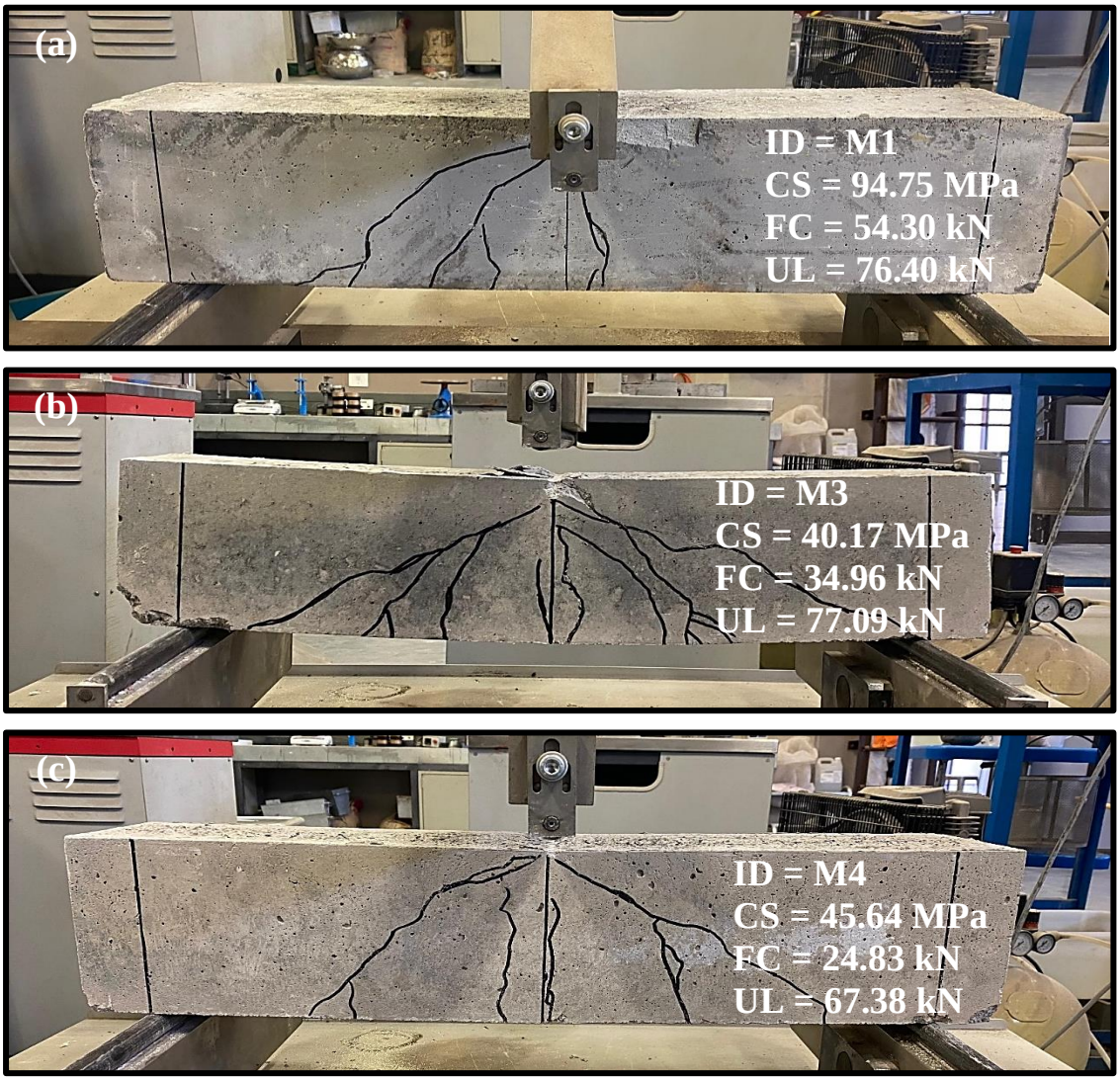

Fig. 6.5: Observed failure modes of beams showing flexural cracking in (**a**) M1 (**b**) M2 (**c**) M3

Note: *ID = mix ID; CS = compressive strength; FC = first crack load at 28 days; UL = Ultimate load at 28 days.*

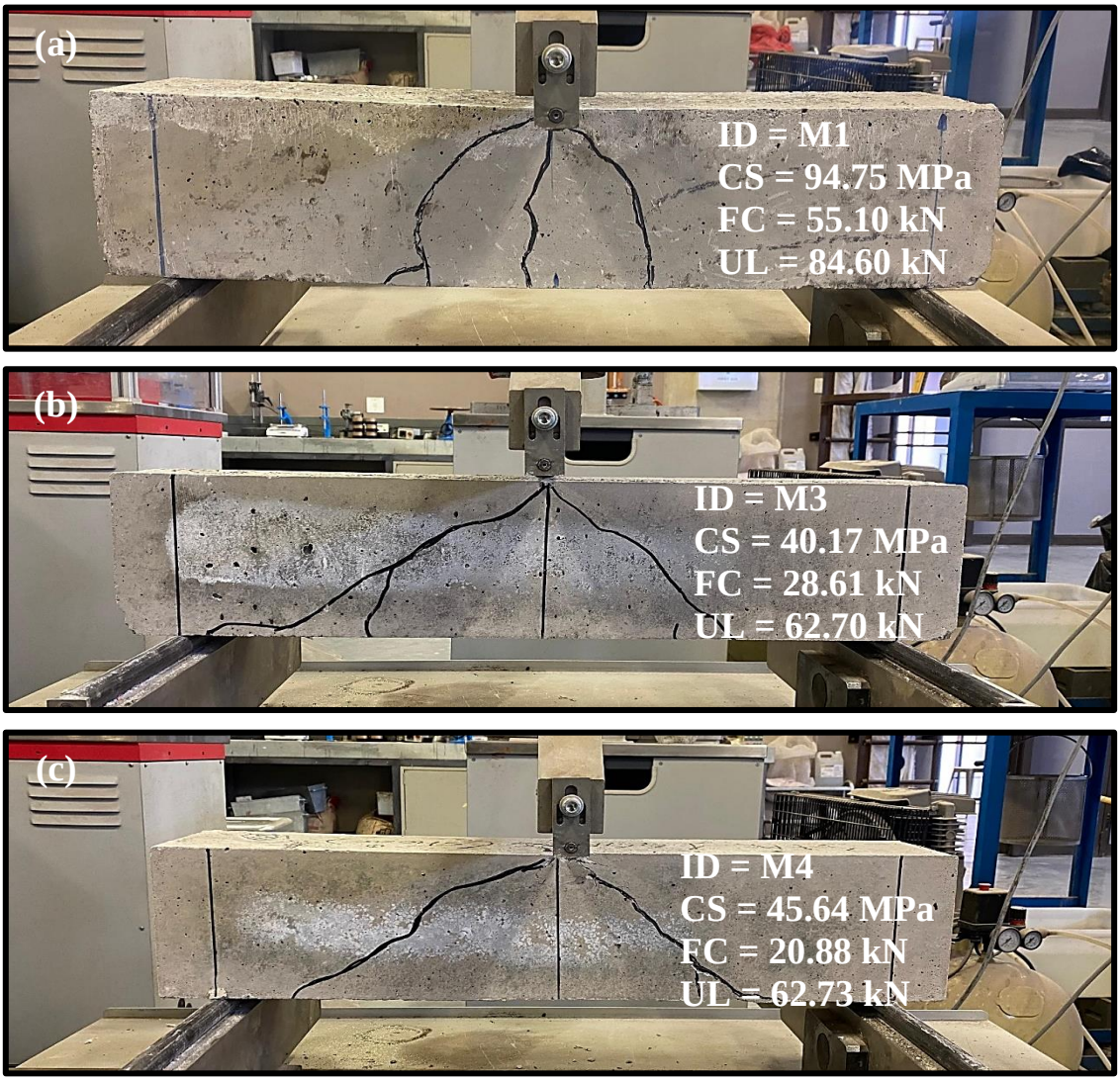

Fig. 6.6: Observed failure modes of beams showing shear cracking in (**a**) M1 (**b**) M2 (**c**) M3

Note: *ID = mix ID; CS = compressive strength; FC = first crack load at 28 days; UL = Ultimate load at 28 days.*

6.4.4 Summary of Structural Performance of GPC Mixes

It can be deduced from the experimental results that the CSS control beams combined very high compressive strength with high cracking resistance and superior shear capacity, but their failure was comparatively brittle and sudden. WGSS beams exhibited a contrasting performance profile, as they cracked earlier but developed more distributed cracking, showed significant age-dependent increases in ultimate capacity and displayed enhanced flexural ductility and energy absorption. M3 is quite noteworthy for matching and slightly exceeding the M1's 28-day flexural capacity despite a much lower compressive strength, which demonstrates the efficiency of WGSS in translating microstructural improvements into

structural performance. Thus, these results indicate that although CSS systems offer superior early-age strength and shear resistance, WGSS-based GPCs provide improved toughness and post-crack resilience, making them attractive for flexure-dominated structural elements where serviceability and ductility are important, in addition to their sustainability advantages.

6.5 Microstructural Analysis of GPC Mixes Using SEM

The SEM micrographs of the GPC mixes (Fig. 6.7) provide insight into the effects of activator type and GGBFS incorporation on matrix densification and pore structure, which are directly related to the mechanical performance observed in mortar tests.

M1 (Fig. 6.7a) displays a dense, well-polymerized gel matrix with minimal porosity, which corresponds to its high compressive strength and superior performance obtained under CSS activation and heat curing (Yılmaz et al., 2024). However, M2 (Fig. 6.7b) reveals numerous unreacted fly ash particles within a porous and loosely bonded matrix, reflecting limited dissolution and the absence of calcium contributions, which also explains its weak mechanical behavior and earlier findings on non-CSS activators (Lin et al., 2025). The inclusion of GGBFS significantly enhanced the WGSS-based systems. M3 (Fig. 6.7c) shows a more consolidated binder phase with fewer residual particles, indicating calcium-driven formation of additional C–A–S–H gels and greater matrix densification (Hu et al., 2019), which explains its higher strength relative to M2. M4 (Fig. 6.7d) presents the densest matrix among the WGSS mixtures, although residual pores are still visible. This accounts for its strength improvement over M2, while also clarifying why the margin of gain beyond M3 was limited. Similar plateau effects from high GGBFS incorporation have been reported in earlier studies (Hu et al., 2019).

Conclusively, the SEM analysis confirms that CSS activation produces the most compact and mechanically robust systems, whereas WGSS requires moderate GGBFS addition to achieve comparable matrix densification. Also, even though the SEM was performed on concrete samples, the microstructural trends observed are consistent with the mechanical behaviour of mortar mixes, providing qualitative validation for the compressive strength results presented in Section 5.3.3.1.

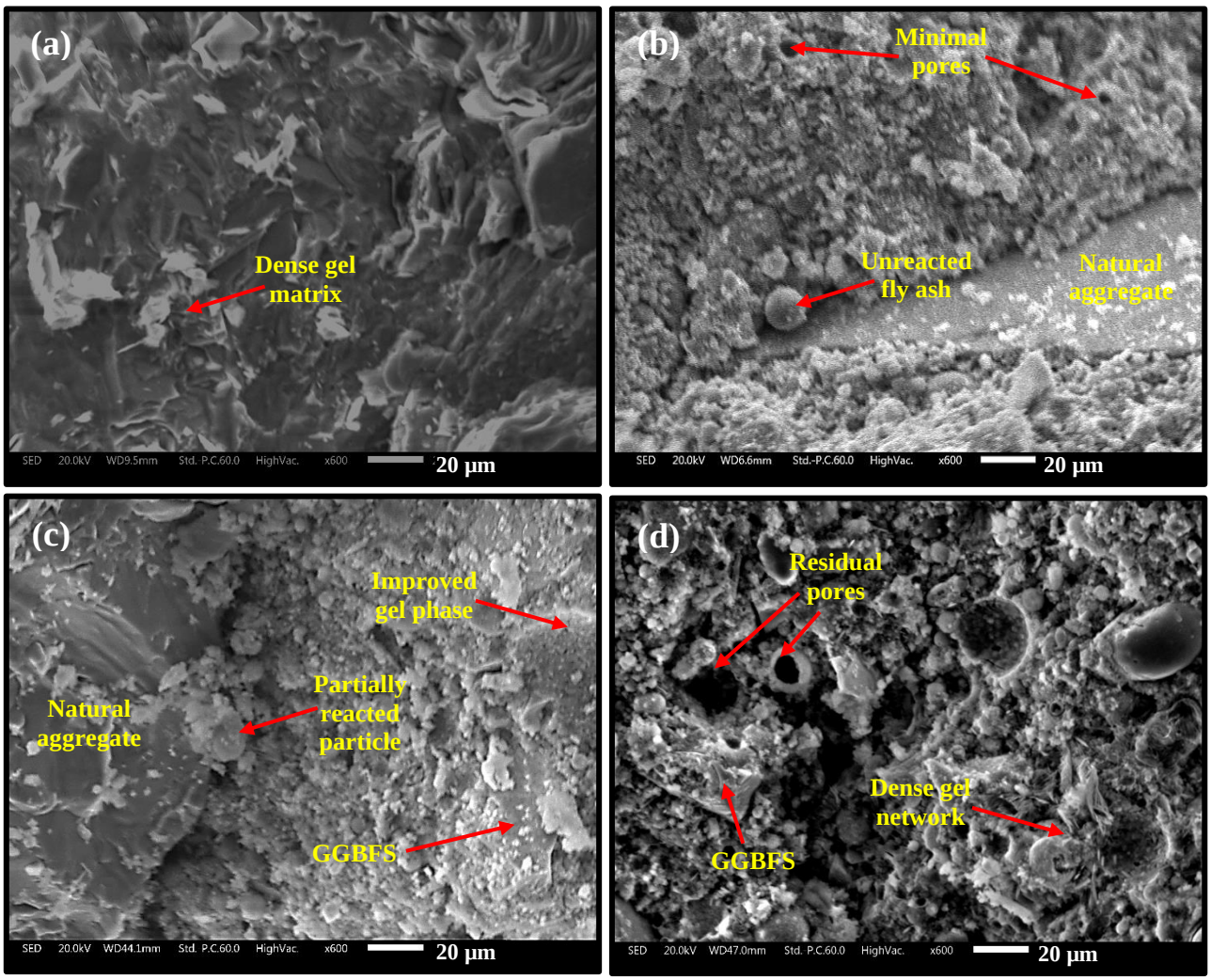

Fig. 6.7: Microstructural features of (**a**) M1 (**b**) M2 (**c**) M3 (**d**) M4 from SEM analysis

CHAPTER 7

7 SUSTAINABILITY EVALUATION OF GEOPOLYMER CONCRETE MIXES

The adoption of GPC as a sustainable alternative to PC-based systems is motivated not only by its superior mechanical performance and durability but also by its environmental and economic advantages. The GPC formulations assessed in this chapter are those established in Chapter 6 (Table 6.1), with the 28-day compressive strength results providing the mechanical benchmark for connecting performance outcomes to the environmental and economic evaluations undertaken in the LCA framework. This chapter evaluates the sustainability of the WGSS activator in comparison with CSS. The assessment is structured around three key pillars of sustainability: mechanical performance, environmental footprint and economic viability. Additional discussions focus on material efficiency, resource circularity and carbon reduction potential, thereby providing a comprehensive perspective on the practical adoption of WGSS-based GPC.

7.1 Life Cycle Assessment (LCA)

7.1.1 Goal and Scope Definition

The environmental and economic implications of the fly ash–GGBFS GPC mixes activated with both WGSS and CSS are evaluated. The environmental indicators considered include transportation impact (Ti), embodied energy (EE) and global warming potential (GWP), which are commonly employed in LCA of construction materials. Greenhouse gas (GHG) emissions (CO_2, CH_4 and N_2O) were included due to their dominant role in construction-related emissions. These emissions were expressed as CO_2 equivalents (CO_2-eq) using 100-year GWP conversion factors (ICE, 2024; Turner and Collins, 2013). To provide an integrated evaluation of mechanical, environmental and economic performance, three composite indices were applied: the sustainability index (SI), the economic index (EI) and the CO_2 abatement cost (CAC). These indices allow a structured analysis of trade-offs, supporting a more holistic and informed decision-making framework (Kolade et al., 2026c).

In addition, the system boundary for the GPC mixes is shown in Fig. 7.1 and adopts a cradle-to-site perspective, covering raw material acquisition, processing and transportation to the production site at the University of South Africa (UNISA), Science Campus, Florida, Johannesburg. The functional unit was set as 1 m^3 of fresh GPC, ensuring consistent

comparison of inputs, outputs and performance across all mix designs (Oyebisi et al., 2022; Turner and Collins, 2013).

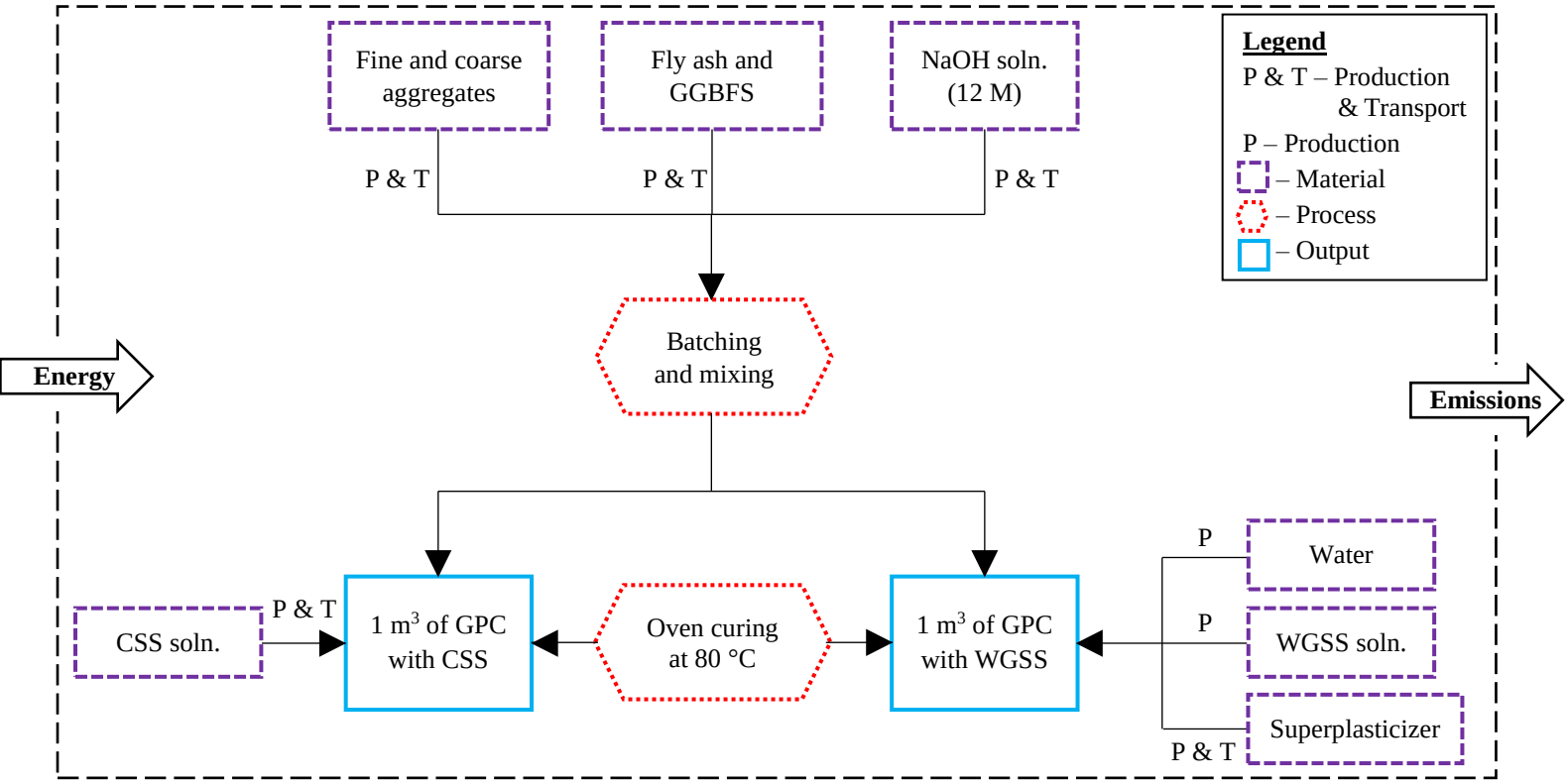

Fig. 7.1: System boundary and resource flows for GPC production

7.1.2 Life Cycle Inventory (LCI)

The inventory data used to evaluate environmental impacts (Table 7.1) and transport-related coefficients (Table 7.2) were compiled from multiple sources, including supplier information, the Inventory of Carbon and Energy (ICE, 2024) and peer-reviewed literature. While the ICE database provides standardized cradle-to-gate emission and energy values based on process-based and hybrid input–output LCA methodologies, the present study adopted a cradle-to-site system boundary. Accordingly, transport-related contributions were incorporated from published studies and empirical transport data to extend the boundary from the production gate to the point of material use. This approach ensures consistency with the study's practical scope and provides a more comprehensive representation of embodied impacts associated with material delivery and site application.

Table 7.1: Energy demand and carbon footprint of raw materials and process inputs

Input type	Category	EE_c (MJ-eq/kg)	GWP_c ($kgCO_2$-eq/kg)	References
Fly ash	Binder	0.1	0.008	ICE (2024); Janga et al., 2024; Oyebisi et al. (2022); Sathiparan and Subramaniam (2024)
GGBFS	Binder	1.6	0.0083	ICE (2024); Janga et al., 2024; Oyebisi et al. (2022); Sathiparan and Subramaniam (2024)
Fine aggregate	Aggregate	0.081	0.0051	ICE (2024); Janga et al., 2024; Oyebisi et al. (2022)
Coarse aggregate	Aggregate	0.083	0.0052	ICE (2024); Oyebisi et al. (2022)
WGP	Supplementary	0.137	0.035	Sathiparan and Subramaniam (2024)
NaOH pellets	Activator	18	0.86	Adesina (2021); Oyebisi et al. (2022)
CSS	Activator	5.37	0.78	Fernando et al. (2021); Oyebisi et al. (2022); Turner and Collins (2013)
Superplasticizer	Admixture	1.85	1.26	Sika ViscoCrete®-2100 (2023)
Water	Resource	0.01	0.001	ICE (2024); Oyebisi et al. (2022); Sathiparan and Subramaniam (2024)
WGSS fusion	Processing	0.108	0.028	Computed
WGSS grinding	Processing	0.0072	0.0019	Computed
Thermal curing	Processing	0.091	0.017	Computed

Table 7.2: Transport-related embodied energy and emissions coefficients

Transportation option	EE (MJ-eq/tonne-km)	GWP ($kgCO_2$-eq/tonne-km)	References
Road freight (truck)	2.275	0.159	Fernando et al., 2021; Janga et al., 2024; Oyebisi et al., 2022
Maritime shipping	0.216	0.0165	Fernando et al., 2021; Janga et al., 2024; Oyebisi et al., 2022
Rail freight	0.325	0.039	Janga et al., 2024; Oyebisi et al., 2022

For binders, the EE and GWP values of fly ash, GGBFS and aggregates were primarily derived from the ICE database (ICE, 2024) and corroborated by recent studies (Janga et al., 2024; Kolade et al., 2026c; Oyebisi et al., 2022; Sathiparan and Subramaniam, 2024). Fly ash was treated as a secondary by-product with low associated burdens, requiring only minor processing (drying and grinding). Conversely, the impact of GGBFS reflects its energy-intensive granulation and drying stages, with burdens allocated economically to capture its market value.

For NaOH pellets and CSS, coefficients were taken from detailed LCA datasets such as Turner and Collins (2013), which explicitly consider the high energy demands of chlor-alkali electrolysis and fusion processes. The elevated EE and GWP values of these activators align with their energy-intensive manufacturing routes. SP impacts were also estimated using data for Sika ViscoCrete®-2100 (2023), modelled from a process-based LCA of polycarboxylate admixtures manufactured via etherification.

In addition, the environmental burdens of WGSS production were determined directly from operational energy requirements. Fusion was modeled as a 10 kW furnace operating for 3 hours per 1000 kg batch, resulting in an energy intensity of 0.108 MJ-eq/kg. Subsequent grinding contributed an additional 0.0072 MJ-eq/kg, based on empirical ball-milling data (Bianco et al., 2021; Kolade et al., 2026c). Using South Africa's national grid emission factor of 0.931 $kgCO_2$-eq/kWh (South Africa Grid Emission Factors Report, 2024), the combined GWP of WGSS fusion and grinding was estimated at about 0.03 $kgCO_2$-eq/kg.

Furthermore, the curing stage (80 °C for 24 hours) was also accounted for, consuming an estimated 200 MJ per cubic meter of GPC, corresponding to a GWP of 37 $kgCO_2$-eq/m^3 (Alsalman et al., 2021). Assuming an average GPC density of 2200 kg/m^3, this translates to 0.091 MJ-eq/kg of EE and 0.017 $kgCO_2$-eq/kg of GWP attributable to curing.

Transport distances (Table 7.3) were calculated using Google Maps, based on the locations of suppliers in South Africa. On-site resources such as WGSS and mixing water were assumed to have negligible transport impacts, although upstream transportation (delivery of WGP and NaOH pellets to the WGSS unit) was included where relevant. Cost data were also compiled using industrial-scale pricing applicable in South Africa, incorporating material purchase, processing energy and transportation where applicable.

Table 7.3: Haulage distances for raw materials and inputs used in GPC mixes

Material / Input	Supply location	Distance (km)	Coordinates (lat, long)
Fly ash	Vereeniging	98.1	-26.74191, 27.96416
GGBFS	Vanderbijl Park	69.6	-26.67279, 27.79873
Fine aggregate	Midrand	35.2	-26.02686, 28.11360
Coarse aggregate	Midrand	35.2	-26.02686, 28.11360
Waste glass powder	Meyerton	69.1	-26.56419, 28.01359
NaOH pellets	Laser Park	11.6	-26.08127, 27.91454
CSS	Aston Manor	60.2	-26.09375, 28.26327
WGSS	UNISA	0	-26.15863, 27.90328
Superplasticizer	Boksburg	52.8	-26.15156, 28.21679
Water	UNISA	0	-26.15863, 27.90328

7.1.3 Life Cycle Impact Assessment (LCIA)

7.1.3.1 Transportation Impact (TI)

The TI represents the environmental cost associated with hauling raw materials from their point of origin to the production facility (Janga et al., 2024). This parameter was included in the present assessment because previous studies have demonstrated that the distance travelled by alternative binders can strongly affect the overall life-cycle footprint of GPCs (Kolade et al., 2026c; Umer et al., 2024) Transport-related emissions were quantified using Eq. (7.1), which applies fuel consumption data and emission factors for heavy-duty diesel trucks under typical payload conditions and round-trip delivery.

$$TI = \sum_{i=1}^{n} \left(\frac{M_w \times D_t \times T_c}{1000} \right) \quad (7.1)$$

Where: M_w = material weight (kg); D_t = truck distance travelled (km); T_c = EE and GWP transport factor (Fernando et al., 2021; Janga et al., 2024; Oyebisi et al., 2022).

7.1.3.2 Embodied Energy (EE)

EE, expressed in MJ-eq/m^3, represents the cumulative primary energy demand associated with raw material extraction, processing, transportation and the thermal curing of GPC. The value

was determined using Eq. (7.2). For WGSS, only the energy inputs from secondary processing were included, since production occurred on-site and no transportation stage was required.

$$EE = (1 + a) \sum_{i=1}^{n} (M_w \times EE_c) + TiEE \quad (7.2)$$

Where: a = EE wastage factor = 22%; M_w = material weight (kg); EE_C = EE factors; TIEE = transport impact of EE (Adesina, 2021; Fernando et al., 2021; Oyebisi et al., 2022).

7.1.3.3 Global Warming Potential (GWP)

The GWP ($kgCO_2$-eq/m^3) represents the aggregated effect of GHGs linked to the production of the GPC mixes within the defined cradle-to-site boundary. The calculation incorporates emissions arising from raw material production, transportation and the energy used for thermal curing, as outlined in Eq. (7.3).

$$GWP = (1 + b) \sum_{i=1}^{n} (M_w \times GWP_c) + TiGWP \quad (7.3)$$

Where: b = GWP wastage factor = 19%; M_w = material weight (kg); GWP_C = GWP factors; TIGWP = transport impact of GWP (Adesina, 2021; Fernando et al., 2021; Oyebisi et al., 2022).

7.1.3.4 Sustainability Index (SI)

The SI (expressed as $kgCO_2$-eq/m^3/MPa) provides an environmental indicator that is normalized by structural performance. It is calculated by dividing the overall GWP of a mix by its corresponding 28-day compressive strength, as given in Eq. (7.4). This approach facilitates direct comparison of environmental efficiency in relation to strength, with lower SI values reflecting higher sustainability per unit of mechanical performance (Adesina, 2021; Kolade et al., 2026c; Ma et al., 2018).

$$SI = \frac{GWP + (CO_{2e} \times EE)}{f_{cu}} \quad (7.4)$$

Where: CO_2e = carbon equivalent = 0.05 $kgCO_2$/MJ; f_{cu} = 28-day compressive strength (MPa) (Adesina, 2021; Janga et al., 2024; Oyebisi et al., 2022).

7.1.3.5 Economic Index (EI)

The EI ($/m^3/MPa) evaluates the cost-effectiveness of each mix by normalizing total production cost against compressive strength, as defined in Eq. (7.5) (Kolade et al., 2026c; Ma et al., 2018; Oyebisi et al., 2022). The overall cost per cubic meter includes material procurement, processing and transport, with rates reflecting industrial-scale pricing from South African suppliers. As such, average unit costs for each constituent were established from multiple vendor quotations and recent purchase records to ensure representativeness. Where direct data were unavailable, costs were estimated from associated energy and labour inputs. Consequently, the EI serves as a standardized metric for comparing the economic competitiveness of the different GPC formulations.

$$EI = \frac{Cost_t}{f_{cu}} \tag{7.5}$$

Where: EI = $Cost_t$ = total cost per m^3; fcu = 28-day compressive strength (MPa) (Ma et al., 2018; Oyebisi et al., 2022).

7.1.3.6 CO_2 Abatement Cost (CAC)

The CAC, expressed in $/kg$CO_2$-eq) quantifies the extra expenditure required to prevent the release of one kilogram of CO_2 emissions relative to the reference mix (M1) (Kolade et al., 2026c; Umer et al., 2024). As defined in Eq. (7.6), it is determined by dividing the incremental cost difference between a test mix and the control by the corresponding reduction in GWP. This indicator is particularly valuable for evaluating the financial implications of carbon mitigation strategies in GPC production, highlighting the balance between environmental gains and economic feasibility.

$$CAC = \frac{C\,(alt) - C\,(ref)}{E\,(ref) - E\,(alt)} \tag{7.6}$$

Where: C (alt) = cost of low CO_2 option; C (ref) = cost of conventional option; E (ref) = emissions of conventional option; E (alt) = emissions of low CO_2 option (Umer et al., 2024).

7.2 LCIA Results and Discussion

7.2.1 Transportation Impact (TI)

As illustrated in Fig. 7.2, the transportation-related impacts show a consistent reduction from the control mix to the WGSS-based alternatives. The TIEE dropped from 291.39 MJ-eq/m^3 in

M1 to 275.65, 270.40 and 265.53 MJ-eq/m³ for M2, M3 and M4, respectively, reflecting a 5 – 9% reduction. A similar trend was observed for TIGWP, which decreased from 20.37 $kgCO_2$-eq/m^3 in M1 to 19.27, 18.90 and 18.56 $kgCO_2$-eq/m^3 in the WGSS mixes, representing reductions of approximately 5.4%, 7.2% and 8.9%, respectively.

In the control mix, fly ash transport alone contributed roughly 41% of the total burden, while fine and coarse aggregates accounted for 22% and 29%, respectively (see Tables A4 and A5). CSS, responsible for about 7.5% of the TIEE and TIGWP in M1, was fully substituted by WGSS in M2 – M4. Since WGSS was processed on-site, its transport footprint was negligible, leading to marked reductions. Additional decreases in M3 and M4 were achieved through partial replacement of fly ash with GGBFS, sourced from a nearer location. This substitution aligns with the findings of Oyebisi et al. (2022), who observed that fly ash typically requires longer haulage than GGBFS. While GGBFS accounted for about 9% of TI in M4, this was offset by the decline in fly ash and CSS contributions. Although the WGSS systems required extra inputs in the form of SP and WGP, their combined share of transport emissions was below 2% of the total. These results underscore the importance of local sourcing and material substitution strategies in enhancing the environmental efficiency of GPC production (Abdulkareem et al., 2021; Bianco et al., 2021; Janga et al., 2024; Umer et al., 2024).

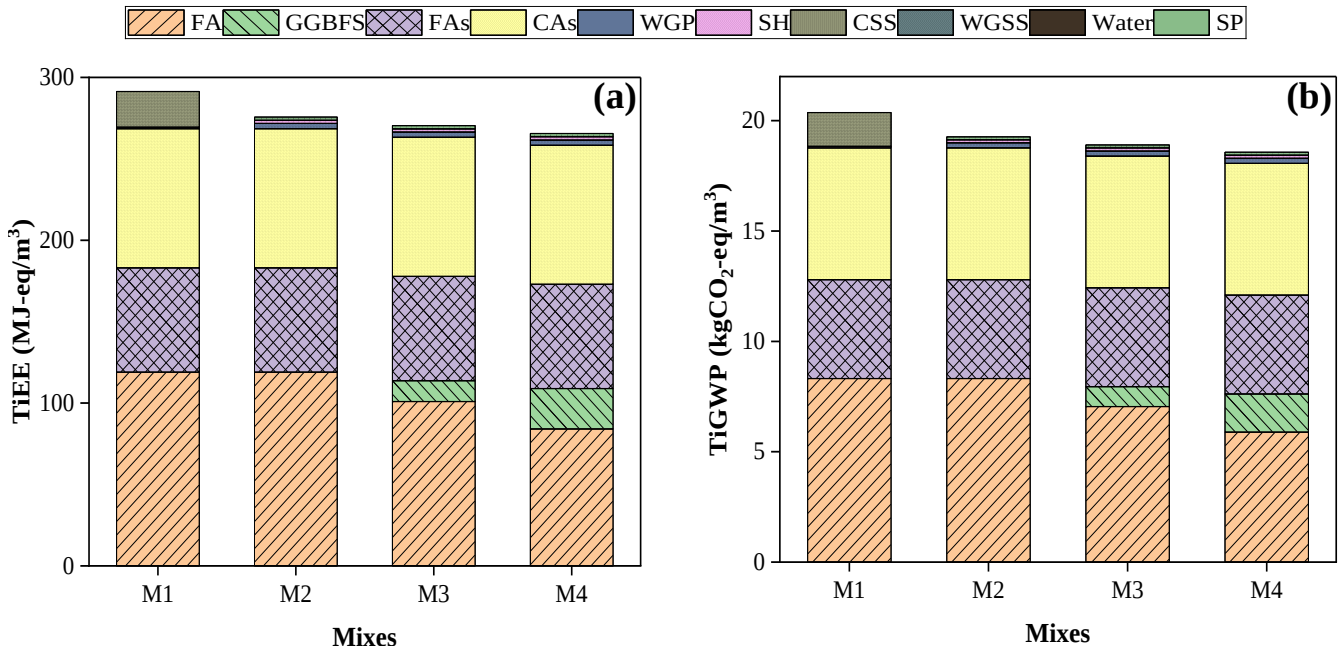

Fig. 7.2: Transport-related impacts of the GPC mixes expressed as (**a**) embodied energy (TIEE) and (**b**) global warming potential (TIGWP)

7.2.2 Embodied Energy (EE)

The total EE of the GPC mixes ranged between 2491.65 MJ-eq/m^3 for M2 and 2767.01 MJ-eq/m^3 for M4, while the reference mix (M1) exhibited 2651.55 MJ-eq/m^3 (Fig. 7.3). The 6% reduction observed in M2 relative to M1 can be attributed mainly to the removal of CSS, which alone contributed 39.5% of the total EE in M1, as presented in Table A6. Together with NaOH, which accounted for 30.7%, alkali activators made up about 70% of M1's total EE, a figure closely matching the 73.38% reported by Oyebisi et al. (2022). In the WGSS-based systems (M2 – M4), the higher NaOH requirement used during activator synthesis increased its share to 60 – 67% of total EE, partially diminishing the benefits gained from eliminating CSS. Similar findings in prior studies have highlighted NaOH as the dominant contributor to GPC's energy demand (Alsalman et al., 2021; Assi et al., 2018; Kolade et al., 2026c; Turner and Collins, 2013).

In addition, thermal curing was a relatively steady contributor across all mixes, representing about 8 – 10% of total EE, in line with the 5 – 10% range reported by Alsalman et al. (2021). TIEE also contributed a smaller share, approximately 10 – 11%, with slightly higher values in M1 owing to CSS transport. The higher energy intensity of GGBFS also explains the greater EE values of M3 and M4 compared to M2. For instance, the proportion of EE linked to GGBFS in M4 (11%) was nearly double that of M3 (6%), raising M4's total EE above the control mix. As such, the findings suggest that although substituting CSS with WGSS reduces EE substantially (as seen in M2), the benefit is progressively counterbalanced by the increased use of GGBFS in M3 and M4. Thus, achieving an optimal balance between precursor proportions and activator dosage is therefore critical for enhancing both performance and energy efficiency in WGSS-based GPC systems.

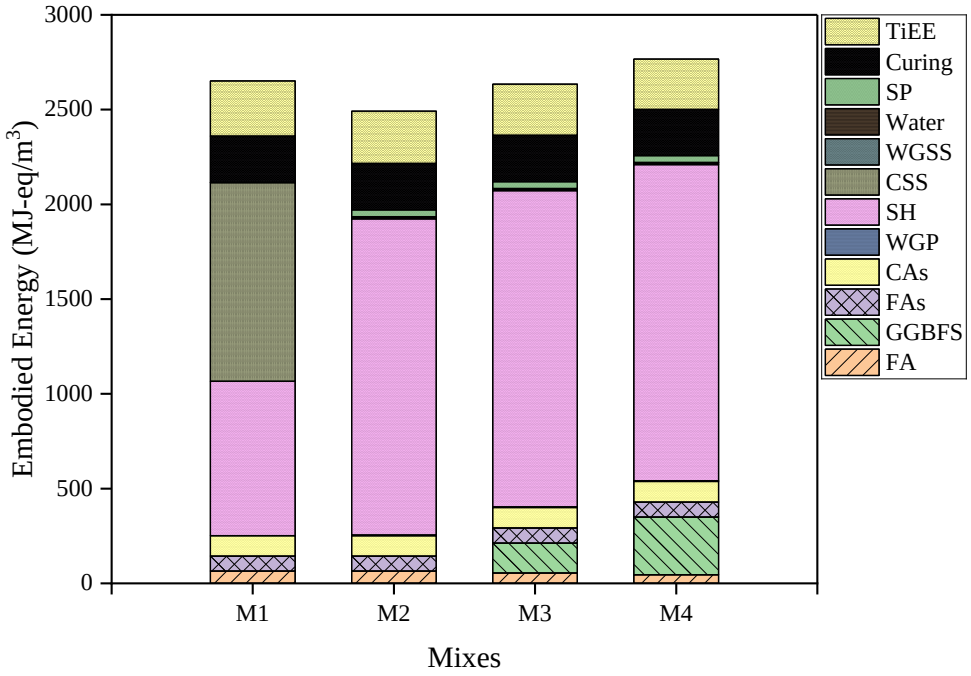

Fig. 7.3: Distribution of EE across constituent materials and processes for the GPC mixes

7.2.3 Global Warming Potential (GWP)

As illustrated in Fig. 7.4, the WGSS-activated mixes achieved a marked reduction in GHGs, with values approximately 31% lower than the control mix. This confirms the environmental benefit of replacing CSS with WGSS, consistent with the 30 – 32% reduction reported by Bianco et al. (2021). Specifically, the total GWP decreased from 267.97 $kgCO_2$-eq/m^3 in M1 to 185.31, 184.97 and 184.66 $kgCO_2$-eq/m^3 in M2, M3 and M4, respectively. NaOH was consistently the dominant contributor, responsible for 14% of the total GWP in M1 and rising to about 42% in the WGSS mixes due to the higher dosage required (Table A7). In M1, activators together accounted for roughly 70% of the carbon footprint, aligning with the 74% contribution reported by Fernando et al. (2021). CSS alone made up 55% of M1's GWP, which is comparable to the 49 – 60% range observed in previous studies (Fernando et al., 2021; Oyebisi et al., 2022; Turner and Collins, 2013). This confirms that CSS is among the most carbon-intensive inputs in GPC production and its removal in M2 – M4 was the main driver of emission reductions, despite the higher NaOH demand and a minor GWP addition from WGSS (≈1.15%).

Furthermore, thermal curing consistently contributed around 44.5 $kgCO_2$-eq/m^3 across all formulations, which is slightly above the 39 $kgCO_2$-eq/m^3 reported by Fernando et al. (2021) under comparable curing regimes. TIGWP also decreased gradually from M1 to M4 due to

differences in raw material sourcing. In contrast, the SP became more significant in the WGSS-based mixes, accounting for roughly 13% of total emissions. A small increase in GWP was observed between M2 and M4, attributable to the greater proportion of GGBFS, which carries a higher emission factor than fly ash. Nonetheless, the total GWP of the WGSS mixes remained substantially below that of the control. Also, the WGSS-activated mixes exhibited about 42% lower GWP compared to a conventional C40 geopolymer produced with CSS and NaOH, as reported by Turner and Collins (2013). Hence, these findings clearly demonstrate that substituting CSS with WGSS can deliver substantial carbon savings while preserving material performance, reinforcing the case for adopting WGSS as a sustainable activator in GPC systems (Kolade et al., 2026c; Samarakoon et al., 2020).

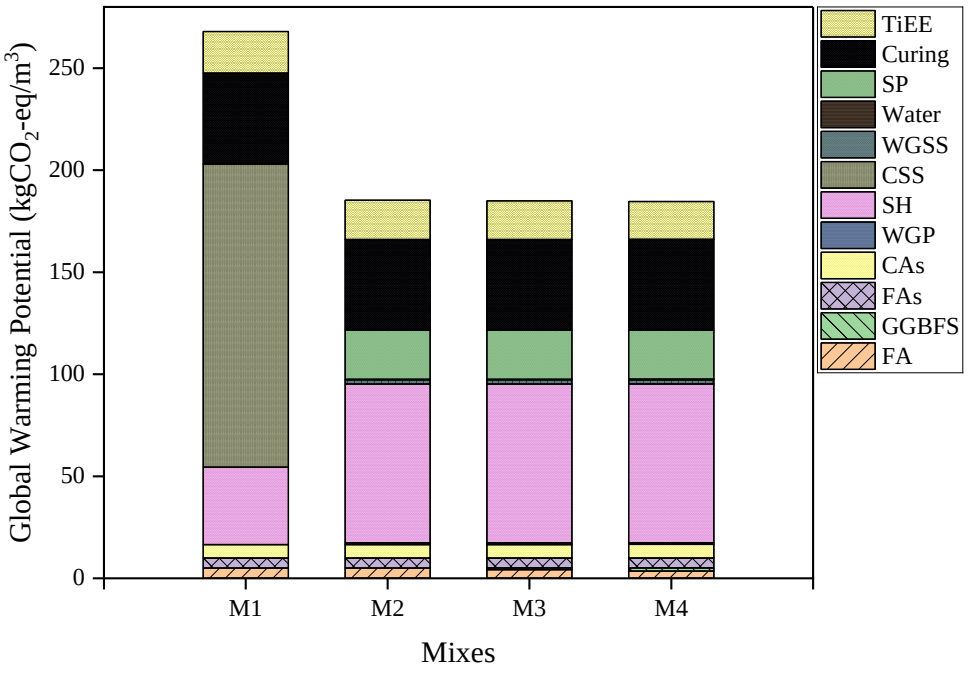

Fig. 7.4: Distribution of GWP across constituent materials and processes for the GPC mixes

7.2.4 Sustainability Index (SI)

The SI outcomes for the GPC mixes are shown in Fig. 7.5, with its breakdown presented in Table A8. The control mix achieved the lowest SI of 4.23 $kgCO_2$-eq/m^3/MPa, a result largely attributed to its high 28-day compressive strength of about 95 MPa. This suggests M1 to be the most efficient mix in terms of strength-normalized emissions. However, this advantage must be contextualized: such ultra-high strength is often unnecessary in routine structural applications, making the sustainability benefit somewhat situational.

Notably, M1 also carried the highest overall environmental burden due to the dominant role of CSS, which accounted for more than half of its total GWP. In comparison, the WGSS-based formulations demonstrated much lower GWP and EE values, yet their SI values were higher because of lower compressive strengths. For instance, M2 registered the highest SI of 11.65 $kgCO_2$-eq/m^3/MPa, reflecting its moderate strength of 26.64 MPa. With increasing strength in M3 (40.17 MPa) and M4 (45.74 MPa), SI values improved to 7.91 and 7.06 $kgCO_2$-eq/m^3/MPa, respectively. Although these values are 67 – 87% greater than M1's SI, they coincide with an overall reduction in carbon footprint of more than 30%, indicating a stronger balance between performance and environmental impact.

When benchmarked within the typical structural strength range (40 – 50 MPa), M3 and M4 emerge as practical, lower-emission alternatives to the control mix. This underscores that sustainability in GPC cannot be measured on mechanical strength alone (Adesina, 2021; Samarakoon et al., 2020). While M1 appears strength-efficient, the WGSS-based systems offer more comprehensive environmental benefits, particularly in applications where ultra-high strength is not a design requirement.

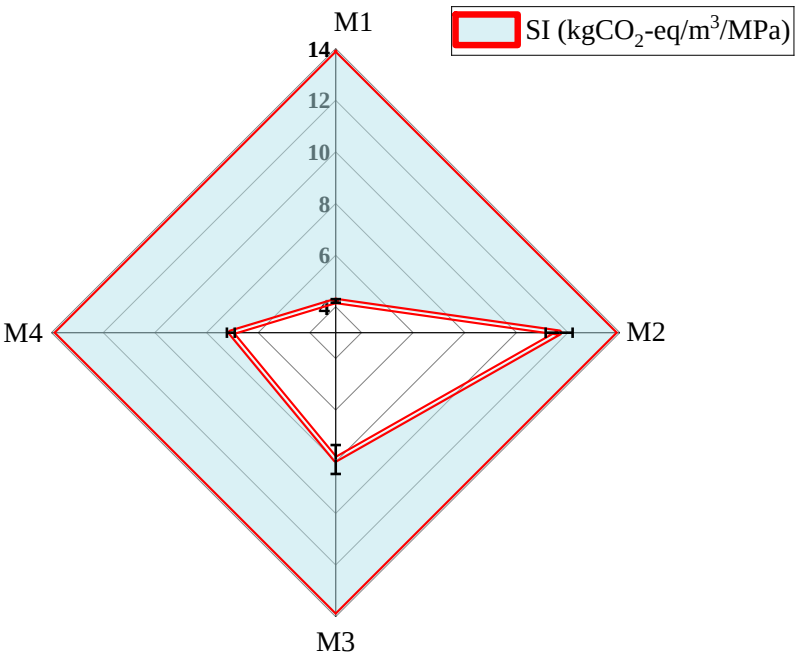

Fig. 7.5: Comparison of SI values across the different GPC formulations

7.2.5 Economic Index (EI)

The industrial-scale costs of individual GPC constituents and the total production cost per cubic meter of the mixes are presented in Tables A9 – A11. As depicted in Fig. 7.6, the control mix achieved the lowest EI of 2.43 $/m^3/MPa, reflecting the most favourable strength-to-cost ratio. However, this outcome is strongly influenced by its very high compressive strength (95 MPa), as shown in Table A12, which surpasses the requirements of many conventional structural applications and therefore needs to be interpreted cautiously.

Despite its efficiency on a performance-normalized basis, M1 was also the most expensive to produce, with a unit cost of $230.15/m^3. This was mainly due to its reliance on CSS, which alone accounted for about 41.7% of the total cost. In contrast, the mixes incorporating WGSS were cheaper to produce, as WGSS is priced at roughly $25/m^3, which is about 74% lower than CSS ($96/m^3). Similar cost savings have been reported in prior studies. For instance, Samarakoon et al. (2020) noted reductions of around 65%, while Vinai and Soutsos (2019) found savings of 30 – 35% for one-part systems using WGSS. In the present work, total cost reductions of 8 – 10% were observed, with potential for even greater savings in one-part mixes where additional NaOH requirements are avoided.

Within the WGSS-based group, M2 had the lowest strength and therefore recorded the least favourable EI of 7.81 $/m^3/MPa, despite its lower unit cost ($207.68/m^3). M3, with a compressive strength of 40.17 MPa, reduced its EI to 5.24 $/m^3/MPa, while M4 delivered the most balanced outcome. Specifically, M4 combined the highest strength among the WGSS mixes (45.74 MPa) with a moderate cost ($211.67/m^3), yielding an EI of 4.63 $/m^3/MPa and representing a 41% improvement compared to M2.

The findings of this evaluation highlight the economic trade-offs inherent in GPC mix design. While M1 appears the most efficient when normalized by strength, its high absolute cost and substantial carbon footprint limit its suitability for moderate-strength applications. In contrast, WGSS-based mixes, particularly M4, offer a more balanced solution by combining reduced cost and lower environmental burden with adequate mechanical performance (< 50 MPa range). These results emphasize the value of waste-derived materials and locally sourced resources in advancing the sustainability and cost competitiveness of GPC (Kolade et al., 2026c; Samarakoon et al., 2020).

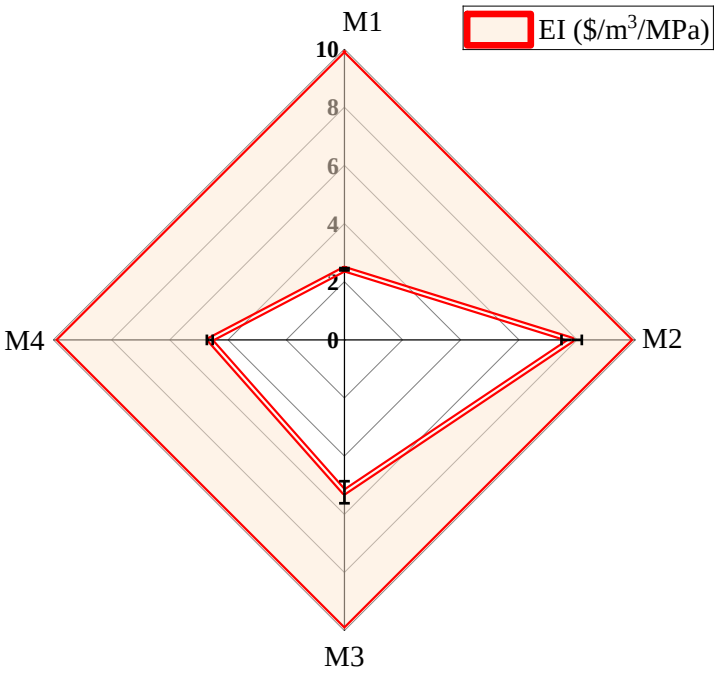

Fig. 7.6: Comparison of EI values across the different GPC formulations

7.2.6 CO_2 Abatement Cost (CAC)

A negative CAC reflects a dual advantage, that is, lowering carbon emissions while simultaneously reducing production costs (Hasanbeigi et al., 2010; Umer et al., 2024). This outcome was observed across all WGSS-based mixes, which outperformed the control mix (M1) by being both less carbon-intensive and more economical per cubic meter. As shown in Fig. 7.7, M2 delivered the most favourable result among them, with a CAC of –\$0.272/kgCO_2, meaning that each kilogram of CO_2 avoided relative to M1 corresponded to a saving of around 27 cents. Mixes M3 and M4 also showed strong cost-effective performance, recording CAC values of –\$0.246 and –\$0.222/kgCO_2, respectively.

These gains stem largely from the use of WGSS as a local, low-impact replacement for CSS, which substantially lowered both costs and emissions. Thus, the WGSS-based mixes achieved a roughly 31% reduction in GWP compared to M1, while delivering these improvements more economically. Although M2 had the lowest compressive strength and EI among the WGSS mixes, its minimal emissions gave it the strongest abatement advantage.

This evidence underscores the strategic importance of waste-derived binders in GPC production. The negative CAC values demonstrate that environmental improvements can be achieved without financial penalties. In fact, when properly optimized, sustainable

substitutions not only cut emissions but also provide measurable cost savings (Hasanbeigi et al., 2010; Kolade et al., 2026c).

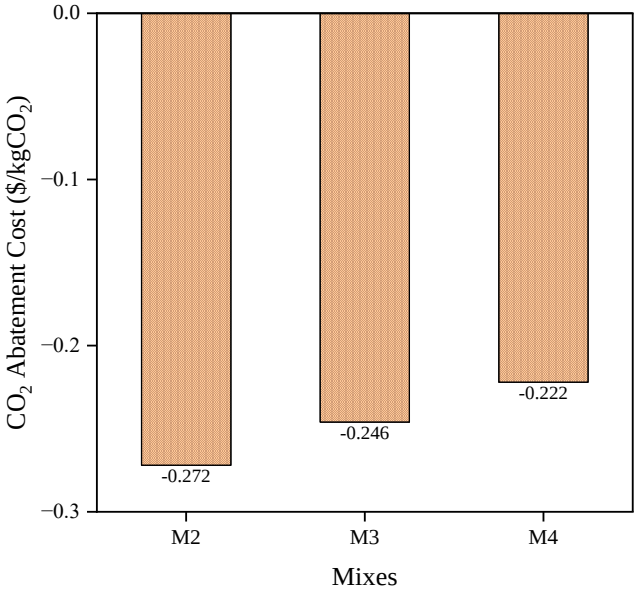

Fig. 7.7: CO_2 mitigation cost of WGSS mixes relative to the reference mix

CHAPTER 8

8 CONCLUSIONS AND RECOMMENDATIONS

8.1 Conclusions

This research comprehensively investigated the structural performance and sustainability of reinforced GPC beams, integrating studies on mix design methodology, waste-derived activator synthesis, binder characterization and beam-scale structural testing. The major conclusions are as follows:

i. A flexible, composition-driven mix design framework was developed for GPC by integrating key chemical ratios (SiO_2/Al_2O_3, W/Gs, Na_2O/SiO_2 and H_2O/Na_2O) with performance-based metrics. The optimal binder composition was achieved at a FA:GGBFS ratio of 7:1, corresponding to SiO_2/Al_2O_3 = 3.46, W/Gs = 0.33, Na_2O/SiO_2 = 0.21 and H_2O/Na_2O = 13.33, which produced compressive strengths of ~40 MPa at 28 days. This framework reduced reliance on trial-and-error, improved reproducibility across variable raw materials and enabled the systematic tailoring of binder properties for sustainable construction works.

ii. Synthesized WGSS produced through alkali fusion was confirmed to be a chemically viable and sustainable activator. Among the fusion conditions evaluated (500°C, 550°C, 600°C and 650°C for 2 – 3 hours), the optimal condition was 500°C for 3 hours, which produced a highly amorphous and reactive WGSS. Under this condition, the resulting geopolymer binders achieved compressive and flexural strengths of ~35 MPa and ~7 MPa at 28 days, respectively. Although higher fusion temperatures (e.g., 600°C) improved mortar workability, they resulted in reduced mechanical performance due to increased crystallinity and lower solubility of the synthesized activator.

iii. WGSS-activated mortars achieved 28-day compressive strengths of 25.56, 36.72, 45.31 and 43.44 MPa for FA:GGBFS ratios of 1:1, 3:1, 7:1 and 1:0, respectively. The 3:1 mix (36.72 MPa) corresponds to the SANS 50197-1 (2000) strength class of 32.5, while the 7:1 and 1:0 mixes (45.31 and 43.44 MPa) correspond to the 42.5 class. Although these classifications are based on mortar testing, the results indicate that WGSS binders can achieve mechanical performance comparable to conventional PC systems. WGSS mortars also exhibited lower flowability (50 – 75%) and slightly higher water absorption (5.55 – 5.93%) compared with CSS-activated mortars (90 – 145% flow and 4.64 – 5.37% absorption). However, these values remained within acceptable limits (< 6.5%) specified

in SANS 1058 (2012) for mortar applications. In addition, the FA:GGBFS = 7:1 mix exhibited approximately 15% higher flexural strength than the corresponding CSS mix, attributed to the presence of CaO from GGBFS, which promotes the formation of C–A–S–H gel and enhances matrix cohesion and load transfer.

iv. Structural evaluation of reinforced GPC beams showed that the best-performing WGSS beam M3 (FA:GGBFS = 7:1), with a compressive strength of ~40 MPa, achieved a flexural moment capacity of 11.56 kNm, comparable to the CSS control beam (11.46 kNm) despite the CSS concrete having a compressive strength of ~95 MPa. The WGSS beam exhibited greater mid-span deflection (7.2 mm) compared with the CSS beam (5.3 mm), together with more numerous and uniformly distributed cracks along the span. This behaviour indicates greater strain capacity and improved stress redistribution within the WGSS-activated system. In contrast, the CSS beam developed fewer but wider cracks (~3 mm) and exhibited a more brittle failure following shear crack initiation near the stirrups.

v. The LCAs demonstrated that replacing CSS with WGSS significantly improved the environmental and economic sustainability of the geopolymer system. For the best-performing WGSS mix (M3), EE was reduced by ~1%, GWP decreased by ~31% and production cost was reduced by ~10% compared with the CSS-activated system. This mix therefore represents the most viable WGSS-based alternative for sustainable construction applications requiring medium-strength geopolymer binders.

vi. Statistical analysis verified the reliability and significance of the experimental results. For mortar workability, the difference between CSS and WGSS-activated systems was statistically significant ($p = 0.005$) with a large effect size, indicating a strong practical distinction. Although differences in compressive and flexural strength were not statistically significant at $p < 0.05$, the large effect sizes suggest meaningful performance variations that may become more evident with larger sample sizes. One-way ANOVA further showed that mix composition had a highly significant effect on concrete compressive strength ($p < 0.001$, $\eta^2 = 0.997$), indicating that nearly all observed variability was attributable to formulation differences rather than experimental error.

8.2 Recommendations

8.2.1 Recommendations Based on Study Findings

Drawing from the outcomes of this research, the following recommendations are proposed for practical implementation:

i. The composition-driven mix design approach developed in this study can be adopted as a rational framework for designing geopolymer mortars and concretes, especially those incorporating waste-derived activators, to enhance reproducibility and reduce reliance on trial-and-error methods.

ii. The optimized WGSS activator synthesized at 500°C for 3 hours is suitable for producing medium-strength geopolymer binders corresponding to 32.5 and 42.5 strength classes and can be considered for structural and non-structural applications.

iii. WGSS-based GPCs can be applied in reinforced members subjected to flexural loading, where their improved ductility and distributed cracking behaviour may enhance serviceability performance compared to CSS-based systems.

iv. In view of the observed reductions in EE, GWP and production cost, WGSS activators can be considered as sustainable alternatives to CSS, especially in low to medium-strength construction applications.

8.2.2 Recommendations for Future Research

i. Based on the successful development of the composition-driven mix design framework, further research should validate and extend this approach across a wider range of precursor materials, activator chemistries and curing conditions to support its standardization and broader applicability.

ii. Given that optimal WGSS synthesis was achieved at 500°C for 3 hours, but energy demand remains a concern, future studies should investigate lower-temperature or alternative synthesis methods to reduce EE while maintaining activator reactivity.

iii. Considering the demonstrated structural performance of WGSS-based beams but the limited scope of structural testing, further research should evaluate additional structural elements (such as slabs and columns) and loading conditions, including cyclic and sustained loading.

iv. In light of instrumentation limitations that prevented full load–deflection measurements, future studies should incorporate displacement-controlled testing to enable accurate assessment of stiffness, ductility and post-cracking behaviour.

v. Given that long-term durability and bond behaviour were beyond the scope of this study, further research should investigate durability under aggressive environmental conditions and the bond performance between WGSS-based geopolymer matrices and steel reinforcement.

vi. Considering that sustainability assessment was based on simplified LCA and laboratory-scale production, future work should incorporate detailed life cycle modelling and pilot-scale or field applications to evaluate real-world performance and scalability of WGSS-based systems.

REFERENCES

Abbas, R., Khereby, M.A., Ghorab, H.Y. and Elkhoshkhany, N., 2020. Preparation of geopolymer concrete using Egyptian kaolin clay and the study of its environmental effects and economic cost. *Clean Technologies and Environmental Policy*, 22, pp. 669–687. Available at: https://doi.org/10.1007/s10098-020-01811-4.

Abdel-Gawwad, H.A. and Khalil, K.A., 2018. Application of thermal treatment on cement kiln dust and feldspar to create one-part geopolymer cement. *Construction and Building Materials*, 187, pp. 231–237. Available at: https://doi.org/10.1016/j.conbuildmat.2018.07.161.

Abdulkareem, M., Havukainen, J., Nuortila-Jokinen, J. and Horttanainen, M., 2021. Environmental and economic perspective of waste-derived activators on alkali-activated mortars. *Journal Cleaner Production*, 280, p. 124651. Available at: https://doi.org/10.1016/j.jclepro.2020.124651.

Abdullah, M., Qazi, A.U., Khan, Q.S., Kazmi, S.M.S. and Munir, M.J., 2024. Experimental and analytical investigations on shear performance of Ambient-Cured reinforced geopolymer concrete beams. *Buildings*, 14(1), p. 204. Available at: https://doi.org/10.3390/buildings14010204.

ACI Committee 318, 2019. *Building Code Requirements for Structural Concrete*. American Concrete Institute, Farmington Hills, MI, USA.

Adesina, A., 2021. Performance and sustainability overview of sodium carbonate activated slag materials cured at ambient temperature. *Resources, Environment and Sustainability*, 3, p. 100016. Available at: https://doi.org/10.1016/j.resenv.2021.100016.

Ahmad, J., Kontoleon, K.J., Majdi, A., Naqash, M.T., Deifalla, A.F., Ben Kahla, N., Isleem, H.F. and Qaidi, S.M., 2022. A comprehensive review on the ground granulated blast furnace slag (GGBS) in concrete production. *Sustainability*, 14(14), p. 8783. Available at: https://doi.org/10.3390/su14148783.

Ahmed, F.B., Biswas, R.K., Ahsan, K.A., Islam, S. and Rahman, M.R., 2021. Estimation of strength properties of geopolymer concrete. *Materials Today: Proceedings*, 44, pp. 871–877. Available at: https://doi.org/10.1016/j.matpr.2020.10.790.

Ahmed, H.U., Abdalla, A.A., Mohammed, A.S., Mohammed, A.A. and Mosavi, A., 2022. Statistical methods for modeling the compressive strength of geopolymer mortar. *Materials*, 15(5), p.1868. Available at: https://doi.org/10.3390/ma15051868.

Alaneme, G.U., Olonade, K.A. and Esenogho, E., 2023. Eco-friendly agro-waste based geopolymer-concrete: a systematic review. *Discover Materials*, 3(14). Available at: https://doi.org/10.1007/s43939-023-00052-8.

Alaneme, G.U., Olonade, K.A., Esenogho, E. and Lawan, M.M., 2024. Proposed simplified methodological approach for designing geopolymer concrete mixtures. *Scientific Reports*, 14, p. 15191. Available at: https://doi.org/10.1038/s41598-024-66093-y.

Albidah, A., Alghannam, M., Abbas, H., Almusallam, T. and Al-Salloum, Y., 2021. Characteristics of metakaolin-based geopolymer concrete for different mix design parameters. *Journal of Materials Research and Technology*, 10, pp. 84–98. Available at: https://doi.org/10.1016/j.jmrt.2020.11.104.

Almutairi, A.L., Tayeh, B.A., Adesina, A., Isleem, H.F. and Zeyad, A.M., 2021. Potential applications of geopolymer concrete in construction: A review. *Case Studies in Construction Materials*, 15, p. e00733. Available at: https://doi.org/10.1016/j.cscm.2021.e00733.

Alnahhal, M.F., Kim, T. and Hajimohammadi, A., 2021. Waste-derived activators for alkali-activated materials: A review. *Cement and Concrete Composites*, 118, p. 103980. Available at: https://doi.org/10.1016/j.cemconcomp.2021.103980.

Alsalman, A., Assi, L.N., Kareem, R.S., Carter, K. and Ziehl, P., 2021. Energy and CO_2 emission assessments of alkali-activated concrete and Ordinary Portland Cement concrete: A comparative analysis of different grades of concrete. *Cleaner Environmental Systems*, 3, p. 100047. Available at: https://doi.org/10.1016/j.cesys.2021.100047.

Amorim Jr., N.S., Neto, J.S.A. and Santana, H.A., 2021. Durability and service life analysis of metakaolin-based geopolymer concretes with respect to chloride penetration using chloride migration test and corrosion potential. *Construction and Building Materials*, 287, p. 122970. Available at: https://doi.org/10.1016/j.conbuildmat.2021.122970.

Amran, M., Al-Fakih, A., Chu, S.H., Fediuk, R., Haruna, S., Azevedo, A. and Vatin, N., 2021. Long-term durability properties of geopolymer concrete: An in-depth review. *Case Studies in Construction Materials*, 15, p. e00661. Available at: https://doi.org/10.1016/j.cscm.2021.e00661.

Amran, Y.H.M., Alyousef, R., Alabduljabbar, H. and El-Zeadani, M., 2020. Clean production and properties of geopolymer concrete; A review. *Journal of Cleaner Production*, 251, p. 119679. Available at: https://doi.org/10.1016/j.jclepro.2019.119679.

Antunes, M., Santos, R.L., Pereira, J., Horta, R.B. and Colaço, R., 2024. The use of solid sodium silicate as activator for an amorphous wollastonitic hydraulic binder. *Materials*, 17(3), p. 626. Available at: https://doi.org/10.3390/ma17030626.

Anudeep, P., Reddy, M.A., Khed, V.C., Adamu, M., Varalakshmi, M., Ibrahim, Y.E. and Ahmed, O.S., 2024. Effect of superplasticizer in geopolymer and alkali-activated cement mortar/concrete: A review. *Reviews on Advanced Materials Science*, 63(1), p. 20230173. Available at: https://doi.org/10.1515/rams-2023-0173.

Assi, L., Carter, K., Deaver, E.E., Anay, R. and Ziehl, P., 2018. Sustainable concrete: Building a greener future. *Journal of Cleaner Production*, 198, pp. 1641–1651. Available at: https://doi.org/10.1016/j.jclepro.2018.07.123.

ASTM C143, 2012. *Standard Test Method for Slump of Hydraulic-Cement Concrete.* ASTM International, West Conshohocken, PA.

ASTM C1437, 2015. *Standard Test Method for Flow of Hydraulic Cement Mortar.* ASTM International, West Conshohocken, PA.

ASTM C191, 2021. *Standard Test Methods for Time of Setting of Hydraulic Cement by Vicat Needle*. ASTM International, West Conshohocken, PA.

ASTM C230, 2020. *Standard Specification for Flow Table for Use in Tests of Hydraulic Cement.* ASTM International, West Conshohocken, PA.

ASTM C596, 2023. *Standard Test Method for Drying Shrinkage of Mortar Containing Hydraulic Cement*. ASTM International, West Conshohocken, PA.

ASTM C618, 2022. *Standard Specification for Coal Fly Ash and Raw or Calcined Natural Pozzolan for Use in Concrete.* ASTM International, West Conshohocken, PA.

ASTM C666, 1997. *Standard Test Method for Resistance of Concrete to Rapid Freezing and Thawing.* ASTM International, West Conshohocken, PA.

ASTM C78, 2009. *Standard Test Method for Flexural Strength of Concrete (Using Simple Beam with Third-Point Loading).* ASTM International, West Conshohocken, PA.

ASTM G109, 2021. *Standard Test Methods for Determining Effects of Chemical Admixtures on Corrosion of Embedded Steel Reinforcement in Concrete Exposed to Chloride Environments.* ASTM International, West Conshohocken, PA.

Bellum, R.R., Muniraj, K. and Madduru, S.R.C., 2020. Exploration of mechanical and durability characteristics of fly ash-GGBFS based green geopolymer concrete. SN Applied Science, 2(919). Available at: https://doi.org/10.1007/s42452-020-2720-5.

Bhardwaj, B. and Kumar, P., 2019. Comparative study of geopolymer and alkali activated slag concrete comprising waste foundry sand. *Construction and Building Materials*, 209, pp. 555–565. Available at: https://doi.org/10.1016/j.conbuildmat.2019.03.107.

Bhatt, P., MacGinley, T. and Choo, B., 2014. *Reinforced concrete design to Eurocodes* (Vol. 4). CRC press.

Bhutta, A., Farooq, M., Zanotti, C. and Banthia, N., 2017. Pull-out behavior of different fibers in geopolymer mortars: effects of alkaline solution concentration and curing. *Materials and Structures*, 50(1), pp. 1–13. Available at: https://doi.org/10.1617/s11527-016-0889-2.

Bianco, I., Tomos, B.A.D. and Vinai, R., 2021. Analysis of the environmental impacts of alkali-activated concrete produced with waste glass-derived silicate activator – A LCA study. *Journal of Cleaner Production*, 316, p. 128383. Available at: https://doi.org/10.1016/j.jclepro.2021.128383.

BS EN 15167-1, 2006. *Ground Granulated Blast Furnace Slag for Use in Concrete, Mortar and Grout - Definitions, Specifications and Conformity Criteria.* British Standards Institution, London.

Cai, Z., Duan, X., Liu, L., Lu, Z. and Ye, J., 2024. Reinforced ultra-high performance concrete beam under flexure and shear: Experiment and theoretical model. *Case Studies in Construction Materials*, 20, p. e02647. https://doi.org/10.1016/j.cscm.2023.e02647

Cardenas-Pulido, J., Reyes, J.C., Carrillo, J. and Ramirez, F., 2020. Shear behaviour of geopolymer concrete panels under diagonal stress. *Engineering Structures*, 212, p. 110518. Available at: https://doi.org/10.1016/j.engstruct.2020.110518.

Castel, A., Foster, S.J., Ng, T. Sanjayan, J.G. and Gilbert, R.I., 2016. Creep and drying shrinkage of a blended slag and low calcium fly ash geopolymer Concrete. *Materials and Structures*, 49, pp. 1619–1628. Available at: https://doi.org/10.1617/s11527-015-0599-1.

Chen, L., Yang, M., Chen, Z., Xie, Z., Huang, L., Osman, A.I., Farghali, M., Sandanayake, M., Liu, E., Ahn, Y.H. and Ala'a, H., 2024. Conversion of waste into sustainable construction materials: A review of recent developments and prospects. *Materials Today Sustainability*, 27, p. 100930. Available at: https://10.1016/j.mtsust.2024.100930.

Cheng, Z., Zhao, R., Yuan, Y., Li, F., Castel, A. and Xu, T., 2020. Ageing coefficient for early age tensile creep of blended slag and low calcium fly ash geopolymer concrete. *Construction and Building Materials*, 262, p. 119855. Available at: https://dx.doi.org/10.1016/j.conbuildmat.2020.119855.

Chi, M., 2012. Effects of dosage of alkali-activated solution and curing conditions on the properties and durability of alkali-activated slag concrete. *Construction and Building*

Materials, 35, pp. 240–245. Available at: https://doi.org/10.1016/j.conbuildmat.2012.04.005.

Cong, P., Du, R., Gao, H. and Chen, Z., 2024. Comparison and assessment of carbon dioxide emissions between alkali-activated materials and OPC cement concrete. *Journal of Traffic and Transportation Engineering (English Edition)*, 11(5), pp. 918–938. https://doi.org/10.1016/j.jtte.2023.07.011.

Criado, M., Fernández-Jiménez, A., Palomo, A., Sobrados, I. and Sanz, J., 2008. Effect of the SiO_2/Na_2O ratio on the alkali activation of fly ash. Part II: 29Si MAS-NMR Survey. *Microporous and Mesoporous Materials*, 109, pp. 525–534. Available at: https://doi.org/10.1016/j.micromeso.2007.05.062.

Dadsetan, S., Siad, H., Lachemi, M., Mahmoodi, O. and Sahmaran, M., 2022. Sodium glass liquid from glass waste as a user-friendly hardener in structural geopolymer systems. *Cement and Concrete Composites*, 130, p. 104525. Available at: https://doi.org/10.1016/j.cemconcomp.2022.104525.

Davidovits, J., 1991. Geopolymers: inorganic polymeric new materials. *Journal of Thermal Analysis and Calorimetry*, 37, pp. 1633–1656. Available at: https://doi.org/10.1007/BF01912193.

Davidovits, J., 1994. Properties of geopolymer cements. *Proceedings of the 1st International Conference on Alkaline Cements and Concretes, Scientific Research Institute on Binders and Materials*, Kiev State Technical University, Kiev, Ukraine. Available at: https://www.geopolymer.org/wp-content/uploads/KIEV.pdf [Accessed 10 Jul. 2025].

Davidovits, J., 2015. *Geopolymer chemistry & applications*, 5th edn. Institut Géopolymère, France. https://www.geopolymer.org/wp-content/uploads/geopolymer-book-chapter1.pdf

Debbarmaa, S., Ransinchung, G.D.R.N., Singh, S. and Sahdeoa, S.K., 2020. Utilization of industrial and agricultural wastes for productions of sustainable roller compacted concrete pavement mixes containing reclaimed asphalt pavement aggregates. *Resources, Conservation and Recycling*, 152, p. 104504. Available at: https://doi.org/10.1016/j.resconrec.2019.104504.

Delgado-Plana, P., Bueno-Rodríguez, S., Pérez-Villarejo, L. and Eliche-Quesada, D., 2024. Synthesis of solid sodium silicate from waste glass and utilization on one-part alkali-activated materials based on spent oil filtering earth. *Environmental Science and Pollution Research*. Available at: https://doi.org/10.1007/s11356-024-33368-w.

De Weerdt, K., 2011. Geopolymers – State of the art. *Concrete Innovation Center (COIN) Project report 37*, SINTEF Building and Infrastructure. Available at:

https://sintef.brage.unit.no/sintef-xmlui/bitstream/handle/11250/2379051/COIN_report_no37.pdf?sequence=3&isAllowed=y [Accessed 10 Jul. 2025].

Diener, M.J., 2010. Cohen's d. *The Corsini encyclopedia of psychology*, pp.1-1. Available at: https://doi.org/10.1002/9780470479216.corpsy0200.

Dinh, H.L., Doh, J.H., Liu, J., Lu, L., Song, H. and Park, D., 2023. Comprehensive assessment of geopolymer concrete mechanical and environmental performance with glass cullet fine aggregates. *Journal of Building Engineering*, 76, p. 107094. Available at: https://doi.org/10.1016/j.jobe.2023.107094.

Duxson, P., Fernández-Jiménez, A., Provis, J.L., Lukey, G.C., Palomo, A. and van Deventer, J.S.J., 2007. Geopolymer technology: the current state of the art. *Journal of Material Science*, 42, pp. 2917–2933. Available at: https://doi.org/10.1007/s10853-006-0637-z.

de Moraes Pinheiro, S.M., Font, A., Soriano, L., Tashima, M.M., Monzó, J., Borrachero, M.V. and Payá, J., 2018. Olive-stone biomass ash (OBA): An alternative alkaline source for the blast furnace slag activation. *Construction and Building Materials*, 178, pp. 327–338. Available at: https://doi.org/10.1016/j.conbuildmat.2018.05.157.

Eisa, A.S., Sabol, P., Khamis, K.M. and Attia. A.A., 2022. Experimental study on the structural response of reinforced fly ash-based geopolymer concrete members. *Infrastructures*, 7(12), p. 170. Available at: https://doi.org/10.3390/infrastructures7120170.

El-Gamal, S.M.A. and Selim, F.A., 2017. Utilization of some industrial wastes for ecofriendly cement production. *Sustainable Materials and Technology*, 12, pp. 9–17. Available at: https://doi.org/10.1016/j.susmat.2017.03.001.

El-Naggar, M.R. and El-Dessouky, M.I., 2017. Re-use of waste glass in improving properties of metakaolin-based geopolymers: Mechanical and microstructure examinations. *Construction and Building Materials*, 132, pp. 543–555. Available at: https://doi.org/10.1016/j.conbuildmat.2016.12.023.

Elyamany, H.E., Abd Elmoaty, A.E.M. and Elshaboury, A.M., 2018. Magnesium sulfate resistance of geopolymer mortar. *Construction and Building Materials*, 184, pp. 111–127. Available at: https://doi.org/10.1016/j.conbuildmat.2018.06.212.

Emdadi, Z., Asim, N., Amin, M.H., Yarmo, M.A., Maleki, A., Azizi, M. and Sopian, K., 2017. Development of green geopolymer using agricultural and industrial waste materials with high water absorbency. Applied Sciences, 7(5), p. 514. Available at: https://doi.org/10.3390/app7050514.

EN 196-1, 2016. *Methods of Testing Cement - Part 1: Determination of Strength*. European Standards.

EN 1992-1-1, 2004. *Eurocode 2 – Design of concrete structures - Part 1-1 : General rules and rules for buildings*. Brussels: CEN.

EN 206, 2013. *Concrete: Specification, Performance, Production and Conformity*. Brussels: CEN.

Ewa, D.E., Ukpata, J.O., Out, O.N. and Alaneme, G.U., 2023. Optimization of saw dust ash and quarry dust pervious concrete's compressive strength using Scheffe's simplex lattice method. *Innovative Infrastructure Solutions,* 8(64). Available at: https://doi.org/10.1007/s41062-022-01031-3.

Fernandez-Jimenez, A. and Palomo, A., 2005. Composition and microstructure of alkali activated fly ash binder: Effect of the activator. *Cement and Concrete Research*, 35, pp. 1984–1992. Available at: https://doi.org/10.1016/j.cemconres.2005.03.003.

Fernando, S., Gunasekara, C., Law, D.W., Nasvi, M.C.M., Setunge, S. and Dissanayake, R., 2021. Life cycle assessment and cost analysis of fly ash–rice husk ash blended alkali-activated concrete. *Journal of environmental management,* 295, p. 113140. Available at: https://doi.org/10.1016/j.jenvman.2021.113140.

Field, A., 2024. *Discovering statistics using IBM SPSS statistics*. Sage publications limited.

Fu, Y., Cai, L. and Yonggen, W., 2011. Freeze-thaw cycle test and damage mechanics models of alkali-activated slag concrete. *Construction and Building Materials,* 25(7), pp. 3144–3148. Available at: https://doi.org/10.1016/j.conbuildmat.2010.12.006.

Gao, K., Lin, K-L., Wang, D., Hwang, C-L., Shiu, H-S., Chang, Y-M. and Cheng T-W., 2014. Effects of SiO_2/Na_2O molar ratio on mechanical properties and the microstructure of nano-SiO_2 metakaolin-based geopolymers. *Construction and Building Materials*, 53, pp. 503–510. Available at: https://doi.org/10.1016/j.conbuildmat.2013.12.003.

Ge, F.W., Deng, W.Q., Chen, H., Liu, X.H. and Liu, X., 2026. Variability and Probability Distribution Analysis of Geopolymer Concrete Using Response Surface Method. *Buildings*, 16(5), p.933. https://doi.org/10.3390/buildings16050933.

Ghanim, H.A., Alengaram, U.J., Bunnori, N.M. and Ibrahim, M.S.I., 2025. Innovative in-house sodium silicate derived from coal bottom ash and its impact on geopolymer mortar. *Journal of Building Engineering,* 99, p. 111428. Available at: https://doi.org/10.1016/j.jobe.2024.111428.

Gilbert R.I., 2018. *Cracking in concrete structures – Calculation of crack width and crack spacing*. UNSW Sydney, UNICIV Report No. R-467. https://vm.civeng.unsw.edu.au/uniciv/R-467.pdf.

Glasby, T., Day, J., Genrich, R. and Kemp, M., 2015. *Commercial scale geopolymer concrete construction*. [online] Available at: https://earthfriendlyconcrete.com/wp-content/uploads/2022/01/geopolymer-concrete_saudi-conference_2015.pdf [Accessed 8 Jul. 2025].

Gok, S.G. and Sengul, O., 2020. The use of waste glass as an activator in alkali-activated slag mortars. *Proceedings of the Institution of Civil Engineers – Engineering Sustainability*. Available at: https://doi.org/10.1680/jensu.19.00070.

Gok, S.G. and Sengul, O., 2024. Enhancing mechanical properties of alkali-activated slag SIFCON for sustainable construction using recycled glass and tire-derived waste steel fibers. *International Journal of Concrete Structures and Materials,* 18(89). Available at: https://doi.org/10.1186/s40069-024-00724-6.

Guo, S., Wu, Y., Jia, Z., Qi, X. and Wang, W., 2023. Sodium-based activators in alkali-activated materials: Classification and comparison. *Journal of building engineering*, 70, p. 106397. Available at: https://doi.org/10.1016/j.jobe.2023.106397.

Hadi, M.N.S., Zhang, H. and Parkinson, S., 2019. Optimum mix design of geopolymer pastes and concretes cured in ambient condition based on compressive strength, setting time and workability. *Journal of Building Engineering*, 23, pp. 301–313. Available at: https://doi.org/10.1016/j.jobe.2019.02.006.

Hardjito, D. and Rangan, B.V., 2005. *Development and properties of low-calcium fly ash-based geopolymer concrete*. Curtin University of Technology. Available at: http://hdl.handle.net/20.500.11937/5594.

Hardjito, D., Wallah, S.E., Sumajouw, D.M.J. and Rangan, B.V., 2004. On the development of fly ash-based geopolymer concrete. *ACI Materials Journal,* 101(6), pp. 467–472. Available at: https://doi.org/10.14359/13485.

Hasan, B.A. and Saeed, J.A., 2023. Effect of Concrete Strength on Shear Capacity of Reinforced High-Strength Concrete Continuous Beams without Web Reinforcements. *Advances in Civil Engineering*, 2023(1), p. 8784575. https://doi.org/10.1155/2023/8784575

Hasanbeigi, A., Menke, C. and Price, L., 2010. The CO_2 abatement cost curve for the Thailand cement industry. *Journal of Cleaner Production*, 18(15), pp. 1509–1518. Available at: https://doi.org/10.1016/j.jclepro.2010.06.005.

Hassan, A., Arif, M. and Shariq, M., 2022. Age-dependent compressive strength and elastic modulus of fly ash-based geopolymer concrete. *Structural Concrete*, 23(1), pp. 473–487. https://doi.org/10.1002/suco.202000372

Heshmati, M., Sheikh, M.N. and Hadi, M.N.S., 2025. A comprehensive review of the fresh and hardened characteristics of self-compacting geopolymer concrete. Journal of Sustainable Cement-based Materials, pp. 1–20. Available at: https://doi.org/10.1080/21650373.2025.2461182.

Hossain, Md.U., Dong, Y. and Ng, S.T., 2021. Influence of supplementary cementitious materials in sustainability performance of concrete industry: A case study in Hong Kong. *Case Studies in Construction Materials*, 15, p. e00659. Available at: https://doi.org/10.1016/j.cscm.2021.e00659.

Hossain, M.U., Poon, C.S., Dong, Y.H. and Xuan, D., 2018. Environmental impact distribution methods for supplementary cementitious materials. *Renewable and Sustainable Energy Reviews*, 82, pp. 597–608. Available at: https://doi.org/10.1016/j.rser.2017.09.048.

Hu, Y., Tang, Z., Li, W., Li, Y. and Tam, V.W.Y., 2019. Physical-mechanical properties of fly ash/GGBFS geopolymer composites with recycled aggregates. *Construction and Building Materials*, 226, pp. 139–151. Available at: https://doi.org/10.1016/j.conbuildmat.2019.07.211.

Ibrahim, M., Wan Ibrahim, W.M., Al Bakri Abdullah, M.M., Sauffi, A.S. and Vizureanu, P., 2022. Effect of solid-to-liquids and Na_2SiO_3-to-NaOH ratio on metakaolin membrane geopolymers. *Archives of Metallurgy and Materials*, 67. Available at: http://dx.doi.org/10.24425/amm.2022.137808.

Ikotun, J.O., Aderinto, G.E., Madirisha, M.M. and Katte, V.Y., 2024. Geopolymer cement in pavement applications: Bridging sustainability and performance. *Sustainability*, 16(13), p. 5417. Available at: https://doi.org/10.3390/su16135417.

Ikotun, B.D., Senatsi, K.B., Abdulwahab, R. and Nkala, M.L., 2024. Effects of waste glass powder as partial replacement of cement on the structural performance of concrete. *Civil Engineering and Architecture*, 12(4), pp. 2547–2556. Available at: https://doi.org/10.13189/cea.2024.120404.

Ikotun, J., Sithole, D., Ikotun, B., Moonsamy, S. and Adedeji P., 2025. Use of waste glass powder in concrete — A review of microstructure and durability properties. *Proceedings of the 7th International Conference on Concrete Repair, Rehabilitation and Retrofitting (ICCRRR 2024)*, RILEM Bookseries, vol. 59. Available at: https://doi.org/10.1007/978-3-031-75507-1_55.

Inventory of Carbon & Energy Database (ICE), 2024. *Circular Ecology, Educational Version (V4.0)*. Available at: https://circularecology.com/embodied-carbon-footprint-database.html [Assessed 28 April 2025].

Islam, G.M.S., Rahman, M.H. and Kazi, N., 2017. Waste glass as partial replacement of cement for sustainable concrete practice. *International Journal of Sustainable Built Environment*, 6(1), pp. 37–44. Available at: https://doi.org/10.1016/j.ijsbe.2016.10.005.

Iskhakov, I. and Ribakov, Y., 2019. Transverse deformations and structural phenomenon as indicators of steel fibred high-strength concrete nonlinear behavior. *Advances in Materials Science and Engineering*, 2019(1), p. 9147849. https://doi.org/10.1155/2019/9147849

Ismail, K.S., 2016. *Shear behaviour of reinforced concrete deep beams*. Doctoral dissertation, University of Sheffield. https://etheses.whiterose.ac.uk/id/eprint/12600/1/Thesis-white%20rose.pdf.

ISO 14040, 2006. *Environmental management — Life cycle assessment — Principles and framework.* International Organization for Standardization.

Jan, A., Pu, Z., Khan, K.A., Ahmad, I., Shaukat, A.J., Hao, Z. and Khan, I., 2022. A review on the effect of silica to alumina ratio, alkaline solution to binder ratio, calcium oxide + ferric oxide, molar concentration of sodium hydroxide and sodium silicate to sodium hydroxide ratio on the compressive strength of geopolymer concrete. *Silicon*, 14, pp. 3147–3162. Available at: https://doi.org/10.1007/s12633-021-01130-3.

Janga, S., Raut, A.N. and Murmu, A.L., 2024. Assessment of thermal and mechanical properties of fly ash based geopolymer blocks with a sustainability perspective using multi-criteria decision-making approach. *Journal of Building Engineering*, 88, p. 109261. Available at: https://doi.org/10.1016/j.jobe.2024.109261.

Jayaprakash, S., Jegatheeswaran, D., Pandimani, Subbaram, S., Dhamodharan, M., Ramasamy, V., Deivasigamani, V. and Adjei-Fio, F., 2025. Influence of granite powder waste on the flexural and microstructure morphology behaviors of reinforced concrete beams with glass fiber reinforced polymer bars. *Engineering Reports*, 7(8), p. e70304. Available at: https://doi.org/10.1002/eng2.70304.

Kalaivani, M., Shyamala, G., Ramesh, S., Angusenthil, K. and Jagadeesan, R., 2020. Performance evaluation of fly ash/slag based geopolymer concrete beams with addition of lime. *Materials Today: Proceedings*, 27(1), pp. 652–656. Available at: https://doi.org/10.1016/j.matpr.2020.01.596.

Kamseu, E., Beleuk à Moungam, L.M., Cannio, M., Billong, N., Chaysuwan, D., Melo, U.C. and Leonelli, C., 2017. Substitution of sodium silicate with rice husk ash-NaOH solution

in metakaolin based geopolymer cement concerning reduction in global warming. *Journal of Cleaner Production*, 142(4), pp. 3050–3060. Available at: https://10.1016/j.jclepro.2016.10.164.

Kanagaraj, B., Anand, N. and Lubloy, E., 2022. Performance evaluation of sodium silicate waste as a replacement for conventional sand in geopolymer concrete. *Journal of Cleaner Production*, 375, p. 134172. Available at: https://doi.org/10.1016/j.jclepro.2022.134172.

Ken, W.P., Ramli, M. and Ban, C.C., 2015. An overview on the influence of various factors on the properties of geopolymer concrete derived from industrial by-products. *Construction and Building Materials*, 77, pp. 370–395. Available at: https://doi.org/10.1016/j.conbuildmat.2014.12.065.

Khale, D. and Chaudhary, R., 2007. Mechanism of geopolymerization and factors influencing its development: a review. *Journal of Material Science*, 42, pp. 729–746. Available at: https://doi.org/10.1007/s10853-006-0401-4.

Khasawneh, M.A., 2025. Geopolymer concrete in construction projects: a review. *Discover Civil Engineering*, 2(1), p.124. available at: https://doi.org/10.1007/s44290-025-00281-1.

Kheimi, M., Aziz, I.H., Abdullah, M.M.A.B., Almadani, M. and Abd Razak, R., 2022. Waste material via geopolymerization for heavy-duty application: A review. *Materials*, 15(9), p. 3205. Available at: https://doi.org/10.3390/ma15093205.

Kishore, Y.S.N., Nadimpalli, S.G.D., Potnuru, A.K., Vemuri, J. and Khan, M.A., 2022. Statistical analysis of sustainable geopolymer concrete. *Materials Today: Proceedings*, 61, pp.212-223. Available at: https://doi.org/10.1016/j.matpr.2021.08.129.

Kolade, A.S., Ikotun, B.D. and Oyejobi, D.O., 2025. A review of the chemistry, waste utilization, mix design and performance evaluation of geopolymer concrete. *Iranian Journal of Science and Technology, Transactions of Civil Engineering*. Available at: https://doi.org/10.1007/s40996-025-01801-w.

Kolade, A.S., Ikotun, B.D., Oyejobi, D.O., Aderinto, G.E. and Makungu, M.M., 2025. Performance evaluation of geopolymer mortars prepared with waste glass powder-derived sodium silicate solution. *Iranian Journal of Science and Technology, Transactions of Civil Engineering*. Available at: https://doi.org/10.1007/s40996-025-01952-w.

Kolade, A.S., Ikotun, B.D. and Oyejobi, D.O., 2025. Composition and performance-based mix design methodology for geopolymer mortars. *Discover Civil Engineering*, 2(162). Available at: https://doi.org/10.1007/s44290-025-00327-4.

Kolade, A.S., Ikotun, B.D. and Oyejobi, D.O., 2026. Effect of activator-to-binder ratio on workability and strength of sustainable one-part geopolymer mortar. *Materials Research Proceedings*, 63, pp 12–20. Available at: https://doi.org/10.21741/9781644904053-2.

Kolade, A.S., Ikotun, B.D. and Oyejobi, D.O., 2026. Effect of fusion conditions on valorized waste glass solution and its influence on the mechanical strength of geopolymer mortar. *Civil Engineering and Architecture*, 14(2), pp. 917–933. Available at: https://doi.org/10.13189/cea.2026.140218.

Kolade, A.S., Ikotun, B.D. and Oyejobi, D.O., 2026. Life cycle assessment of geopolymer concrete using fly ash–slag binder and waste glass-derived alkali activator. *Next Materials*, 12, p. 102219. Available at: https://doi.org/10.1016/j.nxmate.2026.102219.

Komnitsas, K. and Zaharaki, D., 2007. Geopolymerisation: A review and prospects for the minerals industry. *Minerals Engineering*, 20, pp. 1261–1277. Available at: https://doi.org/10.1016/j.mineng.2007.07.011.

Kong, D., Sanjayan, J.G. and Sagoe-Crentsil, K., 2007. Comparative performance of geopolymers made with metakaolin and fly ash after exposure to elevated temperatures. *Cement and Concrete Research*, 37(12), pp. 1583–1589. Available at: https://doi.org/10.1016/j.cemconres.2007.08.021.

Kumar, B.S.C., Ramesh, K. and Poluraju, P., 2017. An experimental investigation on flexural behavior of GGBFS and metakaolin based geopolymer concrete. *ARPN Journal of Engineering and Applied Sciences*, 12(7), pp. 2052–2062. Available at: https://www.researchgate.net/publication/316934887.

Kuri, J.C., Khan, M.N.N. and Sarker, P.K., 2021. Fresh and hardened properties of geopolymer binder using ground high magnesium ferronickel slag with fly ash. *Construction and Building Materials*, 272, pp. 121877. Available at: https://doi.org/10.1016/j.conbuildmat.2020.121877.

Lee, J., Lee, T., Jeong, J. and Jeong, J., 2021. Mix design optimization and environmental impact assessment of low-carbon materials containing alkali-activated slag and high CaO fly ash. *Construction and Building Materials*, 267, p. 120932. Available at: https://doi.org/10.1016/j.conbuildmat.2020.120932.

Lei, M., Wang, X., Meng, H., Yan, Z., Lin, J. and Wu, Z., 2023. Study of fly ash-slag geopolymer mortar as a rapid strengthening agent for concrete structures. *Construction and Building Materials*, 394, p. 132147. Available at: https://doi.org/10.1016/j.conbuildmat.2023.132147.

Li, B., Li, H., Zhang, X., Fan, P., Liu, L., Li, B., Dong, W. and Zhao, B., 2019. Calcined sodium silicate as an efficient and benign heterogeneous catalyst for the transesterification of natural lecithin to L-α-glycerophosphocholine. *Green Processing and Synthesis*, 8(1), pp. 78–84. Available at: https://doi.org/10.1515/gps-2017-0190.

Li, N., Shi, C., Zhang, Z., Wang, H. and Liu, Y., 2019. A review on mixture design methods for geopolymer concrete. *Composites Part B: Engineering*, 178, p. 10749. Available at: https://doi.org/10.1016/j.compositesb.2019.107490.

Liu, J., Shi, X., Zhang, G. and Li, L., 2023. Study the mechanical properties of geopolymer under different curing conditions. *Minerals*, 13(5), p. 690. Available at: https://doi.org/10.3390/min13050690.

Lloyd, N.A. and Rangan, B.V., 2010. Geopolymer concrete with fly ash. In: *Proceedings of the 2nd International Conference on Sustainable Construction Materials and Technologies*, Università Politecnica delle Marche, Ancona, Italy. Available at: http://hdl.handle.net/20.500.11937/3540.

Lofgren, I., 2007, November. Calculation of crack width and crack spacing. In *Proceedings of the Nordic Mini-Seminar: "Fibre Reinforced Concrete*", Trondheim, Norway (Vol. 15). https://publications.lib.chalmers.se/records/fulltext/248921/local_248921.pdf

Luan, C., Shi, X., Zhang, K., Utashev, N., Yang, F., Dai, J. and Wang, Q., 2021. A mix design method of fly ash geopolymer concrete based on factors analysis. *Construction and Building Materials*, 272, p. 121612. Available at: https://doi.org/10.1016/j.conbuildmat.2020.121612.

Luhar, I. and Luhar, S., 2022. A Comprehensive review on fly ash-based geopolymer. *Journal Composites Science*, 6(8), p. 219. Available at: https://doi.org/10.3390/jcs6080219.

Ma, C., Long, G., Shi, Y. and Xie, Y., 2018. Preparation of cleaner one-part geopolymer by investigating different types of commercial sodium metasilicate in China. *Journal of Cleaner Production*, 201, pp. 636–647. Available at: https://doi.org/10.1016/j.jclepro.2018.08.060.

Madirisha, M.M., Dada, O.R. and Ikotun, B.D., 2024. Chemical fundamentals of geopolymers in sustainable construction. *Materials Today Sustainability*, 27, p. 100842. Available at: https://doi.org/10.1016/j.mtsust.2024.100842.

Malkawi, A.B., Al-Mattarneh, H., Achara, B.E., Muhammed, B.S. and Nuruddin, M.F., 2018. Dielectric properties for characterisation of fly ash-based geopolymer binders. *Construction and Building Materials*, 18, pp. 19–32. Available at: https://doi.org/10.1016/j.conbuildmat.2018.08.180.

Martinez, A. and Miller, S.A., 2025. Life cycle assessment and production cost of geopolymer concrete: A meta-analysis. *Resources, Conservation and Recycling*, 215, p. 108018. Available at: https://doi.org/10.1016/j.resconrec.2024.108018.

Matsimbe, J., Dinka, M., Olukanni, D. and Musonda, I., 2024. Fundamental machine learning algorithms and statistical models applied in strength prediction of geopolymers: a systematic review. *Discover Applied Sciences*, 6(10), p. 538. Available at: https://doi.org/10.1007/s42452-024-06244-y

McCloskey, D.W., Soutsos, M., Kwasny, J., Swadzba-Kwasny, M. and Goodrich, P., 2024. Glass-derived sodium silicate used as an activator for cement-free binders to rival commercial sodium silicate. *Proceedings of the Civil Engineering Research in Ireland 2024 Conference (CERI2024)*, Civil Engineering Research Association of Ireland, Galway. Available at: https://pureadmin.qub.ac.uk/ws/portalfiles/portal/609960698/Accepted_version_-_Glass-Derived_Sodium_Silicate_used_as_an_Activator_for_Cement-Free_Binders_to_rival_commerical_sodium_silicate.pdf [Accessed 12 Jul. 2025].

Meesala, C.R., Verma, N.K. and Kumar, S., 2020. Critical review on fly-ash based geopolymer concrete. *Structural Concrete*, 21(3), pp. 1013–1028. Available at: https://doi.org/10.1002/suco.201900326.

Mo, K.H., Ling, T.C., Alengaram, U.J., Yap, S.P. and Yuen, C.W., 2017. Overview of supplementary cementitious materials usage in lightweight aggregate concrete. *Construction and Building Materials*, 139, pp.403-418. https://doi.org/10.1016/j.conbuildmat.2017.02.081

Mohamad, N., Muthusamy, K., Embong, R., Kusbiantoro, A. and Hashim, M.H., 2021. Environmental impact of cement production and solutions: A review. *Materials Today: Proceedings*, 48(4), pp. 741–746. Available at: https://doi.org/10.1016/j.matpr.2021.02.212.

Mohamed, O., Ahmed, E., Najm, O., Al-Aribe, K. and Hijah E., 2023. Water absorption characteristics and rate of strength development of mortar with slag-based alkali-activated binder and 25% fly ash replacement. *Materials Today: Proceedings*. Available at: https://doi.org/10.1016/j.matpr.2023.02.411.

Mohamed, R., Abd Razak, R., Abdullah, M.M., Abd Rahim, S.Z., Yuan-Li, L., Sandu, A.V. and Wysłocki, J.J., 2022. Heat evolution of alkali-activated materials: a review on influence factors. *Construction and Building Materials*, 314, p. 125651. Available at: https://doi.org/10.1016/j.conbuildmat.2021.125651.

Mordor Intelligence, 2025. *Sodium Silicate Market Size & Share Analysis - Growth Trends & Forecasts (2025 - 2030).* [online] Available at: https://www.mordorintelligence.com/industry-reports/sodium-silicate-market [Accessed 5 May 2025].

Mori, H., 2003. Extraction of silicon dioxide from waste colored glasses by alkali fusion using sodium hydroxide. *Journal of the Ceramic Society of Japan*, 111(6), pp. 376–381. Available at: https://doi.org/10.2109/jcersj.111.376.

Mourougane, R., Puttappa, C.G., Sashidhar, C. and Muthu, K.U., 2012, June. Shear behavior of high strength GPC/TVC beams. In *Proc. Int. Conf. Adv. Arch. Civ. Eng* (Vol. 21, p. 142). Available at: https://bonfring.org/conference/papers/MSR_AARCV2012/SAM116.pdf.

Nadarajah, A., Mohd Nasir, N.A., Abu Bakar, N. and Safiee, N.A., 2024. Fly ash-GGBS blended geopolymer mortar for early engineering characteristic at ambient temperature. *Ain Shams Engineering Journal*, 15(7), p. 102821. Available at: https://doi.org/10.1016/j.asej.2024.102821.

Naghizadeh, A. and Ekolu, S.O., 2019. Method for comprehensive mix design of fly ash geopolymer mortars. *Construction and Building Materials*, 202, pp. 704–717. Available at: https://doi.org/10.1016/j.conbuildmat.2018.12.185.

Ng, T.S., Amin, A. and Foster, S.J., 2013. The behaviour of steel-fibre-reinforced geopolymer concrete beams in shear. *Magazine of Concrete Research*, 65(5), pp. 308-318. Available at: https://doi.org/10.1680/macr.12.00081.

Ng, T.S. and Foster, S.J., 2013. Development of a mix design methodology for high-performance geopolymer mortars. *Structural Concrete*, 14(2), pp. 148–156. Available at: https://doi.org/10.1002/suco.201200018.

Nguyen, T.T., Goodier, C.I. and Austin, S.A., 2020. Factors affecting the slump and strength development of geopolymer concrete. *Construction and Building Materials*, 261, p. 119945. Available at: https://doi.org/10.1016/j.conbuildmat.2020.119945.

Nodehi, M. and Taghvaee, V.M., 2022. Alkali-activated materials and geopolymer: a review of common precursors and activators addressing circular economy. *Circular Economy and Sustainability*, 2(1), pp. 165–196. https://doi.org/10.1007/s43615-021-00029-w.

NT BUILD 492, 1999. *Concrete, Mortar and Cement-Based Repair Materials: Chloride Migration Coefficient from Non-Steady-State Migration Experiments*. Nordtest: Espoo, Finland.

Olivia, M. and Nikraz, H., 2012. Properties of fly ash geopolymer concrete designed by Taguchi method. *Materials & Design (1980-2015)*, 36, pp. 191–198. Available at: https://doi.org/10.1016/j.matdes.2011.10.036.

Olsson, J.A., Miller, S.A. and Kneifel, J.D., 2024. A review of current practice for life cycle assessment of cement and concrete. *Resources, Conservation and Recycling*, 206, p. 107619. Available at: https://doi.org/10.1016/j.resconrec.2024.107619.

Omur, T., Kanat, D. and Kabay, N., 2024. Innovative use of hazelnut shell ash as an alkali activator: A comparative analysis with commercial activators. *Journal of Building Engineering*, 90, p. 109466. Available at: https://doi.org/10.1016/j.jobe.2024.109466.

Oyebisi, S., Olutoge, F., Kathirvel, P., Oyaotuderekumor, I., Lawanson, D., Nwani, J., Ede, A. and Kaze, R., 2022. Sustainability assessment of geopolymer concrete synthesized by slag and corncob ash. *Case Studies in Construction Materials*, 17, p. e01665. Available at: https://doi.org/10.1016/j.cscm.2022.e01665.

Oyejobi, D.O., Firoozi, A.A., Fernández, D.B. and Avudaiappan, S., 2024. Integrating circular economy principles into concrete technology: Enhancing sustainability through industrial waste utilization. *Results in Engineering*, 24, p. 102846. Available at: https://doi.org/10.1016/j.rineng.2024.102846.

Oyejobi, D., Jameel, M., Adewuyi, A., Aina, S., Avudaiappan, S. and Maureira-Carsalade, N., 2023. Analyzing influence of mix design constituents on compressive strength, setting times and workability of geopolymer mortar and paste. *Advances in Civil Engineering*, pp. 1–15. Available at: https://doi.org/10.1155/2023/5522056.

Ozkilic, Y.O., Celik, A.I., Aksoylu, C., Karalar, M., Mydin, M.A.O., Althaqafi, E., Yilmaz, F. and Umiye, O.A., 2025. Shear and flexural performance of reinforced geopolymer concrete beams cured under ambient and oven conditions with environmentally friendly waste steel tire wire additives. *Scientific Reports*, 15(1), p. 22765. Available at: https://doi.org/10.1038/s41598-025-05546-4.

Ozturk, M. and Arslan, G., 2023. Flexural behavior of GBFS-based geopolymer-reinforced concrete beams. *Buildings*, 13(1), p. 141. Available at: https://doi.org/10.3390/buildings13010141.

Pam, H.J., Kwan, A.K.H. and Islam, M.S., 2001. Flexural strength and ductility of reinforced normal-and high-strength concrete beams. *Proceedings of the Institution of Civil Engineers-Structures and Buildings*, 146(4), pp. 381–389. https://doi.org/10.1680/stbu.2001.146.4.381.

Panneerselvam, V. and Pazhani, K.C., 2024. Experimental studies on the performance of geo-polymer reinforced concrete beams subjected to accelerated corrosion. *Polish Journal of Environmental Studies*, 33(2), pp. 1357–1364. Available at: https://doi.org/10.15244/pjoes/172757.

Parathi, S., Nagarajan, P. and Pallikkara, S.A., 2021. Ecofriendly geopolymer concrete: A comprehensive review. *Clean Technologies and Environmental Policy*, 23, pp. 1701–1713. Available at: https://doi.org/10.1007/s10098-021-02085-0.

Patankar, S.V., Ghugal, Y.M. and Jamkar, S.S., 2015. Mix design of fly ash Based geopolymer concrete. In: Matsagar, V. (edn) *Advanced Structural Engineering*, Springer. Available at: https://doi.org/10.1007/978-81-322-2187-6_123.

Patrick, N.L., Madirisha, M.M. and Mtei, R.P., 2024. Potential of Tanzanian natural pozzolans as geopolymer cement for oil and gas wellbore integrity. *Construction and Building Materials*, 418, p. 135342. Available at: https://doi.org/10.1016/j.conbuildmat.2024.135342.

Podolsky, Z., Liu, J., Dinh, H., Doh, J.H., Guerrieri, M. and Fragomeni, S., 2021. State of the art on the application of waste materials in geopolymer concrete. *Case Studies in Construction Materials*, 15, p. e00637. Available at: https://doi.org/10.1016/j.cscm.2021.e00637.

Passuello, A., Rodríguez, E.D., Hirt, E., Longhi, M., Bernal, S.A., Provis, J.L. and Kirchheim, A.P., 2017. Evaluation of the potential improvement in the environmental footprint of geopolymers using waste-derived activators. *Journal of Cleaner Production*, 166, pp. 680–689. Available at: https://doi.org/10.1016/j.jclepro.2017.08.007.

Provis, J.L., 2014. Geopolymers and other alkali activated materials: why, how and what?. *Materials and Structures*, 47, pp. 11–25. Available at: https://doi.org/10.1617/s11527-013-0211-5.

Provis, J.L., 2018. Alkali-activated materials. *Cement and Concrete Research*, 114, pp. 40–48. Available at: https://doi.org/10.1016/j.cemconres.2017.02.009.

Quadflieg, T., Morozov, N., Karimova, A., Gries, T. and Stolyarov, O., 2020. Experimental analysis of the mechanical properties of concrete using alternative binding agents. *Civil Engineering Design*, 2(5-6), pp. 177–181. Available at: https://doi.org/10.1002/cend.201900017.

Radebe, S.P., Madirisha, M.M., Ikotun, B.D. and Dada, O.R., 2025. Durability and Strength Improvement of Ambient-Cured Geopolymer Concrete Using Polypropylene Fibers.

Iranian Journal of Science and Technology, Transactions of Civil Engineering, pp. 1–20. Available at: https://doi.org/10.1007/s40996-025-01987-z.

Rajan, H.S. and Kathirvel, P., 2021. Sustainable development of geopolymer binder using sodium silicate synthesized from agricultural waste. *Journal of Cleaner Production*, 286, p.124959. available at: https://doi.org/10.1016/j.jclepro.2020.124959.

Rani, A. and Shudha, C., 2024. Mechanical, microstructural, and durability assessment of ambient cured geopolymer concrete. *Multiscale and Multidisciplinary Modeling, Experiments and Design*, 7, pp.6019-6034. Available at: https://doi.org/10.1007/s41939-024-00568-3.

Rao, G.M. and Rao, T.G., 2015. Final setting time and compressive strength of fly ash and GGBS-based geopolymer paste and mortar. *Arabian Journal of Science and Engineering*, 40(11), pp. 3067–3074. Available at: https://doi.org/10.1007/s13369-015-1757-z.

Raveendran, N. and Vasugi, K., 2024. Synergistic effect of nano silica and metakaolin on mechanical and microstructural properties of concrete: An approach of response surface methodology. *Case Studies in Construction Materials*, 20, p. e03196. Available at: https://doi.org/10.1016/j.cscm.2024.e03196.

Reddy, M.S., Dinakar, P. and Rao, B.H., 2018. Mix design development of fly ash and ground granulated blast furnace slag based geopolymer concrete. *Journal of Building Engineering*, 20, pp. 712–722. Available at: https://doi.org/10.1016/j.jobe.2018.09.010.

Samantasinghar, S. and Singh, S.P., 2019. Fresh and hardened properties of fly ash–slag blended geopolymer paste and mortar. *International Journal of Concrete and Structural Materials*, 13(47). Available at: https://doi.org/10.1186/s40069-019-0360-1.

Samarakoon, M.H., Ranjith, P.G., Duan, W.H., Haque, A. and Chen, B.K., 2021. Extensive use of waste glass in one-part alkali-activated materials: Towards sustainable construction practice. *Waste Management*, 130, pp. 1–11. Available at: https://doi.org/10.1016/j.wasman.2021.04.060.

Samarakoon, M., Ranjith, P., Duan, W.H. and De Silva, V., 2020. Properties of one-part fly ash/slag-based binders activated by thermally-treated waste glass/NaOH blends: a comparative study. *Cement and Concrete Composites*, 112, p. 103679. Available at: https://doi.org/10.1016/j.cemconcomp.2020.103679.

SANS 10100-1, 2000. *The Structural Use of Concrete, Part 1: Design*. South African Bureau of Standards, Pretoria.

SANS 1058, 2012. *Concrete Paving Blocks.* South African Bureau of Standards, Pretoria.

SANS 1083, 2013. *Aggregates from natural sources — Aggregates for concrete.* South African Bureau of Standards, Pretoria.

SANS 3001-AG1, 2012. *Civil Engineering Test Methods Part AG1: Particle Size Analysis of Aggregates by Sieving.* South African Bureau of Standards, Pretoria.

SANS 50196-1, 2006. *Methods of Testing Cement. Part 1: Determination of strength.* South African Bureau of Standards, Pretoria.

SANS 50196-3, 2006. *Method of Testing Cement. Part 3: Determination of setting time and soundness.* South African Bureau of Standards, Pretoria.

SANS 50197-1, 2000. *Cement — Part 1: Composition, specifications and conformity criteria for common cements.* South African Bureau of Standards, Pretoria.

SANS 50934-2, 2011. *Admixtures for concrete, mortar and grout – Part 2: Concrete admixtures – Definitions, requirements, conformity, marking and labelling.* South African Bureau of Standards, Pretoria.

SANS 5861-1, 2006. *Concrete Tests: Mixing Fresh Concrete in the Laboratory.* South African Bureau of Standards, Pretoria.

SANS 5862-1, 2006. *Concrete Tests – Consistency of Freshly Mixed Concrete – Flow Test.* South African Bureau of Standards, Pretoria.

SANS 5863, 2006. *Concrete Tests: Compressive Strength of Hardened Concrete.* South African Bureau of Standards, Pretoria.

SANS 5864, 2006. *Concrete Tests: Flexural Strength of Hardened Concrete.* South African Bureau of Standards, Pretoria.

SANS 6251, 2006. *Concrete Tests –Density of Hardened Concrete.* South African Bureau of Standards, Pretoria.

SANS 6255, 2006. *Mortar Tests – Compressive Strength of Mortar*. South African Bureau of Standards, Pretoria.

SANS 6892-1, 2010. *Metallic Materials – Tensile Testing at Room Temperature*. South African Bureau of Standards, Pretoria.

SANS 920, 2011. *Steel Bars for Concrete Reinforcements*. South African Bureau of Standards, Pretoria.

Sathiparan, N. and Subramaniam, D.N., 2024. Potential use of crushed waste glass and glass powder in sustainable pervious concrete: A review. *Cleaner Waste Systems*, 9, p. 100191. Available at: https://doi.org/10.1016/j.clwas.2024.100191.

Sathonsaowaphak, A., Chindaprasirt, P. and Pimraksa, K., 2009. Workability and strength of lignite bottom ash geopolymer mortar. *Journal of hazardous materials*, 168(1), pp.44-50. Available at: https://doi.org/10.1016/j.jhazmat.2009.01.120

Sharmin, A., Alengaram, U.J., Jumaat, M.Z., Yusuf, M.O., Kabir, S.M.A. and Bashar, I.I., 2017. Influence of source materials and the role of oxide composition on the performance of ternary blended sustainable geopolymer mortar. *Construction and Building Materials*, 144, pp. 608–623. Available at: https://doi.org/10.1016/j.conbuildmat.2017.03.178.

Siddika, A., Hajimohammadi, A., Ferdous, W. and Sahajwalla, V., 2021. Roles of waste glass and the effect of process parameters on the properties of sustainable cement and geopolymer concrete – A state-of-the-art review," *Polymers*, 13(22), p. 3935. Available at: https://10.3390/polym13223935.

Siddika, A., Hajimohammadi, A., Mamun, M.A.A., Alyousef, R. and Ferdous, W., 2021. Waste glass in cement and geopolymer concretes: A review on durability and challenges. *Polymers*, 13(13), p. 2071. Available at: https://doi.org/10.3390/polym13132071.

SikaViscoCrete®-2100, 2023. *Environmental product declaration*. Available at: https://usa.sika.com/dam/dms/us01/5/Sika%20ViscoCrete-2100%20EPD%202023.pdf [Accessed 13 May 2025].

Singh, A., Bhadauria, S.S., Mudgal, M. and Kushwah, S.S., 2022. Effect of alkali activator dosage on compressive and tensile strength of ground granulated blast furnace slag based geopolymer concrete. *Canadian Journal of Civil Engineering*, 49(1), pp. 73–82. Available at: https://doi.org/10.1139/cjce-2020-0558.

Singh, A., Bhadauria, S.S., Mudgal, M. and Kushwah, S.S., 2020. Engineering properties of geopolymer prepared by mild chemical activation of ground granulated blast furnace slag. *Indian Journal of Engineering and Materials Science*, 27, pp. 996–1008. Available at: https://nopr.niscpr.res.in/bitstream/123456789/56161/1/IJEMS%2027%285%29%20996-1008.pdf

Singh, A., Bhadauria, S.S., Thakare, A.A., Kumar, A., Mudgal, M. and Chaudhary, S., 2024. Durability assessment of mechanochemically activated geopolymer concrete with a low molarity alkali solution. *Case Studies in Construction Materials*, 20, p. e02715. Available at: https://doi.org/10.1016/j.cscm.2023.e02715.

Singh, B., Ishwarya, G., Gupta, M. and Bhattacharyya, S.K., 2015. Geopolymer concrete: A review of some recent developments. *Construction and Building Materials* 85, pp. 78–90. Available at: http://dx.doi.org/10.1016/j.conbuildmat.2015.03.036.

Singh, J. and Singh, S.P., 2019. Geopolymerization of solid waste of non-ferrous metallurgy – A review. *Journal of Environmental Management*, 251, p. 109571. Available at: https://doi.org/10.1016/j.jenvman.2019.109571.

Department of Forestry, Fisheries and the Environment, 2024. *South Africa's 2022 Grid Emission Factors Report*. Available at: https://www.gov.za/sites/default/files/gcis_document/202411/51495gon5498.pdf [Assessed 17 May 2025].

Sumajouw, D.M.J., Malingkas, G., Pandaleke, R. and Handono, B.D., 2023. Geopolymer concrete (GPC) as a suitable green solution for building and construction material. *IOSR Journal of Mechanical and Civil Engineering*, 20(1), pp. 61–72. Available at: https://www.iosrjournals.org/iosr-jmce/papers/vol20-issue1/Ser-2/D2001026172.pdf.

Sunarsih, E.S., As'ad, S. Mohd.Sam, A.R. and Kristiawan, S., 2024. The effect of alkali activator to binder ratio on workability, density and compressive strength of fly ash-slag based geopolymer mortar. *Nano Hybrids and Composites*, 45, pp. 121–127. Available at: https://doi.org/10.4028/p-MfE2js.

Tchakouté, H.K., Rüscher, C.H., Kong, S. and Ranjbar, N., 2016. Synthesis of sodium waterglass from white rice husk ash as an activator to produce metakaolin-based geopolymer cements. *Journal of Building Engineering*, 6, pp. 252–261. Available at: https://doi.org/10.1016/j.jobe.2016.04.007.

Tchakouté, H.K., Rüscher, C.H., Kong, S., Kamseu, E. and Leonelli, C., 2016. Geopolymer binders from metakaolin using sodium waterglass from waste glass and rice husk ash as alternative activators: A comparative study. *Construction and Building Materials*, 114, pp. 276–289. Available at: http://dx.doi.org/10.1016/j.conbuildmat.2016.03.184.

Temuujin, J.V., Van Riessen, A. and Williams, R., 2009. Influence of calcium compounds on the mechanical properties of fly ash geopolymer pastes. *Journal of Hazardous Materials*, 167(1), pp. 82–88. Available at: https://doi.org/10.1016/j.jhazmat.2008.12.121.

Terrones-Saeta, J.M., Luís, A.T., Romero, E., Fortes Garrido, J.C., Diaz-Curiel, J. and Grande, J.A., 2023. Factor Analysis of the Physical–Mechanical Properties for Geopolymers Based on Brick Dust and Biomass Bottom Ash as Eco-Friendly Building Materials. Processes, 11(8), p. 2491. Available at: https://doi.org/10.3390/pr11082491.

Tiainen, M., Daavitsainen, J. and Laitinen, R.S., 2002. The role of amorphous material in ash on the agglomeration problems in FB boilers. A powder XRD and SEM-EDS study. *Energy Fuel*, 16(4), pp. 871–877. Available at: https://doi.org/10.1021/ef010269j.

Torres-Carrasco, M. and Puertas, F., 2017. Waste glass as a precursor in alkaline activation: chemical process and hydration products. *Construction and Building Materials*, 135, pp. 342–354. Available at: https://doi.org/10.1016/j.conbuildmat.2017.02.071.

Turner, L.K. and Collins, F.G., 2013. Carbon dioxide equivalent (CO_2-e) emissions: A comparison between geopolymer and OPC cement concrete. *Construction and Building Materials*, 43, pp. 125–130. Available at: https://10.1016/j.conbuildmat.2013.01.023.

Umer, M., Ahmad, J. and Mukhtar, H., 2024. Innovative valorization of biomass waste-derived sodium silicate for geopolymer concrete synthesis: Sustainability assessment and circular economy potential. *Journal of Cleaner Production*, 452, p. 142181. Available at: https://doi.org/10.1016/j.jclepro.2024.142181.

Vinai, R. and Soutsos, M., 2019. Production of sodium silicate powder from waste glass cullet for alkali activation of alternative binders. *Cement and Concrete Research*, 116, pp. 45–56. Available at: https://10.1016/j.cemconres.2018.11.008.

Visintin, P., Ali, M.M., Albitar, M. and Lucas, W., 2017. Shear behaviour of geopolymer concrete beams without stirrups. *Construction and Building Materials*, 148, pp. 10-21. Available at: https://doi.org/10.1016/j.conbuildmat.2017.05.010.

van Deventer, J.S.J., Provis, J.L., Duxson, P., 2012. Technical and commercial progress in the adoption of geopolymer cement. *Minerals Engineering*, 29, pp. 89–104. Available at: https://doi.org/10.1016/j.mineng.2011.09.009.

Wadstrom, C., Johansson, M. and Wallén, M., 2021. A framework for studying outcomes in industrial symbiosis. *Renewable and Sustainable Energy Reviews*, 151, p. 111526. Available at: https://doi.org/10.1016/j.rser.2021.111526.

Wallah, S.E. and Rangan, B.V., 2006. *Low-calcium fly ash-based geopolymer concrete: long-term properties*. Curtin University of Technology. Available at: http://hdl.handle.net/20.500.11937/34322.

Wang, S., Huang, Q. and Xu, Z., 2025. Performance and statistical characteristics of ferronickel slag geopolymer concrete. Scientific Reports, 15(1), p. 37639. Available at: https://doi.org/10.1038/s41598-025-21614-1.

Waqas, R.M., Butt, F., Zhu, X., Jiang, T. and Tufail, R.F., 2021. A comprehensive study on the factors affecting the workability and mechanical properties of ambient cured fly ash and slag based geopolymer concrete. *Applied Sciences*, 11(18), p. 8722. https://doi.org/10.3390/app11188722.

Wong, L.S., 2022. Durability performance of geopolymer concrete: A review. *Polymers*, 14, p. 868. Available at: https://doi.org/10.3390/polym14050868.

Wu, Y., Lu, B.., Bai, T., Wang, H., Du, F., Zhang, Y., Cai, L., Jiang, C. and Wang, W., 2019. Geopolymer, green alkali activated cementitious material: Synthesis, applications and challenges. *Construction and Building Materials*, 224, pp. 930–949. Available at: https://doi.org/10.1016/j.conbuildmat.2019.07.112.

Xie, Z.L., Zhou, H.F., Lu, L.J. and Chen, Z.A., 2017. An investigation into fracture behavior of geopolymer concrete with digital image correlation technique. *Construction and Building Materials*, 155, pp. 371–380. https://doi.org/10.1016/j.conbuildmat.2017.08.041.

Yilmaz, A., Degirmenci, F.N. and Aygörmez, Y., 2024. Effect of initial curing conditions on the durability performance of low-calcium fly ash-based geopolymer mortars. *Boletín de la Sociedad Española de Cerámica y Vidrio*, 63, pp. 238–254. Available at: https://doi.org/10.1016/j.bsecv.2023.10.006.

Zhao, Y., Gong, J. and Zhao, S., 2017. Experimental study on shrinkage of HPC containing fly ash and ground granulated blast-furnace slag. *Construction and Building Materials*, 155, pp.145-153. Available at: https://doi.org/10.1016/j.conbuildmat.2017.07.020.

Zhuang, X.Y., Chen, L., Komarneni, S., Zhou, C.H., Tong, D.S., Yang, H.M., Yu, W.H. and Wang, H., 2016. Fly ash-based geopolymer: Clean production, properties and applications. *Journal of Cleaner Production*, 125, pp. 253–267. Available at: https://doi.org/10.1016/j.jclepro.2016.03.019.

APPENDIX A: Supporting Experimental and Sustainability Data

Table A1: Sieve analysis results for standard sand

Sieve sizes (mm)	Mass retained (g)	% retained	% cumulative retained	% passing	SANS 1083 (2013) range for % passing
5	0	0	0	100	92 – 100 %
2	0.9	0.09	0.09	99.91	–
1	312.3	31.23	31.32	68.68	–
0.6	241.4	24.14	55.46	44.54	–
0.3	208.2	20.82	76.28	23.72	–
0.15	171.1	17.11	93.39	6.61	5 – 25%
0.075	65.3	6.53	99.92	0.08	–
Pan	0.8	0.08	100	0	–
	1000 g	100 %			

Table A2: Sieve analysis results for crusher sand

Sieve sizes (mm)	Mass retained (g)	% retained	% cumulative retained	% passing	SANS 1083 (2013) range for % passing
5	22.22	4.44	4.44	95.60	92 – 100 %
2	131.70	26.34	30.78	69.22	–
1	87.10	17.42	48.20	51.80	–
0.6	54.40	10.88	59.08	40.92	–
0.3	65.50	13.10	72.18	27.82	–
0.15	61.30	12.26	84.44	15.56	5 – 25%
0.075	33.70	6.74	91.18	8.82	–
Pan	44.10	8.82	100	0	–
	500 g	100 %			

Table A3: Sieve analysis results for coarse aggregates

Sieve sizes (mm)	Mass retained (g)	% retained	% cumulative retained	% passing	SANS 1083 (2013) range for % passing
26.5	0	0	0	100	100 %
19	1490.6	59.620	59.620	40.380	85 – 100 %
14	953.7	38.150	97.770	2.230	15 – 55 %
10	42.9	1.720	99.490	0.510	0 – 28 %
7.1	1.5	0.060	99.550	0.450	0 – 9 %
5	0	0	99.550	0.450	5 – 25 %
2	0.4	0.016	99.566	0.434	–
1	0.3	0.012	99.578	0.422	–
Pan	10.6	0.422	100	0	–
	2500 g	100 %			

Table A4: TIEE of the GPC formulations in MJ-eq/m^3

Mix ID	Fly ash	GGBFS	Fine agg	Coarse agg	WGP	NaOH	CSS	WGSS	Water	SP	Total
M1	119.02	–	64.06	85.41	–	0.98	21.91	–	–	0	291.39
M2	119.02	–	64.06	85.41	3.22	2.01	–	–	–	1.92	275.65
M3	100.94	12.83	64.06	85.41	3.22	2.01	–	–	–	1.92	270.40
M4	84.20	24.70	64.06	85.41	3.22	2.01	–	–	–	1.92	265.53

Table A5: TIGWP of the GPC formulations in kgCO_2-eq/m^3

Mix ID	Fly ash	GGBFS	Fine agg	Coarse agg	WGP	NaOH	CSS	WGSS	Water	SP	Total
M1	8.32	–	4.48	5.97	–	0.07	1.53	–	–	–	20.37
M2	8.32	–	4.48	5.97	0.23	0.14	–	–	–	0.13	19.27
M3	7.05	0.90	4.48	5.97	0.23	0.14	–	–	–	0.13	18.90
M4	5.89	1.73	4.48	5.97	0.23	0.14	–	–	–	0.13	18.56

Table A6: EE of the GPC formulations in MJ-eq/m^3

Mix ID	Fly ash	GGBFS	Fine agg	Coarse agg	WGP	NaOH	CSS	WGSS	Water	SP	Curing	TIEE	Total
M1	65.06	–	79.06	108.00	–	814.72	1048.22	–	0.85	–	244.24	291.39	2651.55
M2	65.06	–	79.06	108.00	3.43	1668.96	–	8.41	2.73	36.11	244.24	275.648	2491.65
M3	55.18	158.11	79.06	108.00	3.43	1668.96	–	8.41	2.73	36.11	244.24	270.396	2634.62
M4	46.03	304.51	79.06	108.00	3.43	1668.96	–	8.41	2.73	36.11	244.24	265.533	2767.01

Table A7: GWP of the GPC formulations in kgCO_2-eq/m^3

Mix ID	Fly ash	GGBFS	Fine agg	Coarse Agg	WGP	NaOH	CSS	WGSS	Water	SP	Curing	TIGWP	Total
M1	5.08	–	4.86	6.60	–	37.97	148.51	–	0.08	–	44.51	20.3653	267.97
M2	5.08	–	4.86	6.60	0.85	77.78	–	2.12	0.27	23.99	44.51	19.2651	185.31
M3	4.31	0.80	4.86	6.60	0.85	77.78	–	2.12	0.27	23.99	44.51	18.898	184.97
M4	3.59	1.54	4.86	6.60	0.85	77.78	–	2.12	0.27	23.99	44.51	18.5582	184.66

Table A8: SI of the GPC formulations in kgCO_2-eq/m^3/MPa

Mix ID	GWP	EE	F_{cu}	SI	Mean ± SD
M1	267.97	2651.55	94.75	4.23	4.23 ± 0.07
			93.24	4.30	
			96.27	4.16	
M2	185.31	2491.65	27.79	11.15	11.65 ± 0.52
			25.43	12.19	
			26.71	11.60	
M3	184.97	2634.62	41.51	7.63	7.91 ± 0.56
			42.01	7.54	
			37.00	8.56	
M4	184.66	2767.01	45.65	7.08	7.06 ± 0.15
			44.80	7.21	
			46.77	6.91	

Table A9: Mix constituent breakdown for cost analysis evaluation (kg/m^3)

Mix ID	Fly ash	GGBFS	Fine agg	Coarse agg	WGP	NaOH	CSS	WGSS	Water	SP
M1	533.3	–	800	1066.6	0	37.1	160	–	69.6	0
M2	533.3	–	800	1066.6	20.5	76	–	59.4	223.5	16
M3	452.3	81	800	1066.6	20.5	76	–	59.4	223.5	16
M4	377.3	156	800	1066.6	20.5	76	–	59.4	223.5	16

Table A10: Estimated cost of GPC constituent materials and processing ($/kg)

Item	Processing	Material	Transport.	Total
Fly ash	–	0.082	0.0083	0.0903
GGBFS	–	0.110	0.0059	0.1159
Fine aggregates	–	0.032	–	0.0320
Coarse aggregates	–	0.030	–	0.030
WGP	–	0.230	0.0059	0.2359
NaOH pellets	–	0.500	–	0.500
CSS	–	0.600	–	0.600
WGSS	0.0055	–	–	0.0055
Superplasticizer	–	3.000	0.0045	3.0045
Water	–	0.0055	–	0.0055
Curing	0.0043	–	–	0.0043

Table A11: Total cost of the GPC formulations ($/m^3)

Mix ID	Fly ash	GGBFS	Fine agg	Coarse agg	WGP	NaOH	CSS	WGSS	Water	SP	Curing	Total
M1	48.16	–	25.60	32.00	–	18.55	96.00	–	0.38	–	9.46	230.15
M2	48.16	–	25.60	32.00	4.84	38.00	–	0.33	1.23	48.07	9.46	207.68
M3	40.84	9.39	25.60	32.00	4.84	38.00	–	0.33	1.23	48.07	9.46	209.75
M4	34.07	18.08	25.60	32.00	4.84	38.00	–	0.33	1.23	48.07	9.46	211.67

Table A12: EI of the GPC formulations in $/m^3/MPa

Mix ID	$Cost_t$	F_{cu}	EI	Mean ± SD
M1	230.15	94.75	2.43	2.43 ± 0.04
		93.24	2.47	
		96.27	2.39	
M2	207.68	27.79	7.47	7.81 ± 0.35
		25.43	8.17	
		26.71	7.78	
M3	209.75	41.51	5.05	5.24 ± 0.38
		42.01	4.99	
		37.00	5.67	
M4	211.67	45.65	4.64	4.63 ± 0.10
		44.8	4.72	
		46.77	4.53	

APPENDIX B: Photographic Documentation of Laboratory Work

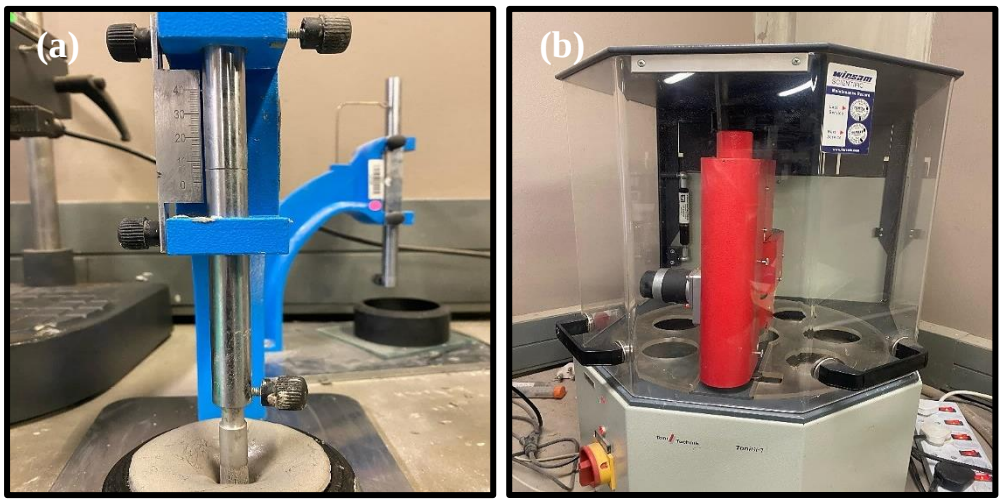

Fig. B1: Vicat apparatus used for testing geopolymer pastes for (**a**) consistency (**b**) setting time

Fig. B2: Flow spread assessment of mortar mixes

Fig. B3: Strength testing of mortar specimens (**a**) compressive (**b**) flexural

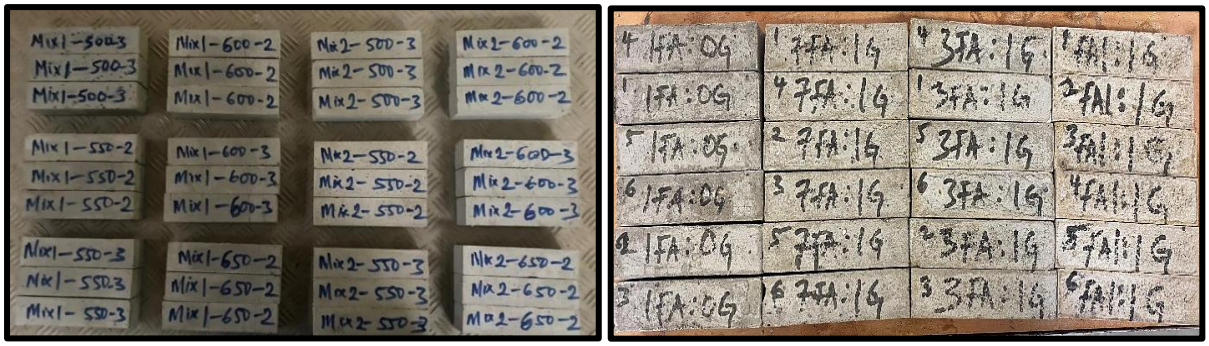

Fig. B4: Geopolymer mortar specimens

Fig. B5: Measurement of slump for geopolymer concrete mixes

Fig. B6: (**a**) Hardened concrete cubes after demoulding and (**b**) oven curing of specimens (**c**) compressive testing of cubes

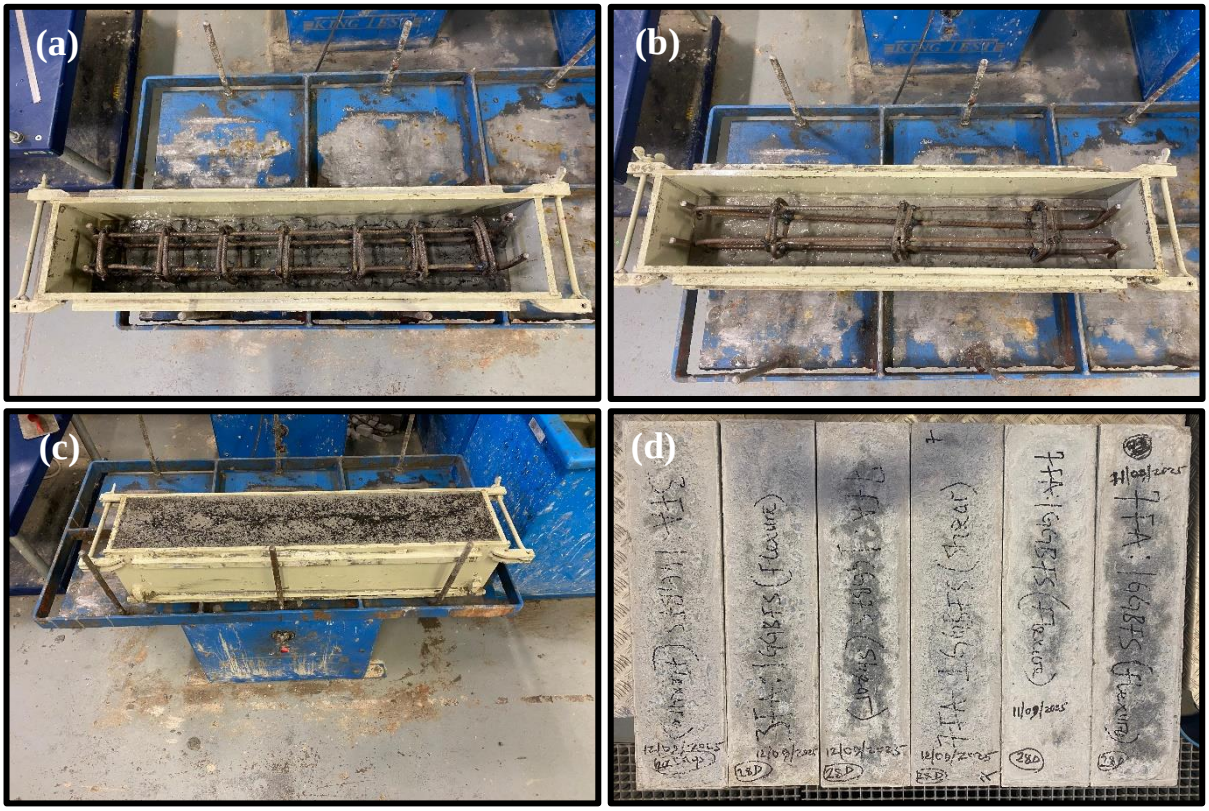

Fig. B7: Beam casting stages (**a**) placement of flexural rebar in the mould (**b**) placement of shear rebar in the mould (**c**) freshly cast GPC beam (**d**) hardened beam after demoulding

Fig. B8: Tensile testing setup for reinforcing bars

APPENDIX C: List of Publications

The following are publications arising from this dissertation:

- Kolade, A.S., Ikotun, B.D. and Oyejobi, D.O., 2025. A review of the chemistry, waste utilization, mix design and performance evaluation of geopolymer concrete. *Iranian Journal of Science and Technology, Transactions of Civil Engineering*, 49, pp. 5421–5454. Available at: https://doi.org/10.1007/s40996-025-01801-w.

- Kolade, A.S., Ikotun, B.D., Oyejobi, D.O., Aderinto, G.E. and Makungu, M.M., 2025. Performance evaluation of geopolymer mortars prepared with waste glass powder-derived sodium silicate solution. *Iranian Journal of Science and Technology, Transactions of Civil Engineering*. Available at: https://doi.org/10.1007/s40996-025-01952-w.

- Kolade, A.S., Ikotun, B.D. and Oyejobi, D.O., 2025. Composition and performance-based mix design methodology for geopolymer mortars. *Discover Civil Engineering*, 2(162). Available at: https://doi.org/10.1007/s44290-025-00327-4.

- Kolade, A.S., Ikotun, B.D. and Oyejobi, D.O., 2026. Effect of fusion conditions on valorized waste glass solution and its influence on the mechanical strength of geopolymer mortar. *Civil Engineering and Architecture*, 14(2), pp. 917–933. Available at: https://doi.org/10.13189/cea.2026.140218.

- Kolade, A.S., Ikotun, B.D. and Oyejobi, D.O., 2026. Effect of activator-to-binder ratio on workability and strength of sustainable one-part geopolymer mortar. *Materials Research Proceedings*, 63, pp 12–20. Available at: https://doi.org/10.21741/9781644904053-2.

- Kolade, A.S., Ikotun, B.D. and Oyejobi, D.O., 2026. Life cycle assessment of geopolymer concrete using fly ash–slag binder and waste glass-derived alkali activator. *Next Materials*, 12, p. 102219. Available at: https://doi.org/10.1016/j.nxmate.2026.102219.

- Kolade, A.S., Ikotun, B.D. and Oyejobi, D.O., 2026. Structural performance of reinforced geopolymer concrete beams activated with waste glass-derived sodium silicate. Manuscript under peer review at *Materials and Structures*.